

9-15-2011

Modeling Self-Referencing Interferometers with Extended Beacons and Strong Turbulence

Daniel J. Wheeler

Follow this and additional works at: <https://scholar.afit.edu/etd>

Part of the [Optics Commons](#)

Recommended Citation

Wheeler, Daniel J., "Modeling Self-Referencing Interferometers with Extended Beacons and Strong Turbulence" (2011). *Theses and Dissertations*. 1436.

<https://scholar.afit.edu/etd/1436>

This Dissertation is brought to you for free and open access by the Student Graduate Works at AFIT Scholar. It has been accepted for inclusion in Theses and Dissertations by an authorized administrator of AFIT Scholar. For more information, please contact richard.mansfield@afit.edu.



**MODELING SELF-REFERENCING
INTERFEROMETERS WITH EXTENDED
BEACONS AND STRONG TURBULENCE**

DISSERTATION

Daniel J. Wheeler, Major, USAF
AFIT/DEO/ENG/11-12

**DEPARTMENT OF THE AIR FORCE
AIR UNIVERSITY**

AIR FORCE INSTITUTE OF TECHNOLOGY

Wright-Patterson Air Force Base, Ohio

APPROVED FOR PUBLIC RELEASE; DISTRIBUTION UNLIMITED.

The views expressed in this document are those of the author and do not reflect the official policy or position of the United States Air Force, the United States Department of Defense or the United States Government.

This material is declared the work of the U.S. Government and is not subject to copyright protection in the United States.

AFIT/DEO/ENG/11-12

MODELING SELF-REFERENCING INTERFEROMETERS WITH EXTENDED
BEACONS AND STRONG TURBULENCE

DISSERTATION

Presented to the Faculty
Graduate School of Engineering and Management
Air Force Institute of Technology
Air University
Air Education and Training Command
in Partial Fulfillment of the Requirements for the
Degree of Doctor of Philosophy

Daniel J. Wheeler, B.S.E.E., M.S.
Major, USAF

September 2011

APPROVED FOR PUBLIC RELEASE; DISTRIBUTION UNLIMITED.

AFIT/DEO/ENG/11-12

MODELING SELF-REFERENCING INTERFEROMETERS WITH EXTENDED
BEACONS AND STRONG TURBULENCE

Daniel J. Wheeler, B.S.E.E., M.S.
Major, USAF

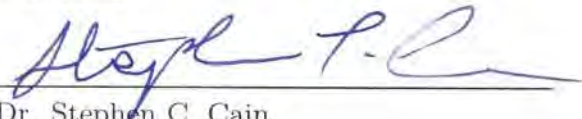
Approved:



Maj Jason D. Schmidt
Chairman

4 Aug 11

Date



Dr. Stephen C. Cain
Member

4 Aug 2011

Date

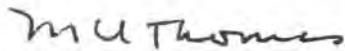


Lt Col John R. Dea
Member

4 AUG 11

Date

Accepted:



M. U. Thomas
Dean, Graduate School of Engineering
and Management

30 Aug 2011

Date

Abstract

The overall purpose of this research was to better understand the performance of a self-referencing interferometer (SRI) when used with extended beacons in strong atmospheric turbulence. It was performed by assuming the extended beacon could be modeled as a Gaussian Schell-model beam, then analyzing the effect of propagating this beam through strong atmospheric turbulence. Since the operation of an SRI requires coupling this light into a single-mode optical fiber, analytic expressions of the mean and normalized variance of the coupling efficiency were derived. An improved noise model for the SRI was then developed that included all potential noise sources such as intensity fluctuations of the incident light, the single-mode fiber coupling efficiency, the spatial and temporal coherence properties of the light, and other additive noise sources. Whenever simplifying assumptions were used, the results were compared to numerically evaluated exact expressions or Monte Carlo simulations. Any resulting error was identified then typically compensated. These results not only serve to address problems when using adaptive optics to correct for strong turbulence using extended beacons, but may also be useful in other applications such as directed energy, free-space optical communications, stellar interferometry, and ladar/lidar systems.

AFIT/DEO/ENG/11-12

To my wife and kids. Your patience and understanding is greatly appreciated.

Acknowledgements

I first must acknowledge the extraordinary assistance provided by my adviser, Maj Jason Schmidt. Not only did he help identify where I should initially focus my research efforts, but he was also there every step of the way with encouragement and counsel. It truly was a pleasure working with him in this endeavor. Additionally, I thank the other members of my committee and the AFIT OPTECS group for their feedback and fruitful conversations. I must also acknowledge Dr. Greg Gbur from the University of North Carolina at Charlotte for providing code to simulate the temporal evolution of a Gaussian Schell-model beam. Not only was this a valuable tool for my Ph.D. research, but it should also be very useful in my future work at the Air Force Research Lab. Finally, I am very grateful to the Air Force Office of Scientific Research for providing the funding for my research through grant F1ATA08350J002.

Daniel J. Wheeler

Table of Contents

	Page
Abstract	iv
Acknowledgements	vi
List of Figures	ix
List of Listings	xi
I. Introduction	1
1.1 Problem Statement	2
1.2 Methodology	3
1.2.1 Source Beacon Characteristics	4
1.2.2 Atmospheric Turbulence	5
1.2.3 SRI Performance	6
1.3 Original Contributions	7
II. Background	9
2.1 Scalar Diffraction Theory	9
2.1.1 Maxwell's Equations	10
2.1.2 Rayleigh-Sommerfeld Equation	12
2.1.3 Non-monochromatic Light	14
2.1.4 Fresnel Approximation	16
2.2 Coherence Theory	17
2.3 Gaussian Schell-Model (GSM) Beams	20
2.4 Atmospheric Turbulence Theory	21
2.4.1 Weak Turbulence	23
2.4.2 Strong Turbulence	40
2.5 Self-Referencing Interferometer (SRI)	49
2.6 Single-Mode Optical Fibers	52
III. Review of Related Research	60
3.1 Partially Coherent Fields in Strong Turbulence	60
3.2 Coupling of Random Fields into Single-mode Fibers	62
3.3 SRI Performance	64
IV. GSM Beams in Atmospheric Turbulence	66
4.1 Introduction	66
4.2 Theoretical Foundation	67
4.2.1 Quadratic Approximation	71

	Page
4.2.2 Effective Parameters	73
4.2.3 Modified Effective Parameters	76
4.3 Coherence Radius Accuracy	78
4.4 Coherence Function Shape	83
4.5 Effect of Source Coherence	87
4.6 Conclusion	88
V. Coupling of GSM Beams Into Single-Mode Optical Fibers	91
5.1 Introduction	91
5.2 Mean Coupling Efficiency	94
5.2.1 Fiber Coupling Overview	94
5.2.2 Mean Coupling of GSM Beams	97
5.2.3 Mean Coupling Efficiency Compensation	101
5.3 Coupling Variance	111
5.3.1 Fully Speckled Beams	112
5.3.2 Computer Simulations	116
5.4 Conclusion	127
VI. General SRI Noise Model	130
6.1 Introduction	130
6.2 SRI Overview	131
6.3 Phase Error Variance	135
6.3.1 Conditioned Phase Error Variance	136
6.3.2 Unconditioned Phase Error Variance	138
6.4 Monte Carlo Simulations	145
6.5 Examples	149
6.6 Conclusion	153
VII. Conclusion	155
7.1 Original Contributions	156
7.2 Future Work	157
Appendix A: Fiber Coupling Integrals	159
Appendix B: σ_ε^2 For Various Probability Distributions of I_i and η_i	164
Appendix C: MATLAB [®] Scripts	168
Bibliography	192

List of Figures

Figure	Page
1. Schematic diagram of the adaptive optics problem to be addressed in this research.	3
2. Scintillation index at various turbulence strengths	46
3. Phase contour plot	49
4. Self-referencing interferometer (SRI) diagram	50
5. Diagram of a single-mode optical fiber	53
6. Difference in the absolute error between various methods of calculating the coherence radius	79
7. Absolute error of different methods of estimating the coherence radius	82
8. Difference in the absolute error between various methods of estimating the coherence radius	84
9. Comparison of different methods of estimating the coherence function exponential power	86
10. Fiber coupling diagram	95
11. Exact and approximate fiber mode comparison	98
12. Mean fiber coupling analytic and algebraic approximation comparison	101
13. Error in the analytic expression and algebraic approximation of mean fiber coupling	105
14. A realization of a speckled field	109
15. Error in mean coupling efficiency expression due to speckle	110
16. Effect of compensation for speckle on mean coupling efficiency expression	111
17. Normalized coupling variance for fully developed speckle fields	115

Figure	Page
18. Error in algebraic approximation of normalized coupling variance for well-developed speckle fields	120
19. Effect of compensation on normalized coupling variance expression for well-developed speckle fields	122
20. Realization of a non-speckled field	125
21. Error in normalized coupling variance expression for non-speckled fields	126
22. Effect of compensation on normalized coupling variance expression for non-speckled fields	127
23. Conceptual diagram of a self-referencing interferometer	132
24. Interference patterns using four-bin phase-shifting interferometry	134
25. Error in Taylor approximation of $1/\text{sinc}^2(x)$	140
26. Comparison between the phase error variance model and Monte Carlo simulations for a given input	146
27. Comparison between the phase error variance model and Monte Carlo simulations for small intensity and coupling efficiency variations	147
28. Comparison between the phase error variance model and Monte Carlo simulations with an exponentially distributed intensity	148
29. Comparison between the phase error variance model and Monte Carlo simulations both the intensity and coupling efficiency are exponentially distributed	148
30. SRI performance in strong turbulence	150
31. SRI performance with an extended source beacon	151

List of Listings

Listing	Page
C.1. AbsorptionBound.m	168
C.2. AngSpecProp.m	168
C.3. AtmosModel.m	169
C.4. GSM_MCF_turb.m	170
C.5. GSMSource.m	172
C.6. GSMSource_temporal.m	173
C.7. Integrate38.m	175
C.8. intvec.m	177
C.9. PhaseScrnGen.m	178
C.10. PointSource.m	181
C.11. PropHorizTurb.m	182
C.12. SMF_coupling_hard.m	184
C.13. SMF_normvar_full_speckle.m	186
C.14. SRIsim.m	187
C.15. param2stats.m	190
C.16. stats2param.m	191

MODELING SELF-REFERENCING INTERFEROMETERS WITH EXTENDED BEACONS AND STRONG TURBULENCE

I. Introduction

The astronomical and military research communities have achieved a great deal of success in improving imaging performance of ground-based telescopes by compensating for distortions due to atmospheric turbulence with adaptive optics (AO) [70, 84]. AO typically compensates for atmospheric distortions in real-time by using a wavefront sensor (WFS) to measure the distortions with respect to a reference wavefront, then uses those measurements to reshape a deformable mirror (DM) in a manner conjugate to the distortion. Not only can this be used to correct incoming light, but it can also be used to precondition outgoing laser beams. Lasers that have been preconditioned in this way put more energy into a smaller area at their target [84]. This technique has military applications in long range imaging, laser communications, and laser weapons. The research reported here focused on two challenging areas for AO: large irradiance fluctuations of the measured light and extended beacons. The overall goal was to better understand and quantify how they affect a specific WFS known as the self-referencing interferometer (SRI).

This chapter states the overall problem the research was designed to address, then outline the methodology used to address it. Background material on the propagation of random electromagnetic fields through atmospheric turbulence and the function of an SRI are given in Chapter II. Chapter III reviews the currently published literature that is relevant to this research, and identifies the areas that were available for additional significant contributions. The bulk of the research, along with the major

results, is located in Chapters IV–VI. Chapter IV describes a more accurate method of estimating a key parameter of random beams as they propagate through atmospheric turbulence of all strengths, Chapter V derives analytic expressions for the average coupling efficiency and its variance of these beams into single-mode optical fibers, and Chapter VI presents a more accurate noise model for the SRI than has been previously published. These results are used in Chapter VII to discuss how strong atmospheric turbulence and extended beacons affect the performance of an SRI. Additionally, it enumerates the novel contributions of this research, and makes suggestions for future applications and work.

1.1 Problem Statement

Much of the success of AO has been limited to circumstances of relatively weak turbulence, for example when imaging a star nearly overhead. Because astronomers are interested in viewing as much of the sky as possible, they are quickly progressing towards similar success in imaging through moderate turbulence caused by propagation through thicker sections of atmosphere associated with lower elevation angles [86]. However, adaptive optics for military applications, like those on airborne platforms, must be able to sense and correct for extremely strong turbulence caused by propagation along horizontal paths through the atmosphere, as well as the turbulence associated with the movement of the platform through the atmosphere [84]. In addition, unlike in many astronomical applications, there is rarely a point source beacon available that can be used as a reference for measuring the atmospheric disturbances, so an extended beacon must be used instead [72] as shown in Fig. 1. The military interest in this area is so significant that the Air Force Scientific Advisory Board (SAB) recently issued a “horizontal propagation compensation” (HPC) challenge to focus research efforts on the problem of AO in deep turbulence engagement scenarios [69].

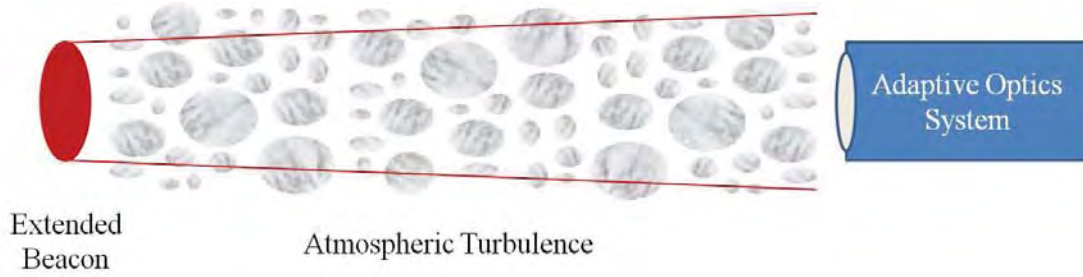


Figure 1. Schematic diagram of the adaptive optics problem to be addressed in this research.

This research into the performance of an SRI when used with strong turbulence and extended beacons serves to address one particular part of this overall problem, and provides some needed analytic tools to aid in further answering this challenge.

1.2 Methodology

As indicated in Fig. 1, there are three primary parts to the problem at hand. The first is to identify an extended source model to generate the fields to be measured by the SRI. Ideally, this source model should be flexible enough to describe a wide range of potential source beacons, yet simple enough to produce analytically tractable results. The second part is to describe the evolution of these fields as they propagate through atmospheric turbulence. The goal here is to analytically relate the key characteristic parameters of the fields at the end of the propagation path to key parameters of the initial fields and the intervening atmospheric turbulence. In keeping with the HPC challenge, it is assumed the turbulence is statistically homogeneous across the entire propagation path. The final part is to analyze the effect of these fields on the performance of an SRI. Since AO system performance is typically directly related to the cumulative phase error variance of the system components [73], the goal here is to derive a noise model for an SRI that estimates its phase error variance given the key characteristics of the incident field and typical noise sources.

By this method, it should be possible to predict the expected performance of an SRI given a particular source and turbulence profile.

1.2.1 Source Beacon Characteristics.

In practice, there are several ways in which an extended beacon can be formed. It can be the result of passive reflection (glint) from a bright third party source (such as the sun), from active illumination by the optical system, or the source may be self-luminescent. Each of these different methods have their own set of benefits and drawbacks, but ultimately what matters most is the nature of the light emanating from the source, not how the light was initially formed. The key characteristics are its size, coherence, and polarization properties.

The source will be of finite size, but typically too large to be considered a point source. While the shape of the source may be oblong or even irregular, to simplify the problem only circularly symmetric sources will be considered in this analysis. The results of this analysis may then be extended to elliptically shaped sources without undue difficulty.

The coherence properties of the source describe its statistical nature and can be defined both spatially and temporally. This research assumes that the source is cross-spectrally pure, meaning the spatial and temporal coherence properties can be treated separately [38,57]. It further assumes that the source is statistically homogeneous, or that correlations of the field depend only on spatial or temporal separation distances and not their actual locations. While it is possible to find situations where these assumptions do not hold, they should still be sufficient to simplify the analysis and yet cover a wide range of expected sources.

While the light emanating from the source comprises a vector field, this analysis assumes that scalar diffraction theory holds. This means that not only is there no

coupling between the various components of the field [39], but there is no coupling between its degree of polarization and degree of coherence [95]. This is the case as long as the source is either linearly polarized, or it is unpolarized and the orthogonal components of the field tangential to the direction of propagation are statistically identical [50]. Since unpolarized light can act as an additional noise source for an SRI, it will generally be assumed the source is linearly polarized (or that a linearly polarized filter is used prior to the SRI.)

One source model that has been used extensively in the literature and fits the above criteria is the Gaussian-Schell model (GSM) [24, 26, 37, 47, 49, 53, 57, 68, 78, 80, 88, 97]. It can be used to model any source size from a point source to a plane wave, or any coherence size from fully coherent to fully incoherent. Since it is completely defined in terms of Gaussian functions, it provides analytically tractable results in many instances. For these reasons, a GSM source was selected to form the basis of this research. Further information on GSM sources and beams is given in Chapter II.

1.2.2 Atmospheric Turbulence.

Characterizing atmospheric turbulence has been a topic of study since the 1940's [48]. While there are several turbulence models available, they mostly differ in the way they characterize very large or very small spatial frequencies [2]. The middle region, known as the inertial subrange, is typically the same in all models. Since separation distances of interest typically fall within the inertial subrange, the research focused on this region.

Turbulence can be characterized as either weak or strong. Weak turbulence is where the turbulence mainly acts to randomly refract the propagating field. This refraction primarily affects the phase of the field, and it can be accurately described using Rytov perturbation theory [2, 43, 82]. However, in strong turbulence, this re-

fraction culminates in diffraction which is observed as large amplitude fluctuations of the field. In this case, Rytov theory is no longer sufficient, and alternative methods must be used to characterize its effects [2, 43].

The intent of this portion of the research is to understand the statistical characteristics of a field at the end of a propagation path given its statistical properties at the beginning of the path and the profile of the intervening turbulence. Since there are no exact solutions to this problem, it becomes an exercise in selecting the best approximation. Not only is it important to understand which method gives the most accurate result for a given condition, but also the size of its error. With this information, empirical compensation can be used to increase its accuracy.

1.2.3 SRI Performance.

The SRI is a relatively simple optical system that comprises beam splitters, mirrors, coupling lenses, a single-mode optical fiber, and a detector. Assuming proper alignment, the only components that contribute significantly to the measurement noise of the SRI are the single-mode fiber and the detector. This portion of the research is therefore broken into two parts: analyzing the effect of coupling random fields into a single-mode fiber, and developing an overall noise model for the SRI.

While much work has been done to characterize the mean coupling efficiency of random fields into single-mode fibers [23, 75, 79, 94], very little has been done on characterizing its variance [75, 79]. Furthermore, past studies have typically assumed insignificant amplitude fluctuations in the incident field. The goal of this study is to not only develop analytic expressions for the mean coupling efficiency and its variance, but also to analyze the effect when the incident field contains significant amplitude fluctuations. This study will not only aid the development of a noise model for an SRI, but it can also contribute to the characterization of other systems that incorporate

single-mode fibers, such as free-space optical communication, stellar interferometry, and lidar/lidar systems [23, 45, 75, 79, 90, 94].

The major sources of detector noise are shot noise, read noise, and quantization noise. Since they are independent noise sources, they can be treated separately. Read noise and quantization noise are due to the electronic read-out circuitry and have been extensively studied [46]. Shot noise is due to the wave/particle duality of light and is fundamental to any light measuring device [38]. As shot noise is directly related to the intensity of the light incident on the detector, all the sources of intensity randomness (partial coherence of the light source, atmospheric turbulence, and the fiber coupling efficiency) contribute to the overall shot noise. By taking into account all of these sources of randomness, it is possible to develop an SRI noise model that is appropriate for nearly any given situation.

1.3 Original Contributions

Some of the significant contributions of this research include

1. A generally more accurate method of estimating the coherence radius of partially coherent Gaussian beams at all levels of turbulence,
2. A better understanding of the shape of the coherence function of partially coherent Gaussian beams at all levels of turbulence,
3. Constraints on the degree of coherence of a GSM source that would allow for the use of an SRI to predominately measure atmospherically induced phase perturbations,
4. Analytic expressions for the mean coupling efficiency of GSM beams into single-mode optical fibers,

5. Analytic expressions for the coupling variance of GSM beams into single-mode optical fibers,
6. A better understanding of the effect of speckle on the coupling of GSM beams into single mode optical fibers,
7. A more accurate noise model for an SRI,
8. A better understanding of the effect of extended beacons and strong turbulence on the performance of an SRI.

Many of these results can be used in other optical applications as well. The first two may be useful in any application where partially coherent Gaussian beams traverse atmospheric turbulence. This includes free-space optical communication and ladar/lidar. Items four through six can be applied to any application where random fields that can be closely approximated as GSM beams couple into single mode optical fibers. These results also provide a method that can be used to analyze the coupling of GSM beams into multi-mode optical fibers. The SRI noise model can not only be used to predict SRI performance in a given situation, but also used as a design aid when building an SRI for a given application. As such, it may serve as the basis for trade studies among the various SRI design parameters.

II. Background

This research required the use of many branches of optics including Fourier optics, statistical optics, atmospheric turbulence theory, interferometry, and guided-wave optics. As a result, it is important to understand the basics of each of these fields and how they apply to the problem at hand. The following overview focuses on the cases where a light source can either be considered a point source or a Gaussian beam.

This chapter begins by outlining scalar diffraction theory and coherence theory. Based on this foundation, GSM sources and fields are then defined. This is followed by an overview of both weak and strong turbulence theory. Finally, the SRI is defined along with the basics of its operations. Particular attention is given to the behavior of single-mode optical fibers and the use of phase shifting interferometry (PSI) to make the SRI measurements.

2.1 Scalar Diffraction Theory

As with any theory that deals with the propagation of electro-magnetic waves, scalar diffraction theory begins with Maxwell's equations. Given certain assumptions regarding the propagation medium, Maxwell's vector equations can be reduced to uncoupled scalar equations. These scalar equations form the basis of the Rayleigh-Sommerfeld equation which can be used to calculate the field at any point given the field along a two-dimensional plane. Assumptions regarding the geometry of this propagation allow for a simplification of the Rayleigh-Sommerfeld equation, known as the Fresnel approximation, which then forms the basis of Fourier optics.

2.1.1 Maxwell's Equations.

The starting point for describing electromagnetic propagation through any medium is Maxwell's equations [44]. They can be expressed in vector form and SI units as

$$\nabla \cdot \mathbf{D} = \rho, \quad (2.1.1)$$

$$\nabla \cdot \mathbf{B} = 0, \quad (2.1.2)$$

$$\nabla \times \mathbf{E} + \frac{\partial \mathbf{B}}{\partial t} = 0, \quad (2.1.3)$$

$$\nabla \times \mathbf{H} - \frac{\partial \mathbf{D}}{\partial t} = \mathbf{J}, \quad (2.1.4)$$

where \mathbf{D} is the electric displacement, ρ is the charge density, \mathbf{B} is the magnetic induction, \mathbf{E} is the electric field, \mathbf{H} is the magnetic field, and \mathbf{J} is the current density. For linear and isotropic materials, such as the atmosphere, there is a simple relationship between \mathbf{D} and \mathbf{E} , and \mathbf{B} and \mathbf{H} such that

$$\mathbf{D} = \epsilon \mathbf{E}, \quad (2.1.5)$$

$$\mathbf{B} = \mu \mathbf{H}, \quad (2.1.6)$$

where ϵ is the electric permittivity of the medium and μ is the magnetic permeability of the medium. With the additional assumptions that there are no free charges or current, the medium is nonmagnetic ($\mu = \mu_0$, the permeability of vacuum), and $\mathbf{E} \partial \epsilon / \partial t \ll \epsilon \partial \mathbf{E} / \partial t$, Eqs. (2.1.1)–(2.1.4) can be expressed in terms of the electric and magnetic fields

$$\nabla \cdot \epsilon \mathbf{E} = 0 \quad (2.1.7)$$

$$\nabla \cdot \mathbf{H} = 0 \quad (2.1.8)$$

$$\nabla \times \mathbf{E} = -\mu_0 \frac{\partial \mathbf{H}}{\partial t} \quad (2.1.9)$$

$$\nabla \times \mathbf{H} = \epsilon \frac{\partial \mathbf{E}}{\partial t}. \quad (2.1.10)$$

Combining the curl of Eq. (2.1.9) with Eq. (2.1.7) produces the wave equation for electromagnetic propagation in a linear, isotropic, nonmagnetic medium

$$\nabla^2 \mathbf{E} + \nabla (\mathbf{E} \cdot \nabla \ln \epsilon) = \mu_0 \epsilon \frac{\partial^2 \mathbf{E}}{\partial t^2}. \quad (2.1.11)$$

An equivalent wave equation can be derived for the magnetic field in the same manner. As long as $\nabla (\mathbf{E} \cdot \nabla \ln \epsilon) \ll \nabla^2 \mathbf{E}$, the second term on the left of Eq. (2.1.11) can be ignored. This is obviously the case in a homogeneous medium where $\nabla \ln \epsilon = 0$, but even in a non-homogeneous medium such as atmospheric turbulence this is often the case [2]. This results in a set of three uncoupled equations which describe the behavior of each component of the electric field. Since the behavior is identical for each component, it is only necessary to solve a single scalar equation to describe the behavior of the entire field.

Assuming the field is monochromatic, one component of \mathbf{E} can be approximated as a complex analytic signal with

$$E(\mathbf{r}, t) \simeq A(\mathbf{r}) \exp \{j [\phi(\mathbf{r}) - 2\pi\nu_t t]\}, \quad (2.1.12)$$

where A is the amplitude and ϕ is the phase at any location in free space, ν_t is the central optical frequency, and $j = \sqrt{-1}$. The physical field is simply found from Eq. (2.1.12) by doubling its real part [57]. Since A and ϕ only depend on position and not time, let

$$U = A \exp(j\phi) \quad (2.1.13)$$

so

$$E(\mathbf{r}, t) \simeq U(\mathbf{r}) \exp(-j2\pi\nu_t t). \quad (2.1.14)$$

Inserting (2.1.14) into the component version of (2.1.11) gives

$$[\nabla^2 + (2\pi\nu_t)^2 \mu_0\epsilon] U = 0. \quad (2.1.15)$$

Using the definitions of $n = (\epsilon/\epsilon_0)^{1/2}$ and $c = (\mu_0\epsilon_0)^{-1/2}$, as well as defining $k = 2\pi\nu_t/c$, Eq. (2.1.15) can be written as the Helmholtz equation

$$(\nabla^2 + k^2 n^2) U = 0. \quad (2.1.16)$$

Assuming a homogeneous medium with $n \cong 1$, one of the simplest solutions to Eq. (2.1.16) is that of a point source located at \mathbf{r}_0 given by

$$U(\mathbf{r}) = \frac{\exp(jk|\mathbf{r} - \mathbf{r}_0|)}{|\mathbf{r} - \mathbf{r}_0|}. \quad (2.1.17)$$

However, what is desired is an expression for the field at one point given the field on a plane a distance L away. This can be found using the Rayleigh-Sommerfeld equation.

2.1.2 Rayleigh-Sommerfeld Equation.

The Rayleigh-Sommerfeld is derived through the use of Green's Theorem

$$\iiint_{\mathcal{V}} (U\nabla^2 G - G\nabla^2 U) dv = \iint_{\mathcal{S}} \left(U \frac{\partial G}{\partial n} - G \frac{\partial U}{\partial n} \right) ds, \quad (2.1.18)$$

where U and G are continuous scalar fields, along with their first and second partial derivatives, \mathcal{V} is a given volume with volume element dv , \mathcal{S} is the surface of the volume with surface element ds , and $\partial/\partial n$ is a partial derivative in the outward normal direction of surface \mathcal{S} . As long as both U and G satisfy Eq. (2.1.16), the left side of Eq. (2.1.18) equals zero.

If the G used is a point source like that of Eq. (2.1.17), that point must be excluded from the volume, otherwise the field within the volume would contain a discontinuity. That means the volume actually has two surfaces: an outer surface and a diminishingly small inner surface. Evaluating the integral along in the inner surface, Eq. (2.1.18) becomes

$$U(\mathbf{r}_0) = \frac{1}{4\pi} \iint_S \left(G \frac{\partial U}{\partial n} - U \frac{\partial G}{\partial n} \right) ds, \quad (2.1.19)$$

where \mathbf{r}_0 is the location of the discontinuity [39] and the integration now only over the outer surface.

If S is composed of two surfaces, a plane located a distance L from \mathbf{r}_0 and a sphere extending out to infinity, then as long as

$$\lim_{R \rightarrow \infty} R \left(\frac{\partial U}{\partial n} - jkU \right) = 0, \quad (2.1.20)$$

where R is the radius of the sphere, the integral over the surface of the sphere does not contribute to the total and can be ignored [39]. The integral in Eq. (2.1.19) now only needs to be performed over the plane.

By choosing G such that it is composed of two point sources, one at \mathbf{r}_0 and the other at the exact opposite side of the plane, which are radiating 180° out of phase, G is exactly zero along the plane. The partial derivative of G with respect to the surface normal along that surface can be expressed as

$$\frac{\partial G}{\partial n} = 2 \cos(\mathbf{n}, \mathbf{r}' - \mathbf{r}_0) \left(jk - \frac{1}{|\mathbf{r}' - \mathbf{r}_0|} \right) \frac{\exp(jk|\mathbf{r}' - \mathbf{r}_0|)}{|\mathbf{r}' - \mathbf{r}_0|}, \quad (2.1.21)$$

where \mathbf{n} is the plane's surface normal vector and \mathbf{r}' is a point on the plane [39].

Assuming $|\mathbf{r}' - \mathbf{r}_0| \gg \lambda$, the second term can be dropped leaving

$$\frac{\partial G}{\partial n} = 2jk \cos(\mathbf{n}, \mathbf{r}' - \mathbf{r}_0) \frac{\exp(jk|\mathbf{r}' - \mathbf{r}_0|)}{|\mathbf{r}' - \mathbf{r}_0|}. \quad (2.1.22)$$

Making all these changes to Eq. (2.1.19) produces the Rayleigh-Sommerfeld equation

$$U(\mathbf{r}_0) = \frac{1}{j\lambda} \iint_{\mathcal{P}} U(\mathbf{r}') \frac{\exp(jk|\mathbf{r}' - \mathbf{r}_0|)}{|\mathbf{r}' - \mathbf{r}_0|} \cos(\mathbf{n}, \mathbf{r}' - \mathbf{r}_0) d\mathbf{r}', \quad (2.1.23)$$

where $U(\mathbf{r}')$ is the field along the plane \mathcal{P} .

2.1.3 Non-monochromatic Light.

While the above analysis only strictly applies to monochromatic waves, it can be extended to non-monochromatic fields using Fourier analysis. A non-monochromatic complex analytic signal can be defined by the inverse Fourier transform of its frequency components as¹

$$E(\mathbf{r}, t) = \int_0^{\infty} \mathcal{U}(\mathbf{r}, \nu_t) \exp(-j2\pi\nu_t t) d\nu_t. \quad (2.1.24)$$

Since the Fourier components are monochromatic, they individually propagate according to the Rayleigh-Sommerfeld equation as

$$\mathcal{U}(\mathbf{r}_0, \nu_t) = \frac{-j\nu_t}{c} \iint_{\mathcal{P}} \mathcal{U}(\mathbf{r}', \nu_t) \frac{\exp(j2\pi\nu_t|\mathbf{r}' - \mathbf{r}_0|/c)}{|\mathbf{r}' - \mathbf{r}_0|} \cos(\mathbf{n}, \mathbf{r}' - \mathbf{r}_0) d\mathbf{r}'. \quad (2.1.25)$$

¹The integral starts at zero since a complex analytic signal has no negative frequency components [57].

Taking the inverse Fourier transform of this expression and changing the order of integration produces

$$E(\mathbf{r}_0, t) = \iint_{\mathcal{P}} \frac{\cos(\mathbf{n}, \mathbf{r}' - \mathbf{r}_0)}{2\pi c |\mathbf{r}' - \mathbf{r}_0|} \times \int_0^\infty (-j2\pi\nu_t) \mathcal{U}(\mathbf{r}', \nu_t) \exp \left[-j2\pi\nu_t \left(t - \frac{|\mathbf{r}' - \mathbf{r}_0|}{c} \right) \right] d\nu_t d\mathbf{r}'. \quad (2.1.26)$$

Given

$$\frac{\partial}{\partial t} E(\mathbf{r}, t) = \int_0^\infty (-j2\pi\nu_t) \mathcal{U}(\mathbf{r}, \nu_t) \exp(-j2\pi\nu_t t) d\nu_t, \quad (2.1.27)$$

Eq. (2.1.26) can be expressed as

$$E(\mathbf{r}_0, t) = \iint_{\mathcal{P}} \frac{\cos(\mathbf{n}, \mathbf{r}' - \mathbf{r}_0)}{2\pi c |\mathbf{r}' - \mathbf{r}_0|} \frac{\partial}{\partial t} E \left(\mathbf{r}', t - \frac{|\mathbf{r}' - \mathbf{r}_0|}{c} \right) d\mathbf{r}'. \quad (2.1.28)$$

If the field only has frequency components close to the central frequency, it is narrowband, or quasi-monochromatic, and can be expressed as

$$E(\mathbf{r}, t) = U(\mathbf{r}, t) \exp(-j2\pi\bar{\nu}_t t), \quad (2.1.29)$$

where $\bar{\nu}_t$ is the central frequency of E . Since the frequency components of U are much lower than $\bar{\nu}_t$, the time derivative of E is well approximated by

$$\frac{\partial}{\partial t} E(\mathbf{r}, t) \simeq -j2\pi\bar{\nu}_t U(\mathbf{r}, t) \exp(-j2\pi\bar{\nu}_t t). \quad (2.1.30)$$

Inserting this into Eq. (2.1.28) produces

$$U(\mathbf{r}_0, t) = \frac{1}{j\lambda} \iint_{\mathcal{P}} U \left(\mathbf{r}', t - \frac{|\mathbf{r}' - \mathbf{r}_0|}{c} \right) \frac{\exp(j\bar{k}|\mathbf{r}' - \mathbf{r}_0|)}{|\mathbf{r}' - \mathbf{r}_0|} \cos(\mathbf{n}, \mathbf{r}' - \mathbf{r}_0) d\mathbf{r}'. \quad (2.1.31)$$

The only differences between this expression and Eq. (2.1.23) come from replacing k

and λ with \bar{k} and $\bar{\lambda}$, and time shifting field at \mathcal{P} . Similar substitutions should change any expression for monochromatic waves into one for a narrowband field.

2.1.4 Fresnel Approximation.

Using Eq. (2.1.23) it is possible to find the field in an observation plane given the field in a parallel source plane a distance L away. While the following derivation assumes a monochromatic field, it can be extended to narrowband fields by making the same substitutions mentioned at the end of the previous section. Aligning the coordinate axis such that the origin lies in the source plane and the z -axis is perpendicular to the two planes, and using the relation $\cos(\mathbf{n}, \mathbf{r}' - \mathbf{r}_0) = L/|\mathbf{r}' - \mathbf{r}_0|$, Eq. (2.1.23) can be written as

$$U(x, y) = \frac{L}{j\lambda} \iint U(u, v) \frac{\exp \left[jk \sqrt{L^2 + (x - u)^2 + (y - v)^2} \right]}{L^2 + (x - u)^2 + (y - v)^2} du dv. \quad (2.1.32)$$

Assuming that $L \gg x - u$ and $L \gg y - v$ wherever the field is non-negligible, the radical in the exponential can be expanded in a Taylor series approximation to

$$\sqrt{L^2 + (x - u)^2 + (y - v)^2} \cong L \left[1 + \frac{1}{2} \left(\frac{x - u}{L} \right)^2 + \frac{1}{2} \left(\frac{y - v}{L} \right)^2 \right]. \quad (2.1.33)$$

This assumption also allows for dropping all but the L^2 term in the denominator under the exponential [39]. These changes comprise the Fresnel approximation, which can be expressed as

$$U(x, y) = \frac{\exp(jkL)}{j\lambda L} \iint U(u, v) \exp \left\{ \frac{jk}{2L} [(x - u)^2 + (y - v)^2] \right\} du dv. \quad (2.1.34)$$

Since this expression is essentially a convolution of $U(u, v)$ and $\exp \left[\frac{jk}{2L} (u^2 + v^2) \right]$, it can be efficiently evaluated using Fourier transforms, and forms the basis of Fourier

optics.

One particular example where this relation is very useful is when a thin spherical lens is used to focus incident light. Since the lens only affects the phase of the impinging light, the field immediately behind the lens can be expressed as

$$U(u, v) = U'(u, v) \exp \left[-\frac{j\pi}{\lambda f} (u^2 + v^2) \right], \quad (2.1.35)$$

where $U'(u, v)$ is the field immediately in front of the lens and f is the lens focal length [39]. Inserting this into Eq. (2.1.34) and using $L = f$ gives

$$U(x, y) = \frac{\exp \left[jkf + \frac{jk}{2f} (x^2 + y^2) \right]}{j\lambda f} \iint_{\mathcal{P}} U'(u, v) P(u, v) \exp \left[-\frac{j2\pi}{\lambda f} (xu + yv) \right] du dv, \quad (2.1.36)$$

where P defines the aperture pupil of the lens (equals 1 within the lens and 0 outside the lens). This expression states that there is a direct Fourier transform relationship between the field incident on the lens and the field in the focal plane. This relation is not exact due to the quadratic phase factor, but this phase factor can be eliminated by simply adding another lens of focal length f at the focal plane.

2.2 Coherence Theory

The fields of interest in this research are random, so statistical means are needed to analyze them. Of primary concern is coherence which describes the degree to which one point of the field is related to any other point of the field in time or space. A field is coherent when there is a fixed relation between one point and all other points of the field. A field is then incoherent when there is no fixed relation between one point and any other points. Fields that are partially coherent fall somewhere between these

two extremes. The primary method to describe the coherence of a field is the mutual coherence function (MCF) defined as

$$\Gamma(\mathbf{r}_1, \mathbf{r}_2; t_1, t_2) = \langle U(\mathbf{r}_1, t_1)U^*(\mathbf{r}_2, t_2) \rangle, \quad (2.2.1)$$

where \mathbf{r}_1 and \mathbf{r}_2 are three-dimensional spatial coordinate vectors, t_1 and t_2 are temporal coordinates, and $\langle \cdot \rangle$ represents ensemble averaging [38, 57]. This research always assumes the fields under consideration are at the very least wide-sense stationary. This means the average field has no time dependence and the MCF depends only on $\tau = t_2 - t_1$ and not the actual values of t_1 and t_2 .

While the MCF describes the second-order statistics of the field as a whole, it is often convenient to normalize it such that

$$\gamma(\mathbf{r}_1, \mathbf{r}_2; \tau) = \frac{\Gamma(\mathbf{r}_1, \mathbf{r}_2; \tau)}{[\Gamma(\mathbf{r}_1, \mathbf{r}_1; 0)]^{1/2} [\Gamma(\mathbf{r}_2, \mathbf{r}_2; 0)]^{1/2}}. \quad (2.2.2)$$

This new quantity is known as the complex degree of coherence and describes the degree to which one point of the field is correlated to another point in time and/or space [38, 57]. If two different points in space or time are directly related, then the magnitude of γ is 1. However, if there is no correlation between the points, its value would be zero. For partial correlation between the two points, the magnitude falls somewhere between 0 and 1. The phase of γ simply defines the average phase difference between the two points.

When the random field can be considered narrowband, the Fresnel approximation of Eq. (2.1.34) can be used to derive an expression for the propagation of the MCF. Making the appropriate changes to Eq. (2.1.34) then inserting it into Eq. (2.2.1)

produces

$$\begin{aligned}
\Gamma(\boldsymbol{\rho}_1, \boldsymbol{\rho}_2; \tau) &= \left\langle \frac{1}{(\lambda L)^2} \iint_{\mathcal{P}} \iint_{\mathcal{P}} U(\boldsymbol{\rho}'_1, t - L/c) U^*(\boldsymbol{\rho}'_2, t + \tau - L/c) \right. \\
&\quad \times \exp \left[\frac{j\bar{k}}{2L} \left(|\boldsymbol{\rho}_1 - \boldsymbol{\rho}'_1|^2 - |\boldsymbol{\rho}_2 - \boldsymbol{\rho}'_2|^2 \right) \right] d^2\boldsymbol{\rho}'_1 d^2\boldsymbol{\rho}'_2 \left. \right\rangle \\
&= \frac{1}{(\lambda L)^2} \iint_{\mathcal{P}} \iint_{\mathcal{P}} \Gamma(\boldsymbol{\rho}'_1, \boldsymbol{\rho}'_2; \tau) \\
&\quad \times \exp \left[\frac{j\bar{k}}{2L} \left(|\boldsymbol{\rho}_1 - \boldsymbol{\rho}'_1|^2 - |\boldsymbol{\rho}_2 - \boldsymbol{\rho}'_2|^2 \right) \right] d^2\boldsymbol{\rho}'_1 d^2\boldsymbol{\rho}'_2, \quad (2.2.3)
\end{aligned}$$

where $\boldsymbol{\rho}'$ is a two-dimensional coordinate vector in the source plane while $\boldsymbol{\rho}$ is a two-dimensional coordinate vector in the receiver plane.

Occasionally, the MCF is insufficient to describe the necessary statistics of the field. For example, describing the spatial and/or temporal correlations of the intensity of the field requires knowledge of the fourth-order statistics of the field. This is found with the fourth-order coherence function defined as

$$\Gamma(\boldsymbol{\rho}_1, \boldsymbol{\rho}_2, \boldsymbol{\rho}_3, \boldsymbol{\rho}_4; \tau_1, \tau_2, \tau_3) = \langle U(\boldsymbol{\rho}_1, t_1) U^*(\boldsymbol{\rho}_2, t_2) U(\boldsymbol{\rho}_3, t_3) U^*(\boldsymbol{\rho}_4, t_4) \rangle, \quad (2.2.4)$$

where $\tau_1 = t_2 - t_1$, $\tau_2 = t_3 - t_1$, and $\tau_3 = t_4 - t_1$. While the fourth-order coherence function may be difficult to calculate in general, there is one case where it can be calculated quite simply. That is when the random field is a circular complex Gaussian random process. This is where the real and imaginary parts of every point in the field are zero mean, independent, identically distributed Gaussian random variables. In this case, the coherence function of any even order can be found using the complex Gaussian moment theorem which is given by

$$\langle X_1 \cdots X_k X_{k+1}^* \cdots X_{2k}^* \rangle = \sum \langle X_1 X_{n_1}^* \rangle \cdots \langle X_k X_{n_k}^* \rangle, \quad (2.2.5)$$

where n_1, \dots, n_k is a permutation of $k + 1, \dots, 2k$, and the sum is over all possible permutations [38]. As such, the fourth-order coherence function of a circular complex Gaussian random field can be expressed in terms of its MCF as

$$\Gamma(\boldsymbol{\rho}_1, \boldsymbol{\rho}_2, \boldsymbol{\rho}_3, \boldsymbol{\rho}_4; \tau_1, \tau_2, \tau_3) = \Gamma(\boldsymbol{\rho}_1, \boldsymbol{\rho}_2; \tau_1)\Gamma(\boldsymbol{\rho}_3, \boldsymbol{\rho}_4; \tau_3 - \tau_2) + \Gamma(\boldsymbol{\rho}_1, \boldsymbol{\rho}_4; \tau_3)\Gamma(\boldsymbol{\rho}_3, \boldsymbol{\rho}_2; \tau_2 - \tau_1). \quad (2.2.6)$$

2.3 Gaussian Schell-Model (GSM) Beams

There is a special class of random fields where the magnitude of the complex degree of coherence given by Eq. (2.2.2) depends only on the separation difference $\boldsymbol{\rho}_1 - \boldsymbol{\rho}_2$ and not the actual values of $\boldsymbol{\rho}_1$ and $\boldsymbol{\rho}_2$. These fields are known as Schell-model fields [57, 78]. Of particular interest is when the spatial component of the MCF of a Schell-model field within a two-dimensional plane can be expressed as

$$\Gamma(\boldsymbol{\rho}_1, \boldsymbol{\rho}_2) = \langle U(\boldsymbol{\rho}_1) \rangle \langle U^*(\boldsymbol{\rho}_2) \rangle \mu(\boldsymbol{\rho}_1 - \boldsymbol{\rho}_2), \quad (2.3.1)$$

where μ is the spatial coherence function of the field. If both $\langle U \rangle$ and μ can be expressed in terms of Gaussian functions, the spatial portion of the MCF can be expressed as

$$\Gamma(\boldsymbol{\rho}_1, \boldsymbol{\rho}_2) = \Gamma(\mathbf{0}, \mathbf{0}) \exp \left[-\frac{|\boldsymbol{\rho}_1|^2 + |\boldsymbol{\rho}_2|^2}{w_g^2} - \frac{|\boldsymbol{\rho}_1 - \boldsymbol{\rho}_2|^2}{\rho_g^2} - \frac{jk}{2R_g} (|\boldsymbol{\rho}_1|^2 - |\boldsymbol{\rho}_2|^2) \right]. \quad (2.3.2)$$

where w_g is the mean field radius, ρ_g is the field coherence radius, and R_g is the field radius of curvature. This relation defines a Gaussian Schell-model (GSM) field, and when used as a source it produces GSM beams.

The three parameters w_g , ρ_g , and R_g completely define the second-order statistics

of a GSM field. The mean field radius w_g gives the size of the overall field. It is defined as the distance from the field center where the magnitude of the mean field falls to e^{-1} \times the value at the field center. The coherence radius ρ_g is defined as the separation distance between two points where the magnitude of the complex degree of coherence is e^{-1} . Within this separation distance, the field can be considered to be coherent. The field radius of curvature R_g defines surfaces of constant average phase. When it is positive the field is converging, when it is negative the field is diverging, and when it is infinite the field is collimated.

GSM beams have been extensively studied in the literature due to its simple form, its ability to represent a variety of fields of practical interest, and since it often gives tractable results [24, 26, 37, 47, 49, 53, 68, 80, 88, 97]. For example, it reduces to a point source when $w_0 \rightarrow 0$, or a plane wave as $w_0 \rightarrow \infty$. It can also be used to model a completely coherent Gaussian beam, such as a laser, when $\rho_g \rightarrow \infty$, or a completely incoherent Gaussian source when $\rho_g \sim \lambda$. These properties make it an ideal source model for this research.

2.4 Atmospheric Turbulence Theory

To fully describe the turbulent flow of the atmosphere would require the use of the Navier-Stokes equations. However, since they are non-linear partial differential equations, they are very difficult to work with. Instead, Russian mathematician Andrei Kolmogorov used statistical analysis to describe the turbulent nature of fluid flow [48]. Using dimensional analysis, and assuming the statistical nature of the turbulence is homogeneous and isotropic, he deduced that within the inertial subrange of turbulent flow (for distances smaller than the largest turbulence cells, or eddies, of size L_0 and larger than the smallest eddies of size l_0) the longitudinal structure

function of wind velocity can be expressed as

$$\mathcal{D}_v(r) = \langle (v_1 - v_2)^2 \rangle = C_v^2 r^{2/3}, \quad l_0 \ll r \ll L_0, \quad (2.4.1)$$

where v_1 and v_2 are velocity components separated by a distance r , and C_v^2 is known as the velocity structure constant (in units of $\text{m}^{4/3}/\text{s}^2$) which can be used as a measure of the strength of the turbulence.

After determining the structure function of the turbulence, the spatial power spectral density (PSD) of the turbulence can be found by using the relation

$$\Phi(\kappa) = \frac{1}{4\pi^2\kappa^2} \int_0^\infty \frac{\sin \kappa r}{\kappa r} \frac{d}{dr} \left[r^2 \frac{d}{dr} \mathcal{D}(r) \right] dr, \quad (2.4.2)$$

where κ is a scalar spatial frequency (in units of rad/m) [2]. Entering Eq. (2.4.1) into Eq. (2.4.2) results in

$$\Phi_v(\kappa) = 0.033 C_v^2 \kappa^{-11/3}, \quad 1/L_0 \ll \kappa \ll 1/l_0, \quad (2.4.3)$$

and is known as the Kolmogorov power-law spectrum.

The same type of analysis on fluctuations in the index of refraction of the atmosphere, based on temperature fluctuations as studied independently by Obukhov [61] and Corrsin [20], produces similar results [82]. As with velocity fluctuations, the structure function and spatial PSD of the index of refraction can be expressed as

$$\mathcal{D}_n(r) = C_n^2 r^{2/3}, \quad l_0 \ll r \ll L_0, \quad (2.4.4)$$

$$\Phi_n(\kappa) = 0.033 C_n^2 \kappa^{-11/3}, \quad 1/L_0 \ll \kappa \ll 1/l_0, \quad (2.4.5)$$

where C_n^2 is the index of refraction structure constant (in units of $\text{m}^{-2/3}$). While there are models of the index of refraction structure function and spatial PSD which extend

beyond the inertial subrange, they are often only for mathematical convenience and only accurately model the correct behavior within the inertial subrange [2]. For this reason the Kolmogorov spectrum was used in this research.

There are two main approaches to dealing with atmospheric turbulence. The first is to assume the index-of-refraction fluctuations only cause the field to deviate slightly from how it would behave in the absence of the fluctuations. This is known as weak turbulence, and it is appropriate to use perturbation theory to describe these deviations. For those cases where the deviations become large, known as strong turbulence, perturbation theory is no longer appropriate, and alternative means must be used. Both of these approaches are summarized below.

2.4.1 Weak Turbulence.

As is shown in Sec. 2.1.1, the governing stochastic equation that models the propagation of scalar electromagnetic waves through a linear, isotropic, nondispersive, and nonmagnetic medium is the Helmholtz equation given by Eq. (2.1.16). While it was originally assumed the index-of-refraction n was constant, it becomes a function of position with atmospheric turbulence. Since n consists of random perturbations about a nominal value, it can be expressed as

$$n = n_0 + n_1 \quad (2.4.6)$$

where $n_0 = \langle n \rangle \cong 1$ so $\langle n_1 \rangle = 0$. Since $n_1 \ll 1$, n^2 can be approximated with

$$n^2 \cong 1 + 2n_1, \quad (2.4.7)$$

which allows Eq. (2.1.16) to be expressed as

$$[\nabla^2 + k^2(1 + 2n_1)] U = 0. \quad (2.4.8)$$

Exact solutions to this equation have not been computed [2], but low-order statistical moments of the field can be computed by applying perturbation theory. This is appropriate so long as the effect of the n_1 fluctuations is small compared to vacuum propagation.

2.4.1.1 Rytov Theory.

One common perturbation method, known as the Born approximation, writes the perturbations in the form $U = U_0 + \epsilon U_1 + \epsilon^2 U_2 + \dots$ and then equates terms of the same order of ϵ . However, the statistics produced by this method have been shown to be valid only for very short propagation paths [2]. An alternate method, known as the Rytov approximation, writes the perturbations in the form of $U = \exp(\psi_0 + \epsilon\psi_1 + \epsilon^2\psi_2 + \dots)$. This method gives better agreement with experiment for long propagation paths, and is the basis for modeling electromagnetic propagation through weak atmospheric turbulence [2].

Applying the Rytov approximation to Eq. (2.4.8) and equating terms of similar order up to the second order produces

$$\nabla^2\psi_0 + \nabla\psi_0 \cdot \nabla\psi_0 = -k^2, \quad (2.4.9)$$

$$\nabla^2\psi_1 + 2\nabla\psi_0 \cdot \nabla\psi_1 = -2k^2n_1, \quad (2.4.10)$$

$$\nabla^2\psi_2 + 2\nabla\psi_0 \cdot \nabla\psi_2 = -(\nabla\psi_1)^2. \quad (2.4.11)$$

The first equation is equivalent to the Helmholtz equation and describes electromagnetic propagation through vacuum. The solution to the other two equations can be

found using Green's functions and shown to be

$$\psi_1(\mathbf{r}) = \frac{k^2}{2\pi U_0(\mathbf{r})} \iiint U_0(\mathbf{r}') n_1(\mathbf{r}') \frac{\exp(jk|\mathbf{r} - \mathbf{r}'|)}{|\mathbf{r} - \mathbf{r}'|} d\mathbf{r}', \quad (2.4.12)$$

$$\psi_2(\mathbf{r}) = \frac{1}{4\pi U_0(\mathbf{r})} \iiint U_0(\mathbf{r}') [\nabla \psi_1(\mathbf{r}')]^2 \frac{\exp(jk|\mathbf{r} - \mathbf{r}'|)}{|\mathbf{r} - \mathbf{r}'|} d\mathbf{r}', \quad (2.4.13)$$

where $U_0 = \exp(\psi_0)$ [77, 82]. Once a solution is found for ψ_1 it can be used to find a solution for ψ_2 , and so forth.

As the only randomness in ψ_1 comes from n_1 , Eq. (2.4.12) expresses ψ_1 as the superposition of independent random contributions from throughout the medium. Because an optical field encounters many random fluctuations through its propagation path, the central limit theorem implies ψ_1 should exhibit Gaussian statistics. This allows for estimating some statistical quantities of the field without needing to explicitly evaluate the integral.

2.4.1.2 Optical Transfer Function.

One such quantity is the optical transfer function (OTF). The OTF is defined as the normalized Fourier transform of the point spread function (PSF) of an incoherent imaging system. The PSF is simply the image of a point source made by the optical system. The OTF is then expressed mathematically as

$$\mathcal{H}(\nu_x, \nu_y) = \frac{\mathcal{F}\{|h|^2\}}{\iint_{-\infty}^{\infty} |h(x, y)|^2 dx dy}, \quad (2.4.14)$$

where $\mathcal{H}(\nu_x, \nu_y)$ is the OTF, $\mathcal{F}\{\cdot\}$ is the Fourier transform operator, and $h(x, y)$ is the field in the image plane for a point source [39].

As shown in Sec. 2.1.4, there is a Fourier transform relationship between the the system's exit-pupil and image-plane fields. Assuming the system is diffraction limited,

this relation can be expressed as

$$\begin{aligned}
 h(x, y) &= \frac{a}{\lambda f} \iint_{-\infty}^{\infty} P(u, v) \exp \left[-j \frac{2\pi}{\lambda f} (xu + yv) \right] du dv, \\
 &\propto \mathcal{F} \{P(u, v)\} |_{\nu_u=x/\lambda f, \nu_v=y/\lambda f},
 \end{aligned} \tag{2.4.15}$$

where a is a proportionality constant, λ is the wavelength of the light, f is the distance between the exit pupil and focal plane, P is the system's pupil function (1 within the pupil and 0 outside the pupil), while x and y are the image coordinates, u and v are the pupil coordinates, and ν_u and ν_v are the Fourier transform coordinates. Taking the Fourier transform of Eq. (2.4.15) and assuming the pupil function is even in each coordinate direction, gives

$$H(\nu_x, \nu_y) \propto P(\lambda f \nu_x, \lambda f \nu_y), \tag{2.4.16}$$

where $H = \mathcal{F}\{h\}$. This relationship, the autocorrelation and Parseval's theorems of Fourier transforms, and a simple change of variables allows us to express the OTF in terms of the pupil function with

$$\mathcal{H}(\nu_x, \nu_y) = \frac{\iint_{-\infty}^{\infty} P(u, v) P^*(u - \lambda f \nu_x, v - \lambda f \nu_y) du dv}{\iint_{-\infty}^{\infty} |P(u, v)|^2 du dv}. \tag{2.4.17}$$

In the case of optical aberrations due to atmospheric turbulence, the pupil function can be modified by multiplying it by the aberrated field at the pupil

$$P'(u, v) = P(u, v)U(u, v). \tag{2.4.18}$$

With this adjustment Eq. (2.4.17) can be expressed as

$$\mathcal{H}(\nu_x, \nu_y) = \frac{\iint_{-\infty}^{\infty} P(u, v)P^*(u - \lambda f\nu_x, v - \lambda f\nu_y)U(u, v)U^*(u - \lambda f\nu_x, v - \lambda f\nu_y) du dv}{\iint_{-\infty}^{\infty} |P(u, v)|^2|U(u, v)|^2 du dv}. \quad (2.4.19)$$

Since the field aberrations are not fixed, the question becomes how to describe the average OTF. Taking the expectation of both sides of Eq. (2.4.19) results in the expected value of a ratio of correlated random variables which can be difficult to work with. Instead, the average OTF is defined as

$$\overline{\mathcal{H}}(\nu_x, \nu_y) = \frac{\langle \text{numerator of the OTF} \rangle}{\langle \text{denominator of the OTF} \rangle}. \quad (2.4.20)$$

The only random part of Eq. (2.4.19) is the field U , and assuming its spatial statistics are wide-sense stationary, its expectation can be moved outside the integrals. The average OTF can then be expressed as a product of the diffraction limited OTF given by Eq. (2.4.17) and the average OTF of the atmosphere given by

$$\overline{\mathcal{H}}_{atm}(\nu_x, \nu_y) = \frac{\langle U(u, v)U^*(u - \lambda f\nu_x, v - \lambda f\nu_y) \rangle}{\langle |U(u, v)|^2 \rangle}. \quad (2.4.21)$$

This is simply the normalized autocorrelation of the field. The unaberrated portion of the field U_0 can be moved outside the expectation operator of both the numerator and denominator where they divide out. This just leaves the Rytov perturbation $U_1 = \exp(\psi_1)$. Expressing ψ_1 in complex notation gives

$$\psi_1 = \chi + jS, \quad (2.4.22)$$

where χ is known as the log-amplitude aberration and S is the phase aberration. The

numerator of Eq. (2.4.21) can now be expressed as

$$\Gamma(\Delta u, \Delta v) = \langle \exp [(\chi_1 + \chi_2) + j(S_1 - S_2)] \rangle, \quad (2.4.23)$$

where Γ is the spatial autocorrelation function, also known as the mutual coherence function (MCF), while the subscripts of χ and S refer to two points separated by Δu and Δv . While there is no particular reason to believe χ and S are independent, since n_1 was assumed to be homogeneous and isotropic, χ and S must also be homogeneous and isotropic. This implies that

$$\langle \chi_1 S_1 \rangle = \langle \chi_2 S_2 \rangle, \quad (2.4.24)$$

$$\langle \chi_1 S_2 \rangle = \langle \chi_2 S_1 \rangle. \quad (2.4.25)$$

It is thus plain to see that

$$\langle (\chi_1 + \chi_2)(S_1 - S_2) \rangle = \langle \chi_1 S_1 \rangle - \langle \chi_2 S_2 \rangle - \langle \chi_1 S_2 \rangle + \langle \chi_2 S_1 \rangle = 0, \quad (2.4.26)$$

which means $(\chi_1 + \chi_2)$ and $(S_1 - S_2)$ are uncorrelated. Since they are both Gaussian, they must also be independent and thus their expectations are separable.

The expectation of an exponent of a Gaussian random variable can easily be found by using its characteristic equation

$$\begin{aligned} \mathbf{M}_G(\omega) &= \langle \exp(j\omega g) \rangle \\ &= \exp \left(j\omega \bar{g} - \frac{\omega^2 \sigma^2}{2} \right), \end{aligned} \quad (2.4.27)$$

where \bar{g} and σ^2 are respectively the mean and variance of the Gaussian random variable g [38]. The phase aberration difference has a zero mean and its variance is

equal to the phase aberration structure function \mathcal{D}_S [see Eq. (2.4.1)], so using $\omega = 1$ yields

$$\langle \exp [j(S_1 - S_2)] \rangle = \exp \left(-\frac{1}{2} \mathcal{D}_S \right). \quad (2.4.28)$$

As for the log-amplitude portion, letting $\bar{\chi}$ be the log-amplitude mean, and σ_χ^2 be the log-amplitude variance, using $\omega = -j$ yields

$$\begin{aligned} \langle \exp(\chi_1 + \chi_2) \rangle &= \exp \left\{ \langle \chi_1 + \chi_2 \rangle + \frac{1}{2} [\langle (\chi_1 + \chi_2)^2 \rangle - \langle \chi_1 + \chi_2 \rangle^2] \right\} \\ &= \exp \left[2\bar{\chi} + \frac{1}{2} (\langle \chi_1^2 \rangle + \langle \chi_2^2 \rangle + 2\langle \chi_1 \chi_2 \rangle - 4\bar{\chi}^2) \right] \\ &= \exp (2\bar{\chi} + \langle \chi^2 \rangle + \langle \chi_1 \chi_2 \rangle - 2\bar{\chi}^2). \end{aligned} \quad (2.4.29)$$

The denominator of Eq. (2.4.21) can also be expressed as

$$\begin{aligned} \Gamma(0, 0) &= \langle \exp(2\chi) \rangle \\ &= \exp(2\bar{\chi} + 2\sigma_\chi^2) \\ &= \exp (2\bar{\chi} + 2\langle \chi^2 \rangle - 2\bar{\chi}^2). \end{aligned} \quad (2.4.30)$$

Dividing Eq. (2.4.29) by Eq. (2.4.30) gives

$$\begin{aligned} \frac{\langle \exp(\chi_1 + \chi_2) \rangle}{\langle \exp(2\chi) \rangle} &= \exp (\langle \chi_1 \chi_2 \rangle - \langle \chi^2 \rangle) \\ &= \exp \left[-\frac{1}{2} (\langle \chi_1^2 \rangle + \langle \chi_2^2 \rangle - 2\langle \chi_1 \chi_2 \rangle) \right] \\ &= \exp \left[-\frac{1}{2} \langle (\chi_1 - \chi_2)^2 \rangle \right] \\ &= \exp \left(-\frac{1}{2} \mathcal{D}_\chi \right), \end{aligned} \quad (2.4.31)$$

using the definition of the log-amplitude structure function. Defining the wave structure function (WSF) as the sum of the log-amplitude and phase structure functions

produces

$$\mathcal{D} = \mathcal{D}_x + \mathcal{D}_s, \quad (2.4.32)$$

so that Eq. (2.4.21) can be expressed as

$$\overline{\mathcal{H}}_{atm}(\nu_x, \nu_y) = \exp \left[-\frac{1}{2} \mathcal{D}(\lambda f \nu_x, \lambda f \nu_y) \right]. \quad (2.4.33)$$

Further analysis requires an expression for the WSF.

2.4.1.3 Wave Structure Function.

Using cylindrical coordinates, the WSF of the field in the pupil plane for a point source a distance L away can be expressed as

$$\begin{aligned} \mathcal{D}(\rho, L) &= \langle |\psi_1(\boldsymbol{\rho}_1, L) - \psi_1(\boldsymbol{\rho}_2, L)|^2 \rangle \\ &= \langle |\psi_1(\boldsymbol{\rho}_1, L)|^2 + |\psi_1(\boldsymbol{\rho}_2, L)|^2 - 2 \operatorname{Re}[\psi_1(\boldsymbol{\rho}_1, L)\psi_1^*(\boldsymbol{\rho}_2, L)] \rangle, \end{aligned} \quad (2.4.34)$$

where $\rho = |\boldsymbol{\rho}_1 - \boldsymbol{\rho}_2|$ and $\operatorname{Re}(\cdot)$ is the real operator. It is a simple matter to show that this can be reduced to the sum of the log-amplitude and phase structure functions. All that is needed is to use Eq. (2.4.12) to find $\langle \psi(\boldsymbol{\rho}_1, L)\psi^*(\boldsymbol{\rho}_2, L) \rangle$ for a point source. This derivation is quite involved and is found in many references (see [2, 38, 77]), so only the final result is provided here as

$$\langle \psi_1(\boldsymbol{\rho}_1, L)\psi_1^*(\boldsymbol{\rho}_2, L) \rangle = 4\pi^2 k^2 \int_0^L \int_0^\infty \kappa \Phi_n(\kappa, z) J_0(\kappa \rho z / L) d\kappa dz, \quad (2.4.35)$$

where J_0 is the zero-order Bessel function of the first kind. Substituting this into Eq. (2.4.34) gives

$$\mathcal{D}(\rho, L) = 8\pi^2 k^2 \int_0^L \int_0^\infty \kappa \Phi_n(\kappa, z) [1 - J_0(\kappa \rho z / L)] d\kappa dz. \quad (2.4.36)$$

Using the Kolmogorov PSD given in Eq. (2.4.5) and allowing C_n^2 to slowly vary over the propagation distance, the WSF can be explicitly written as

$$\mathcal{D}(\rho, L) = 2.914k^2\rho^{5/3} \int_0^L C_n^2(z)(z/L)^{5/3} dz, \quad (2.4.37)$$

or for constant C_n^2

$$\mathcal{D}(\rho, L) = 1.093k^2C_n^2L\rho^{5/3}. \quad (2.4.38)$$

The average OTF of the atmosphere can now be explicitly written for constant C_n^2 as

$$\overline{\mathcal{H}}_{atm}(\nu_\rho) = \exp \left[-11.7k^{1/3}C_n^2L(f\nu_\rho)^{5/3} \right], \quad (2.4.39)$$

where $\nu_\rho = (\nu_x^2 + \nu_y^2)^{1/2}$.

2.4.1.4 Coherence Length (r_0).

An additional measure for the performance of an optical system is its resolution. While there are different ways to define a system's resolution, a useful one for this analysis is the integral of the average OTF [29]

$$\mathcal{R} = \iint_{-\infty}^{\infty} \overline{\mathcal{H}}(\nu_x, \nu_y) d\nu_x d\nu_y. \quad (2.4.40)$$

If λ , f , C_n^2 , and L are kept fixed, \mathcal{R} becomes a function of the system aperture diameter D . For small D , it increases with the square of D as would be expected, but at a certain point the curve levels off to a constant value. These two asymptotes cross at a point called the atmospheric coherence length r_0 which is given by

$$r_0 = \left[0.423k^2 \int_0^L C_n^2(z)(z/L)^{5/3} dz \right]^{-3/5}, \quad (2.4.41)$$

for a point source in the case C_n^2 changes over the path length, or

$$r_0 = (0.159k^2C_n^2L)^{-3/5}, \quad (2.4.42)$$

for the case of constant C_n^2 . This is essentially the length over which the atmosphere has a negligible effect on high-order wavefront aberrations. It is a useful parameter since many of the quantities discussed above can be expressed in terms of r_0 . For instance, the WSF becomes

$$\mathcal{D}(\rho) = 6.88 \left(\frac{\rho}{r_0} \right)^{5/3}, \quad (2.4.43)$$

which makes the average OTF degradation due to the atmosphere

$$\overline{\mathcal{H}}_{atm}(\nu_\rho) = \exp \left[-3.44 \left(\frac{\lambda f \nu_\rho}{r_0} \right)^{5/3} \right]. \quad (2.4.44)$$

2.4.1.5 Isoplanatic angle (θ_0).

While r_0 expresses the coherence width of the atmosphere in terms of length, often it is better to express it in terms of angle. For instance, at what angular extent do two different point sources' phase perturbations become uncorrelated with each other? This is known as anisoplanatism, with the maximum angular extent of correlation being called the isoplanatic angle θ_0 [30]. The WSF can be expressed in terms of angular extent θ by simply replacing ρ in Eq. (2.4.37) with $L\theta$ giving

$$\mathcal{D}(\theta) = 2.914k^2\theta^{5/3} \int_0^L C_n^2(z)z^{5/3}dz. \quad (2.4.45)$$

θ_0 is then defined as the angle where $\mathcal{D}(\theta) = 1$, or

$$\theta_0 = \left[2.914k^2 \int_0^L C_n^2(z) z^{5/3} dz \right]^{-3/5}, \quad (2.4.46)$$

for a variable C_n^2 and

$$\theta_0 = (1.093k^2 C_n^2 L^{8/3})^{-3/5}, \quad (2.4.47)$$

for a constant C_n^2 . By comparing Eq. (2.4.46) with Eq. (2.4.41) it can be readily seen that for a point source

$$\theta_0 = 0.314 \frac{r_0}{L}. \quad (2.4.48)$$

It should be noted, that θ_0 is defined as the offset angle whereby performance is degraded by e^{-1} in the limit of an infinite aperture [30]. For telescopes with finite apertures, the true angular extent of the isoplanatic patch may be several times θ_0 [18].

2.4.1.6 Rytov Number (\mathcal{R}).

Another useful statistical quantity is the log-amplitude variance σ_χ^2 . As explained earlier, Rytov theory predicts a Gaussian distribution for the log-amplitude perturbation χ , so all its statistics should be described by its mean and variance. From Eq. (2.4.12) it can be seen that that $\langle \psi_1 \rangle = 0$, so $\langle \chi \rangle = 0$ as well. The log-amplitude variance can be calculated by using the relationship

$$\chi = \frac{1}{2} (\psi_1 + \psi_1^*). \quad (2.4.49)$$

This then implies

$$\begin{aligned}\sigma_\chi^2 &= \langle \chi^2 \rangle \\ &= \frac{1}{2} \text{Re} (\langle |\psi_1|^2 \rangle + \langle \psi_1^2 \rangle). \end{aligned} \quad (2.4.50)$$

$\langle |\psi_1|^2 \rangle$ is found by using Eq. (2.4.35), but $\langle \psi_1^2 \rangle$ still needs to be calculated. As with Eq. (2.4.35), this derivation is quite involved (see [2]) so only the final result is given here for a point source as

$$\langle \psi_1^2 \rangle = -4\pi k^2 \int_0^L \int_0^\infty \kappa \Phi_n(\kappa, z) \exp \left[-\frac{j\kappa^2 z}{k} \left(1 - \frac{z}{L} \right) \right] d\kappa dz. \quad (2.4.51)$$

Using Eqs. (2.4.35) and (2.4.51) with Eq. (2.4.50) gives

$$\sigma_\chi^2 = 2\pi^2 k^2 \int_0^L \int_0^\infty \kappa \Phi_n(\kappa, z) \left[1 - \cos \frac{\kappa^2 z (1 - z/L)}{k} \right] d\kappa dz. \quad (2.4.52)$$

With the Kolmogorov PSD from Eq. (2.4.5), this reduces to

$$\sigma_\chi^2 = 0.5631 k^{7/6} \int_0^L C_n^2(z) z^{5/6} (1 - z/L)^{5/6} dz. \quad (2.4.53)$$

If C_n^2 is constant along the path, it can be further reduced to

$$\sigma_\chi^2 = 0.1242 k^{7/6} C_n^2 L^{11/6}. \quad (2.4.54)$$

This shows that for a given wavelength and C_n^2 , the log-amplitude variance increases with nearly the square of the distance propagated. While there is no limit to this growth given by Eq. (2.4.54), experiments show that it eventually saturates, and even then decreases asymptotically to a constant value [2]. The reason for this failure to accurately predict the correct statistics has to do with the assumptions that went

into the Rytov approximation. Perturbation theory assumes that each additional perturbation is much smaller than the previous one. This assumption is generally only valid when $\sigma_\chi^2 < 0.35$ [77]. As a result, the regime where Eq. (2.4.54) holds is known as weak turbulence and can be described by Rytov theory, while the regime where it fails is known as medium to strong turbulence and requires a different theory to accurately describe the log-amplitude statistics.

Despite this shortcoming, Eq. (2.4.54) is still useful as a measure of the strength of turbulence. As a result it is designated as the point source Rytov number \mathcal{R} to differentiate it from the actual log-amplitude variance of a field [32].

2.4.1.7 Scintillation Index ($\tilde{\sigma}_I^2$).

Since irradiance is what is actually measured by a detector, fluctuations in the log-amplitude of a field are measured as fluctuations of the irradiance and are known as scintillation. The scintillation index quantifies scintillation and is defined as the normalized variance of the irradiance

$$\begin{aligned}\tilde{\sigma}_I^2 &= \frac{\sigma_I^2}{\langle I \rangle^2} \\ &= \frac{\langle I^2 \rangle}{\langle I \rangle^2} - 1.\end{aligned}\tag{2.4.55}$$

Since $I = |U|^2$, the irradiance and log-amplitude are related by

$$I = A_0^2 \exp(2\chi),\tag{2.4.56}$$

where $A_0 = |U_0|$. By using the same techniques as in Sec. 2.4.1.2 for the average OTF, it can be shown that $\tilde{\sigma}_I^2$ and σ_χ^2 are related by

$$\tilde{\sigma}_I^2 = \exp(4\sigma_\chi^2) - 1.\tag{2.4.57}$$

As long as σ_χ^2 is small, the exponent can be expanded in a power series such that

$$\tilde{\sigma}_I^2 \cong 4\sigma_\chi^2. \quad (2.4.58)$$

While this approximation works well in weak turbulence, a different theory is needed to describe the scintillation index in strong turbulence.

2.4.1.8 Intensity Probability Distribution.

Assuming χ is Gaussian distributed, an expression for the probability distribution function (pdf) of I can also be derived. The pdf of χ is given as

$$p(\chi) = \frac{1}{\sqrt{2\pi}\sigma_\chi} \exp \left[-\frac{(\chi - \langle \chi \rangle)^2}{2\sigma_\chi^2} \right]. \quad (2.4.59)$$

Expressing χ in terms of I gives

$$\chi = \frac{1}{2} \ln \frac{I}{A_0^2}. \quad (2.4.60)$$

Since this function is monotonic, the transform from χ to I requires that

$$p(I) dI = p(\chi) d\chi. \quad (2.4.61)$$

Taking the derivative of Eq. (2.4.60) with respect to I gives

$$\frac{d\chi}{dI} = \frac{1}{2I}, \quad (2.4.62)$$

so the pdf of I becomes

$$p(I) = \frac{1}{2\sqrt{2\pi}I\sigma_\chi} \exp \left\{ -\frac{[\ln(I/A_0^2) - 2\langle \chi \rangle]^2}{8\sigma_\chi^2} \right\}. \quad (2.4.63)$$

This is known as a log-normal distribution where the mean and variance of I can be found to be

$$\langle I \rangle = A_0^2 \exp(2\langle \chi \rangle + 2\sigma_\chi^2) \quad (2.4.64)$$

$$\sigma_I^2 = \langle I \rangle^2 [\exp(4\sigma_\chi^2) - 1]. \quad (2.4.65)$$

As expected, this reduces to the expression for the scintillation index given by Eq. (2.4.57).

While experiments have demonstrated good agreement between the measured intensity fluctuations and the log-normal distribution in weak turbulence, the agreement lessens with increased turbulence [2]. Different means are required to estimate the pdf of the intensity fluctuations in strong turbulence.

2.4.1.9 Gaussian Beams.

While the above results are primarily based on a point source, Rytov theory allows for the derivation of expressions for other source beacons such as Gaussian beams. In general, the MCF for light after passing through turbulence can be expressed in terms of the Rytov approximation up to second order as

$$\begin{aligned} \Gamma(\mathbf{r}_1, \mathbf{r}_2) &= \langle U(\mathbf{r}_1)U^*(\mathbf{r}_2) \rangle \\ &= U_0(\mathbf{r}_1)U_0^*(\mathbf{r}_2) \langle \exp[\psi_1(\mathbf{r}_1) + \psi_2(\mathbf{r}_1) + \psi_1^*(\mathbf{r}_2) + \psi_2^*(\mathbf{r}_2)] \rangle. \end{aligned} \quad (2.4.66)$$

The ensemble average can be estimated by using the method of cumulants [62] where

$$\langle \exp(X) \rangle \simeq \exp \left[\langle X \rangle + \frac{1}{2}(\langle X^2 \rangle - \langle X \rangle^2) \right]. \quad (2.4.67)$$

This expression becomes an equality only when X is Gaussian. Inserting Eq. (2.4.66) into (2.4.67) and only keeping terms up to the second order produces

$$\Gamma(\mathbf{r}_1, \mathbf{r}_2) = U_0(\mathbf{r}_1)U_0^*(\mathbf{r}_2) \exp \left\{ \langle \psi_2(\mathbf{r}_1) \rangle + \frac{1}{2} \langle [\psi_1(\mathbf{r}_1)]^2 \rangle + \langle \psi_2^*(\mathbf{r}_2) \rangle + \frac{1}{2} \langle [\psi_1^*(\mathbf{r}_2)]^2 \rangle + \langle \psi_1(\mathbf{r}_1)\psi_1^*(\mathbf{r}_2) \rangle \right\}. \quad (2.4.68)$$

If the source is a coherent Gaussian beam, its source field can be expressed as

$$U_0(\boldsymbol{\rho}, 0) = \exp \left[- \left(\frac{1}{w_0^2} + \frac{jk}{2R_0} \right) |\boldsymbol{\rho}|^2 \right], \quad (2.4.69)$$

where w_0 is the source radius and R_0 is the source radius of curvature. If there was no turbulence, its field after propagating a distance L would be given by

$$U_0(\boldsymbol{\rho}, L) = \frac{w_0}{w} \exp \left[- \left(\frac{1}{w^2} + \frac{jk}{2R} \right) |\boldsymbol{\rho}|^2 + j(kL - \varphi) \right], \quad (2.4.70)$$

where

$$\varphi = \arctan \frac{\Lambda_0}{\Theta_0}, \quad (2.4.71)$$

$$w = w_0 \sqrt{\Theta_0^2 + \Lambda_0^2}, \quad (2.4.72)$$

$$R = \frac{R_0 (\Theta_0^2 + \Lambda_0^2) (1 - \Theta_0)}{\Theta_0^2 + \Lambda_0^2 - \Theta_0}, \quad (2.4.73)$$

$$\Theta_0 = 1 - \frac{L}{R_0}, \quad (2.4.74)$$

$$\Lambda_0 = \frac{2L}{kw_0^2}. \quad (2.4.75)$$

Θ_0 and Λ_0 are known as the input beam parameters, where Θ_0 is the curvature parameter (< 1 for a converging beam, > 1 for a diverging beam, and equals 1 for a collimated beam) and Λ_0 is the Fresnel ratio [2]. Alternatively, w and R can define

output beam parameters given by

$$\begin{aligned}\Theta &= 1 + \frac{L}{R} \\ &= \frac{\Theta_0}{\Theta_0^2 + \Lambda_0^2},\end{aligned}\quad (2.4.76)$$

$$\begin{aligned}\Lambda &= \frac{2L}{kw^2} \\ &= \frac{\Lambda_0}{\Theta_0^2 + \Lambda_0^2}.\end{aligned}\quad (2.4.77)$$

If the beam travels through turbulence, the MCF can be computed by using Eqs. (2.4.69) and (2.4.70) in (2.4.68). The derivation is quite complicated and found in [2], so only the final result is given here as

$$\begin{aligned}\Gamma(\boldsymbol{\rho}_1, \boldsymbol{\rho}_2, L) &= \frac{w_0^2}{w^2} \exp \left[-\frac{|\boldsymbol{\rho}_1|^2 + |\boldsymbol{\rho}_2|^2}{w^2} - \frac{jk}{2R} (|\boldsymbol{\rho}_1|^2 - |\boldsymbol{\rho}_2|^2) - 4\pi^2 k^2 L \int_0^1 \int_0^\infty \kappa \Phi_n(\kappa) \right. \\ &\quad \left. \times \left\{ 1 - \exp \left(-\frac{\Lambda L \kappa^2 \xi^2}{k} \right) J_0 \left[|(1 - \bar{\Theta}\xi) \boldsymbol{\rho}_d - 2j\Lambda\xi\boldsymbol{\rho}_s| \kappa \right] \right\} d\kappa d\xi \right],\end{aligned}\quad (2.4.78)$$

where $\bar{\Theta} = 1 - \Theta$, $\boldsymbol{\rho}_d = \boldsymbol{\rho}_1 - \boldsymbol{\rho}_2$, and $\boldsymbol{\rho}_s = (\boldsymbol{\rho}_1 + \boldsymbol{\rho}_2)/2$.

Due to the complexity of this expression, it is difficult to arrive at analytic expressions for specific field statistics. However, good approximations can be obtained. One of particular interest is the wave structure function. As before, the derivation can be found in [2] and only the final result is given here. Using the Kolmogorov power spectrum of Eq. (4.2.6) and assuming constant turbulence along the path, it can be closely estimated as

$$\mathcal{D}(\rho, L) = 8.80\mathcal{R} \left[a \left(\frac{k\rho^2}{L} \right)^{5/6} + 0.618\Lambda^{11/6} \left(\frac{k\rho^2}{L} \right) \right], \quad (2.4.79)$$

where

$$a = \begin{cases} \frac{1 - \Theta^{8/3}}{1 - \Theta} & \text{for } \Theta \geq 0, \\ \frac{1 + |\Theta|^{8/3}}{1 - \Theta} & \text{for } \Theta < 0. \end{cases} \quad (2.4.80)$$

One final statistical quantity of interest is the scintillation index. It is again computed through Eqs. (2.4.50) and (2.4.58), but this time ψ_1 is based on a Gaussian beam source instead of a point source. The required quantities are found to be [2]

$$\langle |\psi_1|^2 \rangle = 4\pi^2 k^2 L \int_0^1 \int_0^\infty \kappa \Phi_n(\kappa) \exp\left(-\frac{\Lambda L \kappa^2 \xi^2}{k}\right) I_0(2\Lambda |\boldsymbol{\rho}| \kappa \xi) d\kappa d\xi, \quad (2.4.81)$$

$$\langle \psi_1^2 \rangle = -4\pi^2 k^2 L \int_0^1 \int_0^\infty \kappa \Phi_n(\kappa) \exp\left(-\frac{\Lambda L \kappa^2 \xi^2}{k}\right) \exp\left[-\frac{jL\kappa^2}{k} \xi(1 - \bar{\Theta}\xi)\right] d\kappa d\xi, \quad (2.4.82)$$

where I_0 is a modified Bessel function of the first kind. When these expressions are inserted into the relevant equations and evaluated using the Kolmogorov power spectrum, they produce

$$\tilde{\sigma}_I^2 = 38.4\mathcal{R} \operatorname{Re} \left[j^{5/6} {}_2F_1 \left(-\frac{5}{6}, \frac{11}{6}; \frac{17}{6}; \bar{\Theta} + j\Lambda \right) \right] - 26.3\mathcal{R} \Lambda^{5/6} {}_1F_1 \left(-\frac{5}{6}; 1; \frac{2|\boldsymbol{\rho}|^2}{w^2} \right), \quad (2.4.83)$$

where ${}_1F_1$ is the confluent hypergeometric function and ${}_2F_1$ is the hypergeometric function. In contrast to the scintillation index for a point source, the scintillation index for a Gaussian beam is not constant across the beam cross section.

2.4.2 Strong Turbulence.

While the Rytov approximation is adequate to predict the second-order statistics for a point source, such as the OTF, WSF, and r_0 at all turbulence strengths, this is not necessarily the case for Gaussian beams. Strong turbulence also presents its own set of challenges. The most obvious is the failure of Rytov theory to accurately

predict $\tilde{\sigma}_I^2$. An additional issue deals with the creation of optical vortices in the wavefront which lead to discontinuities in the phase of the field. While many theories have been developed to model strong turbulence [12, 21, 22, 27, 35, 53, 54, 93], it has been demonstrated that most are equivalent up to the second-order under appropriate assumptions [13]. This section summarizes a few of the more useful theories including the parabolic equation method, the effective parameters method, and extended Rytov theory. The intent is to better estimate the statistical properties of a Gaussian beam traveling through strong turbulence.

2.4.2.1 Parabolic Equation Method.

As with Rytov theory, the starting point for the parabolic method is the stochastic Helmholtz equation given by Eq. (2.4.8). This time the substitution $U(\mathbf{r}) = V(\mathbf{r}) \exp(jkz)$ is made to produce

$$2jk \frac{\partial V(\mathbf{r})}{\partial z} + \frac{\partial^2 V(\mathbf{r})}{\partial z^2} + \nabla_T^2 V(\mathbf{r}) + 2k^2 n_1(\mathbf{r}) V(\mathbf{r}) = 0, \quad (2.4.84)$$

where $\nabla_T^2 = \partial^2/\partial x^2 + \partial^2/\partial y^2$ is the transverse Laplace operator. Making the paraxial approximation that $\partial^2 V/\partial z^2$ is much smaller than any of the other terms, it is dropped thereby producing the parabolic differential equation

$$2jk \frac{\partial V(\mathbf{r})}{\partial z} + \nabla_T^2 V(\mathbf{r}) + 2k^2 n_1(\mathbf{r}) V(\mathbf{r}) = 0. \quad (2.4.85)$$

The parabolic equation for the MCF of a general field can be found by first replacing $V(\mathbf{r})$ in Eq. (2.4.85) with $V(\boldsymbol{\rho}_1, z)$ then multiplying this expression by $V^*(\boldsymbol{\rho}_2, z)$. The process is then repeated except $\boldsymbol{\rho}_1$ and $\boldsymbol{\rho}_2$ are switched and the complex conjugate of the expression is taken. These two expressions are then subtracted and averaged

producing

$$2jk \frac{\partial}{\partial z} \Gamma(\boldsymbol{\rho}_1, \boldsymbol{\rho}_2, z) + (\nabla_{T1}^2 - \nabla_{T2}^2) \Gamma(\boldsymbol{\rho}_1, \boldsymbol{\rho}_2, z) + 2k^2 \langle [n_1(\boldsymbol{\rho}_1, z) - n_1(\boldsymbol{\rho}_2, z)] V(\boldsymbol{\rho}_1, z) V^*(\boldsymbol{\rho}_2, z) \rangle = 0, \quad (2.4.86)$$

where ∇_{T1}^2 and ∇_{T2}^2 are transverse Laplace operators over $\boldsymbol{\rho}_1$ and $\boldsymbol{\rho}_2$ respectively. As demonstrated by Ishimaru [43], assuming n_1 is a Gaussian random field that is delta correlated in z such that $\langle n_1(\boldsymbol{\rho}_1, z_1) n_1(\boldsymbol{\rho}_2, z_2) \rangle = \delta(z_1 - z_2) A_n(\boldsymbol{\rho}_1 - \boldsymbol{\rho}_2)$ allows for Eq. (2.4.86) to be expressed as

$$\left\{ 2jk \frac{\partial}{\partial z} + (\nabla_{T1}^2 - \nabla_{T2}^2) + 2jk^3 [A_n(0) - A_n(\boldsymbol{\rho}_1 - \boldsymbol{\rho}_2)] \right\} \Gamma(\boldsymbol{\rho}_1, \boldsymbol{\rho}_2, z) = 0. \quad (2.4.87)$$

Using the relation for isotropic turbulence of [2, 43]

$$A_n(\boldsymbol{\rho}) = 4\pi^2 \int_0^\infty \kappa \Phi_n(\kappa) J_0(|\boldsymbol{\rho}| \kappa) d\kappa, \quad (2.4.88)$$

a lengthy derivation given in [43] ultimately results in a solution to this differential equation which can be expressed as

$$\begin{aligned} \Gamma(\boldsymbol{\rho}_1, \boldsymbol{\rho}_2, L) = & \frac{1}{(\lambda L)^2} \iint_{\mathcal{P}} \iint_{\mathcal{P}} \Gamma(\boldsymbol{\rho}'_1, \boldsymbol{\rho}'_2, 0) \exp \left[\frac{jk}{2L} (|\boldsymbol{\rho}_1 - \boldsymbol{\rho}'_1|^2 - |\boldsymbol{\rho}_2 - \boldsymbol{\rho}'_2|^2) \right] \\ & \times \exp \left(-4\pi^2 k^2 L \int_0^1 \int_0^\infty \kappa \Phi_n(\kappa) \{1 - J_0[\xi(\boldsymbol{\rho}'_1 - \boldsymbol{\rho}'_2) \right. \\ & \left. + (1 - \xi)(\boldsymbol{\rho}_1 - \boldsymbol{\rho}_2)|\kappa] \} d\kappa d\xi \right) d^2 \boldsymbol{\rho}'_1 d^2 \boldsymbol{\rho}'_2. \end{aligned} \quad (2.4.89)$$

This expression compares closely to Eq. (2.2.3) where the the only difference is the extra exponential term that accounts for the turbulence along the propagation path.

2.4.2.2 Effective Parameters Method.

One of the drawbacks to the parabolic equation method is that it is analytically intractable for many of the cases of interest, such as when a Gaussian beam is used with the Kolmogorov power spectrum. While Eq. (2.4.89) can be numerically evaluated, this is computationally intensive and it does not allow for further insight to the behavior of the MCF. As a result, other means of estimating the effect of strong turbulence on the propagation of Gaussian beams have been developed. The one summarized here, known as the effective parameters method, allows for the results based on Rytov theory for weak turbulence to be directly extended into the strong turbulence regime.

Studies on the impact of strong turbulence on Gaussian beams indicated that diffraction due to the turbulence caused the mean radius of curvature of the beam to be reduced more than that for a plane wave or spherical wave [9,10]. Since the the radius of curvature and beam size are linked through geometric optics, this then causes the beam size to be larger than otherwise be expected. As the behavior of Gaussian beams depend in large part on their beam size and radius of curvature, further propagation of the beam must take these new values into account. These changes are accounted for by defining new output beam parameters based on the actual effective turbulence induced beam size and radius of curvature instead of those predicted by vacuum propagation [1]. Analysis based on approximations of the parabolic equation indicates the effective beam radius and radius of curvature in strong, constant turbulence can be closely estimated by

$$w_t = w_0 \sqrt{\Theta_0^2 + \Lambda_0^2 + 25.6\mathcal{R}^{6/5}\Lambda_0} \quad (2.4.90)$$

$$R_t = - \frac{L (\Theta_0^2 + \Lambda_0^2 + 25.6\mathcal{R}^{6/5}\Lambda_0)}{\Theta_0^2 + \Lambda_0^2 - \Theta_0 + 38.4\mathcal{R}^{6/5}\Lambda_0}. \quad (2.4.91)$$

The effective beam parameters are then defined as

$$\Theta_e = 1 + \frac{L}{R_t} = \frac{\Theta_0 - 12.8\mathcal{R}^{6/5}\Lambda_0}{\Theta_0^2 + \Lambda_0^2 + 25.6\mathcal{R}^{6/5}\Lambda_0} \quad (2.4.92)$$

$$\Lambda_e = \frac{2L}{kw_t^2} = \frac{\Lambda_0}{\Theta_0^2 + \Lambda_0^2 + 25.6\mathcal{R}^{6/5}\Lambda_0}. \quad (2.4.93)$$

Replacing the output beam parameters in any Rytov theory based expression with these effective beam parameters allows them to be used as good estimates for the behavior of these beams at any turbulence level.

2.4.2.3 Extended Rytov Theory.

While the parabolic and effective parameter methods work well for describing the second-order statistics of the field, such is not the case for fourth-order statistics like $\tilde{\sigma}_I^2$. While the parabolic method can be used to derive the fourth-order statistics, it quickly becomes so complex it is difficult to get any useful results. One method, known as the extended Rytov theory, was developed to avoid these complications by taking a more heuristic approach to the problem. Since it makes use of conventional Rytov theory, its results follow directly from those found for weak turbulence.

Extended Rytov theory is built on the assumption that turbulence causes refraction primarily through the larger eddy sizes, while it causes diffraction primarily through the smaller eddy sizes. Furthermore, it assumes the refractive and diffractive fluctuations are independent of each other. In weak turbulence, all eddy sizes have a role in either refracting or diffracting the beam, but in medium to strong turbulence the mid-scale sizes cease to play a part in either refraction or diffraction. This effect is modeled by introducing filters into the power spectrum of the index-of-refraction fluctuations that only keep the high and low scale factors. The Rytov theory analysis is then re-accomplished using this filtered power spectrum. The cutoffs for these filters

can then be found by matching the results from extended Rytov theory to those of conventional Rytov theory in weak turbulence and asymptotic theory for very strong turbulence.

An example of extended Rytov theory is given here by deriving an expression for $\tilde{\sigma}_I^2$ that is accurate at all turbulence levels. The filtering of the index-of-refraction power spectrum results in expressing the Rytov perturbation as $\psi = \psi_X + \psi_Y$, where ψ_X accounts for the refractive effects of the turbulence and ψ_Y accounts for the diffractive effects. The log-amplitude χ is then simply the sum of the real parts of ψ_X and ψ_Y . Since they are independent, the log-amplitude variance can be expressed as $\sigma_\chi^2 = \sigma_X^2 + \sigma_Y^2$, where X and Y are the real parts of ψ_X and ψ_Y . Inserting this into Eq. (2.4.57) gives

$$\tilde{\sigma}_I^2 = \exp(4\sigma_X^2 + 4\sigma_Y^2) - 1. \quad (2.4.94)$$

For a point source, the scintillation index in weak turbulence or very strong turbulence are found to be [2]

$$\tilde{\sigma}_I^2 \simeq \begin{cases} 4\mathcal{R} & \text{for } \mathcal{R} \ll 1, \\ 1 + \frac{1.09}{\mathcal{R}^{2/5}} & \text{for } \mathcal{R} \gg 1. \end{cases} \quad (2.4.95)$$

Using the filter functions

$$G_X(\kappa) = \exp\left(-\frac{\kappa^2}{\kappa_X^2}\right), \quad (2.4.96)$$

$$G_Y(\kappa) = \frac{\kappa^{11/3}}{(\kappa^2 + \kappa_Y^2)^{11/6}} \quad (2.4.97)$$

in Eq. (2.4.52) and matching the relevant constraints produces

$$\sigma_X^2 \simeq \frac{0.49\mathcal{R}}{(1 + 3.0\mathcal{R}^{6/5})^{7/6}}, \quad (2.4.98)$$

$$\sigma_Y^2 \simeq \frac{0.51\mathcal{R}}{(1 + 3.6\mathcal{R}^{6/5})^{5/6}}. \quad (2.4.99)$$

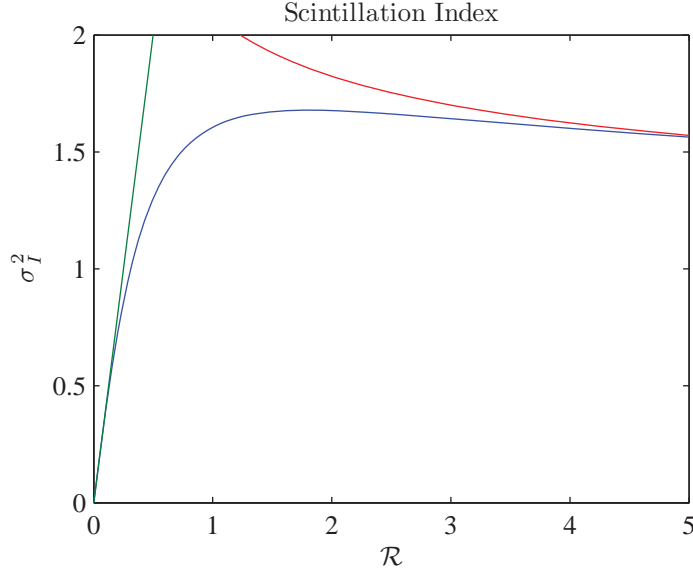


Figure 2. Comparison of $\tilde{\sigma}_I^2$ for weak (green), all (blue) and very strong (red) turbulence levels.

Inserting this into Eq. (2.4.94) gives the final expression for the scintillation index as

$$\tilde{\sigma}_I^2 = \exp \left[\frac{2.0\mathcal{R}}{(1 + 3.0\mathcal{R}^{6/5})^{7/6}} + \frac{2.0\mathcal{R}}{(1 + 3.6\mathcal{R}^{6/5})^{5/6}} \right] - 1. \quad (2.4.100)$$

This behavior is shown in Fig. 2 along with the limiting values given in Eq. (2.4.95). Equation (2.4.100) has demonstrated good agreement with both experimental and simulation results at all turbulence strength levels [2]. Following the same procedure, the scintillation index for a non-converging Gaussian beam can be found to be [2]

$$\tilde{\sigma}_I^2 = \exp \left[\frac{0.49\sigma_B^2}{\left[1 + 0.56(1 + \Theta)\sigma_B^{12/5}\right]^{7/6}} + \frac{0.51\sigma_B^2}{\left(1 + 0.69\sigma_B^{12/5}\right)^{5/6}} \right] - 1 + 44.0\mathcal{R}\Lambda_e^{5/6} \frac{|\rho|^2}{w_t^2}, \quad (2.4.101)$$

where

$$\sigma_B^2 = 38.4\mathcal{R} \operatorname{Re} \left[j^{5/6} {}_2F_1 \left(-\frac{5}{6}, \frac{11}{6}; \frac{17}{6}; \bar{\Theta} + j\Lambda \right) - \frac{11}{16}\Lambda^{5/6} \right]. \quad (2.4.102)$$

Another advantage of treating the large-scale and small-scale fluctuations independently is that this can be used to derive the probability density of the intensity fluctuations. Based on the previous example, it is reasonable to assume the intensity can be represented as

$$I = \langle I \rangle I_X I_Y, \quad (2.4.103)$$

where both I_X and I_Y are independent unit-mean random variables. It is further assumed that they are gamma distributed with distributions given by

$$p_X(I_X) = \frac{\alpha(\alpha I_X)^{\alpha-1}}{\Gamma(\alpha)} \exp(-\alpha I_X) \quad \text{for } \alpha > 0 \text{ and } I_X > 0, \quad (2.4.104)$$

$$p_Y(I_Y) = \frac{\beta(\beta I_Y)^{\beta-1}}{\Gamma(\beta)} \exp(-\beta I_Y) \quad \text{for } \beta > 0 \text{ and } I_Y > 0, \quad (2.4.105)$$

where $\alpha = 1/\sigma_{I_X}^2$, $\beta = 1/\sigma_{I_Y}^2$, and Γ is the gamma function. By fixing I_X and using $dI_Y = dI/(\langle I \rangle I_X)$, the pdf of I conditioned on I_X can be expressed as

$$p_I(I|I_X) = \frac{\beta}{\Gamma(\beta) \langle I \rangle I_X} \left(\frac{\beta I}{\langle I \rangle I_X} \right)^{\beta-1} \exp\left(-\frac{\beta I}{\langle I \rangle I_X}\right) \quad \text{for } I > 0. \quad (2.4.106)$$

The unconditioned pdf is found by averaging over I_X which produces

$$p_I(I) = \frac{2}{\Gamma(\alpha)\Gamma(\beta)I} \left(\frac{\alpha\beta I}{\langle I \rangle} \right)^{(\alpha+\beta)/2} K_{\alpha-\beta} \left(2\sqrt{\frac{\alpha\beta I}{\langle I \rangle}} \right) \quad \text{for } I > 0, \quad (2.4.107)$$

where K_ν is a modified Bessel function of the second kind. This pdf is known as the gamma-gamma distribution and has a mean of $\langle I \rangle$ and variance of $\langle I \rangle^2 [1/\alpha + 1/\beta + 1/(\alpha\beta)]$. By using

$$\sigma_{I_X}^2 = \exp(4\sigma_X) - 1, \quad (2.4.108)$$

$$\sigma_{I_Y}^2 = \exp(4\sigma_Y) - 1, \quad (2.4.109)$$

α and β can be defined entirely in terms of the turbulence parameters through expressions such as Eqs. (2.4.98) and (2.4.99). Simulations have shown that the gamma-gamma distribution makes a good fit with the strong turbulence intensity fluctuations [2].

2.4.2.4 Branch points and branch cuts.

Another characteristic of strong turbulence is the appearance of unavoidable phase discontinuities in the wavefront [31, 34]. While the phase of a field can take on any value, it is defined as the imaginary part of an exponential, so phases that are multiple values of 2π apart from each other are indistinguishable when measured. As a result, when the phase is calculated, by taking the arctangent of the imaginary part of the field divided by the real part of the field, it is bounded between $-\pi$ and π (or any other 2π interval). This places a discontinuity between the second and third quadrants of the imaginary plane, or wherever the real part of the field is negative and the imaginary part switches signs. As long as the discontinuity follows a closed loop, or enters and exits through the boundaries of the region of interest, it can be accounted for by simply adding or subtracting 2π to the appropriate side of the discontinuity. However, if this is not the case, the discontinuity cannot be eliminated.

Branch points are locations of zero intensity in the field, and they create optical vortices in the phase. Zeros in the intensity come about whenever both the real and imaginary portions of the field equal zero at the same point. Since the real and imaginary portions of the field must be continuous, this only happens when zero contours of the real part cross zero contours of the imaginary part. This is illustrated in two dimensions in Fig. 3 where phase discontinuities occur at all the red-to-blue transitions. As long as the zero contours of the real and imaginary parts of the field do not cross, as at the top or the lower right corner, the discontinuity can easily be

Phase Contours

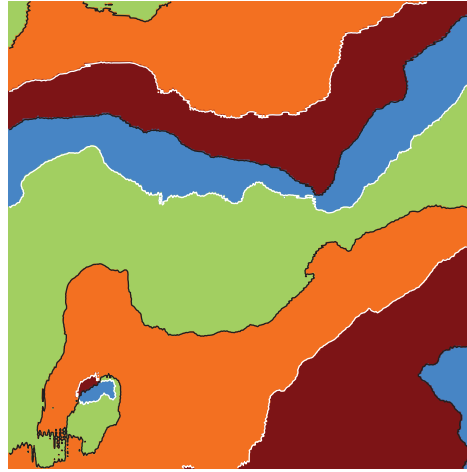


Figure 3. Contour plot of the phase of a field after passing through turbulence. The zero of the real part is indicated by white lines, while the zero of the imaginary part is indicated by black lines. The phase range $(-\pi, -\pi/2)$ is indicated by blue, $(-\pi/2, 0)$ is in green, $(0, \pi/2)$ is in orange, and $(\pi/2, \pi)$ is in red. Branch points occur wherever the white and black lines cross. Phase cuts occur wherever red and blue portions meet.

remedied. But when they do cross, such as in the lower left corner, branch points are created which serve as a starting or ending point for a discontinuity. These discontinuities can be moved by changing the 2π wrapping interval, but they cannot be eliminated. The density of branch points grows with increasing turbulence [85] so while they are of little concern in weak turbulence, they can have a considerable effect in strong turbulence.

2.5 Self-Referencing Interferometer (SRI)

The self-referencing interferometer (SRI) directly measures the phase aberrations of incident light by interfering this light with a temporally coherent plane wave [65]. The way this is accomplished is shown conceptually in Fig. 4. The SRI first splits the light into two branches: a reference branch and a beacon branch. The light in the reference branch is coupled into a single mode optical fiber which only allows

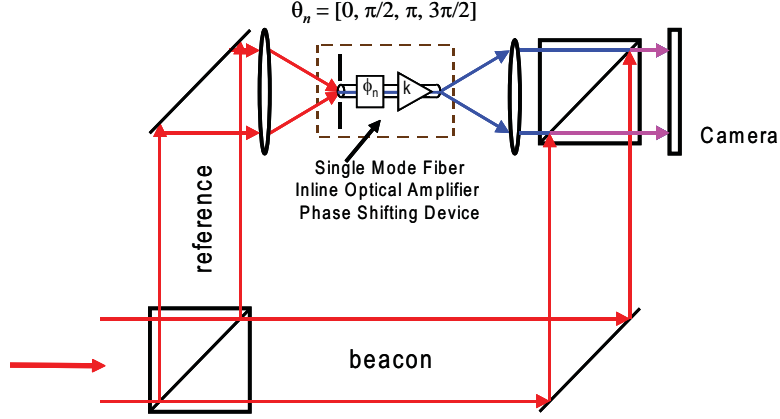


Figure 4. Diagram of a self-referencing interferometer. Light is split between a reference path and a beacon path. The light in the reference path is spatially filtered by a single mode fiber, and potentially phase shifted, then recombined with the light in the reference path. The resulting interference pattern is directly related to the phase aberration.

the unaberrated portion of the field to pass through. It is then recombined with the original wavefront from the beacon branch which produces an interference pattern on a detector.

If the field in the beacon path is $U = A \exp(j\phi)$ and the field exiting the reference path is $U_r = A_r \exp(j\phi_r)$, then the intensity pattern over the detector is given by

$$\begin{aligned}
 I &= |U + U_r|^2 \\
 &= (U + U_r)(U^* + U_r^*) \\
 &= (Ae^{j\phi} + A_r e^{j\phi_r}) (Ae^{-j\phi} + A_r e^{-j\phi_r}) \\
 &= A^2 + A_r^2 + AA_r [e^{j(\phi-\phi_r)} + e^{-j(\phi-\phi_r)}] \\
 &= A^2 + A_r^2 + 2AA_r \cos(\phi - \phi_r).
 \end{aligned} \tag{2.5.1}$$

Using the relations $A = A_0 \exp(\chi)$ and $\phi = \phi_r + S$, this becomes

$$I = A_0^2 \exp(2\chi) + A_r^2 + 2A_0 A_r \exp(\chi) \cos S. \tag{2.5.2}$$

This indicates the resulting interference pattern is directly related to the phase aberration S .

All that is now required is to determine S from this interference pattern. This can be accomplished through the use of phase shifting interferometry (PSI) [56]. In PSI, the phase in one of the branches is shifted by a known amount with respect to the other branch. For instance, if the reference branch makes the four phase shifts of 0 , $-\pi/2$, $-\pi$, and $-3\pi/2$, then the four resulting interference patterns can be represented as

$$\begin{aligned} I_1 &= A_0^2 \exp(2\chi) + A_r^2 + 2A_0A_r \exp(\chi) \cos(S + 0) \\ &= A_0^2 \exp(2\chi) + A_r^2 + 2A_0A_r \exp(\chi) \cos S, \end{aligned} \quad (2.5.3)$$

$$\begin{aligned} I_2 &= A_0^2 \exp(2\chi) + A_r^2 + 2A_0A_r \exp(\chi) \cos(S + \pi/2) \\ &= A_0^2 \exp(2\chi) + A_r^2 - 2A_0A_r \exp(\chi) \sin S, \end{aligned} \quad (2.5.4)$$

$$\begin{aligned} I_3 &= A_0^2 \exp(2\chi) + A_r^2 + 2A_0A_r \exp(\chi) \cos(S + \pi) \\ &= A_0^2 \exp(2\chi) + A_r^2 - 2A_0A_r \exp(\chi) \cos S, \end{aligned} \quad (2.5.5)$$

$$\begin{aligned} I_4 &= A_0^2 \exp(2\chi) + A_r^2 + 2A_0A_r \exp(\chi) \cos(S + 3\pi/2) \\ &= A_0^2 \exp(2\chi) + A_r^2 + 2A_0A_r \exp(\chi) \sin S. \end{aligned} \quad (2.5.6)$$

A little algebra produces

$$\frac{I_4 - I_2}{I_1 - I_3} = \tan S, \quad (2.5.7)$$

or

$$S = \arctan \left(\frac{I_4 - I_2}{I_1 - I_3} \right). \quad (2.5.8)$$

By keeping track of the signs of the numerator and denominator in Eq. (2.5.8), S can be recovered within a 2π interval. As can be seen from Eq. (2.5.7), all the χ terms divide out, so the log-amplitude variations have no part in the phase calculation. This

means the SRI is theoretically immune to scintillation [6]. For this reason, the SRI makes an attractive WFS for use with strong turbulence.

These phase shifts can be made spatially, temporally, or both [66]. Performing them spatially is advantageous in that the four measurements can be made simultaneously which mitigates temporal effects. The drawback to this method is it requires splitting the light into four different paths. Not only must these paths must be closely aligned and matched, but this splitting of the light lowers the overall signal strength of each path. This may be an issue in very low-light conditions. Making the phase shifts temporally requires much less hardware and does not require splitting the light as much. However, if the incident light is dynamic, then it may change from one measurement to the next thereby decreasing the measurement accuracy. Additionally, the phase shift cannot be made temporally as accurately as they can be made spatially. These inaccuracies in the phase shifts also lead to less accurate phase measurements [56]. A third approach is to make two measurements at a time, which strikes a balance between the purely spatial and temporal approaches.

To keep things simple, this research assumed spatial PSI. However, these results can be extended to temporal PSI by including the temporal effects as described in [66] and the phase shift error effects as described in [56].

2.6 Single-Mode Optical Fibers

As explained above, an SRI makes use of a single-mode optical fiber to optically filter the incident wavefront. As a result, it is important to understand the operation of single-mode fibers before it is possible to fully understand the operation of an SRI. A conceptual diagram of an optical fiber is found in Fig. 5. As indicated, it is composed of an optically clear material where the index-of-refraction in the core n_1 is slightly greater than that in the cladding n_2 . This difference in the index-or-

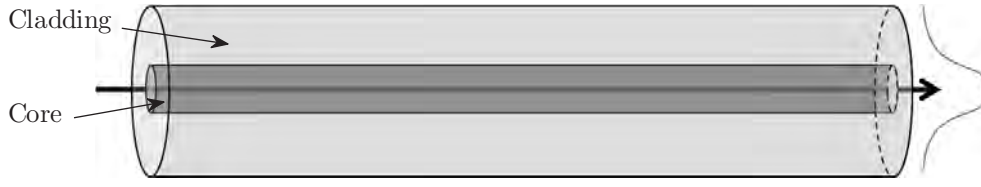


Figure 5. Diagram of a single-mode optical fiber

refraction is typically about 0.2% for single-mode fibers, while it is closer to 1% in multi-mode fibers [14]. While the following analysis assumes the index-of-refraction is constant within the core or cladding, this is not necessarily the case in practice. Frequently, fibers are constructed such that there is a smooth transition from the core to cladding. These are known as graded index (GRIN) fibers. However, this fact is not limiting since behavior of GRIN fibers can be closely approximated by an effective step-index fiber. Therefore, understanding the operation of step-index fibers is sufficient for understanding the operation of optical fibers in general [14, 59].

Since the difference in index-of-refraction between the core and cladding is so small, optical fibers are weak waveguides that only confine wavefronts that are very nearly linearly polarized in the transverse plane of the fiber. For this reason, the propagation modes of optical fibers are known as LP_{lm} modes. As usual, the derivation for the expressions of the LP_{lm} modes begins with the Helmholtz equation of Eq. (2.1.16). This time it is assumed $U(\mathbf{r}) = V(\boldsymbol{\rho}) \exp(j\beta z)$, where

$$kn_2 < \beta < kn_1. \quad (2.6.1)$$

Inserting this into the Helmholtz equation and using the paraxial approximation produces

$$(\nabla_T^2 + \beta_t^2)V(\boldsymbol{\rho}) = 0, \quad (2.6.2)$$

where $\beta_t = (k^2 n_x^2 - \beta)^{1/2}$ and n_x is the index-of-refraction in either the core or cladding. Since the fiber displays cylindrical symmetry, it can be assumed the solution to Eq. (2.6.2) is of the form $V(\boldsymbol{\rho}) = R(\rho)\Phi(\phi)$, where ρ and ϕ are respectively the radial and azimuthal coordinates. Expressing ∇_T^2 in cylindrical coordinates and making this substitution produces

$$\frac{\rho^2}{R} \frac{d}{d\rho} \left(\rho \frac{dR}{d\rho} \right) + \rho^2 \beta_t^2 = -\frac{1}{\Phi} \frac{d^2\Phi}{d\phi^2}. \quad (2.6.3)$$

Since the left side of the equation is only a function of ρ and the right side of the equation is only a function of ϕ , each side must be equal to the same constant l^2 . This implies two ordinary differential equations of

$$\frac{d^2\Phi}{d\phi^2} + l^2\Phi = 0, \quad (2.6.4)$$

$$\frac{d}{d\rho} \left(\rho \frac{dR}{d\rho} \right) + \left(\beta_t^2 - \frac{l^2}{\rho^2} \right) R = 0. \quad (2.6.5)$$

The solution to Eq. (2.6.4) can be readily found to be

$$\Phi(\phi) = C_1 \exp(jl\phi) + C_2 \exp(-jl\phi), \quad (2.6.6)$$

where C_1 and C_2 are arbitrary constants. Since Φ must be periodic over a range of 2π , l must be an integer.

Equation (2.6.5) can be recognized as a form of Bessel's equation [42, Eq. (8.491 1)] with the solution

$$R(\rho) = \begin{cases} C_3 J_l(\beta_t \rho) + C_4 Y_l(\beta_t \rho) & \text{for } \beta_t \in \Re, \\ C_5 I_l(|\beta_t| \rho) + C_6 K_l(|\beta_t| \rho) & \text{for } \beta_t \in \Im, \end{cases} \quad (2.6.7)$$

where $J_l(\cdot)$ and $Y_l(\cdot)$ are Bessel functions of the first and second kind, $I_l(\cdot)$ and $K_l(\cdot)$

are modified Bessel functions of the first and second kind, and all the C coefficients are arbitrary constants. From the definition of β_t and the constraint given by Eq. (2.6.1), it can be seen that β_t is real in the core and imaginary in the cladding. The fact $Y_l(0) = -\infty$ requires $C_4 = 0$. Furthermore, $I_l(\rho)$ grows with increasing ρ , but the field should attenuate in the cladding, so $C_5 = 0$. This means the expression for R must be of the form

$$R(\rho) = \begin{cases} C_3 J_l(u\rho/a) & \text{for } \rho \leq a, \\ C_6 K_l(w\rho/a) & \text{for } \rho \geq a, \end{cases} \quad (2.6.8)$$

where $u = a(k^2 n_1^2 - \beta^2)^{1/2}$, $w = a(\beta^2 - k^2 n_2^2)^{1/2}$, and a is the core radius.

One of the coefficients can be determined by analyzing the field boundary conditions at the core/cladding interface. The boundary condition for the electric field normal to this interface is [44]

$$n_1^2 E(a^-) = n_2^2 E(a^+), \quad (2.6.9)$$

where the superscripts on a mean slightly more than or slightly less than. Since $n_1 \simeq n_2$, this boundary condition can be closely approximated as

$$R(a^-) = R(a^+), \quad (2.6.10)$$

$$C_3 J_l(u) = C_6 K_l(w), \quad (2.6.11)$$

$$C_6 = C_3 \frac{J_l(u)}{K_l(w)}. \quad (2.6.12)$$

Another boundary condition is that the z component of the magnetic field must be consistent across this interface [44]. The z component of the magnetic field is related to tangential components of the electric field by Eq. (2.1.9). This constraint

implies that

$$\left. \frac{d}{d\rho} \left[\rho J_l \left(\frac{u\rho}{a} \right) \right] \right|_{\rho=a} = \frac{J_l(u)}{K_l(w)} \left. \frac{d}{d\rho} \left[\rho K_l \left(\frac{w\rho}{a} \right) \right] \right|_{\rho=a} \quad (2.6.13)$$

$$u J_{l-1}(u) - (l-1) J_l(u) = - \frac{J_l(u)}{K_l(w)} [w K_{l-1}(w) + (l-1) K_l(w)] \quad (2.6.14)$$

$$u J_{l-1}(u) K_l(w) = - w J_l(u) K_{l-1}(w). \quad (2.6.15)$$

Both u and w are functions of β , so Eq. (2.6.15) is actually a constraint on the frequencies that propagate through the fiber. However, instead of solving for β it is more convenient to define a normalized frequency parameter $v = (u^2 + w^2)^{1/2} = ak(n_1^2 + n_2^2)^{1/2}$. Since v is defined by the fiber characteristics, it is set when the fiber is manufactured. The definition of v along with Eq. (2.6.15) provides two equations with two unknowns. As these equations are non-linear, they may have no solutions or potentially many solutions for a given value of l . The LP_{lm} propagation modes are then defined by the values of u and w that solve these equations, where m represents a particular solution for a given l .

When $v < 2.405$, there is only one possible solution and it requires $l = 0$ [14]. This condition on v defines a single-mode fiber that can only propagate the LP_{01} mode given by

$$M_0(\boldsymbol{\rho}) = \begin{cases} C J_0 \left(\frac{u|\boldsymbol{\rho}|}{a} \right) & \text{for } |\boldsymbol{\rho}| \leq a \\ C \frac{J_0(u)}{K_0(w)} K_0 \left(\frac{w|\boldsymbol{\rho}|}{a} \right) & \text{for } |\boldsymbol{\rho}| \geq a, \end{cases} \quad (2.6.16)$$

where $C = C_3(C_1 + C_2)$. It is convenient to normalize this mode such that its inner product is unity, or

$$\iint |M_0(\boldsymbol{\rho})|^2 d^2\boldsymbol{\rho} = 1. \quad (2.6.17)$$

When this normalization is carried out, the expression for the LP_{01} mode becomes

$$M_0(\boldsymbol{\rho}) = \begin{cases} \frac{w}{av\sqrt{\pi}J_1(u)} J_0\left(\frac{u|\boldsymbol{\rho}|}{a}\right) & \text{for } |\boldsymbol{\rho}| \leq a \\ \frac{u}{av\sqrt{\pi}K_1(w)} K_0\left(\frac{w|\boldsymbol{\rho}|}{a}\right) & \text{for } |\boldsymbol{\rho}| \geq a. \end{cases} \quad (2.6.18)$$

When normalized in the manner of Eq. (2.6.17), the LP_{lm} modes form a complete orthonormal set [14]. This means that any wavefront may be decomposed into the LP_{lm} modes as

$$U(\boldsymbol{\rho}) = \sum_i b_i M_i(\boldsymbol{\rho}), \quad (2.6.19)$$

where b_i are the mode coefficients and $M_i(\cdot)$ represent the modes. These coefficients can be determined by

$$b_i = \iint U(\boldsymbol{\rho}) M_i^*(\boldsymbol{\rho}) d^2\boldsymbol{\rho}. \quad (2.6.20)$$

It is a simple matter to show that the power carried in each of these modes is $|b_i|^2$. If an electromagnetic field impinges on an optical fiber, the fiber will only pass the portions of the field that match its propagation modes. The total power transmitted through the fiber is then found by summing the magnitude squared of the coupling coefficients of the propagation modes. The coupling efficiency can then be defined as the ratio of the propagated power to the power in the original field. This is expressed as

$$\eta = \frac{\sum_i |b_i|^2}{\iint |U(\boldsymbol{\rho})|^2 d^2\boldsymbol{\rho}} = \frac{\sum_i \iint \iint U(\boldsymbol{\rho}_1) M_i^*(\boldsymbol{\rho}_1) U^*(\boldsymbol{\rho}_2) M_i(\boldsymbol{\rho}_2) d^2\boldsymbol{\rho}_1 d^2\boldsymbol{\rho}_2}{\iint |U(\boldsymbol{\rho})|^2 d^2\boldsymbol{\rho}}, \quad (2.6.21)$$

where the summation is only over the propagation modes. For a single-mode fiber, this simplifies to

$$\eta = \frac{\iint \iint U(\boldsymbol{\rho}_1) M_0^*(\boldsymbol{\rho}_1) U^*(\boldsymbol{\rho}_2) M_0(\boldsymbol{\rho}_2) d^2 \boldsymbol{\rho}_1 d^2 \boldsymbol{\rho}_2}{\iint |U(\boldsymbol{\rho})|^2 d^2 \boldsymbol{\rho}} \quad (2.6.22)$$

In practice, a lens is normally used to maximize coupling by focusing the light onto the end of the fiber. Due to the Fourier transform relation between the focal plane and pupil plane as indicated by Eq. (2.1.36), the decomposition given in Eq. (2.6.19) applies just as well in the pupil plane. In this case, the modes for the decomposition are found by back-propagating the LP_{lm} modes to the pupil plane. A big advantage in performing the calculation in the pupil plane instead of the focal plane is that the effect of the aperture becomes multiplicative. The expression for the coupling efficiency of a single-mode fiber then becomes

$$\eta = \frac{\iint_{\mathcal{P}} \iint_{\mathcal{P}} U(\boldsymbol{\rho}_1) \mathcal{M}_0^*(\boldsymbol{\rho}_1) U^*(\boldsymbol{\rho}_2) \mathcal{M}_0(\boldsymbol{\rho}_2) P(\boldsymbol{\rho}_1) P(\boldsymbol{\rho}_2) d^2 \boldsymbol{\rho}_1 d^2 \boldsymbol{\rho}_2}{\iint |U(\boldsymbol{\rho})|^2 P(\boldsymbol{\rho}) d^2 \boldsymbol{\rho}}, \quad (2.6.23)$$

where $\mathcal{M}_0(\cdot)$ is the back-propagated LP_{01} mode and $P(\cdot)$ defines the effect of the pupil. Since M_0 is radially symmetric, \mathcal{M}_0 can be found by way of the Fourier-Bessel transform with [39]

$$\mathcal{M}_0(\boldsymbol{\rho}) = \frac{k}{f} \int_0^\infty r M_0(r) J_0 \left(\frac{kr|\boldsymbol{\rho}|}{f} \right) dr, \quad (2.6.24)$$

where f is the distance between the focal plane and the pupil plane and the phase factors were ignored. After a lengthy derivation, the back-propagated LP_{01} mode is

found to be

$$\mathcal{M}_0(\boldsymbol{\rho}) = \left(\frac{kawv}{\sqrt{\pi}f} \right) \frac{uJ_0\left(\frac{ka|\boldsymbol{\rho}|}{f}\right) - \frac{ka|\boldsymbol{\rho}|}{f} \frac{J_0(u)}{J_1(u)} J_1\left(\frac{ka|\boldsymbol{\rho}|}{f}\right)}{\left[u^2 - \left(\frac{ka|\boldsymbol{\rho}|}{f}\right)^2 \right] \left[w^2 + \left(\frac{ka|\boldsymbol{\rho}|}{f}\right)^2 \right]}. \quad (2.6.25)$$

Since this expression for the fiber mode can be analytically unwieldy, it can be closely approximated with a Gaussian function given by

$$\mathcal{M}_0(\boldsymbol{\rho}) = 2A\sqrt{\frac{2}{\pi}} \exp(-4A^2|\boldsymbol{\rho}|^2), \quad (2.6.26)$$

where A can be found by the expression [58]

$$A = \frac{ka}{4f} \left(0.65 + \frac{1.619}{v^{3/2}} + \frac{2.879}{v^6} \right). \quad (2.6.27)$$

The goodness of fit, found by taking the inner product of Eqs. (2.6.25) and (2.6.27), is a function of v and ranges from 0.946 for $v = 1.2$ to 0.9965 for $v = 2.4$ [58].

III. Review of Related Research

The purpose of this chapter is to overview previously published research that directly relates to the new research presented in this dissertation. This dissertation research was primarily motivated by the hybrid wavefront sensor work of Ellis [25]. In his work, two different wavefront sensors, including the self-referencing interferometer (SRI), were combined in a way that increased performance over either wavefront sensor alone. While he was able to validate this hybrid wavefront sensor concept, he identified some shortcomings with his SRI model. The primary shortcoming was the absence of any fiber coupling efficiency variations. Furthermore, only point sources were used as beacons due to shortcomings in atmospheric theory when using extended, partially coherent sources.

This dissertation research was intended to overcome these identified shortcomings. It does so by focusing on three specific areas of analysis. The first deals with the propagation of partially coherent fields through strong atmospheric turbulence. The second examines the coupling of random fields into single-mode optical fibers. The third analyzes the performance of self-referencing interferometers (SRI), particularly with strong turbulence and extended beacons, including the fiber coupling efficiency variations. The results from this research not only serve to strengthen the work by Ellis, but also provides analytic tools that may be used in many other fields of research.

3.1 Partially Coherent Fields in Strong Turbulence

In the late 1960's and throughout the 1970's, much work was done on characterizing the propagation of partially coherent fields through atmospheric turbulence at all turbulence strength levels. Many different methods were proposed includ-

ing the operational method [35], the extended Huygens-Fresnel principle [54], the extended Rayleigh-Sommerfeld integral method [53], difference equations [12], the diagram method [22], integral equations [93], transport theory [27], Markov approximations [82], and Feynman path integrals [21]. It has been shown that to the second order when approximations similar to the paraxial approximation are used, all these methods result in Eq. (2.4.89) [13]. When used with the Kolmogorov power spectrum of Eq. (2.4.5), the integral in the exponential function becomes

$$\begin{aligned}
 & -4\pi^2 k^2 L \int_0^1 \int_0^\infty \kappa \Phi_n(\kappa) \{1 - J_0 [|\xi(\boldsymbol{\rho}'_1 - \boldsymbol{\rho}'_2) + (1 - \xi)(\boldsymbol{\rho}_1 - \boldsymbol{\rho}_2)|\kappa]\} d\kappa d\xi \\
 & = -1.46 C_n^2 K^2 L \int_0^1 |\xi(\boldsymbol{\rho}'_1 - \boldsymbol{\rho}'_2) + (1 - \xi)(\boldsymbol{\rho}_1 - \boldsymbol{\rho}_2)|^{5/3} d\xi \quad (3.1.1)
 \end{aligned}$$

This integral has no known analytic solution and must therefore be solved numerically.

While exact analytic solutions cannot be found from Eq. (3.1.1), a common method to find approximate solutions is to change the 5/3-power to a 2 [7, 15, 26, 53, 68, 88]. When the light source is a Gaussian beam, this quadratic approximation has little effect on estimating the average beam size or radius of curvature [47, 76], but it may have a significant effect on the estimate of the beam's coherence size. Assuming a coherent source, comparisons between estimates of the coherence radius using the quadratic approximation and that found by numerically integrating Eq. (3.1.1) have demonstrated errors as high as 12% [1, 8]. However, no references could be found that make this comparison when the source is partially coherent.

An alternative method of estimating mutual coherence function (MCF) of partially coherent beams as they travel through atmospheric turbulence is an extension of the effective parameters method described in Sec. 2.4.2.2. In this method, it is assumed

that a field after propagating a distance L through turbulence can be modeled as

$$U(\boldsymbol{\rho}, L) = U_0(\boldsymbol{\rho}, L) \exp [\Psi_S(\boldsymbol{\rho}, L)] \exp [\psi(\boldsymbol{\rho}, L)], \quad (3.1.2)$$

where $U_0(\cdot)$ represents the field as it would be with a coherent source and no turbulence, $\Psi_S(\cdot)$ is the complex phase perturbations due to the partial coherence of the source, and $\psi(\cdot)$ is the complex phase perturbation due to atmospheric turbulence [2]. By further assuming the source perturbations and atmospheric perturbations are independent, the MCF of the field can be expressed as

$$\Gamma(\boldsymbol{\rho}_1, \boldsymbol{\rho}_2, L) = \Gamma_c(\boldsymbol{\rho}_1, \boldsymbol{\rho}_2, L) \Gamma_a(\boldsymbol{\rho}_1, \boldsymbol{\rho}_2, L), \quad (3.1.3)$$

where $\Gamma_c(\cdot)$ is the MCF absent of atmospheric turbulence as found using Eq. (2.2.3), and $U_0(\boldsymbol{\rho}_1, L)U_0^*(\boldsymbol{\rho}_2, L)\Gamma_a(\boldsymbol{\rho}_1, \boldsymbol{\rho}_2, L)$ would be the MCF if the source was coherent as found using the effective parameters method. While no references could be found comparing the accuracy of this method to that of the quadratic approximation when the source is partially coherent, it has been shown that this method is generally more accurate when the source was coherent [1, 2].

3.2 Coupling of Random Fields into Single-mode Fibers

The coupling of an aberrated wavefront into a single-mode fiber was first extensively studied by Wagner and Tomlinson [87]. However, their focus was on static aberrations as well as fiber misalignments and fiber-mode mismatch.

This was followed by Shaklan and Roddier [79] who studied the effect of atmospheric turbulence on the mean coupling efficiency and its fluctuations, defined as the mean normalized standard deviation (std). Assuming weak atmospheric turbulence, they demonstrated how the mean coupling efficiency decreases with increasing

D/r_0 , where D is the pupil diameter and r_0 is the atmospheric coherence length of Eq. (2.4.41). They also demonstrated through computer simulations that the coupling efficiency fluctuations saturated at ~ 1 for large D/r_0 .

Winzer and Leeb [94] expressed the mean fiber coupling efficiency of random fields when the complex degree of coherence as given by Eq. (2.2.2) can be expressed as a Gaussian function. They demonstrated the dependence of the mean coupling efficiency on the ratio between the receiver diameter and the coherence diameter. This analysis also assumed a uniform average irradiance over the receiver aperture.

Ruilier and Cassaing [74, 75] analyzed the coupling efficiency of light degraded by weak atmospheric turbulence as decomposed into Zernike polynomials. By expressing the coupling efficiency in terms of the Zernike polynomial coefficients, it was possible to derive approximate expressions for the mean coupling efficiency and coupling fluctuations after some of the Zernike modes had been eliminated by use of adaptive optics. However, as D/r_0 increased, the approximations began to deviate from the simulations, particularly for the coupling fluctuations. As with [79], the coupling fluctuations saturated near 1 for large D/r_0 .

As many of the previous studies assumed the complex degree of coherence had a Gaussian shape, Dikmelik and Davidson [23] compared the effect of a 5/3-power law (as predicted by a Kolmogorov power spectrum) on the coupling efficiency to that of a Gaussian. They demonstrated that the Gaussian approximation slightly overestimates the true coupling efficiency when coherence area of the field on the order of or larger than the receiver area, while it slightly underestimated the coupling efficiency when the coherence area of the field as much smaller than the receiver area. However, the two cases were very close across the entire range of values which indicated the Gaussian degree of coherence was an excellent approximation of the true degree of coherence.

The expressions for the coupling efficiency as given in the previous papers all required numerical evaluation. Chen *et al.* [17] derived an exact expression for the coupling of a random plane wave with a Gaussian complex degree of coherence into an annular-aperture receiver. This expression involves an infinite sum of confluent hypergeometric functions, so while it does aid further analysis in some cases, it can be cumbersome in other situations. This is particularly the case when the coherence size of the field is small with respect to the receiver.

All of these studies assumed the average intensity was constant across the receiver aperture. While this may frequently be the case, this cannot always be assumed for Gaussian Schell-model (GSM) beams. They also all assumed that any amplitude fluctuations of the field were negligible. This may be true for coherent sources in weak turbulence, but it is not true for partially coherent sources or strong turbulence. As a result further study was required to better understand the coupling of GSM beams into single-mode optical fibers.

3.3 SRI Performance

The SRI was initially developed due to its theoretical insensitivity to scintillation [6]. This insensitivity is due to its measurements comprising linear combinations of the complex field, so its average estimation accuracy is governed by the statistics of the complex field. Since the statistics of the complex field are defined by the MCF, and the MCF does not functionally depend on the scintillation index, its measurement accuracy must also be independent of scintillation [5]. Neglecting other error sources, its performance is only limited by the size of the subapertures with respect to r_0 and the coherence time of the light with respect to the detector integration time. Simulations have demonstrated this invariance to scintillation and dependence on subaperture size [6, 25].

In contrast to noise-free simulations, real-world implementations of an SRI have demonstrated a susceptibility to scintillation [19,60]. This susceptibility is likely due not only to measurement noise (such as shot noise, read noise, and quantization noise), but also to changes in the amount of power coupled into the single-mode fiber [23,83]. While work has been done to analyze the noise characteristics of the SRI accounting for shot noise, read noise, quantization noise, and amplified spontaneous emission (ASE), it assumed no scintillation [66]. This study also only analyzed the effect of these noise sources on the full field estimation error instead of the phase estimation error. The only analytic model that directly addressed how scintillation along with shot noise affects the phase estimation error of an SRI is by Ellis [25]. However, this analysis disregards fiber coupling variations and the other additive noise sources. This indicated there still existed a need for an SRI noise model that takes all of these noise sources into account. Additionally, no study had yet been performed analyzing the use of non-point sources, nor the effects of the partial temporal coherence of the incident light.

IV. GSM Beams in Atmospheric Turbulence

4.1 Introduction

Random variations in the index of refraction of the atmosphere have a direct impact on the degree of coherence of any electromagnetic wave that traverses it [82]. While much literature has been produced describing the nature of this effect on light in a variety of conditions, analytic expressions for the coherence function of the light are either approximations or of limited applicability. While exact solutions to the relevant propagation equations do exist under certain conditions, such as weak turbulence or separation distances much smaller than the inner scale of the turbulence, these equations are intractable in the inertial subrange of atmospheric turbulence where separation distances fall between the turbulence inner and outer scales [2]. Since this is the region of interest for many practical applications, solutions in these cases require either simplifying approximations or numerical evaluation.

One particular example deals with the coupling of atmospherically perturbed light into single-mode mode optical fibers. Optical fibers are used in this manner in many fields, such as free-space optical communications, ladar/lidar, stellar interferometry, and adaptive optics [23, 45, 55, 65, 75, 79, 83, 90, 94]. When the coherence radius of the light is much smaller than the receiver aperture radius, the average coupling efficiency is directly proportional to the square of the coherence length of the incident light [91]. This means that any error in estimating the coherence radius of the light is at least doubled when estimating the average optical fiber coupling efficiency. Since some methods for estimating the coherence radius have been shown to have errors as large as 12% [8], it is important to understand which method has the best accuracy for a given condition.

For the purpose of this study, the light source was considered to be a Gaussian

Schell-model (GSM) beam [57]. GSM beams have been extensively used as source models in the literature due to their analytic convenience and their broad applicability [24, 26, 37, 47, 49, 53, 68, 80, 88, 97]. They are analytically simple in that their second-order statistics, as described by their mutual coherence function (MCF), are expressed entirely in terms of Gaussian functions. They can also be used to model any source size from a point source to a plane wave, and any degree of spatial coherence from incoherent to fully coherent. This study was also limited to the case where scalar diffraction theory holds [39]. This is case as long as the source is either linearly polarized, or it is unpolarized and the orthogonal components of the field tangential to the direction of propagation are statistically identical [50].

This chapter is organized as follows. Section 4.2 establishes the theoretic foundation used in this study. It also discuss the two primary methods for estimating the beam coherence function: the quadratic approximation and effective beam parameters. A third method to estimate the coherence function is then introduced whereby the effective parameters are modified according to the full results of the quadratic approximation. Section 4.3 compares the accuracy of the three estimation methods throughout the relevant parameter space. Numerically evaluated results from the MCF propagation equation form the basis of this comparison. The parameter space is divided into three general regions, and the best estimation method and maximum error are given for each region. Section 4.4 then compares the the shape of the coherence function to that given by each approximation method throughout the parameter space. A summary of the main results and concluding remarks are given in Sec. 4.6.

4.2 Theoretical Foundation

This section forms the basis from which the various estimation methods are evaluated. For a scalar component of a random optical field E located a distance L

from the source, the MCF of the field in a plane perpendicular to the direction of propagation can be defined as

$$\Gamma(\boldsymbol{\rho}_1, \boldsymbol{\rho}_2, L) = \langle E(\boldsymbol{\rho}_1, L)E^*(\boldsymbol{\rho}_2, L) \rangle, \quad (4.2.1)$$

where $\boldsymbol{\rho}$ is the two-dimensional coordinate vector in the plane perpendicular to the direction of propagation, the asterisk represents the complex conjugate, and the brackets represent ensemble averaging ¹. If the source is considered to be a GSM beam, its MCF can be expressed as

$$\Gamma(\boldsymbol{\rho}_1, \boldsymbol{\rho}_2, 0) = \exp \left[-\frac{|\boldsymbol{\rho}_1|^2 + |\boldsymbol{\rho}_2|^2}{w_0^2} - \frac{|\boldsymbol{\rho}_1 - \boldsymbol{\rho}_2|^2}{l_c^2} - \frac{jk}{2F_0} (|\boldsymbol{\rho}_1|^2 - |\boldsymbol{\rho}_2|^2) \right], \quad (4.2.2)$$

where w_0 is the source radius, l_c is the source coherence radius, F_0 is the source radius of curvature (negative for a diverging beam, positive for a converging beam, and infinite for a collimated beam), $j = \sqrt{-1}$, and $k = 2\pi/\lambda$ where λ is the wavelength of the light [57].

The coherence function of a random field is defined in terms of its MCF as ²

$$|\mu(\boldsymbol{\rho}_1, \boldsymbol{\rho}_2, L)| = \frac{|\Gamma(\boldsymbol{\rho}_1, \boldsymbol{\rho}_2, L)|}{[\Gamma(\boldsymbol{\rho}_1, \boldsymbol{\rho}_1, L)\Gamma(\boldsymbol{\rho}_2, \boldsymbol{\rho}_2, L)]^{1/2}}. \quad (4.2.3)$$

Inserting Eq. (5.2.10) into Eq. (4.2.3) gives the coherence function of a GSM source

¹Since the fields used to calculate Γ are always taken at the same instant in time, it can alternatively be referred to as the mutual intensity J instead of the MCF [38, 41, 57]. However, to maintain consistency with other published literature [2, 23, 49], it is referred to here as the MCF. Consequently, the time dependence of the field E is ignored.

²This relationship is often referred to as the modulus of the complex degree of coherence [2] or the modulus of the complex coherence factor [38]. It is referred to here as the coherence function to emphasize its functional relationship.

which can be expressed as

$$|\mu(\boldsymbol{\rho}_1, \boldsymbol{\rho}_2, 0)| = \exp\left(-\frac{|\boldsymbol{\rho}_1 - \boldsymbol{\rho}_2|^2}{l_c^2}\right). \quad (4.2.4)$$

Since the coherence function depends only on the distance between two points in the field, and not the locations of the points themselves, the field is coherently homogeneous. The coherence radius l_c is then seen to be the separation distance where the coherence function falls to the value e^{-1} .

While several methods have been proposed to describe the propagation of scalar electromagnetic fields through atmospheric turbulence [12, 21, 22, 27, 35, 53, 54, 93], they have all been shown to be equivalent to the second-order moment of the field under commonly used assumptions [13]. Assuming isotropic turbulence, the MCF propagation equation can be expressed in integral form as

$$\begin{aligned} \Gamma(\boldsymbol{\rho}_1, \boldsymbol{\rho}_2, L) = & \frac{1}{(\lambda L)^2} \iint_S \iint_S d^2 \boldsymbol{\rho}'_1 d^2 \boldsymbol{\rho}'_2 \Gamma(\boldsymbol{\rho}'_1, \boldsymbol{\rho}'_2, 0) \exp\left[\frac{jk}{2L} \left(|\boldsymbol{\rho}_1 - \boldsymbol{\rho}'_1|^2 - |\boldsymbol{\rho}_2 - \boldsymbol{\rho}'_2|^2\right)\right] \\ & \times \exp\left(-4\pi^2 k^2 L \int_0^1 dt \int_0^\infty d\kappa \kappa \Phi_n(\kappa) \{1 - J_0[|t(\boldsymbol{\rho}'_1 - \boldsymbol{\rho}'_2) \right. \\ & \left. + (1-t)(\boldsymbol{\rho}_1 - \boldsymbol{\rho}_2)|\kappa]\}\right), \end{aligned} \quad (4.2.5)$$

where \iint_S represent integration over the entire source plane, $\Phi_n(\cdot)$ is the spectral density of the index-of-refraction fluctuations in the atmospheric path, and $J_0(\cdot)$ is the zero-order Bessel function of the first kind [100]. Since this study focuses on the inertial subrange, the Kolmogorov spectral density is used given by

$$\Phi_n(\kappa) = 0.033 C_n^2 \kappa^{-11/3}, \quad (4.2.6)$$

where C_n^2 is the refractive-index structure constant (units of $\text{m}^{-2/3}$) [48]. Following the procedure outlined in Ishimaru [43, Chap. 20], the substitutions $\boldsymbol{\rho}_s = (\boldsymbol{\rho}_1 + \boldsymbol{\rho}_2)/2$,

$\rho_d = \rho_1 - \rho_2$, $\rho'_s = (\rho'_1 + \rho'_2)/2$, $\rho'_d = \rho'_1 - \rho'_2$, and $\mathbf{u} = k(\rho_d - \rho'_d)/L$ are used to simplify the notation aid in the evaluation of Eq. (4.2.5). Using the GSM source MCF of Eq. (5.2.10) and assuming a constant C_n^2 along the propagation path, Eq. (4.2.5) can be simplified to

$$\Gamma(\rho_s, \rho_d, L) = \frac{w_0^2}{8\pi} \iint_{\mathcal{U}} d^2\mathbf{u} \exp \left[-A |\rho_d|^2 - B |\mathbf{u}|^2 + (C \rho_d + j \rho_s) \cdot \mathbf{u} - \frac{1}{\rho_p^{5/3}} \int_0^1 dt \left| \rho_d - \frac{Lt}{k} \mathbf{u} \right|^{5/3} \right], \quad (4.2.7)$$

where

$$\begin{aligned} A &= \frac{1}{2w_0^2} + \frac{1}{l_c^2} + \frac{k^2 w_0^2}{8F_0^2}, \\ B &= \frac{L^2}{2k^2 w_0^2} + \frac{L^2}{k^2 l_c^2} + \frac{w_0^2}{8} \left(1 - \frac{L}{F_0}\right)^2, \\ C &= \frac{L}{k w_0^2} + \frac{2L}{k l_c^2} - \frac{k w_0^2}{4F_0} \left(1 - \frac{L}{F_0}\right), \end{aligned}$$

and $\rho_p = (1.46 C_n^2 k^2 L)^{-3/5}$ is the coherence radius of a plane wave traveling through the turbulence [2].

While Eq. (4.2.7), known as the parabolic equation [1, 43], sufficiently defines the propagation of GSM beams through atmospheric turbulence, it is convenient to express it in terms of the non-dimensional parameters

$$\Theta_0 = 1 - \frac{L}{F_0}, \quad \Lambda_0 = \frac{2L}{k w_0^2}, \quad q_c = \frac{L}{k l_c^2}, \quad \text{and} \quad q = \frac{L}{k \rho_p^2}, \quad (4.2.8)$$

where Θ_0 is often referred to as source curvature parameter (greater than one for a diverging beam, less than one for a converging beam, and equal to one for a collimated beam), Λ_0 is the Fresnel ratio (equals zero for a plane wave and is infinite for a point source), q_c is a measure of the incoherence of the source (equals zero for a perfectly

coherent source), and q is a measure of the strength of atmospheric turbulence (it is related to the Rytov number with $q = 19.2\mathcal{R}^{6/5}$). With the additional normalizations of $\tilde{\rho}_s = \rho_s/\rho_p$, $\tilde{\rho}_d = \rho_d/\rho_p$, and $\tilde{\mathbf{u}} = \rho_p\mathbf{u}$, the parabolic equation becomes

$$\Gamma(\tilde{\rho}_s, \tilde{\rho}_d, L) = \frac{q}{4\pi\Lambda_0} \iint_{\tilde{\mathbf{u}}} d^2\tilde{\mathbf{u}} \exp \left[-\tilde{A}|\tilde{\rho}_d|^2 - \tilde{B}|\tilde{\mathbf{u}}|^2 + (\tilde{C}\tilde{\rho}_d + j\tilde{\rho}_s) \cdot \tilde{\mathbf{u}} - \int_0^1 dt |\tilde{\rho}_d - tq\tilde{\mathbf{u}}|^{5/3} \right], \quad (4.2.9)$$

where

$$\begin{aligned} \tilde{A} &= \frac{1}{4q\Lambda_0} [(1 - \Theta_0)^2 + \Lambda_0^2 + 4q_c\Lambda_0], \\ \tilde{B} &= \frac{q}{4\Lambda_0} (\Theta_0^2 + \Lambda_0^2 + 4q_c\Lambda_0), \\ \tilde{C} &= \frac{1}{2\Lambda_0} (\Theta_0^2 + \Lambda_0^2 - \Theta_0 + 4q_c\Lambda_0). \end{aligned}$$

This expression demonstrates how the four non-dimensional parameters in (4.2.8) completely characterize the propagation of GSM beams through the atmosphere.

4.2.1 Quadratic Approximation.

Since an analytic evaluation of the integral with respect to t in Eq. (4.2.9) has yet to be found, solutions must be determined either through numeric integration or simplifying approximations. The most common simplification is known as the quadratic approximation, whereby the 5/3 power is replaced with a 2 [7, 15, 26, 53, 68, 88]. Since this approximation plays an important part in all further derivations, its

procedure and results are briefly reviewed here. As such, Eq. (4.2.9) is modified to

$$\Gamma(\tilde{\boldsymbol{\rho}}_s, \tilde{\boldsymbol{\rho}}_d, L) = \frac{q}{4\pi\Lambda_0} \iint_{\tilde{\mathcal{U}}} d^2\tilde{\mathbf{u}} \exp \left[-\tilde{A} |\tilde{\boldsymbol{\rho}}_d|^2 - \tilde{B} |\tilde{\mathbf{u}}|^2 + (\tilde{C}\tilde{\boldsymbol{\rho}}_d + j\tilde{\boldsymbol{\rho}}_s) \cdot \tilde{\mathbf{u}} - 3\alpha \int_0^1 dt |\tilde{\boldsymbol{\rho}}_d - tq\tilde{\mathbf{u}}|^2 \right], \quad (4.2.10)$$

where α allows for partial compensation of this approximation. All the integrals can now be analytically evaluated, and the MCF expressed in terms of the original coordinates $\boldsymbol{\rho}_1 = \rho_p(\tilde{\boldsymbol{\rho}}_s + \tilde{\boldsymbol{\rho}}_d/2)$ and $\boldsymbol{\rho}_2 = \rho_p(\tilde{\boldsymbol{\rho}}_s - \tilde{\boldsymbol{\rho}}_d/2)$ as

$$\Gamma(\boldsymbol{\rho}_1, \boldsymbol{\rho}_2, L) = \frac{w_0^2}{w_q^2} \exp \left[-\frac{|\boldsymbol{\rho}_1|^2 + |\boldsymbol{\rho}_2|^2}{w_q^2} - \frac{|\boldsymbol{\rho}_1 - \boldsymbol{\rho}_2|^2}{\rho_q^2} - \frac{jk}{2F_q} (|\boldsymbol{\rho}_1|^2 - |\boldsymbol{\rho}_2|^2) \right], \quad (4.2.11)$$

where

$$w_q = w_0 [\Theta_0^2 + \Lambda_0^2 + 4(q_c + \alpha q)\Lambda_0]^{1/2}, \quad (4.2.12)$$

$$\rho_q = \rho_p \left\{ \frac{q [\Theta_0^2 + \Lambda_0^2 + 4(q_c + \alpha q)\Lambda_0]}{q_c(1 + 4\alpha q\Lambda_0) + \alpha q(1 + \Theta_0^2 + \Lambda_0^2 + \Theta_0 + 3\alpha q\Lambda_0)} \right\}^{1/2}, \quad (4.2.13)$$

and

$$F_q = \frac{-L [\Theta_0^2 + \Lambda_0^2 + 4(q_c + \alpha q)\Lambda_0]}{\Theta_0^2 + \Lambda_0^2 - \Theta_0 + 2(2q_c + 3\alpha q)\Lambda_0}. \quad (4.2.14)$$

Since Eq. (4.2.11) is in the same form as Eq. (5.2.10), the quadratic approximation maintains a GSM beam, but with new beam parameters w_q , ρ_q , and F_q . The resulting coherence function is thus easily found to be

$$|\mu_q(\boldsymbol{\rho}_1, \boldsymbol{\rho}_2, L)| = \exp \left(-\frac{|\boldsymbol{\rho}_1 - \boldsymbol{\rho}_2|^2}{\rho_q^2} \right). \quad (4.2.15)$$

The accuracy of the quadratic approximation varies depending on values of Θ_0 ,

Λ_0 , q_c , q , and α . In the case of a coherent plane wave as the source ($\Theta_0 = 1$, $\Lambda_0 = 0$, and $q_c = 0$), using $\alpha = 1/3$ gives the correct values of $w_q = w_0 = \infty$, $\rho_q = \rho_p$, and $F_q = \infty$. The only error is in the shape of the coherence function where the power in the exponential should be $5/3$ instead of 2 [2]. Using a coherent source ($q_c = 0$), comparisons performed by Belen'kiĭ and Mironov [8] between the coherence radius given by the Eq. (4.2.13) with $\alpha = 1/3$ and that derived through the numerical integration of Eq. (4.2.7) demonstrated that Eq. (4.2.13) underestimates the true coherence radius in all cases, except for a plane wave source, with a maximum deviation of about 12%.

The overall accuracy of ρ_q can be improved by using the value of $\alpha = (3/8)^{6/5}$ which results in the correct values for a point source ($\Theta_0 \rightarrow \infty$ and $\Lambda_0 \rightarrow \infty$ while Θ_0/Λ_0 remains finite) of $w_q = \infty$, $F_q = -L$, and $\rho_q = (8/3)^{3/5}\rho_p$. For coherent sources ($q_c = 0$), this value of α increases all estimates of the coherence radius by nearly 4% over that of $\alpha = 1/3$, thereby reducing the maximum error to about 8%. For this reason, $\alpha = (3/8)^{6/5}$ was used to define the quadratic approximation coherence radius estimate in this study.

4.2.2 Effective Parameters.

An alternative method for calculating the MCF of a GSM beam after propagation through the atmosphere is to assume the field at the receiver can be represented as

$$E(\boldsymbol{\rho}, L) = E_0(\boldsymbol{\rho}, L) \exp [\Psi_S(\boldsymbol{\rho}, L)] \exp [\psi(\boldsymbol{\rho}, L)], \quad (4.2.16)$$

where $E_0(\cdot)$ represents the field at the receiver of an equivalent coherent source in the absence of turbulence, $\Psi_S(\cdot)$ represents the complex phase perturbation due to the partial coherence of the source, and $\psi(\cdot)$ represents the complex phase perturbation due to atmospheric turbulence [2]. By assuming the the complex phase perturbations

due to the source and atmosphere are statistically independent of each other, the MCF of the field can be expressed as

$$\Gamma(\boldsymbol{\rho}_1, \boldsymbol{\rho}_2, L) = \Gamma_c(\boldsymbol{\rho}_1, \boldsymbol{\rho}_2, L)\Gamma_a(\boldsymbol{\rho}_1, \boldsymbol{\rho}_2, L), \quad (4.2.17)$$

where $\Gamma_c(\cdot)$ is the MCF of the GSM beam through free space and $\Gamma_a(\cdot)$ is the MCF of an equivalent coherent beam through the atmosphere. In the absence of atmospheric turbulence, the coherence function of a GSM beam can be derived directly from Eqs. (4.2.13) and (4.2.15) by allowing $\rho_p \rightarrow \infty$, and correspondingly $q \rightarrow 0$. It can then be expressed as

$$|\mu_c(\boldsymbol{\rho}_1, \boldsymbol{\rho}_2, L)| = \exp\left(-\frac{|\boldsymbol{\rho}_1 - \boldsymbol{\rho}_2|^2}{\rho_c^2}\right), \quad (4.2.18)$$

where

$$\rho_c = l_c (\Theta_0^2 + \Lambda_0^2 + 4q_c\Lambda_0)^{1/2}. \quad (4.2.19)$$

When deriving the coherence function due to turbulence alone, a method based on the Rytov approximation has been shown to be more accurate at times than that derived from the quadratic approximation [1]. As the details of the Rytov approximation are readily available elsewhere [2, 77], only the relevant results are given here. According to the Rytov approximation, the coherence function of a coherent Gaussian beam after propagating through atmospheric turbulence can be expressed as [2]

$$|\mu_R(\boldsymbol{\rho}_1, \boldsymbol{\rho}_2, L)| = \exp\left\{-\frac{3}{8}\left[a\left(\frac{|\boldsymbol{\rho}_1 - \boldsymbol{\rho}_2|}{\rho_p}\right)^{5/3} + 0.618\frac{\Lambda^{11/6}}{q^{1/6}}\left(\frac{|\boldsymbol{\rho}_1 - \boldsymbol{\rho}_2|}{\rho_p}\right)^2\right]\right\}, \quad (4.2.20)$$

where

$$a = \begin{cases} \frac{1 - \Theta^{8/3}}{1 - \Theta} & \text{for } \Theta \geq 0 \\ \frac{1 + |\Theta|^{8/3}}{1 - \Theta} & \text{for } \Theta < 0 \end{cases}, \quad \Theta = 1 + \frac{L}{F}, \quad \Lambda = \frac{2L}{kw^2}, \quad (4.2.21)$$

and w and F are derived from Eqs. (4.2.12) and (4.2.14) respectively by setting $q_c = q = 0$. Not only does Eq. (4.2.20) give the correct values for the coherence radius using both a coherent plane wave source ($\Theta = 1$ and $\Lambda = 0$) and a point source ($\Theta = \Lambda = 0$), but also the correct coherence function shape.

While the Rytov approximation is very accurate in weak turbulence ($q < 1$ and $q\Lambda < 1$) [2] it becomes less accurate as the turbulence strength increases. In strong turbulence and with coherent sources, the quadratic approximation has been shown to be more accurate at estimating the coherence radius than the Rytov approximation [1]. To remedy this situation, Andrews *et al.* [1] heuristically introduced effective beam parameters that take into account the additional beam spreading and reduced radius of curvature evident in strong turbulence. This is accomplished by replacing Θ and Λ in Eqs. (4.2.20) and (4.2.21) with

$$\Theta_a = 1 + \frac{L}{F_a}, \quad \Lambda_a = \frac{2L}{kw_a^2}, \quad (4.2.22)$$

where w_a and F_a can be derived from Eqs. (4.2.12) and (4.2.14) respectively by setting $q_c = 0$ and $\alpha = 1/3$. (While $\alpha = (3/8)^{6/5}$ could be used instead, the difference is minimal so $\alpha = 1/3$ is used to maintain consistency with previous work [1,2].) With this change, Eq. (4.2.20) becomes

$$|\mu_a(\boldsymbol{\rho}_1, \boldsymbol{\rho}_2, L)| = \exp \left\{ -\frac{3}{8} \left[a_a \left(\frac{|\boldsymbol{\rho}_1 - \boldsymbol{\rho}_2|}{\rho_p} \right)^{5/3} + 0.618 \frac{\Lambda_a^{11/6}}{q^{1/6}} \left(\frac{|\boldsymbol{\rho}_1 - \boldsymbol{\rho}_2|}{\rho_p} \right)^2 \right] \right\}, \quad (4.2.23)$$

where

$$a_a = \begin{cases} \frac{1 - \Theta_a^{8/3}}{1 - \Theta_a} & \text{for } \Theta_a \geq 0, \\ \frac{1 + |\Theta_a|^{8/3}}{1 - \Theta_a} & \text{for } \Theta_a < 0. \end{cases} \quad (4.2.24)$$

The overall coherence function can now be found by multiplying together Eqs. (4.2.18) and (4.2.23), and expressed as

$$|\mu_e(\boldsymbol{\rho}_1, \boldsymbol{\rho}_2, L)| = \exp \left[- \left(\frac{|\boldsymbol{\rho}_1 - \boldsymbol{\rho}_2|}{\rho_a} \right)^{5/3} - \left(\frac{|\boldsymbol{\rho}_1 - \boldsymbol{\rho}_2|}{\rho'_c} \right)^2 \right], \quad (4.2.25)$$

where

$$\rho_a = \rho_p \left(\frac{8}{3a_a} \right)^{3/5} \quad (4.2.26)$$

and

$$\rho'_c = \rho_p \left[\frac{q_c}{q(\Theta_0^2 + \Lambda_0^2 + 4q_c\Lambda_0)} + 0.232 \frac{\Lambda_a^{11/6}}{q^{1/6}} \right]^{-1/2}. \quad (4.2.27)$$

Finding the e^{-1} point of Eq. (4.2.25) requires finding the real and positive root of a sixth-order polynomial, so there is no direct algebraic expression for the coherence radius. However, the coherence radius can be approximated as [2]

$$\rho_e = \rho_p \left[\frac{q_c}{q(\Theta_0^2 + \Lambda_0^2 + 4q_c\Lambda_0)} + 0.232 \frac{\Lambda_a^{11/6}}{q^{1/6}} + \left(\frac{3a_a}{8} \right)^{6/5} \right]^{-1/2}. \quad (4.2.28)$$

This approximation has its largest error of 3.53% when $\rho'_c/\rho_a = 0.75$, and the error is less than 1% when $\rho'_c/\rho_a < 0.15$ or $\rho'_c/\rho_a > 2.88$. While the exact coherence length found from Eq. (4.2.25) was primarily used in this study, the effects of the approximation given by Eq. (4.2.28) were also evaluated.

4.2.3 Modified Effective Parameters.

The new method presented here of estimating the coherence function of GSM beams in turbulence analyzed by this study combines elements from both the quadratic

approximation and the effective parameters method. While the coherence function is formed in the same manner as in Sec. 4.2.2, the MCF due to the atmosphere is not considered completely independent from the source coherence. Instead, coupling effects between the source and atmosphere are included by modifying the effective parameters of Eq. (4.2.22) such that beam width and radius of curvature are precisely those given by the quadratic approximation. The resulting coherence function is

$$|\mu_m(\rho_1, \rho_2, L)| = \exp \left\{ -\frac{3a_q}{8} \left(\frac{|\rho_1 - \rho_2|}{\rho_p} \right)^{5/3} - \left[\frac{q_c}{q(\Theta_0^2 + \Lambda_0^2 + 4q_c\Lambda_0)} + 0.232 \frac{\Lambda_q^{11/6}}{q^{1/6}} \right] \left(\frac{|\rho_1 - \rho_2|}{\rho_p} \right)^2 \right\}, \quad (4.2.29)$$

where

$$a_q = \begin{cases} \frac{1 - \Theta_q^{8/3}}{1 - \Theta_q} & \text{for } \Theta_q \geq 0 \\ \frac{1 + |\Theta_q|^{8/3}}{1 - \Theta_q} & \text{for } \Theta_q < 0 \end{cases}, \quad \Theta_q = 1 + \frac{L}{F_q}, \quad \Lambda_q = \frac{2L}{kw_q^2}. \quad (4.2.30)$$

While either $\alpha = 1/3$ or $\alpha = (3/8)^{6/5}$ could be used to define w_q and F_q with Eqs. (4.2.12) and (4.2.14), this study used the former to maintain consistency with Sec. 4.2.2. As before, the coherence radius can be approximated with

$$\rho_m = \rho_p \left[\frac{q_c}{q(\Theta_0^2 + \Lambda_0^2 + 4q_c\Lambda_0)} + 0.232 \frac{\Lambda_q^{11/6}}{q^{1/6}} + \left(\frac{3a_q}{8} \right)^{6/5} \right]^{-1/2}. \quad (4.2.31)$$

In the case of a perfectly coherent source when $q_c = 0$, the modified effective parameters method is equivalent to the effective parameters method.

4.3 Coherence Radius Accuracy

The relative accuracy of the different methods of estimating the coherence radius of GSM beams in turbulence were evaluated throughout the parameter space defined by Eq. (4.2.8). To simplify the analysis, this four-dimensional parameter space was reduced to three dimensions by assuming a collimated source ($\Theta_0 = 1$). This assumption was justified by observing Θ_0 primarily appears as additive terms in the above expressions for the coherence length, so the primary interplay is among parameters Λ_0 , q_c , and q .

An analytic estimation of the coherence function based on the numerical integration of Eq. (4.2.9) was used to assess the relative accuracy of each estimation method. Since all of the expressions for the coherence function in Sec. 4.2 are coherently homogeneous, it can be evaluated by setting $\boldsymbol{\rho}_1 = \boldsymbol{\rho}$ and $\boldsymbol{\rho}_2 = 0$. The coherence function at distance L can now be expressed in terms of the displacement distance $\rho = |\boldsymbol{\rho}|$ as

$$|\mu(\rho, L)| = \frac{|\Gamma(\boldsymbol{\rho}, 0, L)|}{[\Gamma(\boldsymbol{\rho}, \boldsymbol{\rho}, L)\Gamma(0, 0, L)]^{1/2}}. \quad (4.3.1)$$

Samples of Eq. (4.3.1) were computed using Listing C.4 by numerically evaluating Eq. (4.2.9) when $\tilde{\boldsymbol{\rho}}_s = \tilde{\boldsymbol{\rho}}_d/2 = \boldsymbol{\rho}/(2\rho_p)$, and when $\tilde{\boldsymbol{\rho}}_s = \boldsymbol{\rho}/\rho_p$ with $\tilde{\boldsymbol{\rho}}_d = 0$. The analytic estimation of the coherence function was then determined by making a nonlinear least-squares fit of the sample data points to

$$|\mu(\rho)| = \exp \left[- \left(\frac{\rho}{\rho_0} \right)^n \right], \quad (4.3.2)$$

where ρ_0 and n are the fit parameters. In this study, the fit was made using 12 evenly spaced sample points from 0 to $1.1\rho_m$ inclusive.

The differences between the absolute errors of the various methods of estimating the coherence radius with respect to ρ_0 are shown in Fig. 6. The four Λ_0 values of

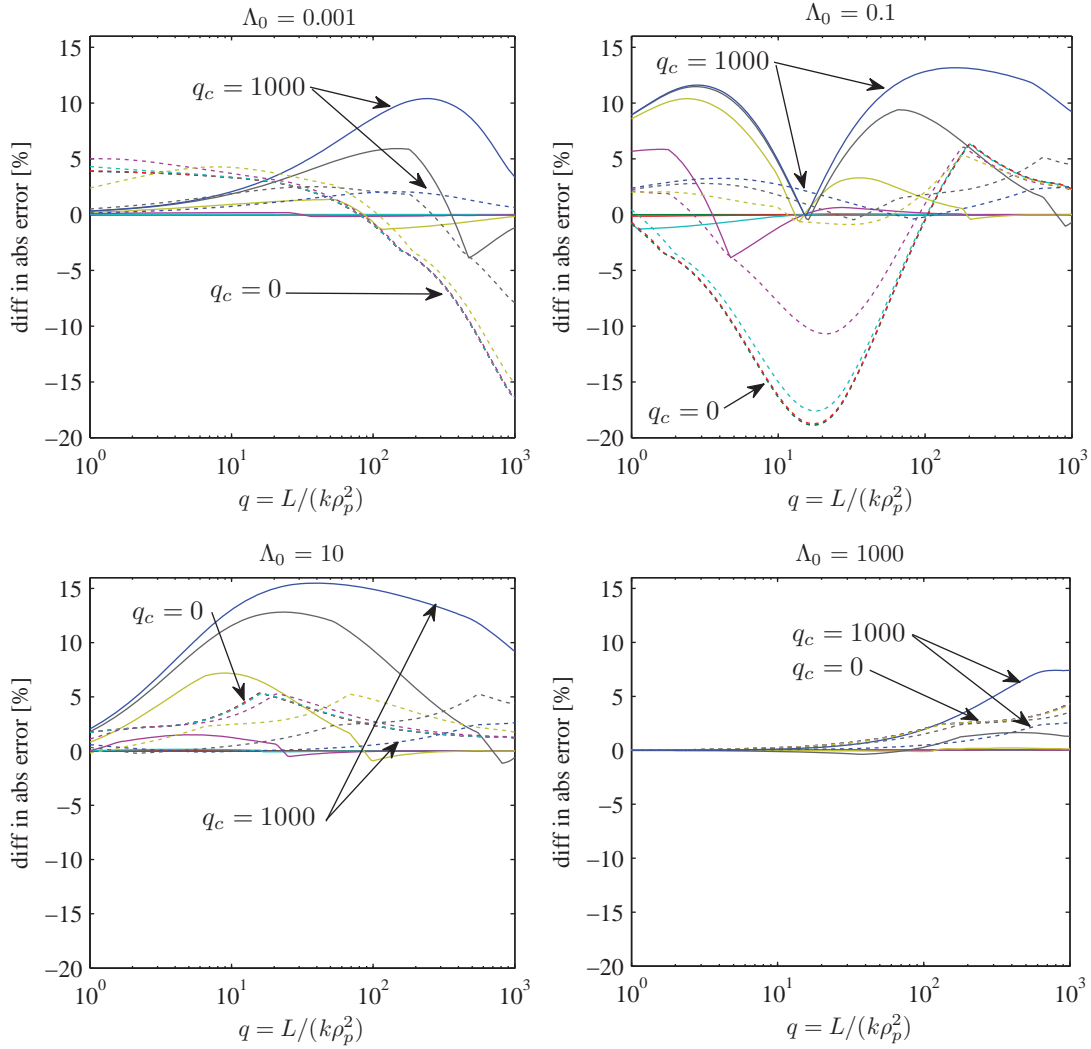


Figure 6. The difference in the absolute error between various methods of estimating the coherence radius. Lines are for the q_c values of 0, 0.001, 0.01, 0.1, 1, 10, 100, and 1000. The solid lines are the difference between the absolute error using effective parameters as given in Eq. (4.2.25) and using modified effective parameters as given in Eq. (4.2.29). The dotted lines are the difference between the absolute error using the quadratic approximation as given in Eq. (4.2.13) and using modified effective parameters as given in Eq. (4.2.29). The difference is positive when using modified effective parameters is more accurate, and negative when using modified effective parameters is less accurate.

0.001, 0.1, 10, and 1000 are shown along with the q_c values of 0, 0.001, 0.01, 0.1, 1, 10, 100, and 1000. (Note that a range in q from 1 to 1000 corresponds to a range in \mathcal{R} from 0.085 to 26.) Absolute error is defined as

$$\text{err}_x = 100 \left| \frac{\rho_x}{\rho_0} - 1 \right|, \quad (4.3.3)$$

where x is q , e , or m and the coherence radii are defined respectively by Eqs. (4.2.13), (4.2.25), and (4.2.29). Solid lines indicate the difference in absolute error between the effective parameters method of Eq. (4.2.25) and the modified effective parameters method of Eq. (4.2.29), while dotted lines indicate the difference in absolute error between the quadratic approximation method of Eq. (4.2.13) and the modified effective parameters method of Eq. (4.2.29). Positive values occur when the modified effective parameters method is more accurate, and negative values occur when it is less accurate.

According to these plots, the parameters space can be divided into three general regions: $q\Lambda_0 < 0.1$, $0.1 < q\Lambda_0 < 10$, and $q\Lambda_0 > 10$. In the transitory region of $0.1 < q\Lambda_0 < 10$, the quadratic approximation tends give the most accurate estimate with the best performance advantage when the source is nearly coherent. For a perfectly coherent source ($q_c = 0$), the quadratic approximation is up to 18.9% more accurate than the other methods in this region, but as the source coherence decreases this performance advantage also decreases. Once the value of $q_c\Lambda_0$ becomes larger than 1, the modified effective parameter method actually tends to do better than the quadratic approximation in this region with a performance advantage as high as 3.3%. While there are instances in this region where the effective parameters method outperforms the other two, this performance advantage is transitory and of very small magnitude ($< 1\%$).

In the other two regions of weak turbulence and/or plane wave-like source ($q\Lambda_0 <$

0.1), and strong turbulence and/or point-like source ($q\Lambda_0 > 10$), the modified effective parameters method tends to be the most accurate. Since there is no difference between the effective parameters method and the modified effective parameters method for a perfectly coherent source, the modified effective parameters method is seen to have the greatest advantage when the source is very incoherent (high q_c). While the modified effective parameters method can be more accurate than the effective parameters method by as much as 15.5%, it tends to only outperform the quadratic approximation to within 5%, with a maximum advantage of 6.35%. While there are instances in these regions where either the quadratic approximation or effective parameters method has the best accuracy, the performance advantage is only transitory and of very small magnitude ($< 1\%$).

While Fig. 6 compares the difference in absolute error between the various coherence radius estimation methods, Fig. 7 compares the absolute errors directly. Since the effective parameters method tends to be less accurate than the other methods across the parameter space, its absolute error is not shown. Figure 7 indicates that by choosing the appropriate method to estimate the coherence radius, the error can normally be kept to under 5%. When $q\Lambda_0 < 0.1$ (weak turbulence and/or plane wave-like source), the quadratic approximation has its maximum absolute error of 5.5% with weak turbulence and moderate source coherence (small q and $q_c = 1$). However, the modified effective parameters method keeps its absolute error under 1.7% with the maximum error occurring with strong turbulence and coherent source (large q and $q_c = 0$). In the transitory region of $0.1 < q\Lambda_0 < 10$, the modified effective parameters method has an error as large as 21.5% for a coherent source, but as the source coherence decreases the maximum error is reduced to 3.35%. Conversely the quadratic approximation has its largest error of 5.2% in strong turbulence (large q) with a coherent source. When $q\Lambda_0 > 10$ (strong turbulence and/or point-like source),

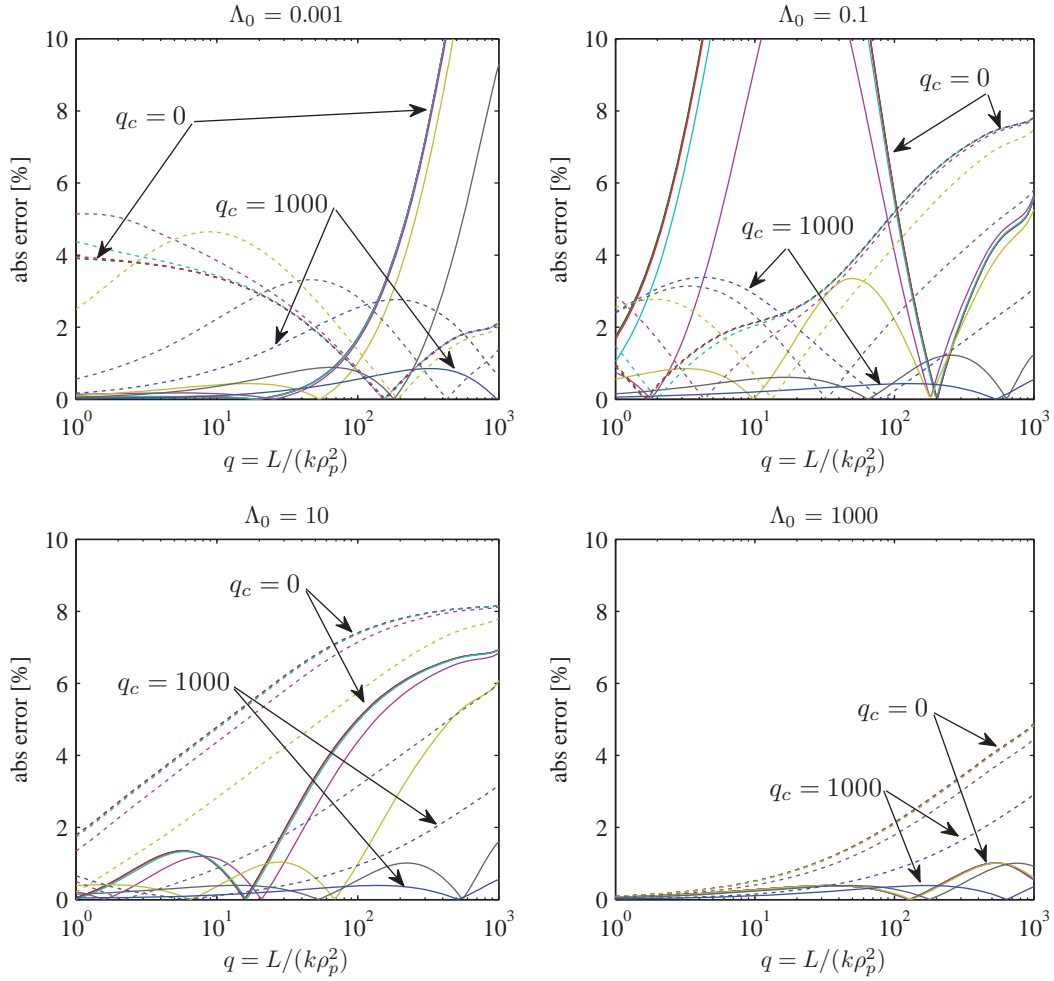


Figure 7. The absolute error of different methods of estimating the coherence radius. Lines are for the q_c values of 0, 0.001, 0.01, 0.1, 1, 10, 100, and 1000. The solid lines are the absolute error of the modified effective parameters method given by Eq. (4.2.29), and the dotted lines are the absolute error of the quadratic approximation given by Eq. (4.2.13).

the modified effective parameters method has a maximum error of 7.0% while the quadratic approximation has a maximum error of 8.2%. In both cases this occurs with strong turbulence and a coherent source, with the maximum error decreasing as the source coherence decreases.

Since Eqs. (4.2.28) and (4.2.31) will normally be used to calculate the coherence radius, it is important to evaluate their relative accuracy as well. The comparison of difference in absolute errors using these approximate expressions for the coherence radius is shown in Fig. 8. While using the approximate expressions does not appreciably change the results when $q\Lambda_0 > 10$ (strong turbulence and/or point-like source), they do have an effect on the other two regions. When $q\Lambda_0 < 0.1$ and $q_c\Lambda_0 < 0.1$ (plane wave-like and nearly coherent source with weak turbulence), the effective parameters method now beats the modified effective parameters method by as much as 2.8%. As the source coherence decreases, the effective parameters method continues to beat the modified parameters method for weak turbulence, but starts to lose out at stronger turbulence values. In the transitory region, the quadratic approximation is now seen to be more accurate than the modified effective parameters method at source coherence values.

4.4 Coherence Function Shape

The final piece of analysis deals with the accuracy of the overall coherence function shape. The quadratic approximation produces a Gaussian coherence function while both of the effective parameter methods result in coherence functions that are the product of a Gaussian and the exponential of a 5/3 power. As a result, the effective shape of the coherence function should fall somewhere in between the two. Figure 9 contains plots of n when the numerically derived coherence function, as well as Eqs. (4.2.25) and (4.2.29), are fit to Eq. (4.3.2). As before, the lines represent the

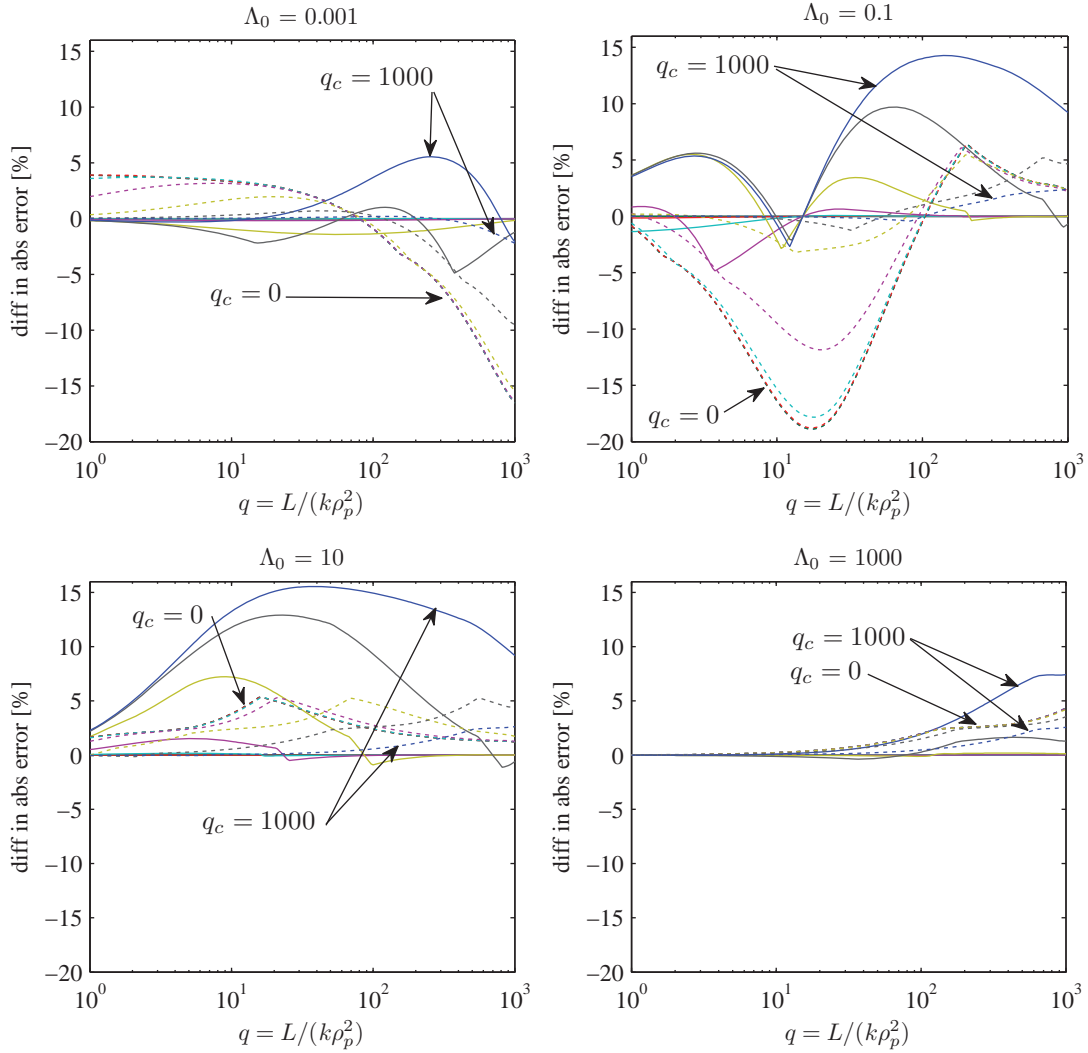


Figure 8. The difference in the absolute error between various methods of estimating the coherence radius. Lines are for the q_c values of 0, 0.001, 0.01, 0.1, 1, 10, 100, and 1000. The solid lines are the difference between the absolute error using the effective parameters approximate expression as given in Eq. (4.2.28) and using modified effective parameters approximate expression as given in Eq. (4.2.31). The dotted lines are the difference between the absolute error using the quadratic approximation as given in Eq. (4.2.13) and using modified effective parameters approximate expression as given in Eq. (4.2.31). The difference is positive when using modified effective parameters is more accurate, and negative when using modified effective parameters is less accurate.

q_c values of 0, 0.001, 0.01, 0.1, 1, 10, 100, and 1000. The solid lines are the fit of the numerically derived coherence function, the dash-dotted lines are the fit of the modified effective parameters result given by Eq. (4.2.29), and the dotted lines are the fit of the effective parameters result given by Eq. (4.2.25).

In every instance, the numerically derived coherence function is more Gaussian in shape than predicted by either of the effective parameters methods. The best agreement is when q is small and q_c is large (weak turbulence and incoherent source). This should be expected since this is case where the integral over t in Eq. (4.2.9) has the smallest impact. However, as the turbulence strength increases, the numerically derived coherence function becomes more Gaussian, while both of the effective parameters coherence functions become less Gaussian. In fact once $q\Lambda_0$ becomes larger than 1, the coherence function for more coherent sources is more Gaussian than the coherence function for less coherent sources. When the source is plane wave-like and coherent while the turbulence is strong, the quadratic approximation actually better estimates the the coherence function shape than either of the effective parameters methods. With very strong turbulence, the shape of the numerically derived coherence function tends toward 9/5 rather than 5/3 as predicted by both of the effective parameters methods. While the coherence function shapes of both effective parameters methods are very similar to each other across the entire parameter space, the modified method tends to slightly better agree with the numerically derived results. For analytic convenience, the coherence function of atmospherically perturbed light is sometimes approximated by a Gaussian shape [23]. These results indicate that such an approximation may be more accurate than would have been otherwise expected.

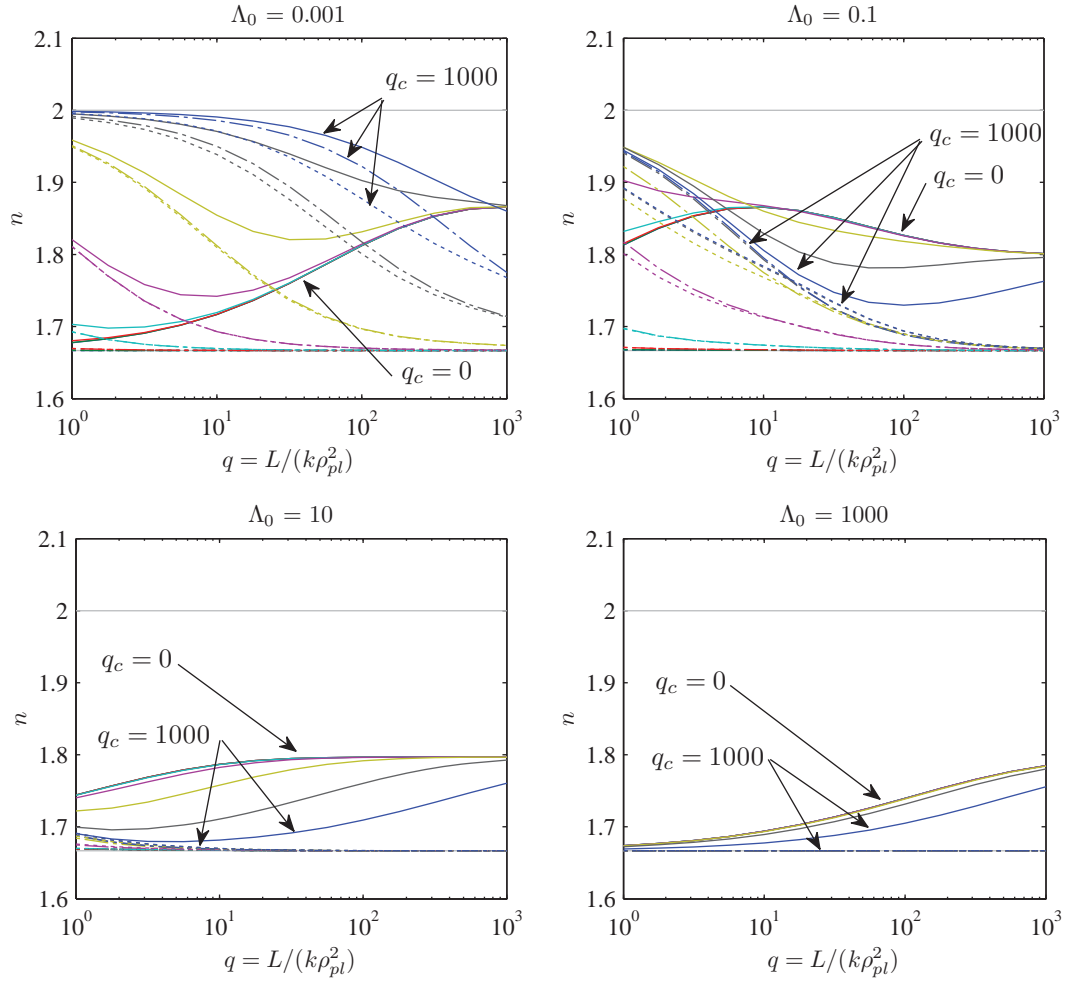


Figure 9. Comparison of the exponential power n as different methods of estimating the coherence function are fit to Eq. (4.3.2). Lines are for the q_c values of 0, 1/1000, 1/100, 1/10, 1, 10, 100, and 1000. Solid lines are from the numerically derived coherence function, dash-dotted lines are from the modified effective parameters method as given in Eq. (4.2.29), and the dotted lines are from the effective parameters method as given in Eq. (4.2.25).

4.5 Effect of Source Coherence

The above expressions for the coherence function of Gaussian beams in turbulence can also be used to measure the respective effects of the beam source to that of the atmospheric turbulence. An example of an application where this may be important is adaptive optics (AO) where the intent is to correct phase perturbations due to the atmospheric turbulence alone. In this application, the phase perturbations due to the partial coherence of the source may act as an additional noise source, particularly when using an interferometric wavefront sensor such as a self-referencing interferometer (SRI).

For an SRI to predominately measure the atmospherically induced phase perturbations, the effect of partial coherence of the source needs to be negligible when compared to that of the atmosphere. This condition can be expressed as constraints on the value of q_c . In the situations where these constraints are not satisfied, alternate wavefront sensors should be used, such as the Shack-Hartmann wavefront sensor.

If the AO system is operating in a regime where the quadratic approximation gives the best result, this constraint can be found from Eq. (4.2.13) and simply expressed as

$$q_c \ll \alpha q. \quad (4.5.1)$$

However, if the modified effective parameters method gives the best result, then it may be possible to find less restrictive constraints on q_c . Since the modified effective parameters method assumes the beam MCF may be separated into two parts, one due to the partial coherence of the beam source and the other due to the turbulence in the atmosphere, the coherence radius resulting from each source of randomness may be considered separately. If the coherence radius due to the beam source as given by Eq. (4.2.19) is sufficient large, then only the effects of the atmosphere should be

measured by the SRI. This constraint can be expressed as

$$\rho_c > D/2, \quad (4.5.2)$$

where D is the diameter of the AO system receiver aperture. Using Eq. (4.2.19) along with some algebra results in the constraints

$$q_c < \frac{(\Theta_0^2 + \Lambda_0^2)\Lambda_D/2}{1 - 2\Lambda_D\Lambda_0} \quad \text{for } 2\Lambda_D\Lambda_0 < 1, \quad (4.5.3)$$

or

$$\Lambda_D \geq \frac{1}{2\Lambda_0}, \quad (4.5.4)$$

where

$$\Lambda_D = \frac{8L}{kD^2}. \quad (4.5.5)$$

For the beam source to have a negligible effect on the atmospheric term, there must be little difference between between the effective parameters method and the modified method. This is true so long as

$$q_c \ll \alpha q + \frac{1}{4\Lambda}. \quad (4.5.6)$$

4.6 Conclusion

An alternative method of estimating the coherence function of a partially coherent Gaussian beam after propagation through atmospheric turbulence was introduced, and its accuracy was compared to those of the previously published estimation methods based on the quadratic approximation and perturbation theory using effective pa-

rameters. The basis of comparison was found by numerically integrating the parabolic equation, and fitting samples of the resulting numeric coherence function to the exponential of a power. Assuming a collimated source beam, this study demonstrated that the alternative method using modified effective parameters more accurately estimated both the coherence radius and functional shape than the original effective parameters method throughout the entire parameter space. However, the quadratic approximation was shown to be the more accurate estimate in the transitory region of $0.1 < q\Lambda_0 < 10$ with a nearly coherent source subject to the constraint $q_c\Lambda_0 < 1$. By selecting the appropriate estimation method, the coherence radius estimation error can usually be kept to within 5%, with a maximum error of 7% for very strong turbulence and a nearly coherent source. Analysis of the numerically evaluated coherence function shape revealed that it is more Gaussian than predicted by either of the effective parameter methods, especially in strong turbulence. This means a Gaussian approximation of the coherence function, such as given by the quadratic approximation, is a better approximation than would have otherwise been expected. Finally, constraints were found on the beam source degree of coherence that would allow an interferometric wavefront sensor, such as the SRI, to predominately measure phase perturbations due to atmospheric turbulence alone.

This analysis is useful for any application that depends on accurate estimates of the coherence size of incident light. As the coherence radius estimation error can be as large as 20%, selecting the wrong method can have a large negative impact on any further performance analysis. This is particularly the case when atmospherically perturbed light is coupled into single-mode optical fibers. Since the mean coupling efficiency may be proportional to the square of the coherence radius of the field, errors in estimating the coherence radius result in even larger errors in estimating the mean coupling efficiency. This study also indicates the use effective beam parame-

ters may be most effective when they includes both turbulence strength and source coherence effects. Since effective beam parameters have been used to estimate beam wander, scintillation index, free-space optical communication performance, and ladar performance [2], these applications also stand to benefit from the results of this study whenever the light source is partially coherent.

V. Coupling of GSM Beams Into Single-Mode Optical Fibers

5.1 Introduction

The coupling of random light into single-mode optical fibers has found application in a wide range of fields such as free-space optical communication, stellar interferometry, ladar/lidar, and wavefront sensing [23, 45, 55, 65, 75, 79, 83, 90, 94]. The randomness of the incident light can be due to a partially coherent or incoherent light source, variations due to atmospheric turbulence, localized effects, or combinations of the above [28, 55, 68, 82, 89, 101]. If the light incident on the fiber is random, the resulting coupling efficiency is a random variable. While a general expression for the average coupling efficiency of stochastic light into optical fibers is available, it is not generally analytically tractable and usually requires numerical integration methods or simplifying approximations to solve [23, 94]. In the particular case of coupling a partially coherent plane wave where an analytical expression has been derived, the solution involves an infinite series of confluent hypergeometric functions [17]. As both numerical techniques and this analytic expression are computationally intensive, it would be useful to have an algebraic expression for the coupling efficiency, even if it is only an approximation. As long as this algebraic expression is reasonably accurate, it could facilitate additional insight into the relative interactions of the beam and atmospheric parameters. Its use would also considerably decrease the simulation time of dynamic systems, such as when there is relative motion between the light source and the receiver.

While a general expression for the average coupling efficiency has been published, one has not been found in the literature for its variance. Ruilier and Cassaing [75] developed an expression for the relative fluctuations of the coupling efficiency (de-

ned as the standard deviation divided by the mean), but it is quite inaccurate when the spatial coherence length of the light is small relative to the receiver diameter. Evaluating the variance of the coupling efficiency has generally required the use of a large number of computer simulation runs [75, 79]. If the coupling efficiency variance is needed for noise analysis or similar system characterizations, the need to run thousands of simulations is obviously burdensome. As with the coupling efficiency, an algebraic expression for the coupling efficiency variance in terms of the light and optical fiber parameters would be greatly useful.

One final consideration when analyzing the coupling of stochastic light into optical fibers is the nature of the fluctuations of the light. Previous analysis has generally assumed the random fluctuations lie primarily in the phase of the field. Any fluctuations in the field amplitude are assumed to be negligible and are ignored [79]. Such assumptions are valid in cases such as coherent light passing through weak atmospheric turbulence, but may not be appropriate when the light is initially spatially incoherent, or if it passes through strong turbulence. In these latter cases, the light would contain significant amplitude fluctuations, known as speckle [40] or scintillation [2] (this chapter exclusively uses the term speckle). While speckle is a fourth-order characteristic of the stochastic field, it plays a dominant role in determining the coupling efficiency variance, and even affects the mean coupling efficiency in certain cases. Winzer and Leeb [94] studied the effect of speckle on coupling efficiency, but the assumptions implicit in their analysis are only valid when the speckle size is either small or large with respect to the receiver aperture. As far as has been determined, this is the first study that specifically examines the effects of speckle on the coupling efficiency of random light into optical fibers in all conditions.

While it may be possible to extend the analysis of this chapter to more general classes of random light or multi-mode optical fibers, the focus here is on Gaussian

Schell-model (GSM) beams and step-index, single-mode fibers. GSM beams have been extensively studied in the literature and can be used to model some partially coherent light sources [24,26,37,47,49,53,68,80,88,97]. It has also been shown that GSM beams remain GSM beams to a good approximation as they propagate through atmospheric turbulence, where only the values of their characteristic parameters change [68,88]. Since these beams can be completely described in terms of Gaussian functions, their use also permits many tractable expressions in the analysis. The use of a step-index optical fiber is not limiting since many other fiber configurations, such as graded-index fibers, can be closely approximated by an equivalent step-index fiber [14,59]. Therefore, these results should be applicable to a large variety of conditions and configurations.

This chapter is organized as follows. Section 5.2 analyzes the mean coupling efficiency of GSM beams into single mode optical fibers. This results in an analytic expression and algebraic approximation of the coupling efficiency based on the beam and fiber parameters. The effects of the various approximations used in completing the analysis are studied both analytically and through computer simulations. Empirical compensation for errors due to these approximations is then developed to increase the accuracy of the coupling efficiency equations. This is accomplished using both non-speckled and speckled beams. Section 5.3 analyzes the coupling efficiency variance. Expressions for the mean squared normalized variance are derived for the cases of fully developed speckle, well-developed speckle, and no speckle. Computer simulations are used to evaluate the accuracy of these results, and identify potential compensation for the observed inaccuracies. Concluding remarks are given in Section 5.4.

5.2 Mean Coupling Efficiency

This section details the development of analytic expressions for the mean coupling efficiency of GSM beams into single-mode optical fibers. This development begins by defining the the general expression for coupling efficiency, then applying it to GSM beams and single-mode optical fibers. With the use of simplifying approximations, an expression for the mean coupling efficiency and an algebraic approximation are derived. These expressions are compared to the results of numerically integrating the exact original expression and those of computer simulations using speckled fields. Inaccuracies stemming from the simplifying approximations are thereby identified, and appropriate compensation is suggested.

5.2.1 Fiber Coupling Overview.

The geometric configuration assumed by this analysis is indicated in Fig. 10. A lens of focal length f and circular aperture diameter D is used to focus light contained in the random wave E onto the end of a single-mode optical fiber with a step-index core radius of a . While the coupling efficiency calculations can be performed in the focal plane \mathcal{F} , they can equally be performed at the exit pupil plane \mathcal{P} due to the Fourier transform relationship between the two planes [39]. At plane \mathcal{P} , the mean coupling efficiency can be expressed as

$$\langle \eta \rangle = \frac{\iint_{\mathcal{P}} \iint_{\mathcal{P}} \Gamma(\boldsymbol{\rho}_1, \boldsymbol{\rho}_2) \mathcal{M}_0^*(\boldsymbol{\rho}_1) \mathcal{M}_0(\boldsymbol{\rho}_2) P(\boldsymbol{\rho}_1) P(\boldsymbol{\rho}_2) d^2 \boldsymbol{\rho}_1 d^2 \boldsymbol{\rho}_2}{\iint_{\mathcal{P}} \Gamma(\boldsymbol{\rho}, \boldsymbol{\rho}) P(\boldsymbol{\rho}) d^2 \boldsymbol{\rho}}, \quad (5.2.1)$$

where $\iint_{\mathcal{P}}$ represents integration over the entire plane \mathcal{P} , $\boldsymbol{\rho}$ is the two-dimensional coordinate vector of plane \mathcal{P} with the origin at the optical axis, $\Gamma(\boldsymbol{\rho}_1, \boldsymbol{\rho}_2) = \langle E(\boldsymbol{\rho}_1) E^*(\boldsymbol{\rho}_2) \rangle$ is the mutual coherence function (MCF) of the incident field with $\langle \cdot \rangle$ representing en-

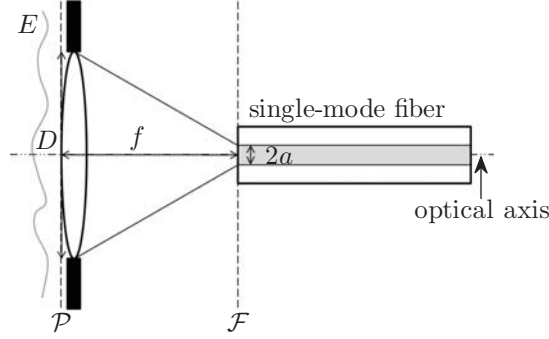


Figure 10. Geometric representation of the coupling of a random wave E into a single-mode optical fiber with a step-index core radius a . A circular aperture of diameter D and a focusing lens are assumed to be located at the system exit pupil plane \mathcal{P} , which is separated from the end of the optical fiber located in the focal plane \mathcal{F} by the lens focal length f . All components are assumed to be properly aligned along the optical axis.

semble averaging, $\mathcal{M}_0(\boldsymbol{\rho})$ is the back-propagated LP_{01} fiber mode, and $P(\boldsymbol{\rho})$ is the aperture transmittance pupil function [23, 94].

The derivation of Eq. (5.2.1) requires not only the assumptions and approximations inherent in scalar wave theory and Fourier optics [39], but also the approximation that the mean of a ratio of random variables can be treated as the ratio of the mean of those random variables, or

$$\left\langle \frac{|\iint_{\mathcal{P}} E(\boldsymbol{\rho}) \mathcal{M}_0^*(\boldsymbol{\rho}) P(\boldsymbol{\rho}) d^2 \boldsymbol{\rho}|^2}{\iint_{\mathcal{P}} |E(\boldsymbol{\rho})|^2 P(\boldsymbol{\rho}) d^2 \boldsymbol{\rho}} \right\rangle \simeq \frac{\left\langle |\iint_{\mathcal{P}} E(\boldsymbol{\rho}) \mathcal{M}_0^*(\boldsymbol{\rho}) P(\boldsymbol{\rho}) d^2 \boldsymbol{\rho}|^2 \right\rangle}{\left\langle \iint_{\mathcal{P}} |E(\boldsymbol{\rho})|^2 P(\boldsymbol{\rho}) d^2 \boldsymbol{\rho} \right\rangle}. \quad (5.2.2)$$

This approximation contains two inherent assumptions. The first is that the the numerator and denominator are statistically independent of each other. Since the numerator can never be greater than the denominator, this assumption is only strictly true when the denominator is constant. However, if their respective standard deviations (std) are sufficiently small relative to their means, they may be considered approximately independent. The second assumption is that the mean of the reciprocal

of the denominator is approximately equal to the reciprocal of its mean, or

$$\left\langle \frac{1}{\iint_{\mathcal{P}} |E(\boldsymbol{\rho})|^2 P(\boldsymbol{\rho}) d^2\boldsymbol{\rho}} \right\rangle \simeq \frac{1}{\langle \iint_{\mathcal{P}} |E(\boldsymbol{\rho})|^2 P(\boldsymbol{\rho}) d^2\boldsymbol{\rho} \rangle}. \quad (5.2.3)$$

Since this assumption only deals with the amplitude of the incident field, if all the randomness of the field is limited to its phase, then Eq. (5.2.3) becomes an equality. Otherwise, Eq. (5.2.3) is only a valid assumption when $\iint_{\mathcal{P}} |E(\boldsymbol{\rho})|^2 P(\boldsymbol{\rho}) d^2\boldsymbol{\rho}$ once again has a sufficiently small std relative to its mean. The impact of the approximation given in Eq. (5.2.2) on the following analysis can be evaluated through Monte Carlo methods. This evaluation is conducted in Sec. 5.2.3.2.

The back-propagated LP₀₁ fiber mode $\mathcal{M}_0(\boldsymbol{\rho})$ can be expressed as [52]

$$\mathcal{M}_0(\boldsymbol{\rho}) = \left(\frac{kawV}{\sqrt{\pi}f} \right) \frac{uJ_0\left(\frac{ka|\boldsymbol{\rho}|}{f}\right) - \frac{ka|\boldsymbol{\rho}|}{f} \frac{J_0(u)}{J_1(u)} J_1\left(\frac{ka|\boldsymbol{\rho}|}{f}\right)}{\left[u^2 - \left(\frac{ka|\boldsymbol{\rho}|}{f}\right)^2 \right] \left[w^2 + \left(\frac{ka|\boldsymbol{\rho}|}{f}\right)^2 \right]}, \quad (5.2.4)$$

where $k = 2\pi/\lambda$ with λ the center wavelength of the light (assumed to be narrow-band), $V = ka(n_1^2 - n_2^2)^{1/2}$ is the normalized frequency of the fiber with n_1 and n_2 the index of refraction of the fiber core and cladding respectively, u and w are determined by the relations $u^2 + w^2 = V^2$ and $uJ_1(u)K_0(w) = wK_1(w)J_0(u)$, J_0 and J_1 are Bessel functions of the first kind of order 0 and 1, and K_0 and K_1 are modified Bessel functions of the second kind of order 0 and 1 [58]. This mode has been normalized such that its inner product with itself is unity, or

$$\iint_{\mathcal{P}} \mathcal{M}_0(\boldsymbol{\rho}) \mathcal{M}_0^*(\boldsymbol{\rho}) d^2\boldsymbol{\rho} = 1. \quad (5.2.5)$$

Equation (5.2.4) is obviously difficult to work with, so for analytic convenience it can

be approximated with a normalized Gaussian shape given by [23]

$$\mathcal{M}_0(\boldsymbol{\rho}) = \frac{2\sqrt{2\pi}A}{\pi D} \exp \left[- \left(\frac{2A}{D} \right)^2 |\boldsymbol{\rho}|^2 \right], \quad (5.2.6)$$

where A can be determined from [58]

$$A = \frac{\pi Da}{2\lambda f} \left(0.65 + \frac{1.619}{V^{3/2}} + \frac{2.879}{V^6} \right). \quad (5.2.7)$$

Coupling efficiency tends to be maximized when $A = 1.121$ [23]. As seen in Fig. 11, when $V = 2.4$ (near the cut-off frequency for step-index single-mode fibers), the Gaussian approximation reasonably resembles the exact mode shape. The goodness of fit, as defined by the inner product of Eqs. (5.2.4) and (5.2.6), is a function of V and falls from 0.9965 for $V = 2.4$ to 0.946 for $V = 1.2$ [58]. Since more power is carried in the core of the fiber at higher V , and is therefore less susceptible to bending losses [14], a high V can be reasonably assumed. For this reason, $V = 2.4$ was used in this analysis.

5.2.2 Mean Coupling of GSM Beams.

The MCF of any Schell-model field can be expressed in a functional form as [57,78]

$$\Gamma(\boldsymbol{\rho}_1, \boldsymbol{\rho}_2) = [S(\boldsymbol{\rho}_1)]^{1/2} [S^*(\boldsymbol{\rho}_2)]^{1/2} g(\boldsymbol{\rho}_1 - \boldsymbol{\rho}_2). \quad (5.2.8)$$

One characteristic of Schell-model fields is that their coherence function, as defined by

$$\mu(\boldsymbol{\rho}_1, \boldsymbol{\rho}_2) = \frac{|\Gamma(\boldsymbol{\rho}_1, \boldsymbol{\rho}_2)|}{[\Gamma(\boldsymbol{\rho}_1, \boldsymbol{\rho}_1)]^{1/2} [\Gamma(\boldsymbol{\rho}_2, \boldsymbol{\rho}_2)]^{1/2}}, \quad (5.2.9)$$

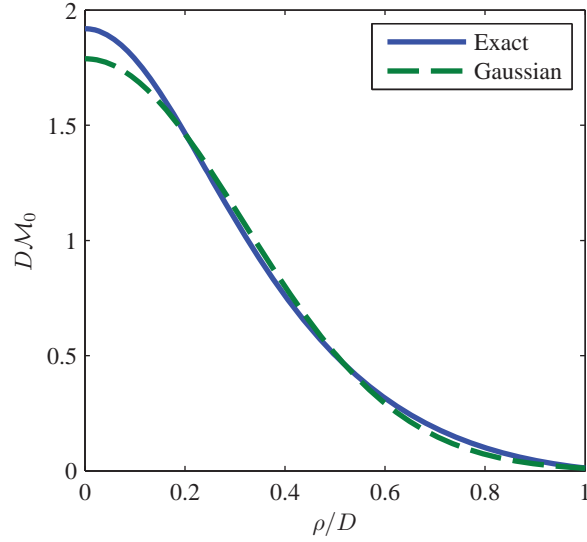


Figure 11. A comparison between the exact expression and Gaussian approximation of the back-propagated single-mode fiber transmission mode. For this figure, $\lambda = 1.315\mu\text{m}$, $V = 2.4$, $A = 1.121$, and $f/D = 2$.

depends only on the difference $\rho_1 - \rho_2$, and not the individual locations of ρ_1 and ρ_2 . In this sense they are coherently homogeneous.¹ If both $S(\rho)$ and $g(\rho)$ are Gaussian functions, then they define a GSM beam with a MCF that can be expressed as

$$\Gamma(\rho_1, \rho_2) = \exp \left[-\frac{|\rho_1|^2 + |\rho_2|^2}{w_g^2} - \frac{|\rho_1 - \rho_2|^2}{\rho_g^2} - \frac{jk}{2R_g} (|\rho_1|^2 - |\rho_2|^2) \right], \quad (5.2.10)$$

where w_g is the average beam radius, ρ_g is the coherence radius, R_g is the radius of curvature, $j = \sqrt{-1}$, and the MCF has been normalized such that $\Gamma(\mathbf{0}, \mathbf{0}) = 1$. The beam radius w_g defines the average size of the beam. While it is defined in terms of an ensemble average, by assuming ergodicity it is also equal to the long-time average beam radius. It would therefore account for atmospheric effects such as beam wander and spreading. The coherence radius ρ_g is defined by the separation distance whereby the the coherence function $\mu(\rho_1 - \rho_2)$ falls to e^{-1} . It effectively defines the circular area within which the field can be considered coherent. The radius of curvature R_g

¹Note that this relationship is often referred to as the modulus of the complex degree of coherence [2] or the modulus of the complex coherence factor [38].

describes the surfaces of constant average phase. R_g is positive for a converging beam, negative for a diverging beam, and infinite for a collimated beam. These three parameters completely characterize the statistics of GSM beams. It should be noted that the following analysis makes no assumptions about how the field in plane \mathcal{P} originated, only that the MCF of the field is well approximated by Eq. (5.2.10).

Using the integrals Int₁–Int₄ defined in Appendix A, the mean coupling efficiency equation given in Eq. (5.2.1) is expressed as

$$\langle \eta \rangle = \frac{\text{Int}_1}{\text{Int}_2}. \quad (5.2.11)$$

If a clear, “hard” aperture of diameter D is assumed, then the pupil function is given by

$$P(\boldsymbol{\rho}) = \begin{cases} 1 & \text{if } |\boldsymbol{\rho}| \leq D/2, \\ 0 & \text{if } |\boldsymbol{\rho}| > D/2. \end{cases} \quad (5.2.12)$$

The analytic solution is determined using Eqs. (A.10) and (A.11) and given by

$$\begin{aligned} \langle \eta \rangle_{\text{hard}} = 4A^2 \left(\frac{D}{2w_g} \right)^2 & \left\{ 1 - \exp \left[-2 \left(\frac{D}{2w_g} \right)^2 \right] \right\}^{-1} \sum_{i=0}^{\infty} \left| \frac{1}{(i+1)!} \left(\frac{D}{2\rho_g} \right)^{2i} \right. \\ & \left. \times {}_1F_1 \left[i+1; i+2; - \left(\frac{D}{2w_g} \right)^2 - \left(\frac{D}{2\rho_g} \right)^2 - A^2 - \frac{jkD^2}{8R_g} \right] \right|^2, \end{aligned} \quad (5.2.13)$$

where ${}_1F_1(\cdot)$ is the confluent hypergeometric function. For a given value of A , the mean coupling efficiency is dependent on the ratios of the aperture area to the beam area $(\pi D^2/4)/(\pi w_g^2)$, the coherence area $(\pi D^2/4)/(\pi \rho_g^2)$, and the product of the wavelength and radius of curvature $(\pi D^2/4)/(\lambda R_g)$. While this expression for the mean coupling efficiency is useful in many instances, it is analytically difficult to work with and its utility may be limited by computational precision. For example, using double-precision floating-point numbers as in Listing C.12, the confluent hypergeometric

function causes an underflow condition prior to convergence when $D/(2\rho_g)$ is larger than about 27. The evaluation of Eq. (5.2.13) for larger values of $D/(2\rho_g)$ therefore requires either increased computational precision, such as using quadruple-precision floating-point numbers, or numerically integrating Eq. (5.2.1). For the results in this chapter, numerical integration was used.

To overcome the limitations of of Eq. (5.2.13), an alternative analytic method is developed here. By approximating the “hard” aperture with a Gaussian “soft” aperture whereby [2]

$$P(\boldsymbol{\rho}) = \exp\left(-\frac{8|\boldsymbol{\rho}|^2}{D^2}\right), \quad (5.2.14)$$

Eqs. (A.19) and (A.20) are used in Eq. (5.2.11) to produce the algebraic approximation

$$\langle \eta \rangle_{\text{soft}} = \frac{4A^2 \left[\left(\frac{D}{2w_g} \right)^2 + 1 \right]}{\left| \left(\frac{D}{2w_g} \right)^2 + \left(\frac{D}{2\rho_g} \right)^2 + A^2 + 2 + \frac{jkD^2}{8R_g} \right|^2 - \left(\frac{D}{2\rho_g} \right)^4}. \quad (5.2.15)$$

A comparison of Eqs. (5.2.13) and (5.2.15) is found in Fig. 12. This figure demonstrates how the average coupling efficiency is only weakly dependent on the beam size, but is strongly dependent on the coherence size. As long as the coherence area is larger than the aperture area, the coupling efficiency remains fairly constant, but once the coherence area becomes smaller than the aperture area, the coupling efficiency rapidly diminishes. It also demonstrates that what Eq. (5.2.15) makes up for in simplicity and ease of use, it lacks in accuracy. This accuracy shortcoming can be ameliorated though the use of compensation. Using compensation is important in cases where Eq. (5.2.15) is used in further analytic work, such as the coupling variance analysis of Sec. 5.3 where any errors are at the very least doubled.

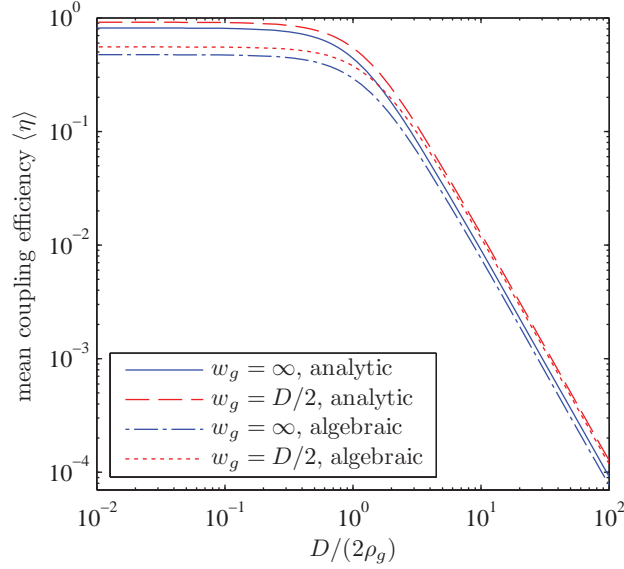


Figure 12. Plots of the analytic expression of Eq. (5.2.13) and the algebraic approximation of Eq. (5.2.15) of the mean coupling efficiency $\langle \eta \rangle$ for a Gaussian Schell-model beam into a single-mode optical fiber with differing values of the average beam radius w_g and coherence radius ρ_g . In both cases the beam is considered collimated with $R_g = \infty$. All other values are the same as in Fig. 11.

5.2.3 Mean Coupling Efficiency Compensation.

There were three main approximations required to arrive at Eqs. (5.2.13) and (5.2.15):

1. The statistical approximation of Eq. (5.2.2),
2. The exact fiber mode of Eq. (5.2.4) was approximated with a Gaussian shape of Eq. (5.2.6), and
3. The “hard” aperture pupil function of Eq. (5.2.12) was approximated as a Gaussian “soft” aperture of Eq. (5.2.14).

The first two were necessary to derive Eq. (5.2.13), while all three were necessary to derive Eq. (5.2.15). To have confidence in these equations and gain insight, it is necessary to analyze the effects of each of these approximations. While approximation #3 can be analyzed by direct comparison, computer simulations are needed to analyze the other two approximations. By assuming non-speckle conditions, whereby

Eq. (5.2.2) becomes an equality, approximation #1 is eliminated. After separately analyzing approximations #2 and #3, well-developed speckle conditions are considered where approximation #1 may lead to errors. Following this methodology, the accuracy of Eqs. (5.2.13) and (5.2.15) are determined, and any necessary adjustments are made to compensate for the resulting inaccuracies.

5.2.3.1 Compensation for Non-speckled Beams.

While random light is typically characterized by speckle, there are some cases where nearly all the randomness occurs in the phase of the light resulting in very little to no speckle. One particular instance of this is when coherent light passes through weak atmospheric turbulence [2]. Since the field amplitude can be considered deterministic, the denominator of Eq. (5.2.2) can be moved outside the averaging operator, and this expression becomes an equality. While the coherence function resulting from this scenario is not quite Gaussian, Dikmelik and Davidson [23] have shown that a Gaussian coherence function is an excellent approximation to the true coherence function when calculating coupling efficiency. Additionally, Wheeler and Schmidt [92] have shown that the coherence function becomes more Gaussian as the turbulence strength increases. Alternatively, when a coherent Gaussian beam passes through a phase screen which possesses a Gaussian power spectrum, the resulting beam is well approximated with a GSM MCF [2, 24, 99].

The effect of approximation #3 in isolation of the other two approximations can be directly observed in Fig. 12. While Eqs. (5.2.13) and (5.2.15) have the same general shape and asymptotic slopes for large and small $D/(2\rho_g)$, Eq. (5.2.15) underestimates Eq. (5.2.13) at all times, with the greatest error at small $D/(2\rho_g)$. The nature of these discrepancies can be directly evaluated from asymptotic approximations of Eqs. (5.2.13) and (5.2.15). For small $D/(2\rho_g)$, only the first term of the summation

in Eq. (5.2.13) is needed. By using the functional relationship [2, Eq. (GH7)]

$${}_1F_1(1; 2; -x) = \frac{1}{x} (1 - e^{-x}), \quad (5.2.16)$$

it can be approximated as²

$$\langle \eta \rangle_{\text{hard}} \simeq \frac{4A^2 \left(\frac{D}{2w_g} \right)^2 \left| 1 - \exp \left[- \left(\frac{D}{2w_g} \right)^2 - \left(\frac{D}{2\rho_g} \right)^2 - A^2 - \frac{jkD^2}{8R_g} \right] \right|^2}{\left| \left(\frac{D}{2w_g} \right)^2 + \left(\frac{D}{2\rho_g} \right)^2 + A^2 + \frac{jkD^2}{8R_g} \right|^2 \left\{ 1 - \exp \left[-2 \left(\frac{D}{2w_g} \right)^2 \right] \right\}}$$

for $\rho_g \gg D/2$. (5.2.17)

The limit of the ratio between Eq. (5.2.17) and Eq. (5.2.15) as ρ_g tends toward infinity can be expressed as

$$\eta_\infty = \lim_{\rho_g \rightarrow \infty} \frac{\langle \eta \rangle_{\text{hard}}}{\langle \eta \rangle_{\text{soft}}} = \frac{\left(\frac{D}{2w_g} \right)^2 \left| \left(\frac{D}{2w_g} \right)^2 + A^2 + 2 + \frac{jkD^2}{8R_g} \right|^2 \left| 1 - \exp \left[- \left(\frac{D}{2w_g} \right)^2 - A^2 - \frac{jkD^2}{8R_g} \right] \right|^2}{\left[\left(\frac{D}{2w_g} \right)^2 + 1 \right] \left| \left(\frac{D}{2w_g} \right)^2 + A^2 + \frac{jkD^2}{8R_g} \right|^2 \left\{ 1 - \exp \left[-2 \left(\frac{D}{2w_g} \right)^2 \right] \right\}}$$

(5.2.18)

In the opposite extreme, the asymptote of $\langle \eta \rangle$ for small ρ_g can be determined through the use of the approximation

$$\exp \left(- \frac{|\boldsymbol{\rho}_1 - \boldsymbol{\rho}_2|^2}{\rho_g^2} \right) \simeq \pi \rho_g^2 \delta(\boldsymbol{\rho}_1 - \boldsymbol{\rho}_2) \quad \text{for } \rho_g \ll D/2, \quad (5.2.19)$$

²Note that as w_g , ρ_g , and R_g tend toward infinity, Eq. (5.2.17) reduces to the expression for the coupling efficiency of a plane wave into a single-mode fiber given by $2[1 - \exp(-A^2)]^2/A^2$ [52].

where $\delta(\boldsymbol{\rho})$ is the two-dimensional Dirac delta function defined by $\iint_{\mathcal{P}} f(\boldsymbol{\rho})\delta(\boldsymbol{\rho}) d^2\boldsymbol{\rho} = f(\mathbf{0})$ for the arbitrary and well-behaved function $f(\boldsymbol{\rho})$. With this approximation, Eq. (A.1) can be reduced to

$$\text{Int}_1 \simeq \frac{8A^2\rho_g^2}{D^2} \iint_{\mathcal{P}} \exp \left[-2 \left(\frac{1}{w_g^2} + \frac{4A^2}{D^2} \right) |\boldsymbol{\rho}|^2 \right] P^2(\boldsymbol{\rho}) d^2\boldsymbol{\rho} \quad \text{for } \rho_g \ll D/2. \quad (5.2.20)$$

This can be directly evaluated for both ‘‘hard’’ and ‘‘soft’’ apertures, and once inserted into Eq. (5.2.11) produces

$$\langle \eta \rangle_{\text{hard}} \simeq \frac{2A^2 \left(\frac{D}{2w_g} \right)^2 \left\{ 1 - \exp \left[-2 \left(\frac{D}{2w_g} \right)^2 - 2A^2 \right] \right\}}{\left(\frac{D}{2\rho_g} \right)^2 \left[\left(\frac{D}{2w_g} \right)^2 + A^2 \right] \left\{ 1 - \exp \left[-2 \left(\frac{D}{2w_g} \right)^2 \right] \right\}} \quad \text{for } \rho_g \ll D/2, \quad (5.2.21)$$

and

$$\langle \eta \rangle_{\text{soft}} \simeq \frac{2A^2 \left[\left(\frac{D}{2w_g} \right)^2 + 1 \right]}{\left(\frac{D}{2\rho_g} \right)^2 \left[\left(\frac{D}{2w_g} \right)^2 + A^2 + 2 \right]} \quad \text{for } \rho_g \ll D/2. \quad (5.2.22)$$

The ratio between Eq. (5.2.21) and Eq. (5.2.22) is then given by

$$\begin{aligned} \eta_0 &= \frac{\langle \eta \rangle_{\text{hard}}}{\langle \eta \rangle_{\text{soft}}} \quad \text{for } \rho_g \ll D/2 \\ &= \frac{\left(\frac{D}{2w_g} \right)^2 \left[\left(\frac{D}{2w_g} \right)^2 + A^2 + 2 \right] \left\{ 1 - \exp \left[-2 \left(\frac{D}{2w_g} \right)^2 - 2A^2 \right] \right\}}{\left[\left(\frac{D}{2w_g} \right)^2 + 1 \right] \left[\left(\frac{D}{2w_g} \right)^2 + A^2 \right] \left\{ 1 - \exp \left[-2 \left(\frac{D}{2w_g} \right)^2 \right] \right\}}. \end{aligned} \quad (5.2.23)$$

While a functional relationship can be found that uses η_∞ and η_0 to compensate for

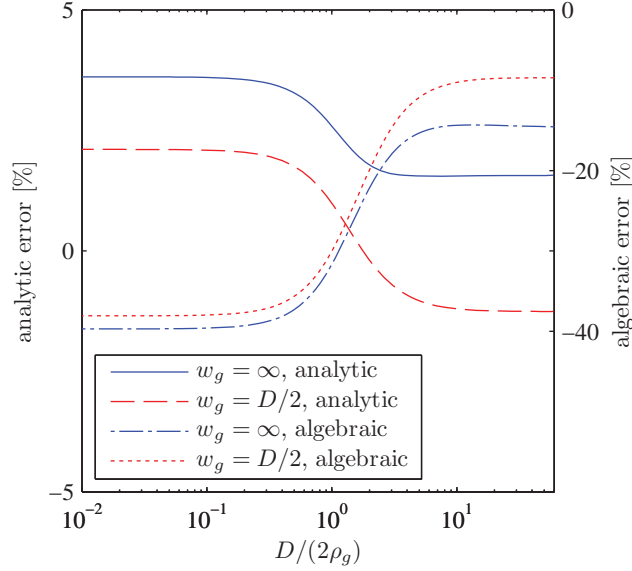


Figure 13. Error inherent in the analytic (left axis) and algebraic (right axis) expressions for the mean coupling efficiency given by Eq. (5.2.13) and (5.2.15) respectively. The error is referenced to the numerical evaluation of Eq. (5.2.1) using the exact back-propagated fiber mode given by Eq. (5.2.4) with differing values of the average beam radius w_g , coherence radius ρ_g , and $R_g = \infty$.

the effects of approximation #3 across all values of $D/(2\rho_g)$, for practical purposes this discussion is reserved for the analysis of the effects of approximation #2.

The effect of approximation #2 can be evaluated by numerically integrating Eq. (5.2.1) using the exact fiber mode of Eq. (5.2.4), and comparing the results to that of Eqs. (5.2.13). Likewise, the combined effects of approximations #2 and #3 are found by comparing the numeric results for the exact fiber mode to that of Eq. (5.2.15). Figure 13 displays the resulting error of Eqs. (5.2.13) and (5.2.15) for $R_g = \infty$ and two values of w_g with $V = 2.4$. As was case with approximation #3, the error due to approximation #2 is nearly constant for large or small $D/(2\rho_g)$, with a smooth transition in the vicinity of $D/(2\rho_g) \sim 1$. The observed error at large and small $D/(2\rho_g)$ due to approximation #2 were empirically evaluated for several values of w_g and are given in Table 1, where c_∞ is the ratio between the numeric results using the exact fiber mode and that of Eq. (5.2.13) for large ρ_g , and c_0 is this ratio for small ρ_g . Highly accurate estimates of c_0 and c_∞ for $V = 2.4$ can be evaluated for

Table 1. Best fit parameters for fiber mode shape compensation with resulting maximum error

w_g	c_0	c_∞	algebraic			analytic		
			b	n	max error [%]	b	n	max error [%]
∞	0.9846	0.9651	0.6884	2.307	0.75	1.081	2.684	0.056
$5D$	0.9849	0.9653	0.6862	2.303	0.74	1.064	2.668	0.054
$2D$	0.9864	0.9660	0.6750	2.279	0.67	0.9839	2.591	0.044
D	0.9920	0.9686	0.6415	2.213	0.47	0.7868	2.385	0.026
$D/2$	1.013	0.9794	0.5549	2.091	0.10	0.4846	2.093	0.0081

$D/(2w_g) \leq 1$ using

$$c_0 = 0.985 + 0.0282 \left(\frac{D}{2w_g} \right)^{1.94}, \quad (5.2.24)$$

and

$$c_\infty = 0.965 + 0.0142 \left(\frac{D}{2w_g} \right)^2. \quad (5.2.25)$$

While the indicated accuracy in Fig. 13 may be sufficient when using Eq. (5.2.13), it is doubtful the accuracy of Eq. (5.2.15) is adequate for many applications. The accuracy of both expressions can be increased through the use of a compensation equation that reasonably fits the curves in Fig. 13. One such equation is

$$\eta_{\text{fit}} = \frac{c_\infty \eta_\infty - c_0 \eta_0}{1 + b \left(\frac{D}{2\rho_g} \right)^n} + c_0 \eta_0, \quad (5.2.26)$$

where b and n are fit parameters. While Eq. (5.2.26) is intended for use with Eq. (5.2.15), it can also be used to correct Eq. (5.2.13) by setting η_0 and η_∞ to 1. Compensation is made by multiplying the relevant mean coupling efficiency equation by the optimally fit Eq. (5.2.26).

The optimum fit parameters, as determined using non-linear least-squares tech-

niques, and the maximum resulting error for $R_g = \infty$ and several values of w_g are given in Table 1. As indicated, the accuracy of Eq. (5.2.15) can be kept to within 0.8% with compensation, while the accuracy of Eq. (5.2.13) can be kept to within 0.06%. Estimates of the the fit parameters b and n for values of $D/(2w_g) \leq 1$ can be found to better than 0.4% accuracy for use with Eq. (5.2.15) by using

$$b = 0.6884 - 0.1335 \left(\frac{D}{2w_g} \right)^{1.561} \quad (5.2.27)$$

and

$$n = 2.307 - 0.2162 \left(\frac{D}{2w_g} \right)^{1.312}, \quad (5.2.28)$$

while they can be found to better than 4% accuracy for use with Eq. (5.2.13) by using

$$b = 1.081 - 0.5962 \left(\frac{D}{2w_g} \right)^{1.173} \quad (5.2.29)$$

and

$$n = 2.684 - 0.5908 \left(\frac{D}{2w_g} \right)^{1.164}. \quad (5.2.30)$$

While these compensation techniques can significantly increase the accuracy of Eqs. (5.2.13) and (5.2.15), they are limited to instances of coupling random fields with deterministic amplitudes. However, these results can be extended to the coupling of specked fields by examining the effect of approximation #1.

5.2.3.2 Compensation for Speckled Beams.

In many (if not most) cases, random light exhibits speckle to some degree. Therefore, it is important to understand the effect of speckle when coupling random light into a single-mode optical fiber. This investigation was primarily conducted using computer simulations. To simulate realizations of a random speckle field, the method described by Gbur [36] and summarized here was used. The fields are generated by combining temporally pulsed plane waves where the number of waves, their departure times, and their directions are all random. Field realizations are written in the form

$$E(\boldsymbol{\rho}) = \sum_{i=1}^N \Theta(\boldsymbol{\rho}) \Phi(t_i) \exp(-j\mathbf{K}_i \cdot \boldsymbol{\rho}), \quad (5.2.31)$$

where $\Theta(\boldsymbol{\rho})$ is the average field shape; $\Phi(t)$ is the temporal pulse shape; N is the random number of pulses, which has a Poisson distribution; t_i is the random pulse departure time, which is uniformly distributed within the pulse shape; and \mathbf{K}_i is the random pulse direction vector, which has a zero-mean Gaussian distribution with a std of $\sigma_{\mathbf{K}}$. As shown in [36], the resulting MCF for these fields can be expressed as

$$\Gamma_G(\boldsymbol{\rho}_1, \boldsymbol{\rho}_2) = \nu_p \Theta(\boldsymbol{\rho}_1) \Theta^*(\boldsymbol{\rho}_2) \exp\left(-\frac{\sigma_{\mathbf{K}}^2}{2} |\boldsymbol{\rho}_1 - \boldsymbol{\rho}_2|^2\right) \int_{-\infty}^{\infty} |\Phi(t)|^2 dt, \quad (5.2.32)$$

where ν_p is the average pulse rate. As long as

$$\Theta(\boldsymbol{\rho}) = \left[\nu_p \int_{-\infty}^{\infty} |\Phi(t)|^2 dt \right]^{-1/2} \exp\left[-\left(\frac{1}{w_g^2} + \frac{jk}{2R_g}\right) |\boldsymbol{\rho}|^2\right], \quad (5.2.33)$$

then Eq. (5.2.32) reduces to Eq. (5.2.10) with $\rho_g = 2^{1/2}/\sigma_{\mathbf{K}}$. An example of a field generated by this method using Listing C.5 is shown in Fig. 14. The amplitude displays well-developed speckle, and as expected the phase displays corresponding branch points and branch cuts [34, 40].

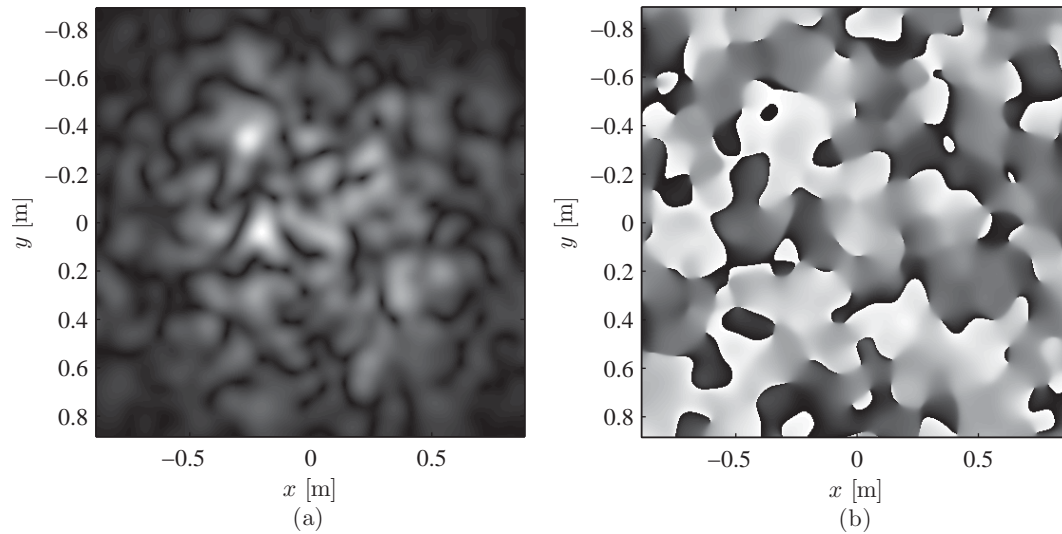


Figure 14. A realization of a speckled field. This realization used a Gaussian temporal pulse with a FWHM bandwidth of $1/100$ the central frequency of 228 THz, an average pulse rate of 5 pulses per cycle, and an overall coherence radius of 10 cm. Image (a) contains the field amplitude which has an average beam radius of 75 cm. Image (b) contains the field phase which is wrapped between $-\pi$ (black) and π (white) radians.

In these runs, as well as all other simulation runs, the coherence radius ρ_g ranged from $50 D$ (practically coherent) to $D/200$ (practically incoherent), the beam radius w_g was varied between $D/2$ and ∞ , and the beams were considered collimated. The simulations used a Gaussian temporal pulse with a full-width, half-max (FWHM) bandwidth of $1/100$ the central frequency of 228 terahertz (THz), and an average pulse rate of 5 pulses per cycle (1140 THz). A total of 2000 independent realizations were used to generate each data point. The average coupling efficiency was calculated using these simulated fields and the exact fiber mode given by Eq. (5.2.4), then compared to the numerically integrated results of Eq. (5.2.1) using the “hard” aperture pupil function of Eq. (5.2.12) and the exact fiber mode. This comparison, as shown in Fig. 15 with 95% confidence levels, demonstrated good agreement when either $\rho_g \gg D/2$ or $\rho_g \ll D/2$. This is as expected since those are the regions where the beam is either nearly coherent, making the beam’s amplitude nearly deterministic, or the beam is nearly incoherent thereby producing many independent regions of

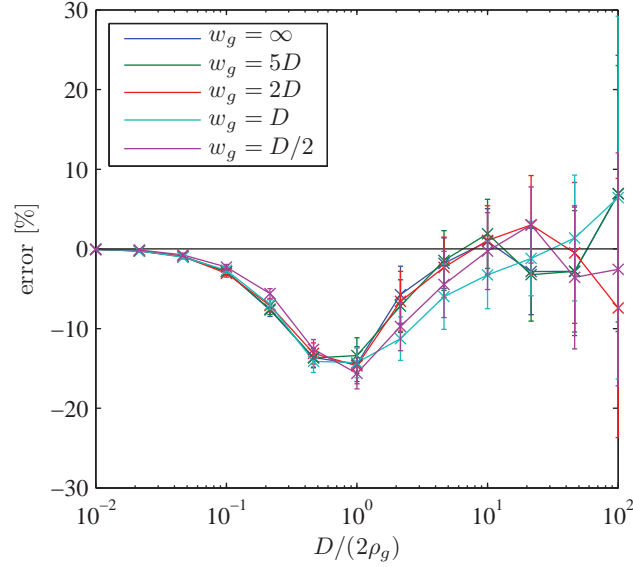


Figure 15. Error of the mean coupling efficiency due to the simplifying statistical approximation given by Eq. (5.2.2) when the incident field is well-speckled. The error is referenced to the numerical evaluation of Eq. (5.2.1) using the exact back-propagated fiber mode given by Eq. (5.2.4) with differing values of the average beam radius w_g , coherence radius ρ_g , and $R_g = \infty$. Error bars represent the 95% confidence level.

amplitude within the aperture which get summed together. Under these conditions, the denominator in Eq. (5.2.2) is nearly deterministic so approximation #1 produces little error. However, when ρ_g is close to $D/2$, the total power within the aperture can vary greatly from one realization to the next resulting in a smaller $\langle \eta \rangle$ than expected. According to the simulations, this discrepancy can be as large as about 15%.

To compensate for this effect when using the algebraic approximation of Eq. (5.2.15), the fit parameters of Eq. (5.2.26) may be adjusted to fit the simulation data. Due to the random nature of this data, there is little practical advantage of optimizing these parameter values in lieu of using the nominal values of $b = 4.5$ and $n = 1.7$. These nominal parameters result in the simulation data falling within 5% of the expected value for all w_g values tested. The effect of this alternate compensation is shown in Fig. 16 for $0.1 < D/(2\rho_g) < 10$, using w_g of ∞ and $D/2$ as examples. However, when using the exact analytic solution of Eq. (5.2.13), simply adjusting the fit parameters of Eq. (5.2.26) does not sufficiently compensate the effect of speckle and requires ad-

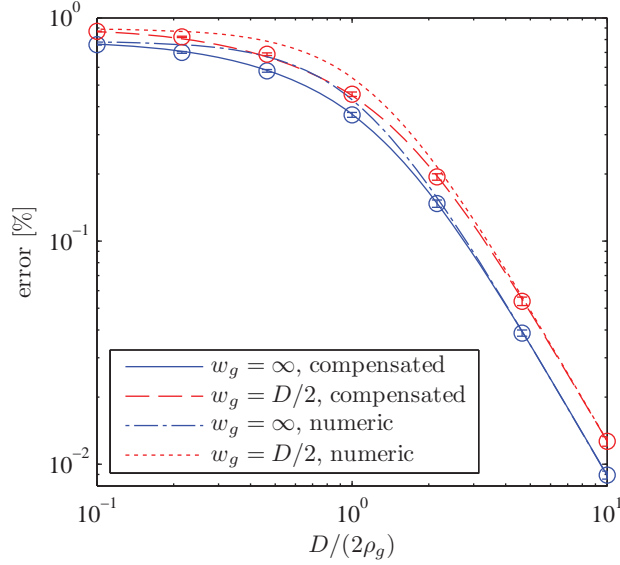


Figure 16. The effect of compensation on the accuracy of the algebraic expression of the mean coupling efficiency given by Eq. (5.2.15) when the incident field is well-speckled with differing values of the average beam radius w_g , coherence radius ρ_g , and $R_g = \infty$. The numeric results using the exact back-propagated fiber mode given by Eq. (5.2.4) is provided for reference. Simulation results are indicated by circles, and error bars represent the 95% confidence level.

ditional compensation measures. Since adequate compensation was achieved using the algebraic approximation, additional compensation for the analytic solution was not sought. This investigation demonstrates that while speckle does effect the $\langle \eta \rangle$ measurement in certain regimes, compensation can be easily made for this effect.

5.3 Coupling Variance

With accurate expressions for the mean coupling efficiency, it is now possible to derive expressions for the coupling efficiency variance. Since the coupling efficiency variance is based on the fourth-order moment of the field, the speckle content of the field has a large impact on the resulting expressions. Expressions are derived for the cases of fully developed speckle, when the speckle is not quite fully developed, and when there is no speckle. These expressions are evaluated by comparisons to either numerical integration or computer simulation results. As was accomplished with the

mean coupling efficiency, the inaccuracies due to the simplifying approximations are identified, and suitable compensation is suggested.

5.3.1 Fully Speckled Beams.

To derive the coupling efficiency variance, it is necessary to determine the second moment of η , which can be most generally expressed as

$$\langle \eta^2 \rangle = \left\langle \frac{|\iint_{\mathcal{P}} E(\boldsymbol{\rho}) \mathcal{M}_0^*(\boldsymbol{\rho}) P(\boldsymbol{\rho}) d^2 \boldsymbol{\rho}|^4}{[\iint_{\mathcal{P}} |E(\boldsymbol{\rho})|^2 P(\boldsymbol{\rho}) d^2 \boldsymbol{\rho}]^2} \right\rangle. \quad (5.3.1)$$

Expanding the terms, applying a similar statistical approximation to that of Eq. (5.2.2), and exchanging the order of integration and averaging produces

$$\begin{aligned} \langle \eta^2 \rangle = & \iint_{\mathcal{P}} \iint_{\mathcal{P}} \iint_{\mathcal{P}} \iint_{\mathcal{P}} \Gamma(\boldsymbol{\rho}_1, \boldsymbol{\rho}_2, \boldsymbol{\rho}_3, \boldsymbol{\rho}_4) \mathcal{M}_0^*(\boldsymbol{\rho}_1) \mathcal{M}_0(\boldsymbol{\rho}_2) \mathcal{M}_0^*(\boldsymbol{\rho}_3) \mathcal{M}_0(\boldsymbol{\rho}_4) \\ & \times P(\boldsymbol{\rho}_1) P(\boldsymbol{\rho}_2) P(\boldsymbol{\rho}_3) P(\boldsymbol{\rho}_4) d^2 \boldsymbol{\rho}_1 d^2 \boldsymbol{\rho}_2 d^2 \boldsymbol{\rho}_3 d^2 \boldsymbol{\rho}_4 \\ & / \iint_{\mathcal{P}} \iint_{\mathcal{P}} \Gamma(\boldsymbol{\rho}_1, \boldsymbol{\rho}_1, \boldsymbol{\rho}_2, \boldsymbol{\rho}_2) P(\boldsymbol{\rho}_1) P(\boldsymbol{\rho}_2) d^2 \boldsymbol{\rho}_1 d^2 \boldsymbol{\rho}_2, \quad (5.3.2) \end{aligned}$$

where $\Gamma(\boldsymbol{\rho}_1, \boldsymbol{\rho}_2, \boldsymbol{\rho}_3, \boldsymbol{\rho}_4) = \langle E(\boldsymbol{\rho}_1) E^*(\boldsymbol{\rho}_2) E(\boldsymbol{\rho}_3) E^*(\boldsymbol{\rho}_4) \rangle$ is the fourth-order coherence function of the field.

In general, the fourth-order coherence function can be very difficult to determine, but one instance where it is simple to calculate is when the field displays fully developed speckle. In this case, the field is defined as a circular complex Gaussian random process, and therefore all of its higher-order statistics can be expressed in terms of its first- and second-order statistics [40]. By the complex Gaussian moment theorem, the fourth-order coherence function can be expressed in terms of the MCF as

$$\Gamma(\boldsymbol{\rho}_1, \boldsymbol{\rho}_2, \boldsymbol{\rho}_3, \boldsymbol{\rho}_4) = \Gamma(\boldsymbol{\rho}_1, \boldsymbol{\rho}_2) \Gamma(\boldsymbol{\rho}_3, \boldsymbol{\rho}_4) + \Gamma(\boldsymbol{\rho}_1, \boldsymbol{\rho}_4) \Gamma(\boldsymbol{\rho}_3, \boldsymbol{\rho}_2). \quad (5.3.3)$$

Inserting this into Eq. (5.3.2), along with performing some algebra, produces

$$\langle \eta^2 \rangle = \frac{2 \left[\iint_{\mathcal{P}} \iint_{\mathcal{P}} \Gamma(\boldsymbol{\rho}_1, \boldsymbol{\rho}_2) \mathcal{M}_0^*(\boldsymbol{\rho}_1) \mathcal{M}_0(\boldsymbol{\rho}_2) P(\boldsymbol{\rho}_1) P(\boldsymbol{\rho}_2) d^2 \boldsymbol{\rho}_1 d^2 \boldsymbol{\rho}_2 \right]^2}{\left[\iint_{\mathcal{P}} \Gamma(\boldsymbol{\rho}, \boldsymbol{\rho}) P(\boldsymbol{\rho}) d^2 \boldsymbol{\rho} \right]^2 + \iint_{\mathcal{P}} \iint_{\mathcal{P}} |\Gamma(\boldsymbol{\rho}_1, \boldsymbol{\rho}_2)|^2 P(\boldsymbol{\rho}_1) P(\boldsymbol{\rho}_2) d^2 \boldsymbol{\rho}_1 d^2 \boldsymbol{\rho}_2} \quad (5.3.4)$$

Alternatively, this can be expressed in term of Eqs. (A.1)–(A.4) as

$$\langle \eta^2 \rangle = \frac{2 \text{Int}_1^2}{\text{Int}_2^2 + \text{Int}_3} \quad (5.3.5)$$

While Eq. (5.3.5) can be directly evaluated using the results of Appendix A, it is more useful to instead evaluate the mean squared normalized variance defined as

$$\tilde{\sigma}_\eta^2 = \frac{\langle \eta^2 \rangle}{\langle \eta \rangle^2} - 1. \quad (5.3.6)$$

Inserting Eqs. (5.2.11) and (5.3.5) into Eq. (5.3.6) produces

$$\tilde{\sigma}_\eta^2 = \frac{\text{Int}_2^2 - \text{Int}_3}{\text{Int}_2^2 + \text{Int}_3} \quad (5.3.7)$$

Since neither Int_2 nor Int_3 uses \mathcal{M}_0 or R_g in their definitions, the fiber mode shape and the radius of curvature have no effect on $\tilde{\sigma}_\eta^2$ for fully specked fields. Using the GSM beam MCF of Eq. (5.2.10) and the “hard” aperture pupil function of Eq. (5.2.12),

Eq. (5.3.7) can be evaluated using Eqs. (A.10) and (A.12) and expressed as

$$\begin{aligned}
\tilde{\sigma}_{\eta,\text{hard}}^2 = & \left(\left\{ 1 - \exp \left[-2 \left(\frac{D}{2w_g} \right)^2 \right] \right\}^2 - 4 \left(\frac{D}{2w_g} \right)^4 \sum_{i=0}^{\infty} \left\{ \frac{2^i}{(i+1)!} \left(\frac{D}{2\rho_g} \right)^{2i} \right. \right. \\
& \times \left. \left. {}_1F_1 \left[i+1; i+2; -2 \left(\frac{D}{2w_g} \right)^2 - 2 \left(\frac{D}{2\rho_g} \right)^2 \right] \right\}^2 \right) \\
& / \left(\left\{ 1 - \exp \left[-2 \left(\frac{D}{2w_g} \right)^2 \right] \right\}^2 + 4 \left(\frac{D}{2w_g} \right)^4 \sum_{i=0}^{\infty} \left\{ \frac{2^i}{(i+1)!} \left(\frac{D}{2\rho_g} \right)^{2i} \right. \right. \\
& \times \left. \left. {}_1F_1 \left[i+1; i+2; -2 \left(\frac{D}{2w_g} \right)^2 - 2 \left(\frac{D}{2\rho_g} \right)^2 \right] \right\}^2 \right). \tag{5.3.8}
\end{aligned}$$

A MATLAB[®] script for evaluating Eq. (5.3.8) is given in Listing C.13.

A simpler algebraic approximation to Eq. (5.3.8) can be derived by using the Gaussian “soft” pupil function of Eq. (5.2.14), where Eqs. (A.14) and (A.15) are used to evaluate Eq. (5.3.7). After some algebraic simplification, the result can be expressed as

$$\tilde{\sigma}_{\eta,\text{soft}}^2 = \frac{\left(\frac{D}{2\rho_g} \right)^2}{\left(\frac{D}{2w_g} \right)^2 + \left(\frac{D}{2\rho_g} \right)^2 + 1}. \tag{5.3.9}$$

A comparison between Eqs. (5.3.8) and (5.3.9) is displayed in Fig. 17 for two values of w_g . While all lines tend toward a value of one for large $D/(2\rho_g)$, the two methods give different results for for small $D/(2\rho_g)$ and finite w_g . The nature of this difference can be evaluated by comparing the asymptotic approximation of Eqs. (5.3.8) at small values of $D/(2\rho_g)$ to Eq. (5.3.9) as was performed in Sec. 5.2.3.1. Using only the first

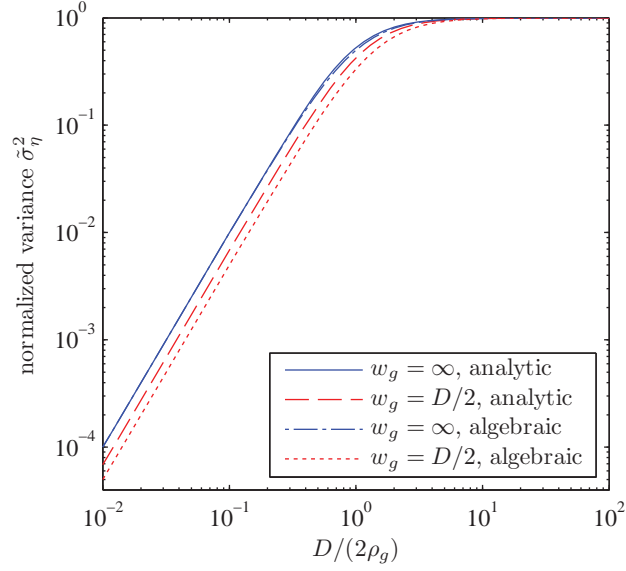


Figure 17. Plots of the analytic expression of Eq. (5.3.8) and the algebraic approximation of Eq. (5.3.9) of the mean squared normalized coupling variance for fully developed speckle fields with differing values of the average beam radius w_g , coherence radius ρ_g , and $R_g = \infty$.

term in each series, along with Eq. (5.2.16), Eq. (5.3.8) becomes

$$\begin{aligned}
\tilde{\sigma}_{\eta,\text{hard}}^2 \simeq & \left(\left[\left(\frac{D}{2w_g} \right)^2 + \left(\frac{D}{2\rho_g} \right)^2 \right]^2 \left\{ 1 - \exp \left[-2 \left(\frac{D}{2w_g} \right)^2 \right] \right\}^2 \right. \\
& \left. - \left(\frac{D}{2w_g} \right)^4 \left\{ 1 - \exp \left[-2 \left(\frac{D}{2w_g} \right)^2 - 2 \left(\frac{D}{2\rho_g} \right)^2 \right] \right\}^2 \right) \\
& / \left(\left[\left(\frac{D}{2w_g} \right)^2 + \left(\frac{D}{2\rho_g} \right)^2 \right]^2 \left\{ 1 - \exp \left[-2 \left(\frac{D}{2w_g} \right)^2 \right] \right\}^2 \right. \\
& \left. + \left(\frac{D}{2w_g} \right)^4 \left\{ 1 - \exp \left[-2 \left(\frac{D}{2w_g} \right)^2 - 2 \left(\frac{D}{2\rho_g} \right)^2 \right] \right\}^2 \right) \quad \text{for } \rho_g \gg D/2.
\end{aligned} \tag{5.3.10}$$

The limit of the ratio between Eq. (5.3.10) and Eq. (5.3.9) as ρ_g tends toward infinity

can be expressed as

$$\begin{aligned} \sigma_\infty^2 &= \lim_{\rho_g \rightarrow \infty} \frac{\tilde{\sigma}_{\eta,\text{hard}}^2}{\tilde{\sigma}_{\eta,\text{soft}}^2} \\ &= \frac{\left[\left(\frac{D}{2w_g} \right)^2 + 1 \right] \left\{ 1 - \left[2 \left(\frac{D}{2w_g} \right)^2 + 1 \right] \exp \left[-2 \left(\frac{D}{2w_g} \right)^2 \right] \right\}}{\left(\frac{D}{2w_g} \right)^2 \left\{ 1 - \exp \left[-2 \left(\frac{D}{2w_g} \right)^2 \right] \right\}}. \end{aligned} \quad (5.3.11)$$

This relationship can be used to compensate Eq. (5.3.9) as was performed for Eq. (5.2.15) in Sec. 5.2.3. However, since an approximation similar to approximation #1 was needed to derive Eq. (5.3.2), one would expect Eq. (5.3.8) to be in error when $D/(2\rho_g) \sim 1$. As a result, any final compensation must take into account the results of empirical evaluations.

5.3.2 Computer Simulations.

Computer simulations not only allow for an evaluation of Eqs. (5.3.8) and (5.3.9) for fully developed speckle fields, but also for fields that do not display fully developed speckle. To this end, the results from two different methods of Monte Carlo field generation were analyzed: one that generates random well-speckled fields, but not necessarily fully developed speckle fields, and another that generates random non-speckled fields. This methodology allows for further insight into the effect on coupling variance by fields that may fall in between one extreme or the other.

5.3.2.1 Coupling Variance of Well-speckled Beams.

The analysis leading to Eqs. (5.3.8) and (5.3.9) required the fields to display fully developed speckle. While the Gbur method as described in Sec. 5.2.3.2 creates fields with well-developed speckle, the speckle is not necessarily fully developed. While it is

possible to create fields that can be considered to have fully developed speckle through the Gbur method, the N in Eq. (5.2.31) must be sufficiently large for the given field parameters, and in some cases this requirement can be prohibitive. Fortunately, it is possible to derive the fourth-order coherence function for the fields generated by this method, and thereby a direct expression for $\tilde{\sigma}_\eta^2$. In practice, the speckle content of random fields coupled into single-mode fibers may not be fully developed, so the results of the following analysis may better approximate the coupling variance in these cases than Eqs. (5.3.8) or (5.3.9).

The fourth-order coherence function for a generated Gbur field is found by evaluating

$$\begin{aligned} \Gamma(\boldsymbol{\rho}_1, \boldsymbol{\rho}_2, \boldsymbol{\rho}_3, \boldsymbol{\rho}_4) = & \left\langle \sum_{k=1}^N \sum_{l=1}^N \sum_{m=1}^N \sum_{n=1}^N \Theta(\boldsymbol{\rho}_1) \Theta^*(\boldsymbol{\rho}_2) \Theta(\boldsymbol{\rho}_3) \Theta^*(\boldsymbol{\rho}_4) \Phi(t_k) \Phi^*(t_l) \Phi(t_m) \Phi^*(t_n) \right. \\ & \left. \times \exp(-j\mathbf{K}_k \cdot \boldsymbol{\rho}_1) \exp(j\mathbf{K}_l \cdot \boldsymbol{\rho}_2) \exp(-j\mathbf{K}_m \cdot \boldsymbol{\rho}_3) \exp(j\mathbf{K}_n \cdot \boldsymbol{\rho}_4) \right\rangle. \end{aligned} \quad (5.3.12)$$

By following the procedure outlined in [36], the resulting expression for the fourth-order coherence function becomes

$$\begin{aligned} \Gamma(\boldsymbol{\rho}_1, \boldsymbol{\rho}_2, \boldsymbol{\rho}_3, \boldsymbol{\rho}_4) = & \nu_p \Theta(\boldsymbol{\rho}_1) \Theta^*(\boldsymbol{\rho}_2) \Theta(\boldsymbol{\rho}_3) \Theta^*(\boldsymbol{\rho}_4) \exp\left(-\frac{|\boldsymbol{\rho}_1 - \boldsymbol{\rho}_2 + \boldsymbol{\rho}_3 - \boldsymbol{\rho}_4|^2}{\rho_g^2}\right) \\ & \times \int_{-\infty}^{\infty} |\Phi(t)|^4 dt + \Gamma_G(\boldsymbol{\rho}_1, \boldsymbol{\rho}_2) \Gamma_G(\boldsymbol{\rho}_3, \boldsymbol{\rho}_4) + \Gamma_G(\boldsymbol{\rho}_1, \boldsymbol{\rho}_4) \Gamma_G(\boldsymbol{\rho}_3, \boldsymbol{\rho}_2). \end{aligned} \quad (5.3.13)$$

Using Eq. (5.2.33) for $\Theta(\boldsymbol{\rho})$, the fourth-order coherence function for the Gbur fields

can be expressed as

$$\Gamma(\boldsymbol{\rho}_1, \boldsymbol{\rho}_2, \boldsymbol{\rho}_3, \boldsymbol{\rho}_4) = \epsilon \Gamma'(\boldsymbol{\rho}_1, \boldsymbol{\rho}_2, \boldsymbol{\rho}_3, \boldsymbol{\rho}_4) + \Gamma(\boldsymbol{\rho}_1, \boldsymbol{\rho}_2) \Gamma(\boldsymbol{\rho}_3, \boldsymbol{\rho}_4) + \Gamma(\boldsymbol{\rho}_1, \boldsymbol{\rho}_4) \Gamma(\boldsymbol{\rho}_3, \boldsymbol{\rho}_2), \quad (5.3.14)$$

where

$$\epsilon = \frac{\int_{-\infty}^{\infty} |\Phi(t)|^4 dt}{\nu_p \left[\int_{-\infty}^{\infty} |\Phi(t)|^2 dt \right]^2}, \quad (5.3.15)$$

and

$$\Gamma'(\boldsymbol{\rho}_1, \boldsymbol{\rho}_2, \boldsymbol{\rho}_3, \boldsymbol{\rho}_4) = \exp \left[-\frac{|\boldsymbol{\rho}_1|^2 + |\boldsymbol{\rho}_2|^2 + |\boldsymbol{\rho}_3|^2 + |\boldsymbol{\rho}_4|^2}{w_g^2} - \frac{|\boldsymbol{\rho}_1 - \boldsymbol{\rho}_2 + \boldsymbol{\rho}_3 - \boldsymbol{\rho}_4|^2}{\rho_g^2} - \frac{jk}{2R_g} (|\boldsymbol{\rho}_1|^2 - |\boldsymbol{\rho}_2|^2 + |\boldsymbol{\rho}_3|^2 - |\boldsymbol{\rho}_4|^2) \right]. \quad (5.3.16)$$

This demonstrates that the only difference in the fourth-order coherence function between a Gbur field and a fully developed speckle field is the additional term of $\epsilon \Gamma'(\boldsymbol{\rho}_1, \boldsymbol{\rho}_2, \boldsymbol{\rho}_3, \boldsymbol{\rho}_4)$. For a given pulse shape, ϵ is dependent on the pulse rate, so the higher the pulse rate, the smaller the ϵ , and the closer the Gbur fields resemble fully developed speckle fields.

Inserting Eq. (5.3.14) into Eq. (5.3.2), $\langle \eta^2 \rangle$ for the Gbur fields can be expressed in terms of the integrals of Eqs. (A.1)–(A.4) as

$$\langle \eta^2 \rangle = \frac{\epsilon \text{Int}_4 + 2\text{Int}_1^2}{(\epsilon + 1)\text{Int}_2^2 + \text{Int}_3}, \quad (5.3.17)$$

while $\tilde{\sigma}_\eta^2$ becomes

$$\tilde{\sigma}_\eta^2 = \frac{[\epsilon (\text{Int}_4/\text{Int}_1^2 - 1) + 1] \text{Int}_2^2 - \text{Int}_3}{(\epsilon + 1)\text{Int}_2^2 + \text{Int}_3}. \quad (5.3.18)$$

The complexity of Int_4 makes it non-amenable to either numerical or exact analytical evaluation using the “hard” aperture pupil function of Eq. (5.2.12). However, it can be evaluated using the Gaussian “soft” aperture approximation of Eq. (5.2.14). While the general expression for $\tilde{\sigma}_\eta^2$ using Eqs. (A.19)–(A.22) is extremely complex, it can be simplified considerably when the beam is collimated where $R_g = \infty$. In this case, $\tilde{\sigma}_\eta^2$ can be reduced to

$$\tilde{\sigma}_\eta^2 = \frac{2\epsilon \left(\frac{D}{2\rho_g}\right)^4 \left[\left(\frac{D}{2w_g}\right)^2 + 2\left(\frac{D}{2\rho_g}\right)^2 + 1 \right] + \left(\frac{D}{2\rho_g}\right)^2}{\frac{\epsilon}{2} \left[\left(\frac{D}{2w_g}\right)^2 + 2\left(\frac{D}{2\rho_g}\right)^2 + 1 \right] + \left(\frac{D}{2w_g}\right)^2 + \left(\frac{D}{2\rho_g}\right)^2 + 1} \cdot \frac{\left[\left(\frac{D}{2w_g}\right)^2 + 4\left(\frac{D}{2\rho_g}\right)^2 + A^2 + 2 \right] \left[\left(\frac{D}{2w_g}\right)^2 + A^2 + 2 \right]}{\left[\left(\frac{D}{2w_g}\right)^2 + 4\left(\frac{D}{2\rho_g}\right)^2 + A^2 + 2 \right] \left[\left(\frac{D}{2w_g}\right)^2 + A^2 + 2 \right]} \quad (5.3.19)$$

The limit of the ratio for small $D/(2\rho_g)$ between Eqs. (5.3.9) and (5.3.19) is found to be $1 + \epsilon/2$. However, when $D/(2\rho_g)$ is large, Eq. (5.3.19) increases as the square of $D/(2\rho_g)$. This means as long as ϵ and $D/(2\rho_g)$ are sufficiently small, the Γ' term in Eq. (5.3.14) is negligible and the Gbur field can be considered to have fully developed speckle. But for sufficiently large $D/(2\rho_g)$, the Γ' term will begin to dominate. This suggests three regions that require matching when compensating for the approximations used to derive Eq. (5.3.19). In the first region where $D/(2\rho_g) < 0.1$, multiplying Eq. (5.3.19) by Eq. (5.3.11) should suffice. In the second region of $0.1 < D/(2\rho_g) < 10$, errors due to the statistical approximation similar to approximation #1 should dominate. Compensation for this approximation can only be evaluated empirically. In the final region of $D/(2\rho_g) > 10$, errors due to the Gaussian “soft” aperture approximation used to evaluate Int_4 dominate. Compensation for this region can be either derived by numerical evaluation of Int_4 or through computer simulation.

To evaluate the accuracy of Eq. (5.3.19), simulations as described in Sec. 5.2.3.2

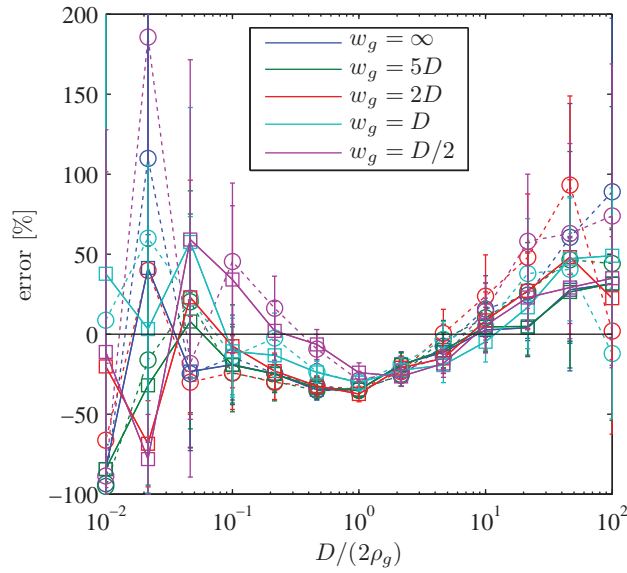


Figure 18. Difference between simulation data and the algebraic approximation for the normalized coupling efficiency variance when the fields are well-speckled with differing values of the average beam radius w_g , coherence radius ρ_g , $R_g = \infty$, and two pulse rates. The error is referenced to Eq. (5.3.19). The simulation results that used an average pulse rate of one pulse per cycle are indicated by circles and connected with dotted lines. The simulation results that used an average pulse rate of five pulses per cycle are indicated by squares and connect by solid lines. Error bars represent two std and were empirically derived from the data.

were run using a pulse rate of one pulse per cycle (228 THz) with $\epsilon = 0.015$, and five pulses per cycle (1140 THz) with $\epsilon = 0.003$. The difference between the simulation-derived normalized variance, where the square of the appropriately compensated Eq. (5.2.15) was used to normalize the data, and Eq. (5.3.19) is displayed in terms of percent error in Fig. 18. Error bars represent two std and were empirically derived from the data by observing the dependence of the std on the number of sample points used. While Fig. 18 clearly demonstrates the effect of the statistical approximation when $0.1 < D/(2\rho_g) < 10$, the simulations do not adequately elucidate the effects of the errors in the other two regions. Since the std of the data decreases as the number of samples increases, additional simulation runs would be needed to better evaluate the effect of the errors in these regions.

Despite its shortcomings, the present data suggest a simple nominal compensation function given by

$$\sigma_{n,\text{fit}}^2 = 0.18 \left| \ln \frac{D}{2\rho_g} \right| + 0.65. \quad (5.3.20)$$

While this compensation works best in the range of values $1 < D/(2\rho_g) < 10$ where the discrepancy is generally kept to within 10% of the estimated value, 70% of all the simulation data points now fall within 20% of the estimated value. The effect of this compensation on the variance is shown in Fig. 19 for two values of w_g and two different pulse rates. As expected, Γ' primarily affects values of $D/(2\rho_g) > 10$, while Eq. (5.3.20) adequately compensates the effect of the statistical approximation in the region of $0.1 < D/(2\rho_g) < 10$. The biggest shortcoming of Eq. (5.3.20) is in the region $D/(2\rho_g) < 0.1$ where the compensated algebraic approximation fails to converge with the analytic solution as desired, and Eq. (5.3.11) should instead be used.

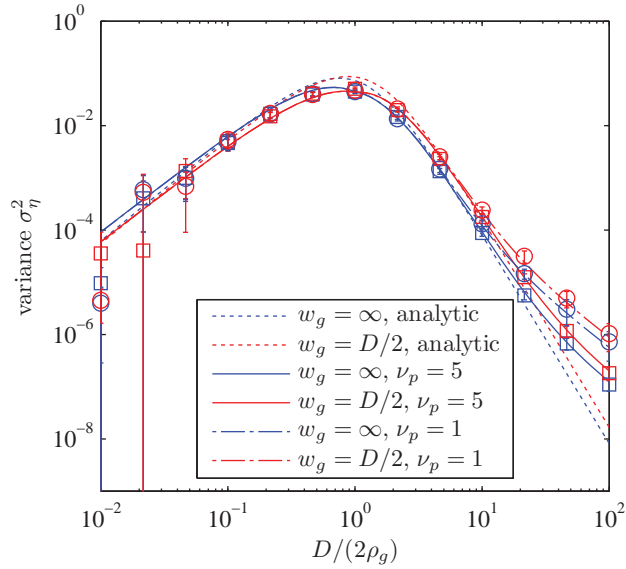


Figure 19. The effect of compensation given by Eq. (5.3.20) on the algebraic approximation of Eq. (5.3.19) for the coupling variance of fields generated using the Gbur method with differing values of the average beam radius w_g , coherence radius ρ_g , $R_g = \infty$, and two pulse rates. A plot of the analytic expression for the variance given by Eq. (5.3.8) and multiplied by the square of the appropriately compensated Eq. (5.2.15) is included for comparison. The simulation results that used an average pulse rate of one pulse per cycle are indicated by circles. The simulation results that used an average pulse rate of five pulses per cycle are indicated by squares. Error bars represent two std and were empirically derived from the data.

5.3.2.2 Coupling Variance of Non-speckled Beams.

The other fields of interest are where there is very little to no speckle in the beam. Since all the randomness is found in the phase of the beam, the fourth-order coherence function is derived by evaluating

$$\Gamma(\boldsymbol{\rho}_1, \boldsymbol{\rho}_2, \boldsymbol{\rho}_3, \boldsymbol{\rho}_4) = \exp \left[-\frac{|\boldsymbol{\rho}_1|^2 + |\boldsymbol{\rho}_2|^2 + |\boldsymbol{\rho}_3|^2 + |\boldsymbol{\rho}_4|^2}{w_g^2} - \frac{jk}{2R_g} (|\boldsymbol{\rho}_1|^2 - |\boldsymbol{\rho}_2|^2 + |\boldsymbol{\rho}_3|^2 - |\boldsymbol{\rho}_4|^2) \right] \times \langle \exp \{j[S(\boldsymbol{\rho}_1) - S(\boldsymbol{\rho}_2) + S(\boldsymbol{\rho}_3) - S(\boldsymbol{\rho}_4)]\} \rangle, \quad (5.3.21)$$

where $S(\boldsymbol{\rho})$ is the stochastic part of the field phase function. This ensemble average can be estimated through the method of cumulants to the second order [62]. By this method

$$\langle \exp(\psi) \rangle \simeq \exp \left[\langle \psi \rangle + \frac{1}{2} (\langle \psi^2 \rangle - \langle \psi \rangle^2) \right], \quad (5.3.22)$$

where the expression becomes an equality when ψ is Gaussian. Assuming $\langle S(\boldsymbol{\rho}) \rangle = 0$, the ensemble average becomes

$$\begin{aligned} \langle \exp \{j[S(\boldsymbol{\rho}_1) - S(\boldsymbol{\rho}_2) + S(\boldsymbol{\rho}_3) - S(\boldsymbol{\rho}_4)]\} \rangle &\simeq \exp \left\{ -\frac{1}{2} \langle [S(\boldsymbol{\rho}_1) - S(\boldsymbol{\rho}_2) + S(\boldsymbol{\rho}_3) - S(\boldsymbol{\rho}_4)]^2 \rangle \right\} \\ &= \exp \left\{ -\Gamma_S(0, 0) \left[2 - \tilde{\Gamma}_S(\boldsymbol{\rho}_1, \boldsymbol{\rho}_2) + \tilde{\Gamma}_S(\boldsymbol{\rho}_1, \boldsymbol{\rho}_3) - \tilde{\Gamma}_S(\boldsymbol{\rho}_1, \boldsymbol{\rho}_4) - \tilde{\Gamma}_S(\boldsymbol{\rho}_2, \boldsymbol{\rho}_3) + \tilde{\Gamma}_S(\boldsymbol{\rho}_2, \boldsymbol{\rho}_4) - \tilde{\Gamma}_S(\boldsymbol{\rho}_3, \boldsymbol{\rho}_4) \right] \right\}, \quad (5.3.23) \end{aligned}$$

where $\tilde{\Gamma}_S(\boldsymbol{\rho}_1, \boldsymbol{\rho}_2) = \Gamma_S(\boldsymbol{\rho}_1, \boldsymbol{\rho}_2)/\Gamma_S(0, 0)$ and statistical homogeneity is assumed. As long as $\Gamma_S(0, 0) \gg 1$ and $\tilde{\Gamma}_S(\boldsymbol{\rho}_1, \boldsymbol{\rho}_2) = \exp(-|\boldsymbol{\rho}_1 - \boldsymbol{\rho}_2|^2/\sigma_S^2) \approx 1 - |\boldsymbol{\rho}_1 - \boldsymbol{\rho}_2|^2/\sigma_S^2$,

then Eq. (5.3.23) can be expressed as

$$\begin{aligned} \langle \exp\{j[S(\boldsymbol{\rho}_1) - S(\boldsymbol{\rho}_2) + S(\boldsymbol{\rho}_3) - S(\boldsymbol{\rho}_4)]\} \rangle \simeq \\ \exp \left[- \left(|\boldsymbol{\rho}_1 - \boldsymbol{\rho}_2|^2 - |\boldsymbol{\rho}_1 - \boldsymbol{\rho}_3|^2 + |\boldsymbol{\rho}_1 - \boldsymbol{\rho}_4|^2 \right. \right. \\ \left. \left. + |\boldsymbol{\rho}_2 - \boldsymbol{\rho}_3|^2 - |\boldsymbol{\rho}_2 - \boldsymbol{\rho}_4|^2 + |\boldsymbol{\rho}_3 - \boldsymbol{\rho}_4|^2 \right) / \rho_g^2 \right], \end{aligned} \quad (5.3.24)$$

where $\rho_g = \sigma_S^2 / \Gamma_S(0, 0)$. By recognizing

$$\begin{aligned} |\boldsymbol{\rho}_1 - \boldsymbol{\rho}_2 + \boldsymbol{\rho}_3 - \boldsymbol{\rho}_4|^2 = |\boldsymbol{\rho}_1 - \boldsymbol{\rho}_2|^2 - |\boldsymbol{\rho}_1 - \boldsymbol{\rho}_3|^2 + |\boldsymbol{\rho}_1 - \boldsymbol{\rho}_4|^2 \\ + |\boldsymbol{\rho}_2 - \boldsymbol{\rho}_3|^2 - |\boldsymbol{\rho}_2 - \boldsymbol{\rho}_4|^2 + |\boldsymbol{\rho}_3 - \boldsymbol{\rho}_4|^2, \end{aligned} \quad (5.3.25)$$

it is plain to see that the fourth-order coherence function of these non-speckle fields is the same as $\Gamma'(\boldsymbol{\rho}_1, \boldsymbol{\rho}_2, \boldsymbol{\rho}_3, \boldsymbol{\rho}_4)$ given in Eq. (5.3.16).

In terms of the integrals given in Eqs. (A.1)–(A.4), the normalized variance of non-speckled beams becomes

$$\tilde{\sigma}_\eta^2 = \frac{\text{Int}_4}{\text{Int}_1^2} - 1. \quad (5.3.26)$$

While the algebraic expression resulting from the use of Eqs. (A.19)–(A.22) is complicated in general, it can be simplified considerably for a collimated beam. In this case, it reduces to

$$\tilde{\sigma}_\eta^2 = \frac{4 \left(\frac{D}{2\rho_g} \right)^4}{\left[\left(\frac{D}{2w_g} \right)^2 + A^2 + 2 \right] \left[\left(\frac{D}{2w_g} \right)^2 + 4 \left(\frac{D}{2\rho_g} \right)^2 + A^2 + 2 \right]}. \quad (5.3.27)$$

As was the case for speckled beams, the accuracy of Eq. (5.3.27) was investigated through the use of computer simulations. Fields were generated using the method described by Xiao and Voelz [99] and summarized here. In this process, an array

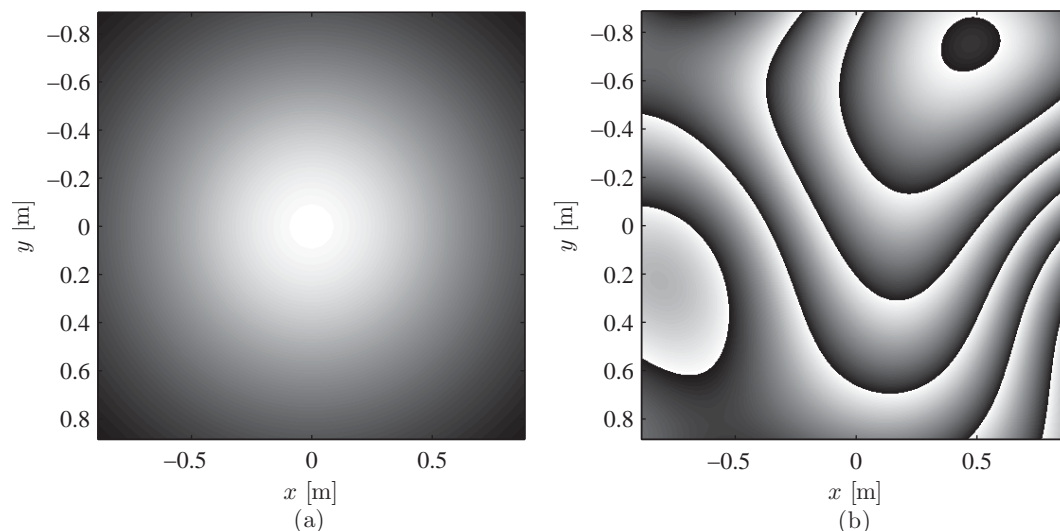


Figure 20. A realization of a field with all the randomness located in the phase. Image (a) contains the field amplitude which has a beam radius w_g of 75 cm. Image (b) contains the random field phase wrapped between $-\pi$ (black) and π (white) radians. The overall coherence radius of this field is 10 cm.

of zero-mean Gaussian random values with std of σ_r were convolved with a 2-D zero-mean Gaussian probability distribution function (pdf) with std of σ_f . The resulting array was used as the phase of a field with a Gaussian amplitude. As long as $\sigma_r^2/(4\pi\sigma_f^2) \gg 1$, the coherence function of the resulting field is very nearly Gaussian with a coherence radius $\rho_g = 4\pi^{1/2}\sigma_f^2/\sigma_r$. This method differed from that of Xiao and Voelz in that these fields were not propagated to the receiver, but directly used in the coupling efficiency calculation. This allowed us to simulate fields of arbitrary beam size. One drawback of this method is that the coherence radius is severely limited by σ_f which can be no larger than about half the grid size. To get around this problem, random subharmonics were added to the frequency spectrum of the phase screens in a manner similar to that described by Lane *et al.* [51] With a sufficient number of subharmonics, fields with any desired coherence radius can be generated. An example of the amplitude and phase of a field generated with this method using Listing C.9 is shown in Fig. 20.

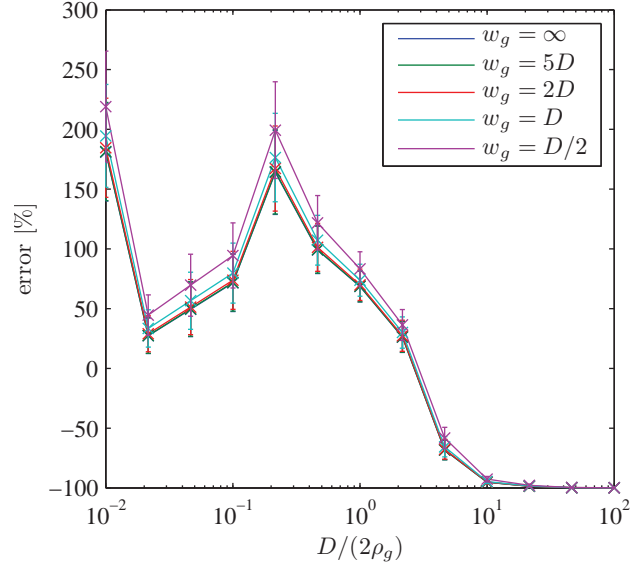


Figure 21. Difference between simulation data and the algebraic approximation for the normalized coupling efficiency variance of non-speckled fields with differing values of the average beam radius w_g , coherence radius ρ_g , and $R_g = \infty$. The simulation data was normalized by the square of the numerical evaluation of Eq. (5.2.1) using the exact back-propagated fiber mode given by Eq. (5.2.4). The error is referenced to Eq. (5.3.27). Error bars represent two std and were empirically derived from the data.

The observed discrepancy between Eq. (5.3.27) and the results from the simulation runs are displayed in Fig. 21 for several values of w_g in terms of percent error. The simulation data were normalized using the square of the numerically derived mean coupling efficiency with the exact fiber mode. When $D/(2\rho_g) < 2$, the predicted value is about half the simulation result. However, for $D/(2\rho_g) > 2$ the difference between the analytic expression and the simulations continuously diverges. The major cause of this divergence can be seen in the form of Eq. (5.3.27). As ρ_g tends toward zero, $\tilde{\sigma}_\eta^2$ should tend toward one [75, 79], but Eq. (5.3.27) instead tends toward infinity. Evidently, using the method of cumulants to only the second order is insufficient to accurately represent the fourth-order MCF at small coherence sizes. While this problem could be addressed by using the method of cumulants to the fourth order, the mathematics involved quickly becomes quite daunting. An alternative method is

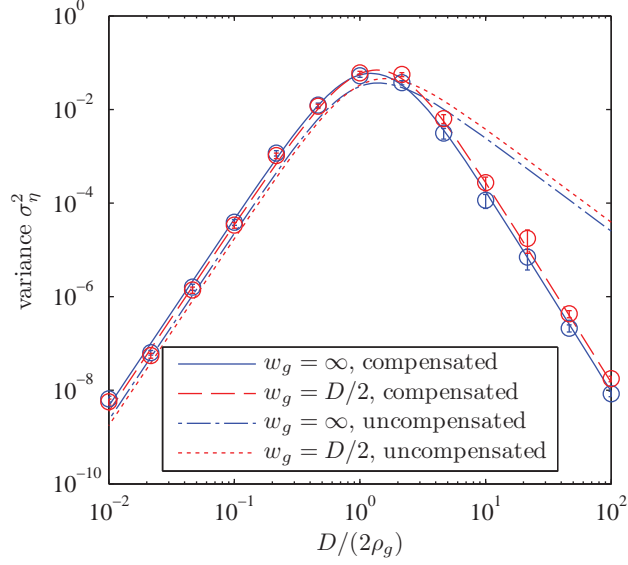


Figure 22. The effect of compensation given by Eq. (5.3.28) on the algebraic approximation of Eq. (5.3.27) for the coupling variance of non-speckled fields with differing values of the average beam radius w_g , coherence radius ρ_g , and $R_g = \infty$. Simulation results are indicated by circles. Error bars represent two std and were empirically derived from the data.

to empirically adjust the expression. One suggested adjustment is given by

$$\sigma_{\eta,\text{fit}}^2 = \frac{15}{7.5 + \left(\frac{D}{2\rho_g}\right)^{2.3}}. \quad (5.3.28)$$

The effect of multiplying Eq. (5.3.27) by Eq. (5.3.28) along with the square of the optimally compensated Eq. (5.2.15) is shown in Fig. 22. With compensation, the simulation results now tend to fall within 40% the predicted value, with more than half falling within 20%.

5.4 Conclusion

In this work, analytic expressions for both the coupling efficiency mean and variance for GSM beams into single-mode optical fibers have been derived and evaluated. These expressions include both exact solutions to the relevant integral equations and

algebraic approximations. While several simplifying approximations were needed to derive these expressions, their effects on the accuracy of the expressions were evaluated through both numerical integration and Monte Carlo simulations. While the algebraic expressions initially demonstrated poor agreement when compared to the numeric, analytic, or simulation results, compensation based on both asymptotic behavior and empirical computer simulation results was shown to greatly increase the concurrence. In the case of the mean coupling efficiency, errors as low as 0.8% were achieved over a wide range of coherence sizes and beam sizes. Even nominal compensation expressions were able to keep the accuracy of the mean coupling efficiency to within 5% over varying coherence sizes, beam sizes, and speckle content.

Different expressions for the mean squared normalized coupling efficiency variance were derived based on the speckle content of the field including fully developed speckle, well-developed speckle, and no speckle. With compensation, agreement between simulations and the analytic expression for well-developed speckle was generally better than 20%. At the other end of the speckle spectrum, compensation of the analytic expression for coupling efficiency variance of fields with no speckle content generally agreed with simulation results to better than 40%, with more than half of the results agreeing to better than 20%. While optimizing the compensation for specific beam parameters have the potential to further increase the accuracy, the main limiting factor in these accuracy values is the random nature of the computer simulation results. A greater number of simulation runs should further reduce the discrepancy spread and allow for more accurate compensation.

These results promise to be useful over a wide range of applications, including free-space optical communication, stellar interferometry, ladar/lidar, and wavefront sensing. They can aid in the characterization, performance modeling, and error analysis of optical systems that involve the coupling of random light into single-mode

optical fibers. This study enables further characterization of the effect of random light that falls between fully developed speckle and no speckle. The methods used in this chapter may also be used to derive expressions for the average coupling efficiency for partially coherent fields other than GSM beams, and also when multi-mode optical fibers are used.

VI. General SRI Noise Model

6.1 Introduction

While most wavefront sensors used in adaptive optics (AO) measure the phase gradient [63,64,98], or even phase Laplacian [71], of the incident field, the self-referencing interferometer (SRI) measures the incident field itself [65]. While any of these methods are sufficient when using AO with weak atmospheric turbulence where the distortions are mainly limited to the field phase, the situation is different in strong turbulence where the field manifests large distortions in both amplitude (known as scintillation) and phase. If the scintillation is large enough to occasionally make the field go to zero, the phase will exhibit branch points wherever the amplitude is zero, and $\pm 2\pi$ phase cuts connecting these branch points [31, 34]. These branch points and cuts in the field phase are due to a rotational component of the phase gradient that is lost when standard least-squares techniques are used to reconstruct the field phase, and therefore AO performance is severely degraded with increasing scintillation. Even when using reconstructors that account for the rotational part of the phase gradient [33], AO performance had been shown to still degrade with increasing scintillation, even in the absence of additive measurement noise [3–5].

Since the SRI measures the field directly, the phase can be calculated from these measurements without the need for phase reconstruction. In the absence of measurement noise, this phase calculation is insensitive to scintillation and depends only on the spatial and temporal averaging used in the field estimation measurement [5,6,65]. This makes the SRI a better choice in an adaptive optics system when scintillation may be an issue. While the SRI is immune to scintillation in theory, such is not the case in practice. Experiments using an SRI, or its predecessor the phase shifting point-diffraction interferometer, have demonstrated a decrease in performance as

scintillation increased [19,60]. This is attributed to the measurement noise that is inherent in any real system. As a result, measurement error must be taken into account in any true performance model of the SRI. The more accurate the performance model, the more useful it is in making performance trade-offs when designing a real AO system.

While a few SRI performance models have been published, they do not take into account all of the potential error sources. A noise model by Rhoadarmer and Barchers [66] takes into account shot noise, read noise, quantization noise, and amplified spontaneous emission (ASE) of the optical fiber, but neglects scintillation and the variability of optical fiber coupling efficiency. A different model by Ellis [25] accounts for shot noise and scintillation, but neglects all other noise sources. The intent of this chapter is to develop a more complete noise model that can account for all of the relevant noise sources. Section 6.2 presents an overview of the workings of an SRI, and defines the relevant parameters. A noise model of the SRI, defined in terms of phase error variance, is then derived in Sec. 6.3. As this noise model strongly depends on the probability distribution function (pdf) of some of the noise sources, specific examples are given for both weak and strong variations. These noise models are then validated through the use of Monte Carlo simulation runs in Sec. 6.4, and examples of its use are given in Sec. 6.5. Concluding remarks are given in Sec. 6.6.

6.2 SRI Overview

A conceptual diagram of an SRI is shown in Fig. 23. This configuration makes use of four-bin phase shifting interferometry (PSI) to make the phase measurement [56]. While the phase shifting can be performed spatially, temporally, or mixed, the spatial configuration shown in Fig. 23 results in smaller error in dynamic situations [19,67], and forms the basis of analysis for this chapter. The input field is first split between

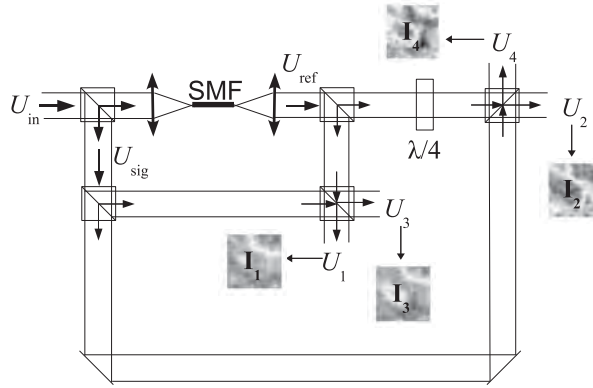


Figure 23. Conceptual diagram of a SRI using spatial 4-bin PSI. From Fig. 32 of [25].

a signal leg and a reference leg. The field in the signal leg can be represented as

$$U_{\text{sig}}(\boldsymbol{\rho}, t) = \sqrt{\beta}U_{\text{in}}(\boldsymbol{\rho}, t), \quad (6.2.1)$$

where $\boldsymbol{\rho}$ is two-dimensional coordinate vector perpendicular to the direction of propagation, t is the temporal coordinate, and β represents the proportion of the input power allocated by the first beam splitter to the signal leg. The light in the reference leg is then coupled into a single-mode optical fiber, which only passes the LP_{01} mode of the incident field. Once this reference field has been collimated by the fiber output lens (assumed to be identical to the fiber input lens), it can be represented as

$$U_{\text{ref}}(\boldsymbol{\rho}, t) = \sqrt{1 - \beta}b_0(t)\mathcal{M}_0(\boldsymbol{\rho}), \quad (6.2.2)$$

where $b_0(t)$ is the fiber coupling coefficient defined as

$$b_0(t) = \iint_{\mathcal{A}_{\mathcal{P}}} U_{\text{in}}(\boldsymbol{\rho}, t)\mathcal{M}_0^*(\boldsymbol{\rho}) d^2\boldsymbol{\rho}, \quad (6.2.3)$$

where $\mathcal{A}_{\mathcal{P}}$ is the area over the fiber coupling lens, and $\mathcal{M}_0(\boldsymbol{\rho})$ is the back-propagated LP_{01} fiber mode given by Eq. (5.2.4). The remaining 50% beam splitters and the

quarter wave plate are intended to produce $\pi/2$ phase shifts between the four different interference paths. The resulting field intensity over each of the four detectors can then be represented as

$$\begin{aligned}
I_n(\boldsymbol{\rho}, t) &= \frac{1}{4} |U_{\text{sig}}(\boldsymbol{\rho}, t) + U_{\text{ref}}(\boldsymbol{\rho}, t) \exp[-j(n-1)\pi/2]|^2 \\
&= \frac{1}{4} \left\{ \beta I_{\text{in}}(\boldsymbol{\rho}, t) + (1-\beta) |b_0(t)|^2 \mathcal{M}_0^2(\boldsymbol{\rho}) + 2\sqrt{\beta(1-\beta)} I_{\text{in}}(\boldsymbol{\rho}, t) |b_0(t)| \mathcal{M}_0(\boldsymbol{\rho}) \right. \\
&\quad \left. \times \cos[\phi_{\text{in}}(\boldsymbol{\rho}, t) - \phi_b(t) + (n-1)\pi/2] \right\}, \tag{6.2.4}
\end{aligned}$$

where $n \in \{1, 2, 3, 4\}$, $I_{\text{in}} = |U_{\text{in}}|^2$, $\phi_{\text{in}} = \arg\{U_{\text{in}}\}$, and $\phi_b = \arg\{b_0\}$. An example of the instantaneous intensity over each detector is shown in Fig. 24. As the $\pi/2$ phase shifts turn the cos in Eq. (6.2.4) to $\pm \cos$ and $\pm \sin$, the input field U_{in} can be recovered to within an unimportant phase piston term with

$$\hat{U}_{\text{in}}(\boldsymbol{\rho}, t) = \frac{[I_1(\boldsymbol{\rho}, t) - I_3(\boldsymbol{\rho}, t)] + j[I_4(\boldsymbol{\rho}, t) - I_2(\boldsymbol{\rho}, t)]}{\sqrt{\beta(1-\beta)} |b_0(t)| \mathcal{M}_0(\boldsymbol{\rho})}. \tag{6.2.5}$$

The phase of \hat{U}_{in} is then derived using

$$\hat{\phi}(\boldsymbol{\rho}, t) = \arctan \left(\frac{\text{Im}\{\hat{U}_{\text{in}}(\boldsymbol{\rho}, t)\}}{\text{Re}\{\hat{U}_{\text{in}}(\boldsymbol{\rho}, t)\}} \right). \tag{6.2.6}$$

In actuality, the detectors do not measure intensity, but photo-counts that have mean values proportional to the spatially and temporally integrated intensity over each detector pixel. Assuming a given incident field where the intensity changes little and the phase gradient is approximately constant over the spatial and temporal

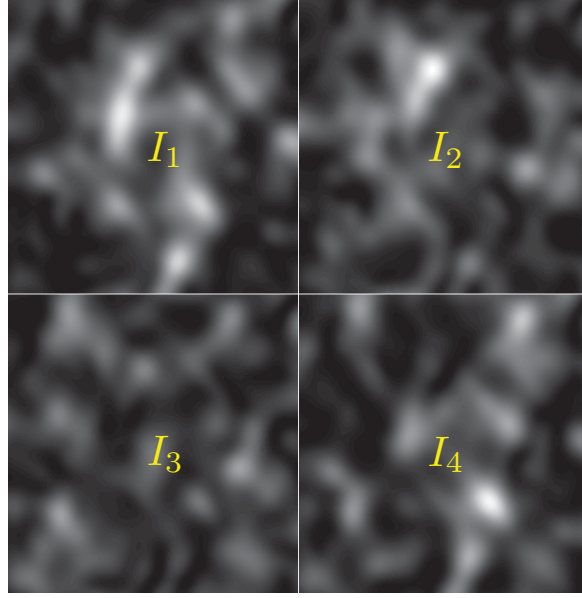


Figure 24. Example of the interference patterns that result from using an SRI with spatial 4-bin PSI

extents of the integration, the mean photo-counts can be expressed as

$$\begin{aligned}
 \langle K_n(\boldsymbol{\rho}_i, t_s) \rangle &= \alpha \int_{\tau_d} \iint_{\mathcal{A}_i} I_n(\boldsymbol{\rho}, t) d^2\boldsymbol{\rho} dt \\
 &\simeq \frac{\alpha d^2 \tau_d}{4} \left\{ \beta I_{\text{in}}(\boldsymbol{\rho}_i, t_s) + (1 - \beta) |b_0(t_s)|^2 \mathcal{M}_0^2(\boldsymbol{\rho}_i) + 2\sqrt{\beta(1 - \beta)} I_{\text{in}}(\boldsymbol{\rho}_i, t_s) \right. \\
 &\quad \times |b_0(t_s)| \mathcal{M}_0(\boldsymbol{\rho}_i) \text{sinc}\left(\frac{\Delta\phi_{x_i}}{2\pi}\right) \text{sinc}\left(\frac{\Delta\phi_{y_i}}{2\pi}\right) \text{sinc}\left(\frac{\Delta\phi_{t_i}}{2\pi}\right) \\
 &\quad \left. \times \cos\left[\phi(\boldsymbol{\rho}_i, t_s) + (n - 1)\frac{\pi}{2}\right] \right\}, \tag{6.2.7}
 \end{aligned}$$

where $\langle \cdot \rangle$ represents ensemble averaging, $\boldsymbol{\rho}_i$ is the location of the i th detector pixel, t_s is the sample time, $\alpha = \eta_q \bar{\lambda} / (hc)$ is the proportionality constant, η_q is the detector quantum efficiency, $\bar{\lambda}$ is the central wavelength of the incident light (assumed quasi-monochromatic), $h = 6.626 \times 10^{-34}$ J-s is Planck's constant, $c = 2.998 \times 10^8$ m/s is the speed of light, τ_d is the detector integration time, \mathcal{A}_i is the area over the i th detector pixel of width d , $\text{sinc}(x) = \sin(\pi x) / (\pi x)$, $\Delta\phi$ is the change in phase over the spatial and temporal extents of the integrations, and ϕ is the spatial and temporal

average phase over the each pixel. Samples of the incident field can be estimated from these photo-counts to within a scaling factor that depends on the pixel location with

$$\hat{U}_{\text{in}}(\boldsymbol{\rho}_i, t_s) = [K_1(\boldsymbol{\rho}_i, t_s) - K_3(\boldsymbol{\rho}_i, t_s)] + j [K_4(\boldsymbol{\rho}_i, t_s) - K_2(\boldsymbol{\rho}_i, t_s)], \quad (6.2.8)$$

while the phase measurement is

$$\hat{\phi}(\boldsymbol{\rho}_i, t_s) = \arctan \left\{ \frac{\text{Im} [\hat{U}_{\text{in}}(\boldsymbol{\rho}_i, t_s)]}{\text{Re} [\hat{U}_{\text{in}}(\boldsymbol{\rho}_i, t_s)]} \right\}. \quad (6.2.9)$$

6.3 Phase Error Variance

In the absence of noise, the phase estimate given by Eq. (6.2.9) would be precisely equal to $\phi(\boldsymbol{\rho}_i, t_s)$. However, noise is inescapable due not only to the fact the photo-counts K_n must be integer values, but also for a given input they are Poisson distributed [38]. These photo-counts are additionally stochastic in that I_{in} , b_0 , and $\nabla\phi$ are all random, so the expected number of photo-counts is also random. Beyond the randomness due to the photo-counts themselves, there will be additional noise sources such as those caused by the electrical amplification of the photo-counts (read noise) and the assigning of the output value to a digitized bin (quantization noise). All of these noise sources play into the overall accuracy of the SRI measurement, and must be accounted for when predicting SRI performance for a given situation. Since the SRI measurements are typically used to drive a single deformable mirror, understanding the phase error variance is necessary to estimate overall system performance [73].

The purpose of this section is to derive a general expression for the phase error variance of an SRI. This is accomplished by first deriving an expression for the phase

error variance conditioned on a given input, then averaging over the random variables that comprise this expression. As there is a significant difference between when the variations are large as opposed to small, both of these cases will be analyzed. Specific examples are then given for conditions that may be expected in practice.

6.3.1 Conditioned Phase Error Variance.

The phase estimate error is defined as

$$\varepsilon(\boldsymbol{\rho}_i, t_s) = \hat{\phi}(\boldsymbol{\rho}_i, t_s) - \phi(\boldsymbol{\rho}_i, t_s), \quad (6.3.1)$$

and can be found using Eq. (6.2.9) by first multiplying Eq. (6.2.8) by $\exp[-j\phi(\boldsymbol{\rho}_i, t_s)]$. The size of the error depends largely on total number of photo-counts accumulated across all four PSI bins. When there are a large number of total photo-counts, Eq. (6.2.8) has a large number of degrees of freedom, and therefore should make a good estimate of the incident field. In this case, the phase error variance should be relatively low. However, when there are a low number of total photo-counts, there is only a limited number of degrees of freedom for the field estimate, so the phase error variance should be much larger. In the limit of zero total photo-counts, the arctan function is typically set to return a value of zero regardless of true phase value. Since the true phase value can take on any value between $-\pi$ and π with equal probability, the phase error variance in this case is simply given by

$$\sigma_\varepsilon^2 \simeq \frac{\pi^2}{3}. \quad (6.3.2)$$

The phase error variance can be estimated for a large number of total photo-counts

using the Delta Method given by

$$\text{Var}[f(\mathbf{X})] \simeq \sum_i \left[\frac{\partial f(\langle \mathbf{X} \rangle)}{\partial X_i} \right]^2 \text{Var}[X_i] + \sum_i \sum_{j \neq i} \left[\frac{\partial f(\langle \mathbf{X} \rangle)}{\partial X_i} \right] \left[\frac{\partial f(\langle \mathbf{X} \rangle)}{\partial X_j} \right] \text{Cov}[X_i X_j], \quad (6.3.3)$$

where $f(\mathbf{X})$ is an arbitrary smooth function of the random vector \mathbf{X} , $\text{Var}[\cdot]$ is the variance operator, and $\text{Cov}[\cdot]$ is the covariance operator [16]. From Eq. (6.2.9), $\hat{\phi}$ is a function of two random variables, the real part of the field estimate \hat{U}_R and the imaginary part of the field estimate \hat{U}_I . It is simple to show \hat{U}_R and \hat{U}_I are independent, and therefore uncorrelated, so the phase error variance can be estimated as

$$\sigma_\varepsilon^2 \simeq \left(\frac{\langle \hat{U}_I \rangle}{\langle \hat{U}_R \rangle^2 + \langle \hat{U}_I \rangle^2} \right)^2 \sigma_{\hat{U}_R}^2 + \left(\frac{\langle \hat{U}_R \rangle}{\langle \hat{U}_R \rangle^2 + \langle \hat{U}_I \rangle^2} \right)^2 \sigma_{\hat{U}_I}^2. \quad (6.3.4)$$

The phase error is zero mean, so the imaginary part of the field estimate should also be zero mean. Equation (6.3.4) therefore reduces to

$$\sigma_\varepsilon^2 \simeq \frac{\sigma_{\hat{U}_I}^2}{\langle \hat{U}_R \rangle^2}. \quad (6.3.5)$$

For a given input and neglecting other measurement noise, \hat{U}_R and \hat{U}_I are each the difference between two independent Poisson random variables. As such, they follow a Skellam distribution giving [81]

$$\langle \hat{U}_R \rangle = \langle K_1 \rangle - \langle K_3 \rangle, \quad (6.3.6)$$

$$\sigma_{\hat{U}_I}^2 = \langle K_2 \rangle + \langle K_4 \rangle. \quad (6.3.7)$$

Using Eq. (6.2.7), and inserting Eqs. (6.3.6) and (6.3.7) into Eq. (6.3.5) produces

$$\sigma_\varepsilon^2(\boldsymbol{\rho}_i, t_s) \simeq \frac{\alpha d^2 \tau_d}{2} [\beta I_{\text{in}}(\boldsymbol{\rho}_i, t_s) + (1 - \beta) |b_0(t_s)|^2 \mathcal{M}_0^2(\boldsymbol{\rho}_i)] \\ \left/ \left[\alpha^2 d^4 \tau_d^2 \beta (1 - \beta) I_{\text{in}}(\boldsymbol{\rho}_i, t_s) |b_0(t_s)|^2 \mathcal{M}_0(\boldsymbol{\rho}_i)^2 \right. \right. \\ \left. \left. \times \text{sinc}^2\left(\frac{\Delta\phi_{x_i}}{2\pi}\right) \text{sinc}^2\left(\frac{\Delta\phi_{y_i}}{2\pi}\right) \text{sinc}^2\left(\frac{\Delta\phi_{t_i}}{2\pi}\right) \right] \right. \quad (6.3.8)$$

By including the additional measurement noise and using

$$|b_0(t_s)|^2 = \eta(t_s) \iint_{\mathcal{A}_P} I_{\text{in}}(\boldsymbol{\rho}, t_s) d^2\boldsymbol{\rho}, \quad (6.3.9)$$

where $\eta(\cdot)$ is the instantaneous fiber coupling efficiency, Eq. (6.3.8) can be expressed as

$$\sigma_\varepsilon^2 \simeq \frac{\beta I_i + (1 - \beta) \eta_i \bar{I} + 2\sigma_{\text{meas}}^2 / (\alpha d^2 \tau_d)}{2\alpha d^2 \tau_d \beta (1 - \beta) I_i \eta_i \bar{I} \text{sinc}^2\left(\frac{\Delta\phi_{x_i}}{2\pi}\right) \text{sinc}^2\left(\frac{\Delta\phi_{y_i}}{2\pi}\right) \text{sinc}^2\left(\frac{\Delta\phi_{t_i}}{2\pi}\right)}, \quad (6.3.10)$$

where $I_i = I_{\text{in}}(\boldsymbol{\rho}_i, t_s)$, $\eta_i = \mathcal{A}_P \mathcal{M}_0^2(\boldsymbol{\rho}_i) \eta(t_s)$, $\bar{I} = \frac{1}{\mathcal{A}_P} \iint_{\mathcal{A}_P} I_{\text{in}}(\boldsymbol{\rho}, t_s) d^2\boldsymbol{\rho}$, and σ_{meas}^2 is the additional measurement error. Equation (6.3.10) gives the conditional error variance of the i th detector pixel, and is the basis of all further analysis. This expression can be identified with $1/SNR_M^2$, where SNR_M is defined by Rhoadarmer and Barchers [66, Eq. (17)]. While Rhoadarmer and Barchers use field Strehl as their performance metric instead of phase error variance, this shows that both are dependent on equivalent expressions for the signal-to-noise ratio.

6.3.2 Unconditioned Phase Error Variance.

While Eq. (6.3.10) may be sufficient when using an SRI to measure static aberrations, in many applications, such as AO, the incident field is dynamic so I_i , η_i , \bar{I} ,

and $\nabla\phi$ may be random to one extent or another. Since they may all be considered independent of each other, the unconditioned phase error variance may be found from Eq. (6.3.10) using the conditional variance identity which can be expressed as

$$\text{Var}[X] = \langle \text{Var}[X|Y] \rangle + \text{Var}[\langle X|Y \rangle], \quad (6.3.11)$$

where $X|Y$ means the random variable X is conditioned on the random variable Y [16]. The unconditioned phase error variance can therefore be found by averaging σ_ε^2 over the component random variables in turn. Since this averaging depends on the nature of the component random variables, it is necessary to analyze two different conditions. The first is when there is low probability of any of the random variables to result in near zero total photo-counts in the phase calculation. The second is when there is significant probability that one or more of the random variables may result in near zero photo-counts.

6.3.2.1 Small variations.

As long as the total number of photo-counts is sufficiently large, and there is little probability that the component random variables will cause the total number of photo-counts to fall to near zero, the σ_ε^2 for a given input is well approximated by Eq. (6.3.10). One example of this condition is when the SRI is used in a closed-loop AO system with weak atmospheric turbulence. While the exact distributions of I_i , η_i , \bar{I} , and $\nabla\phi$ may be unknown, the averaging over these random variables can be approximated using Taylor expansion about the mean. The two required Taylor expansions in this case are

$$\left\langle \frac{1}{X} \right\rangle \simeq \frac{1}{\langle X \rangle} (1 + \tilde{\sigma}_X^2), \quad (6.3.12)$$

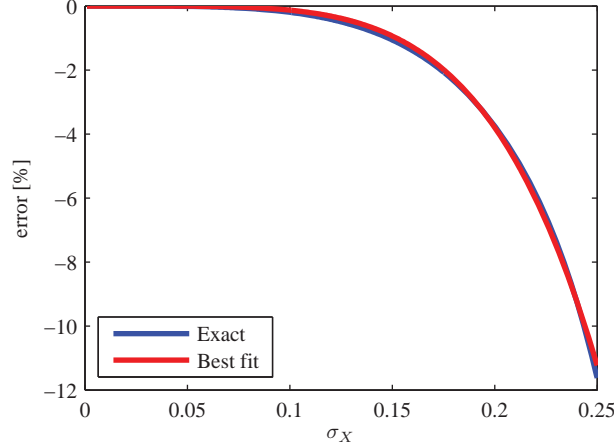


Figure 25. The error due to the approximation of Eq. (6.3.13) assuming a zero-mean Gaussian random variable

$$\left\langle \frac{1}{\text{sinc}^2(X)} \right\rangle \simeq 1 + \frac{\pi^2 \sigma_X^2}{3}, \quad (6.3.13)$$

where $\tilde{\sigma}_X^2 = \sigma_X^2 / \langle X \rangle^2$, and Eq. (6.3.13) assumes $\langle X \rangle = 0$. Using these approximations with Eq. (6.3.10) produces

$$\sigma_\varepsilon^2 \simeq \left[1 + \frac{\mathcal{D}_\phi(d)}{12} \right]^2 \left[1 + \frac{\mathcal{D}_t(\tau_d)}{12} \right] \left[\beta \langle I_i \rangle (1 + \tilde{\sigma}_{\eta_i}^2)(1 + \tilde{\sigma}_{\bar{I}}^2) + (1 - \beta) \langle \eta_i \rangle \langle \bar{I} \rangle (1 + \tilde{\sigma}_{I_i}^2) + \frac{2\sigma_{\text{meas}}^2(1 + \tilde{\sigma}_{\bar{I}}^2)(1 + \tilde{\sigma}_{\eta_i}^2)(1 + \tilde{\sigma}_{\bar{I}}^2)}{\alpha d^2 \tau_d} \right] / [2\alpha d^2 \tau_d \beta (1 - \beta) \langle I_i \rangle \langle \eta_i \rangle \langle \bar{I} \rangle], \quad (6.3.14)$$

where $\mathcal{D}_\phi(\cdot)$ and $\mathcal{D}_t(\cdot)$ are respectively the spatial and temporal phase structure functions of the incident field. Finding the overall phase error variance of the entire detector requires further integration over the values of $\langle I_i \rangle$ and $\langle \eta_i \rangle$.

Due to aperture averaging, the fluctuations of \bar{I} should always be small, so averaging over these fluctuations should always be well approximated by Eq. (6.3.12). However, the accuracy of the estimate given in Eq. (6.3.13) depends in large part on the pdf of X . Since the left side of the equation has a pole at every non-zero integer value of x , the pdf of X must be well contained within the range ± 1 , otherwise the small variations assumption will not apply. This condition can be analyzed by assum-

ing X is zero-mean Gaussian distributed, then setting any probability values outside $\pm 3.5\sigma_X$ to zero. Since 99.95% of the probability falls within $\pm 3.5\sigma_X$, disregarding everything outside this range only produces error on the order of 0.1%. Using this assumption, the error due to the approximation of Eq. (6.3.13) is displayed in Fig. 25. While the error is under 1% for $\sigma_X < 0.15$, it rapidly increases for $\sigma_X > 0.15$.

It is possible to compensate for this error by using a function that closely resembles the error. Figure 25 shows the best fit to $-100(b\sigma_X)^n$, where $b = 2.55$ and $n = 4.86$ were found using nonlinear least-squares techniques. Making use of this compensation, the approximation of Eq. (6.3.13) can be improved to

$$\left\langle \frac{1}{\text{sinc}^2(X)} \right\rangle \simeq \frac{1 + \pi^2 \sigma_X^2 / 3}{1 - (6.51 \sigma_X^2)^{2.43}}, \quad (6.3.15)$$

which is accurate to under 1% for $\sigma_X \leq 1/4$. Given $\sigma_X^2 = \mathcal{D}_\phi(d)/(4\pi^2)$, the constraint on σ_X becomes a constraint on the phase structure function of

$$\mathcal{D}_\phi(d) \leq \pi^2/4 \quad (6.3.16)$$

Assuming a typical spatial phase structure function given by $\mathcal{D}_\phi(d) = 6.88(d/r_0)^{5/3}$, where r_0 is the atmospheric coherence length defined by Eq. (2.4.41) [73], it becomes a constraint on the subaperture size as $d \leq 0.54r_0$. (A similar constraint applies to the temporal phase structure function.) This constraint is typically satisfied in practice, especially during closed-loop AO operation, so it does not unduly limit the applicability of this analysis. With this compensation, the expression for the phase

error variance assuming small variations becomes

$$\sigma_\varepsilon^2 \simeq \left[1 + \frac{\mathcal{D}_\phi(d)}{12} \right]^2 \left[1 + \frac{\mathcal{D}_t(\tau_d)}{12} \right] \left[\beta \langle I_i \rangle (1 + \tilde{\sigma}_{\eta_i}^2)(1 + \tilde{\sigma}_{\bar{I}}^2) + (1 - \beta) \langle \eta_i \rangle \langle \bar{I} \rangle (1 + \tilde{\sigma}_{I_i}^2) + \frac{2\sigma_{\text{meas}}^2(1 + \tilde{\sigma}_{I_i}^2)(1 + \tilde{\sigma}_{\eta_i}^2)(1 + \tilde{\sigma}_{\bar{I}}^2)}{\alpha d^2 \tau_d} \right] / \left(\left\{ 1 - \frac{[\mathcal{D}_\phi(d)]^{2.43}}{80} \right\}^2 \left\{ 1 - \frac{[\mathcal{D}_t(\tau_d)]^{2.43}}{80} \right\} \times 2\alpha d^2 \tau_d \beta (1 - \beta) \langle I_i \rangle \langle \eta_i \rangle \langle \bar{I} \rangle \right). \quad (6.3.17)$$

This is valid so long as $\nabla\phi$ is well approximated as being Gaussian distributed. It has been demonstrated that a Gaussian distribution for $\nabla\phi$ rests on a sound theoretical basis [96], so there is a good reason to believe this expression is valid subject to the constraints described above.

One interesting item of note is if X is a log-normally distributed, then Eq. (6.3.12) is not an approximation, but an exact expression. Since the intensity fluctuations due to weak atmospheric turbulence are well represented with a log-normal distribution [2], the expression given by Eq. (6.3.17) should be especially good when the I_i fluctuations are only caused by weak atmospheric turbulence.

6.3.2.2 Large variations.

While the small variations approximation of the previous section should always be sufficient for \bar{I} and $\nabla\phi$, subject to the condition that σ_ε^2 must always be $\leq \pi^2/3$, such is not necessarily the case with I_i and η_i . There are many conditions that would cause the pdf of I_i and/or η_i to have significant probability near zero (e.g., a negative exponential distribution) thereby invalidating the large total photo-count assumption. In these cases, averaging over these random variable must take into account those situations where σ_ε^2 is better approximated by Eq. (6.3.2) than Eq. (6.3.10).

If the SRI is used in a closed-loop AO system and the incident light displays

fully developed speckle, then η_i should exhibit small fluctuations while I_i obeys the negative exponentially distribution [40] given by

$$p_X(x) = \frac{1}{\langle X \rangle} \exp\left(-\frac{x}{\langle X \rangle}\right). \quad (6.3.18)$$

Once Eq. (6.3.10) has been averaged over η_i , \bar{I} , and $\nabla\phi$ as described in the previous section, it may be approximated as

$$\sigma_{\varepsilon|I_i}^2 \simeq \begin{cases} \frac{\pi^2}{3} & \text{if } I_i \leq \frac{c_I}{a_I - b_I} \text{ or } a_I \leq b_I, \\ \frac{\pi^2}{3} \left(\frac{b_I I_i + c_I}{a_I I_i}\right) & \text{otherwise,} \end{cases} \quad (6.3.19)$$

where

$$a_I = \left\{ 1 - \frac{[\mathcal{D}_\phi(d)]^{2.43}}{80} \right\}^2 \left\{ 1 - \frac{[\mathcal{D}_t(\tau_d)]^{2.43}}{80} \right\} \frac{2\pi^2}{3} d^2 \tau_d \alpha \beta (1 - \beta) \langle \eta_i \rangle \langle \bar{I} \rangle \quad (6.3.20)$$

$$b_I = \left[1 + \frac{\mathcal{D}_\phi(d)}{12} \right]^2 \left[1 + \frac{\mathcal{D}_t(\tau_d)}{12} \right] \beta (1 + \tilde{\sigma}_{\eta_i}^2) (1 + \tilde{\sigma}_{\bar{I}}^2) \quad (6.3.21)$$

$$c_I = \left[1 + \frac{\mathcal{D}_\phi(d)}{12} \right]^2 \left[1 + \frac{\mathcal{D}_t(\tau_d)}{12} \right] \left[(1 - \beta) \langle \eta_i \rangle \langle \bar{I} \rangle + \frac{2\sigma_{\text{meas}}^2 (1 + \tilde{\sigma}_{\eta_i}^2) (1 + \tilde{\sigma}_{\bar{I}}^2)}{\alpha d^2 \tau_d} \right]. \quad (6.3.22)$$

The unconditioned phase error variance is then evaluated as

$$\begin{aligned} \sigma_\varepsilon^2 &\simeq \int_0^\infty \sigma_{\varepsilon|I_i}^2 p_{I_i}(I_i) dI_i \\ &= \begin{cases} \frac{\pi^2}{3} & \text{if } a_I \leq b_I, \\ \frac{\pi^2}{3} \left\{ 1 - \left(1 - \frac{b_I}{a_I}\right) \exp\left[-\frac{c_I}{(a_I - b_I) \langle I_i \rangle}\right] \right. \\ \quad \left. + \frac{c_I}{a_I \langle I_i \rangle} E_1\left[\frac{c_I}{(a_I - b_I) \langle I_i \rangle}\right] \right\} & \text{otherwise,} \end{cases} \end{aligned} \quad (6.3.23)$$

where $E_1(\cdot)$ is the exponential integral defined as

$$E_1(x) = \int_x^\infty t^{-1} e^{-t} dt. \quad (6.3.24)$$

A similar calculation is used in the case where I_i has the small fluctuations (e.g., weak turbulence) while η_i is exponentially distributed (e.g., open-loop AO operation when the coherence area of the light is much smaller than the receiver area [91]). The expression for σ_ε^2 in this case, as well as for additional probability distributions of I_i and η_i , are found in Appendix B.

If both I_i and η_i exhibit negative exponential statistics, then the phase error variance must be explicitly integrated over both of their distribution functions. This situation might be expected when the SRI is used in an open-loop AO system when the incident light exhibits fully developed speckle. An expression for σ_ε^2 conditioned only on η_i for this case can be found directly from Eq. (6.3.23) by setting $\sigma_{\eta_i}^2$ to zero, and replacing $\langle \eta_i \rangle$ with η_i . Making these changes it can be expressed as

$$\sigma_{\varepsilon|\eta_i}^2 \simeq \begin{cases} \frac{\pi^2}{3} & \text{if } \eta_i \leq \frac{b_\eta}{a_\eta} \text{ or } a_\eta \leq b_\eta, \\ \frac{\pi^2}{3} \left[1 - \left(1 - \frac{b_\eta}{a_\eta \eta_i} \right) \exp \left(-\frac{c_\eta \eta_i + d_\eta}{a_\eta \eta_i - b_\eta} \right) \right. \\ \quad \left. + \frac{c_\eta \eta_i + d_\eta}{a_\eta \eta_i} E_1 \left(\frac{c_\eta \eta_i + d_\eta}{a_\eta \eta_i - b_\eta} \right) \right] & \text{otherwise,} \end{cases} \quad (6.3.25)$$

where

$$a_\eta = \left\{ 1 - \frac{[\mathcal{D}_\phi(d)]^{2.43}}{80} \right\}^2 \left\{ 1 - \frac{[\mathcal{D}_t(\tau_d)]^{2.43}}{80} \right\} \frac{2\pi^2}{3} d^2 \tau_d \alpha \beta (1 - \beta) \langle I_i \rangle \langle \bar{I} \rangle \quad (6.3.26)$$

$$b_\eta = \left[1 + \frac{\mathcal{D}_\phi(d)}{12} \right]^2 \left[1 + \frac{\mathcal{D}_t(\tau_d)}{12} \right] \beta \langle I_i \rangle (1 + \tilde{\sigma}_{\bar{I}}^2) \quad (6.3.27)$$

$$c_\eta = \left[1 + \frac{\mathcal{D}_\phi(d)}{12} \right]^2 \left[1 + \frac{\mathcal{D}_t(\tau_d)}{12} \right] (1 - \beta) \langle \bar{I} \rangle \quad (6.3.28)$$

$$d_\eta = \left[1 + \frac{\mathcal{D}_\phi(d)}{12} \right]^2 \left[1 + \frac{\mathcal{D}_t(\tau_d)}{12} \right] \frac{2\sigma_{\text{meas}}^2(1 + \tilde{\sigma}_I^2)}{\alpha d^2 \tau_d}. \quad (6.3.29)$$

Integrating this expression over the pdf of Eq. (6.3.18) produces

$$\sigma_\varepsilon^2 \simeq \begin{cases} \frac{\pi^2}{3} & \text{if } a_\eta \leq b_\eta, \\ \frac{\pi^2}{3} \left\{ 1 - \int_{b_\eta/a_\eta}^{\infty} \left[\left(1 - \frac{b_\eta}{a_\eta \eta_i} \right) \exp \left(-\frac{c_\eta \eta_i + d_\eta}{a_\eta \eta_i - b_\eta} \right) - \frac{c_\eta \eta_i + d_\eta}{a_\eta \eta_i} E_1 \left(\frac{c_\eta \eta_i + d_\eta}{a_\eta \eta_i - b_\eta} \right) \right] \frac{1}{\langle \eta_i \rangle} \exp \left(-\frac{\eta_i}{\langle \eta_i \rangle} \right) d\eta_i \right\} & \text{otherwise,} \end{cases} \quad (6.3.30)$$

where the remaining integral must be evaluated numerically.

6.4 Monte Carlo Simulations

The accuracy of the above phase error variance models were evaluated through Monte Carlo analysis. While these simulation runs were not intended to be exhaustive, they serve to validate the methodology used in Sec. 6.3. Further validation of these models may be accomplished through wave optics simulation runs.

The Monte Carlo runs were designed to only evaluate the effect of the randomness of I_i and η_i . Consequently, \bar{I} was set equal to $\langle I_i \rangle$ with zero variance, \mathcal{D}_ϕ and \mathcal{D}_t were set to 0, and σ_{meas}^2 was also set to 0. Setting \bar{I} to $\langle I_i \rangle$ with zero variance is similar to the situation where the average intensity is constant over the receiver, and the coherence area of the original incident light is much smaller than the receiver area. This results in many independent intensity values being used to calculate \bar{I} , thus making it a good approximation of $\langle I_i \rangle$. Since the variance of \bar{I} would be much less than 1, it would have an insignificant impact on σ_ε^2 . \mathcal{D}_ϕ and \mathcal{D}_t were set to zero since they do not impact the overall shape of σ_ε^2 curve, but only shift where it is located. The additive measurement noise was ignored to focus on the physics of the problem over the engineering. Furthermore, β was set to $\langle \eta_i \rangle / (1 + \langle \eta_i \rangle)$ to maximize fringe

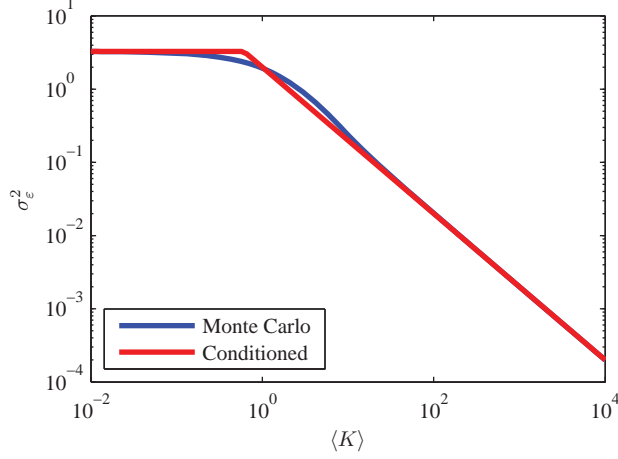


Figure 26. Comparison between Eq. (6.3.10) and Monte Carlo simulation runs for a static input.

visibility, and it was assumed $\mathcal{A}_p \mathcal{M}_0^2(\rho_i) = 1$ so $\eta_i = \eta(t_s)$. One million random draws of I_i , η_i , and ϕ were used for each data point, where I_i and η_i followed the desired distribution while ϕ was uniformly distributed between $-\pi$ and π .

A comparison between the conditioned phase error variance given by Eq. (6.3.10), and the results from the Monte Carlo runs is displayed in Fig. 26. In this plot, as well as all subsequent plots, $\langle K \rangle = \langle K_1 \rangle + \langle K_2 \rangle + \langle K_3 \rangle + \langle K_4 \rangle$. As expected, when there is a large number of total photo-counts, the model and the simulation runs demonstrate excellent agreement. Also, when there are very few total photo-counts, the simulations asymptote to $\pi^2/3$ as expected. The biggest discrepancies occur in the region where the two asymptotes intersect. With relatively few photo-counts, the model overestimates the true phase variance with a maximum discrepancy of 17.5% where the asymptotes intersect. Once the phase error variance model switches to Eq. (6.3.10), the model underestimates the Monte Carlo results by up to 15%, but then converges with the simulations to well within 1%.

An example of the unconditioned phase error variance where the small fluctuations assumption holds is displayed in Fig. 27. The conditioned phase error variance line from Fig. 26 is included as a basis for comparison. For these runs, the distribution

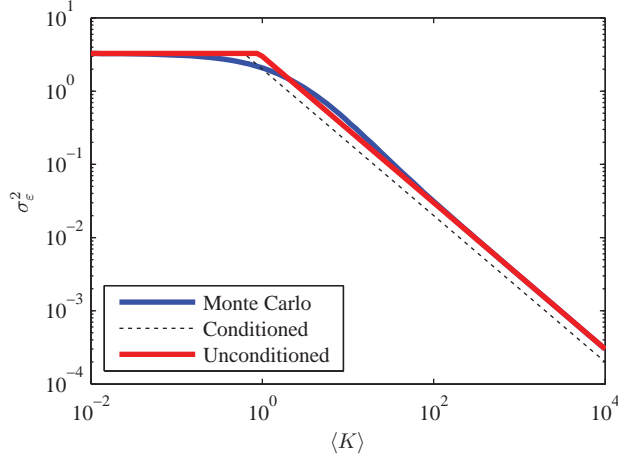


Figure 27. Comparison between Eq. (6.3.14) and Monte Carlo simulation runs for small variations of I_i and η_i .

for I_i was log-normal with a normalized variance of 1, and the distribution for η_i was a shifted exponential. Since the normalized variance for η_i was much less than 1, it had an insignificant effect of the overall results. This plot again demonstrates excellent agreement (less than 1% discrepancy) between the model and simulation in both of the asymptotic regimes, where the large asymptote is given by Eq. (6.3.17). At the point where the asymptotes intersect, the model overestimates the simulations by 22.5%, and then it underestimates the simulations by up to 12% at slightly higher total photo-counts.

Figure 28 displays the Monte Carlo simulation results when I_i follows a negative exponential distribution while the η_i variations remain small. The unconditioned variance is given by Eq. (6.3.23), and the conditioned variance line from Fig. 26 is included as a basis for comparison. There is good agreement over nearly the entire range of total photo-count values. The model overestimates the simulation results by a maximum of 11% and agrees to within 5% at larger total photo-count levels. Both the model and the simulations indicate the large increase in phase error variance due to the significant probability of receiving little to no photo-counts in a given subaperture, regardless of the expected total number of photo-counts.

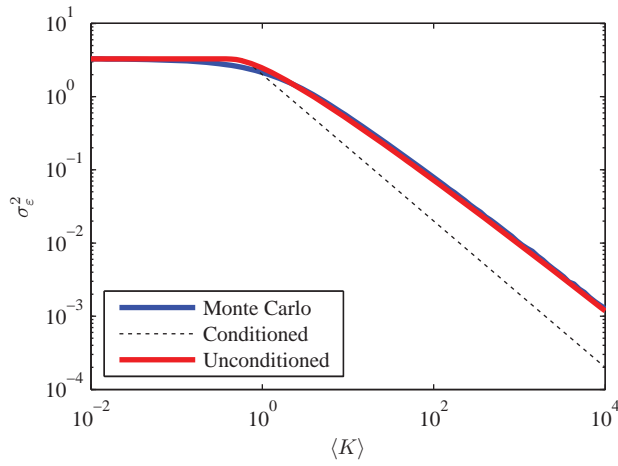


Figure 28. Comparison between Eq. (6.3.23) and Monte Carlo simulation runs when I_i is negative exponentially distributed.

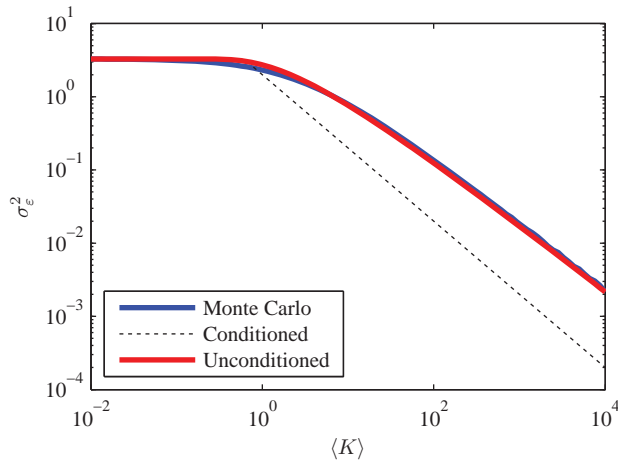


Figure 29. Comparison between Eq. (6.3.30) and Monte Carlo simulation runs when both I_i and η_i are negative exponentially distributed.

An example of when both I_i and η_i have significant probability near zero is displayed in Fig. 29. In this case, both I_i and η_i are negative exponentially distributed. The unconditioned error variance line is the result of numerically integrating Eq. (6.3.30), and the unconditioned error variance line from Fig. 26 is included as a basis for comparison. The model overestimates the error variance by a maximum of 9%, while it agrees with the simulations to within 5% at the higher average total photo-count values.

The good agreement between the phase error variance models and Monte Carlo simulation runs as demonstrated in Figs. 26–29 indicates that the methodology used in deriving the above expressions for the phase error variance is sound. As long as the assumptions used in the above derivations are reasonably close to the truth, these models should accurately predict the performance of an SRI. Additional simulations and experiments can be used to test these assumptions to find regions of applicability, and further refine the models.

6.5 Examples

Predicted SRI performance over a wide range of conditions is indicated in Fig. 30. This figure highlights the effects of various turbulence strengths from very weak to very strong, various subaperture sizes relative to the coherence length of the incident light, and differing signal strength levels. The biggest limiting assumption is that the coherence time of the light is much longer than the detector integration time [$\mathcal{D}_t(\tau_d) \ll 1$]. It further assumes a point source beacon, optimal beam splitting between the SRI reference and beacon legs, a system pupil diameter given by $D = 20\sqrt{2}d$, $\mathcal{D}_\phi(d) = 6.88(d/r_0)^{5/3}$, $\sigma_{\text{meas}}^2 = 0$ and $\langle \bar{I} \rangle = \langle I_i \rangle$. The coupling efficiency η_i is assumed to be negative exponentially distributed (open-loop operation), and $\langle \eta_i \rangle$ is found using Eq. (5.2.15) with compensation as described in Sec. 5.2.3.1. The

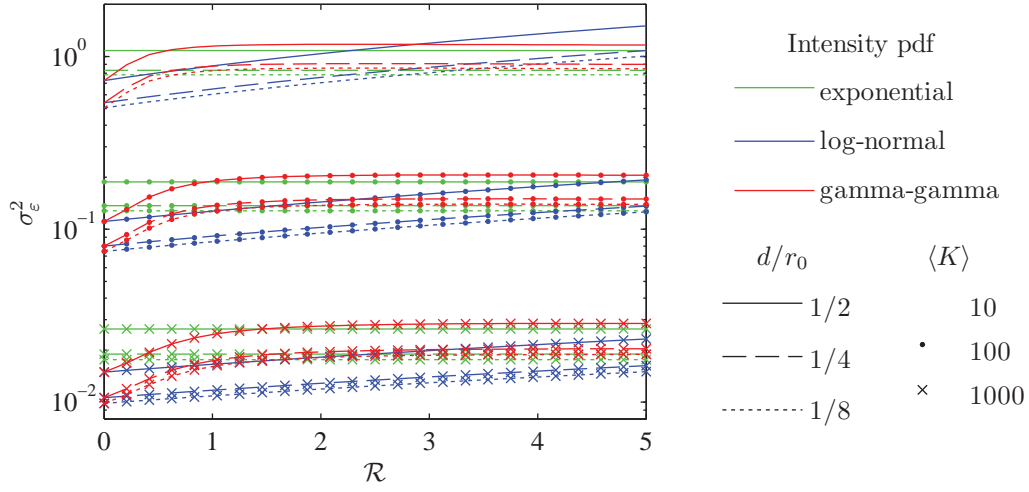


Figure 30. Effect of turbulence on SRI performance with a point source beacon at different noise levels. The coupling efficiency pdf is assumed to be negative exponential, and various intensity probability distributions are compared.

parameters α and β for the gamma-gamma pdf of Eq. (B.4) are found from [2] using

$$\alpha = \left\{ \exp \left[\frac{2.0\mathcal{R}}{(1 + 3.0\mathcal{R}^{6/5})^{7/6}} \right] - 1 \right\}^{-1} \quad (6.5.1)$$

$$\beta = \left\{ \exp \left[\frac{2.0\mathcal{R}}{(1 + 3.6\mathcal{R}^{6/5})^{5/6}} \right] - 1 \right\}^{-1}, \quad (6.5.2)$$

where \mathcal{R} is the Rytov number as defined in Sec. 2.4.1.6 with weak turbulence occurring when $\mathcal{R} \ll 1$.

This figure clearly indicates the effect of scintillation due to strong turbulence on SRI performance. Whether a log-normal distribution or gamma-gamma distribution is assumed for the intensity fluctuations, σ_ϵ^2 increases with increasing \mathcal{R} . While σ_ϵ^2 continues to increase linearly with increasing turbulence strength when using the log-normal distribution, it saturates near the value that would be expected given a negative exponential distribution when the gamma-gamma distribution is used. This matches the behavior of the scintillation index with increasing \mathcal{R} as indicated in Fig. 2.

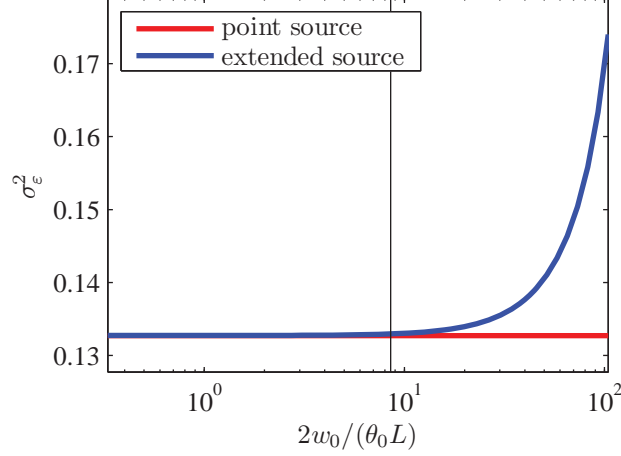


Figure 31. Effect of an incoherent extended beacon on SRI performance. Performance given a point source beacon is provided for comparison. The vertical line indicates the point where the nature of the source begins to impact SRI performance as predicted by Sec. 4.5

Figure 30 also demonstrates how there is little difference in SRI performance between $d/r_0 = 1/4$ and $d/r_0 = 1/8$, but a large difference for $d/r_0 = 1/2$. This is as expected since, as seen in Eq. (6.3.17), \mathcal{D}_ϕ and \mathcal{D}_t have little impact on σ_ϵ^2 so long as they are much less than one, but they can have a large impact once they become greater than one. This is especially true for \mathcal{D}_ϕ since its effect is further squared due to the two spatial degrees of freedom.

Overall, the parameter that has the biggest impact on σ_ϵ^2 is $\langle K \rangle$. This indicates that SRI performance should be good so long as the total available photo-counts are sufficiently high. However, increasing the total photo-counts often involves increasing the subaperture size or detector integration time. Since these actions also increase \mathcal{D}_ϕ and \mathcal{D}_t which in turn decrease SRI performance, these effects need to be balanced against each other to find the optimal operating conditions for a given situation.

The effect of an incoherent Gaussian Schell-model (GSM) source beacon on SRI performance is demonstrated in Fig. 31, where the beacon diameter $2w_0$ is given in terms of the isoplanatic angle θ_0 defined by Eq. (2.4.46). It assumes constant turbulence along the path, a point source $d/r_0 = 1/5$, $\mathcal{R} = 1$, $\langle K \rangle = 100$, and

$\mathcal{D}_t(\tau_d) \ll 1$. Complete spatial incoherence of the source requires its spatial coherence radius l_c to be on order of the wavelength λ , such as when a long-coherence-length laser is reflected off a rough metallic surface. Further assuming the source is initially collimated, the atmospheric turbulence propagation parameters of Eq. (4.2.8) are found to be $\Theta_0 = 1$, $q_c \sim 10^{10}$, $q = 19.2$, and Λ_0 ranges from 10^{-2} to 10^3 . The quantity d/ρ_0 , where ρ_0 is the coherence radius of the light at the receiver found using Eq. (4.2.31), ranges from 0.42 to 0.96. Assuming a phase structure function of $\mathcal{D}_\phi(d) = 2(d/\rho_0)^{5/3}$, this range satisfies the constraint of Eq. (6.3.16). The mean coupling efficiency $\langle \eta_i \rangle$ was found in the same manner as for Fig. 30, and was also assumed to be negative exponentially distributed. As indicated in Fig. 30, the negative exponential distribution and gamma-gamma distribution for I_i very nearly give the same result when $\mathcal{R} = 1$ and $\langle K \rangle = 100$. Consequently, the negative exponential distribution was used here. The result for a point source beacon is included as a comparison.

Figure 31 demonstrates that as long as the GSM beacon is sufficiently small, the phase error variance for a given subaperture is nearly unchanged from that when using a point source. In this case, the beacon size could be nearly as large as $10\theta_0$ before the beacon's size begins to impact σ_ϵ^2 primarily due to the increasing value of \mathcal{D}_ϕ . However, there is no way of telling just from this result the degree to which the subaperture measurement is influenced by the atmospheric turbulence as opposed to the incoherence of the source.

While it may not be possible to completely separate out the two effects, as long as the source beacon affects all the subapertures across the detector in a reasonably coherent manner, then it may be assumed that the higher-order SRI measurements are caused primarily by the atmospheric turbulence. The conditions under which this criterion is met were discussed in Sec. 4.5 and used to derive the constraints given by Eqs. (4.5.3) and (4.5.4). Since q_c is so large in this case, Eq. (4.5.3) is never satisfied,

but the point where Eq. (4.5.4) is an equality with $D = 20\sqrt{2}d$ is indicated in Fig. 31 by the vertical line.

Since θ_0 is often used to define the angular extent over which atmospheric distortions are correlated, also known as isoplanatism, it may be surprising to see this line is located at $8.5\theta_0$. However, this serves to illustrate the fact that the true isoplanatic region for an optical system also depends on the receiver aperture size [18]. Using a different value for D changes the location of the vertical line. For instance, with $D = 10\sqrt{2}d$ the line would be at $17\theta_0$, while with $D = 30\sqrt{2}d$ the line would be at $5.7\theta_0$. As a result, an SRI can be effectively used in an AO system with extended beacons, even when the source beacon may be considered to be anisoplanatic [11].

6.6 Conclusion

This chapter developed analytic noise models for an SRI using spatial four-bin PSI that for the first time takes into account all the potential noise sources. These SRI noise models are useful for analyzing the performance of an SRI as used in a given application, or they can be used as the basis for trade studies when designing an SRI based optical system. These models consist of expressions for the phase error variance in the cases of small variations of all the random parameters, when either the incident field intensity or fiber optic coupling efficiency has significant probability near zero, and when both have significant probability near zero. These expressions were then compared to Monte Carlo simulation runs that conformed to the assumptions inherent in the analysis. The models and simulation runs demonstrated excellent agreement with each other, particularly when there was either very many or very little average photo-counts available for the PSI. The agreement in these limits always fell within 5%, and in some cases less than 1%. As would be expected, they perform the worst in the transition region between many total photo-counts and few total photo-counts.

Examples were provided where the noise model was used to estimate SRI performance under a variety of conditions. These examples demonstrated the effect of different turbulence strengths, field spatial coherence size with respect to subaperture size, differences in intensity distributions, various total photo-count levels, as well as extended GSM beacons on SRI performance. This demonstrated how the noise model would be useful when designing an SRI system for a particular application as the design parameters are traded against each other. Furthermore, an example validated the constraints derived in Chapter IV that describe when the nature of the source beacon impacts wavefront sensor performance.

This analysis assumes the incident intensity fluctuations and the magnitude of the coupling coefficient change little over the spatial and temporal detector integrations, so their average value over these spatial and temporal extents can be well approximated by their value at the center of these extents. It also assumes the spatial and temporal phase gradient over these extents is well approximated as being constant. In the small fluctuations regime, it further assumes that the fluctuations of I_i , η_i , \bar{I} , and $\nabla\phi$ are sufficiently small that the approximations of Eqs. (6.3.12) and (6.3.15) produce little error. In the case of Eq. (6.3.15), this typically means $D_\phi \leq \pi^2/4$, where D_ϕ is either the spatial or temporal phase structure function. These assumptions should be reasonable so long as the detector subaperture size and integration time are small with respect to the coherence size and time of the incident light. Testing the validity and/or applicability of these assumptions can be accomplished with additional wave optics simulation runs. The models can then be adjusted as needed to increase their accuracy based on the results of these simulations.

VII. Conclusion

This research made great progress toward answering the question of how a self-referencing interferometer (SRI) performs when used with extended beacons in strong turbulence. It accomplished this task by analyzing the individual components of the overall problem. The extended beacon was first assumed to be reasonably approximated by a Gaussian Shell-model (GSM) source. In Chapter IV, this assumption was used to determine accurate expressions for the second-order statistical properties of a beam emanating from this source after traversing through atmospheric turbulence of arbitrary strength. These expressions were then used to form constraints on when the coherence properties of the beam source would have little effect on SRI phase measurements. Furthermore, this study demonstrated that the resulting beam can still be well represented as a GSM beam.

This fact was used in Chapter V to analyze the effect of coupling this beam into a single-mode optical fiber. Analytic expressions for the mean coupling efficiency and its normalized variance were expressed in terms of the incident field characteristic parameters, and by extension the original source and atmospheric parameters. This study also took into account some fourth-order characteristics of the field such as its speckle, or scintillation, content.

These coupling efficiency expressions were needed for the SRI noise model derived in Chapter VI. This model depends primarily on the nature of the incident intensity fluctuations, the coupling efficiency fluctuations, the coherence size of the incident field with respect to the subaperture size, and the coherence time of the incident field with respect to SRI integration time. While the actual form of the model depends in large part on the stochastic nature of its component variables, several examples were given when they display both large and small fluctuations. Using these analytic tools, it is now possible to predict the performance of an SRI given a partially

coherent source beacon and intervening atmospheric turbulence strength, subject to appropriate assumptions and constraints.

7.1 Original Contributions

As outlined in Chapter I, this research effort produced several original contributions, many of which apply to fields beyond AO or SRI performance, such as free-space optical communications, stellar interferometry, and ladar/lidar systems. These original contributions include

1. A generally more accurate method of estimating the coherence radius of partially coherent Gaussian beams at all levels of turbulence,
2. A better understanding of the shape of the coherence function of partially coherent Gaussian beams at all levels of turbulence,
3. Constraints on the degree of coherence of a GSM source that would allow for the use of an SRI to predominately measure atmospherically induced phase perturbations,
4. Analytic expressions for the mean coupling efficiency of GSM beams into single-mode optical fibers,
5. Analytic expressions for the coupling variance of GSM beams into single-mode optical fibers,
6. A better understanding of the effect of speckle on the coupling of GSM beams into single mode optical fibers,
7. A more accurate noise model for an SRI,
8. A better understanding of the effect of extended beacons and strong turbulence on the performance of an SRI.

These results, particularly the first two, can also be used to analyze the performance of alternative wavefront sensors when used with extended beacons and strong turbulence. The ultimate product of this research, the SRI noise model, should also be useful aid when designing an SRI for a particular application.

7.2 Future Work

While this research has made great strides in better understanding how extended beacons and strong turbulence affect the performance of an SRI, there is still much work that may yet be done. One area of potential research deals with changing the assumptions that were used throughout this study. These assumptions include modeling the extended beacon as a GSM source, using atmospheric turbulence with zero inner scale, and keeping the turbulence constant across the entire propagation path. Changing these assumptions could make the final results more general, and therefore more useful for a wider range of conditions. The assumptions used to derive the SRI noise model could also be further tested by using wave optics simulations along with an end-to-end SRI simulation. This would test the applicability of the assumptions that the intensity of the incident field and its phase gradient change little over the subaperture size and integration time. These simulations can also be used to characterize the performance of the SRI when the spatial and/or temporal coherence extent of the incident field is no longer large with respect to the subaperture size and integration time. Since the above analysis also generally assumed open-loop operation of the SRI, more can be done studying its performance when it is used in closed-loop as part of entire AO system. Ultimately, the true test of any model is how useful it is in practice, which can only be validated thorough laboratory experiment.

Another area of potential research deals with coming to a better understanding of some of the parameters that constitute the model. This includes the probability

distributions of the intensity and phase gradient of light from a partially coherent source after traveling through weak or strong turbulence. While this has been extensively studied when the source is either completely coherent or incoherent, there is still more that can be done if the source is partially coherent. More work could also be done to better understand the spatial and temporal phase structure functions of this light. Additionally, the probability distribution of the single-mode fiber coupling efficiency both in open- and closed-loop operation could be further analyzed.

This analysis can also be applied to other wavefront sensors to model their performance with extended beacons and strong turbulence. These models could then be used to design hybrid wavefront sensors where complementary sensors may perform better than either in isolation as was demonstrated by Ellis [25]. These tools and models are sure to serve as a useful aids for overcoming many of the challenges that exist when attempting to compensate for strong atmospheric turbulence with extended beacons.

Appendix A: Fiber Coupling Integrals

This appendix derives the solutions to the integrals found in the analysis of Chap. V. The following four integrals are used to define the general expressions for the coupling efficiency mean and variance as presented in that chapter:

$$\text{Int}_1 = \iint_{\mathcal{P}} \iint_{\mathcal{P}} \Gamma(\boldsymbol{\rho}_1, \boldsymbol{\rho}_2) \mathcal{M}_0^*(\boldsymbol{\rho}_1) \mathcal{M}_0(\boldsymbol{\rho}_2) P(\boldsymbol{\rho}_1) P(\boldsymbol{\rho}_2) d^2 \boldsymbol{\rho}_1 d^2 \boldsymbol{\rho}_2, \quad (\text{A.1})$$

$$\text{Int}_2 = \iint_{\mathcal{P}} \Gamma(\boldsymbol{\rho}, \boldsymbol{\rho}) P(\boldsymbol{\rho}) d^2 \boldsymbol{\rho}, \quad (\text{A.2})$$

$$\text{Int}_3 = \iint_{\mathcal{P}} \iint_{\mathcal{P}} |\Gamma(\boldsymbol{\rho}_1, \boldsymbol{\rho}_2)|^2 P(\boldsymbol{\rho}_1) P(\boldsymbol{\rho}_2) d^2 \boldsymbol{\rho}_1 d^2 \boldsymbol{\rho}_2, \quad (\text{A.3})$$

$$\begin{aligned} \text{Int}_4 = & \iint_{\mathcal{P}} \iint_{\mathcal{P}} \iint_{\mathcal{P}} \iint_{\mathcal{P}} \Gamma'(\boldsymbol{\rho}_1, \boldsymbol{\rho}_2, \boldsymbol{\rho}_3, \boldsymbol{\rho}_4) \mathcal{M}_0^*(\boldsymbol{\rho}_1) \mathcal{M}_0(\boldsymbol{\rho}_2) \mathcal{M}_0^*(\boldsymbol{\rho}_3) \mathcal{M}_0(\boldsymbol{\rho}_4) \\ & \times P(\boldsymbol{\rho}_1) P(\boldsymbol{\rho}_2) P(\boldsymbol{\rho}_3) P(\boldsymbol{\rho}_4) d^2 \boldsymbol{\rho}_1 d^2 \boldsymbol{\rho}_2 d^2 \boldsymbol{\rho}_3 d^2 \boldsymbol{\rho}_4. \end{aligned} \quad (\text{A.4})$$

To analytically evaluate these integrals, the MCF for GSM beams given by Eq. (5.2.10), the Gaussian approximation to the back-propagated LP₀₁ fiber mode given by Eq. (5.2.6), and $\Gamma'(\boldsymbol{\rho}_1, \boldsymbol{\rho}_2, \boldsymbol{\rho}_3, \boldsymbol{\rho}_4)$ as given by Eq. (5.3.3) are used. When the circular “hard” pupil function of Eq. (5.2.12) is used, these integrals can be expressed in polar coordinates as

$$\begin{aligned} \text{Int}_1 = & \frac{8A^2}{\pi D^2} \int_0^{D/2} \int_0^{2\pi} \int_0^{D/2} \int_0^{2\pi} \exp \left[-\frac{4B}{D^2} \rho_1^2 - \frac{4B^*}{D^2} \rho_2^2 + \frac{2\rho_1 \rho_2}{\rho_g^2} \cos(\theta_1 - \theta_2) \right] \\ & \times \rho_1 \rho_2 d\theta_1 d\rho_1 d\theta_2 d\rho_2, \end{aligned} \quad (\text{A.5})$$

$$\text{Int}_2 = \int_0^{D/2} \int_0^{2\pi} \exp \left(-\frac{2\rho^2}{w_g^2} \right) \rho d\theta d\rho, \quad (\text{A.6})$$

$$\begin{aligned} \text{Int}_3 = & \int_0^{D/2} \int_0^{2\pi} \int_0^{D/2} \int_0^{2\pi} \exp \left[-2 \left(\frac{1}{w_g^2} + \frac{1}{\rho_g^2} \right) (\rho_1^2 + \rho_2^2) + \frac{4\rho_1 \rho_2}{\rho_g^2} \cos(\theta_1 - \theta_2) \right] \\ & \times \rho_1 \rho_2 d\theta_1 d\rho_1 d\theta_2 d\rho_2, \end{aligned} \quad (\text{A.7})$$

$$\begin{aligned}
\text{Int}_4 = & \frac{64A^4}{\pi^2 D^4} \int_0^{D/2} \int_0^{2\pi} \int_0^{D/2} \int_0^{2\pi} \int_0^{D/2} \int_0^{2\pi} \int_0^{D/2} \int_0^{2\pi} \int_0^{2\pi} \exp \left\{ -\frac{4B}{D^2} (\rho_1^2 + \rho_3^2) \right. \\
& - \frac{4B^*}{D^2} (\rho_2^2 + \rho_4^2) + \frac{2}{\rho_g^2} \left[\rho_1 \rho_2 \cos(\theta_1 - \theta_2) - \rho_1 \rho_3 \cos(\theta_1 - \theta_3) + \rho_1 \rho_4 \cos(\theta_1 - \theta_4) \right. \\
& \left. \left. + \rho_2 \rho_3 \cos(\theta_2 - \theta_3) - \rho_2 \rho_4 \cos(\theta_2 - \theta_4) + \rho_3 \rho_4 \cos(\theta_3 - \theta_4) \right] \right\} \rho_1 \rho_2 \rho_3 \rho_4 \\
& \times d\theta_1 d\rho_1 d\theta_2 d\rho_2 d\theta_3 d\rho_3 d\theta_4 d\rho_4, \tag{A.8}
\end{aligned}$$

where

$$B = \left(\frac{D}{2w_g} \right)^2 + \left(\frac{D}{2\rho_g} \right)^2 + A^2 + \frac{jkD^2}{8R_g}. \tag{A.9}$$

Equation (A.6) can be solved by standard techniques and expressed as

$$\text{Int}_2 = \frac{\pi w_g^2}{2} \left\{ 1 - \exp \left[-2 \left(\frac{D}{2w_g} \right)^2 \right] \right\}. \tag{A.10}$$

Performing the θ_1 and θ_2 integrations in Eqs. (A.5) and (A.7), and making the substitutions $x_1 = 2\rho_1/D$ and $x_2 = 2\rho_2/D$, leads to

$$\begin{aligned}
\text{Int}_1 = & 2\pi A^2 D^2 \int_0^1 \int_0^1 \exp(-Bx_1^2 - B^*x_2^2) I_0 \left[2 \left(\frac{D}{2\rho_g} \right)^2 x_1 x_2 \right] x_1 x_2 dx_1 dx_2 \\
= & 2\pi A^2 D^2 Q \left[1, 2 \left(\frac{D}{2\rho_g} \right)^2, \sqrt{B}, \sqrt{B^*} \right] \\
= & \frac{\pi A^2 D^2}{2} \sum_{i=0}^{\infty} \left| \frac{1}{(i+1)!} \left(\frac{D}{2\rho_g} \right)^{2i} \right. \\
& \left. \times {}_1F_1 \left[i+1; i+2; - \left(\frac{D}{2w_g} \right)^2 - \left(\frac{D}{2\rho_g} \right)^2 - A^2 - \frac{jkD^2}{8R_g} \right] \right|^2 \tag{A.11}
\end{aligned}$$

$$\begin{aligned}
\text{Int}_3 &= \frac{\pi^2 D^4}{4} \int_0^1 \int_0^1 \exp \left\{ -2 \left[\left(\frac{D}{2w_g} \right)^2 + \left(\frac{D}{2\rho_g} \right)^2 \right] (x_1^2 + x_2^2) \right\} I_0 \left[4 \left(\frac{D}{2\rho_g} \right)^2 x_1 x_2 \right] \\
&\quad \times x_1 x_2 dx_1 dx_2 \\
&= \frac{\pi^2 D^4}{4} Q \left[2 \left(\frac{D}{2w_g} \right)^2 + 2 \left(\frac{D}{2\rho_g} \right)^2, 4 \left(\frac{D}{2\rho_g} \right)^2, 1, 1 \right] \\
&= \frac{\pi^2 D^4}{16} \sum_{i=0}^{\infty} \left\{ \frac{2^i}{(i+1)!} \left(\frac{D}{2\rho_g} \right)^{2i} {}_1F_1 \left[i+1; i+2; -2 \left(\frac{D}{2w_g} \right)^2 - 2 \left(\frac{D}{2\rho_g} \right)^2 \right] \right\}^2,
\end{aligned} \tag{A.12}$$

where $I_0(\cdot)$ is a modified Bessel function of imaginary argument, $Q(\cdot)$ is defined and solved in [17], and ${}_1F_1(\cdot)$ is the confluent hypergeometric function. However, Eq. (A.8) is not amenable to analytic evaluation.

When the Gaussian “soft” pupil function of Eq. (5.2.14) is used, Eqs. (A.1)–(A.4) can be expressed as

$$\begin{aligned}
\text{Int}_1 &= \frac{A^2 D^2}{2\pi} \int_0^\infty \int_0^{2\pi} \int_0^\infty \int_0^{2\pi} \exp \left[-C\rho_1^2 - C^*\rho_2^2 + \frac{2\rho_1\rho_2}{\rho_g^2} \cos(\theta_1 - \theta_2) \right] \rho_1 \rho_2 \\
&\quad \times d\theta_1 d\rho_1 d\theta_2 d\rho_2,
\end{aligned} \tag{A.13}$$

$$\text{Int}_2 = \int_0^\infty \int_0^{2\pi} \exp \left[-2 \left(\frac{1}{w_g^2} + \frac{4}{D^2} \right) \rho^2 \right] \rho d\theta d\rho, \tag{A.14}$$

$$\begin{aligned}
\text{Int}_3 &= \int_0^\infty \int_0^{2\pi} \int_0^\infty \int_0^{2\pi} \exp \left[-2 \left(\frac{1}{w_g^2} + \frac{1}{\rho_g^2} + \frac{4}{D^2} \right) (\rho_1^2 + \rho_2^2) + \frac{4\rho_1\rho_2}{\rho_g^2} \cos(\theta_1 - \theta_2) \right] \\
&\quad \times \rho_1 \rho_2 d\theta_1 d\rho_1 d\theta_2 d\rho_2,
\end{aligned} \tag{A.15}$$

$$\begin{aligned}
\text{Int}_4 &= \frac{64A^4}{\pi^2 D^4} \int_0^\infty \int_0^{2\pi} \int_0^\infty \int_0^{2\pi} \int_0^\infty \int_0^{2\pi} \int_0^\infty \int_0^{2\pi} \exp \left\{ -C(\rho_1^2 + \rho_3^2) - C^*(\rho_2^2 + \rho_4^2) \right. \\
&\quad + \frac{2}{\rho_g^2} \left[\rho_1 \rho_2 \cos(\theta_1 - \theta_2) - \rho_1 \rho_3 \cos(\theta_1 - \theta_3) + \rho_1 \rho_4 \cos(\theta_1 - \theta_4) \right. \\
&\quad \left. \left. + \rho_2 \rho_3 \cos(\theta_2 - \theta_3) - \rho_2 \rho_4 \cos(\theta_2 - \theta_4) + \rho_3 \rho_4 \cos(\theta_3 - \theta_4) \right] \right\} \rho_1 \rho_2 \rho_3 \rho_4 \\
&\quad \times d\theta_1 d\rho_1 d\theta_2 d\rho_2 d\theta_3 d\rho_3 d\theta_4 d\rho_4,
\end{aligned} \tag{A.16}$$

where

$$C = \frac{1}{w_g^2} + \frac{1}{\rho_g^2} + (A^2 + 2) \frac{4}{D^2} + \frac{jk}{2R_g}. \quad (\text{A.17})$$

These integrals can be evaluated with use of the trigonometric identity

$$\cos(x \pm y) = \cos x \cos y \mp \sin x \sin y,$$

and the definite integral

$$\int_0^\infty \int_0^{2\pi} x \exp[-\alpha x^2 + x(\beta \cos \phi + \gamma \sin \phi)] d\phi dx = \frac{\pi}{\alpha} \exp\left(\frac{\beta^2 + \gamma^2}{4\alpha}\right), \quad (\text{A.18})$$

where $\text{Re } \alpha > 0$, which is derived from Eqs. (3.338 4) and (6.633 4) of [42]. After some algebraic manipulation, the final results can be expressed as

$$\text{Int}_1 = \frac{2\pi A^2 \left(\frac{D}{2}\right)^2}{\left| \left(\frac{D}{2w_g}\right)^2 + \left(\frac{D}{2\rho_g}\right)^2 + A^2 + 2 + \frac{jkD^2}{8R_g} \right|^2 - \left(\frac{D}{2\rho_g}\right)^4}, \quad (\text{A.19})$$

$$\text{Int}_2 = \frac{\frac{\pi}{2} \left(\frac{D}{2}\right)^2}{\left(\frac{D}{2w_g}\right)^2 + 1}, \quad (\text{A.20})$$

$$\text{Int}_3 = \frac{\left(\frac{\pi}{2}\right)^2 \left(\frac{D}{2}\right)^4}{\left[\left(\frac{D}{2w_g}\right)^2 + \left(\frac{D}{2\rho_g}\right)^2 + 1 \right]^2 - \left(\frac{D}{2\rho_g}\right)^4}, \quad (\text{A.21})$$

and

$$\begin{aligned}
 \text{Int}_4 = & 4\pi^2 A^4 \left(\frac{D}{2} \right)^4 / \left(\left\{ \left| \left(\frac{D}{2w_g} \right)^2 + \left(\frac{D}{2\rho_g} \right)^2 + A^2 + 2 + \frac{jkD^2}{8R_g} \right|^2 \right. \right. \\
 & - 2 \left(\frac{D}{2\rho_g} \right)^2 \left[\left(\frac{D}{2w_g} \right)^2 + \left(\frac{D}{2\rho_g} \right)^2 + A^2 + 2 \right] + \left. \left(\frac{D}{2\rho_g} \right)^4 \right\} \\
 & \times \left\{ \left| \left(\frac{D}{2w_g} \right)^2 + \left(\frac{D}{2\rho_g} \right)^2 + A^2 + 2 + \frac{jkD^2}{8R_g} \right|^2 \right. \\
 & \left. \left. + 2 \left(\frac{D}{2\rho_g} \right)^2 \left[\left(\frac{D}{2w_g} \right)^2 + \left(\frac{D}{2\rho_g} \right)^2 + A^2 + 2 \right] - 3 \left(\frac{D}{2\rho_g} \right)^4 \right\} \right). \quad (\text{A.22})
 \end{aligned}$$

Appendix B: σ_ε^2 For Various Probability Distributions of I_i and η_i

This appendix derives SRI noise models for additional probability distribution functions (pdf) of the incident field intensity fluctuations I_i and effective fiber coupling efficiency η_i . Expressions are only derived for the cases where either one parameter or the other has significant probability near 0. For the instances when both have significant probability near zero, these expressions can easily be converted to the conditioned phase error variance that must be integrated over the appropriate pdf of the other variable. This final integration would most likely require numerical methods similar to what is giving in Eq. (6.3.30).

Gamma Distribution

The gamma distribution is given by

$$p_X(x) = \frac{(\beta x)^\alpha \exp(-\beta x)}{\Gamma(\alpha)x}, \quad (\text{B.1})$$

where $\Gamma(\cdot)$ is the gamma function, $\alpha = 1/\tilde{\sigma}_X^2$, $\beta = 1/(\langle X \rangle \tilde{\sigma}_X^2)$, and $\tilde{\sigma}_X^2 = \sigma_X^2 / \langle X \rangle^2$. Using Eq. (6.3.19) as the expression for the conditioned phase error variance, the unconditioned phase error variance when I_i is gamma distributed can be expressed as

$$\sigma_\varepsilon^2 \simeq \begin{cases} \frac{\pi^2}{3} & \text{if } a_I \leq b_I, \\ \frac{\pi^2}{3} \left\{ 1 - \left(1 - \frac{b_I}{a_I}\right) \Gamma \left[\frac{1}{\tilde{\sigma}_{I_i}^2}, \frac{c_I}{(a_I - b_I) \langle I_i \rangle \tilde{\sigma}_{I_i}^2} \right] / \Gamma \left(\frac{1}{\tilde{\sigma}_{I_i}^2} \right) \right. \\ \left. + \frac{c_I}{a_I \langle I_i \rangle \tilde{\sigma}_{I_i}^2} \Gamma \left[\frac{1}{\tilde{\sigma}_{I_i}^2} - 1, \frac{c_I}{(a_I - b_I) \langle I_i \rangle \tilde{\sigma}_{I_i}^2} \right] / \Gamma \left(\frac{1}{\tilde{\sigma}_{I_i}^2} \right) \right\} & \text{otherwise,} \end{cases} \quad (\text{B.2})$$

where a_I , b_I , and c_I are given by Eqs. (6.3.20)–(6.3.22), and $\Gamma(\alpha, x)$ is the incomplete gamma function defined as

$$\Gamma(\alpha, x) = \int_x^{\infty} t^{\alpha-1} e^{-t} dt. \quad (\text{B.3})$$

By making the appropriate changes, a similar expression can be found when η_i is gamma distributed. Equation (B.2) reduces to Eq. (6.3.23) when $\tilde{\sigma}_{I_i}^2 = 1$ as the gamma distribution reduces to the exponential distribution.

Gamma-Gamma Distribution

The gamma-gamma distribution defines the probability of a random variable that is the product of two unit-mean gamma distributed random variables. Its pdf is given by

$$p_X(x) = \frac{2}{\Gamma(\alpha)\Gamma(\beta)x} \left(\frac{\alpha\beta x}{\langle X \rangle} \right)^{(\alpha+\beta)/2} K_{\alpha-\beta} \left(2\sqrt{\frac{\alpha\beta x}{\langle X \rangle}} \right), \quad (\text{B.4})$$

where $K_\nu(\cdot)$ is a modified Bessel function of the second kind of order ν , and the normalized variance is given by

$$\tilde{\sigma}_X^2 = \frac{1 + \alpha + \beta}{\alpha\beta}. \quad (\text{B.5})$$

Since the mean is given as one of the input parameters to the pdf, the values of α and β are not set by a given mean and variance and must be derived by other means. The gamma-gamma distribution has been used to model the intensity fluctuations of light that has traveled through strong atmospheric turbulence [2]. Assuming I_i is gamma-gamma distributed with α and β as determined by [2, Chap. 9], integrating

Eq. (6.3.19) over Eq. (B.4) produces

$$\sigma_\varepsilon^2 \simeq \begin{cases} \frac{\pi^2}{3} & \text{if } a_I \leq b_I, \\ \frac{\pi^2}{3} \left[\frac{b_I}{a_I} + \frac{c_I \alpha \beta}{a_I \langle I_i \rangle (\alpha - 1)(\beta - 1)} + \left(1 - \frac{b_I}{a_I}\right) \frac{1}{\Gamma(\alpha)\Gamma(\beta)} \right. \\ \quad \times \left(\left[\frac{c_I \alpha \beta}{(a_I - b_I) \langle I_i \rangle} \right]^\alpha \frac{\Gamma(\beta - \alpha)}{\alpha - 1} \left\{ \left(1 - \frac{1}{\alpha}\right) {}_1F_2 \left[\alpha; 1 + \alpha, 1 + \alpha - \beta; \right. \right. \right. \\ \quad \left. \left. \left. \frac{c_I \alpha \beta}{(a_I - b_I) \langle I_i \rangle} \right] - {}_1F_2 \left[\alpha - 1; \alpha, 1 + \alpha - \beta; \frac{c_I \alpha \beta}{(a_I - b_I) \langle I_i \rangle} \right] \right\} \right. \\ \quad \left. + \left[\frac{c_I \alpha \beta}{(a_I - b_I) \langle I_i \rangle} \right]^\beta \frac{\Gamma(\alpha - \beta)}{\beta - 1} \left\{ \left(1 - \frac{1}{\beta}\right) {}_1F_2 \left[\beta; 1 + \beta, 1 + \beta - \alpha; \right. \right. \right. \\ \quad \left. \left. \left. \frac{c_I \alpha \beta}{(a_I - b_I) \langle I_i \rangle} \right] - {}_1F_2 \left[\beta - 1; \beta, 1 + \beta - \alpha; \frac{c_I \alpha \beta}{(a_I - b_I) \langle I_i \rangle} \right] \right\} \right] & \text{otherwise,} \end{cases} \quad (\text{B.6})$$

where ${}_1F_2(\cdot)$ is a generalized hypergeometric function.

Uniform Distribution

The uniform distribution may be used as an approximate pdf for η when $\langle \eta \rangle$ is close to 1/2. Since η can only vary between 0 and 1, the uniform pdf is simply

$$p_X(x) = \begin{cases} 1 & \text{if } 0 \leq x \leq 1 \\ 0 & \text{otherwise} \end{cases} \quad (\text{B.7})$$

Assuming the small fluctuation approximation is valid for I_i , \bar{I} , and $\nabla\phi$, the phase error variance conditioned only on η can be expressed as

$$\sigma_{\varepsilon|\eta}^2 \simeq \begin{cases} \frac{\pi^2}{3} & \text{if } \eta \leq \frac{b_\eta}{a_\eta - c_\eta} \text{ or } a_\eta \leq b_\eta + c_\eta, \\ \frac{\pi^2}{3} \left(\frac{b_\eta + c_\eta \eta}{a_\eta \eta} \right) & \text{otherwise,} \end{cases} \quad (\text{B.8})$$

where

$$a_\eta = \left\{ 1 - \frac{[\mathcal{D}_\phi(d)]^{2.43}}{80} \right\}^2 \left\{ 1 - \frac{[\mathcal{D}_t(\tau_d)]^{2.43}}{80} \right\} \frac{2\pi^2}{3} d^2 \tau_d \alpha \beta (1 - \beta) \langle I_i \rangle \langle \bar{I} \rangle \mathcal{A}_P \mathcal{M}_0^2(\boldsymbol{\rho}_i), \quad (\text{B.9})$$

$$b_\eta = \left[1 + \frac{\mathcal{D}_\phi(d)}{12} \right]^2 \left[1 + \frac{\mathcal{D}_t(\tau_d)}{12} \right] (1 + \tilde{\sigma}_{\bar{I}}^2) \left[\beta \langle I_i \rangle + \frac{2\sigma_{\text{meas}}^2 (1 + \tilde{\sigma}_{\bar{I}}^2)}{\alpha d^2 \tau_d} \right], \quad (\text{B.10})$$

$$c_\eta = \left[1 + \frac{\mathcal{D}_\phi(d)}{12} \right]^2 \left[1 + \frac{\mathcal{D}_t(\tau_d)}{12} \right] (1 - \beta) \langle \bar{I} \rangle \mathcal{A}_P \mathcal{M}_0^2(\boldsymbol{\rho}_i) (1 + \tilde{\sigma}_{\bar{I}}^2). \quad (\text{B.11})$$

Integrating Eq. (B.8) over Eq. (B.7) produces

$$\sigma_\varepsilon^2 \simeq \begin{cases} \frac{\pi^2}{3} & \text{if } a_\eta \leq b_\eta + c_\eta, \\ \frac{\pi^2}{3} \left[\frac{b_\eta + c_\eta}{a_\eta} - \frac{b_\eta}{a_\eta} \ln \left(\frac{b_\eta}{a_\eta - c_\eta} \right) \right] & \text{otherwise.} \end{cases} \quad (\text{B.12})$$

Exponential Distribution

When $\langle \eta \rangle \ll 1$, the distribution of η may be approximated with Eq. (6.3.18). Assuming the intensity fluctuation are small, integrating Eq. (B.8) over Eq. (6.3.18) produces

$$\sigma_\varepsilon^2 = \begin{cases} \frac{\pi^2}{3} & \text{if } a_\eta \leq b_\eta + c_\eta, \\ \frac{\pi^2}{3} \left\{ 1 - \left(1 - \frac{c_\eta}{a_\eta} \right) \exp \left[-\frac{b_\eta}{(a_\eta - c_\eta) \langle \eta \rangle} \right] \right. \\ \quad \left. + \frac{b_\eta}{a_\eta \langle \eta \rangle} E_1 \left[\frac{b_\eta}{(a_\eta - c_\eta) \langle \eta \rangle} \right] \right\} & \text{otherwise.} \end{cases} \quad (\text{B.13})$$

Appendix C: Matlab® Scripts

Listing C.1. AbsorptionBound.m

```
function absorb = AbsorptionBound(N, rho, a1, a2)
% absorb = AbsorptionBound(N, dx, r, a1, a2)
%   Creates a Gaussian absorption boundary to be used with wave optics
%   propagation with phase screens.  It is designed to be the imaginary
%   part of the phase screen:
%       screen = phase - 1j*absorb;
%       field_t = field_i .* exp(1j*screen);
%
%   N:      Size of the propagation grid
%   rho:    Radius of transmission area [pix]
%   a1:    Extinction coefficient in absorption area
%   a2:    Width of Gaussian transition area [pix]
%
%   absorb: Absorption screen
%
% Created:  20 Apr 2010
% Modified: 21 Jul 2010
% By:      Daniel J. Wheeler

x = -N/2:N/2-1;
y = x';
r = sqrt(x(ones(N,1),:).^2 + y(:,ones(1,N)).^2);
absorb = -a1*exp(-1/2*((r-rho)/a2).^2);
absorb(r>rho) = -a1;
```

Listing C.2. AngSpecProp.m

```
function field_out = AngSpecProp(field_in, lambda, d1, d2, L)
% field_out = AngSpecProp(field_in, lambda, dx, L)
%   Performs angular spectrum propagation between planes with scaling
%
%   field_in:  Input complex field (must be NxN with even N)
%   lambda:    Field wavelength
%   d1:        Field sample spacing in source plane [m]
%   d2:        Field sample spacing in observation plane [m]
```

```

% L:          Propagation distance [m]
%
% field_out:  Output complex field
%
% Created:   17 Apr 2010
% Modified:  27 Apr 2010
% By:       Daniel J. Wheeler

N = length(field_in);
df = 1/(N*d1);
x = (-N/2:N/2-1)*d1;
y = x';
x1 = x(ones(N,1),:);
y1 = y(:,ones(1,N));
if d1 == d2
    field_out = ift2(ft2(field_in, d1) .* ...
        exp(-1j*pi*lambda*L*((x1*df/d1).^2 + (y1*df/d1).^2)), df);
else
    k = 2*pi/lambda;
    m = d2/d1;
    field_out = ift2(ft2(field_in .* ...
        exp(1j*k/2*(1-m)/L*(x1.^2 + y1.^2)), d1) .* ...
        exp(-1j*pi*lambda*L/m*((x1*df/d1).^2 + (y1*df/d1).^2)), df) .* ...
        exp(1j*k/2*(m-1)/m/L*((x1*m).^2 + (y1*m).^2))/m;
end

function G = ft2(g, X)

G = fftshift(fft2(fftshift(g))) * X^2;

function g = ift2(G, df)

g = ifftshift(ifft2(ifftshift(G))) * (length(G) * df)^2;

```

Listing C.3. AtmosModel.m

```

function turb = AtmosModel(lambda, Cn2, L, Nscrn, wind)
% turb = AtmosModel(lambda, Cn2, L, Nscrn, [v])
%   Creates an atmospheric model for horizontal propagation.
%
%   lambda: Wavelength of the field [m]

```

```

% Cn2:    Index of refraction structure constant [m^-2/3]
% L:      Total propagation distance [m]
% Nscrn:  Number of phase screens used to model the turbulence
% wind:   Wind velocity vector [m/s] (defaults to [0,0])
%
% turb:   Structure that holds the parameters that define the atmospheric
%         path
%
% Created: 19 Apr 2010
% Modified: 28 Apr 2010
% By: Daniel J. Wheeler

if nargin<5 || isempty(wind), wind = [0 0]; end

k = 2*pi/lambda;

% Calculate statistical properties of turbulence path
r0pw = (0.423*k^2*Cn2*L)^(-3/5);    % Plane wave r0 [m]
r0sw = (0.159*k^2*Cn2*L)^(-3/5);    % Spherical wave r0 [m]
Rpw = 0.307*k^(7/6)*Cn2*L^(11/6);  % Plane wave Rytov number
Rsw = 0.124*k^(7/6)*Cn2*L^(11/6);  % Spherical wave Rytov number

% Calculate position and strength of phase screens
turb.loc = (2*(1:Nscrn)-1)/(2*Nscrn)*L;    % Screen locations
A = [ones(1,Nscrn)                        % For r0,pw
      (turb.loc/L).^ (5/3)                 % For r0,sw
      (1-turb.loc/L).^ (5/6)              % For Rpw
      ((turb.loc/L).*(1-turb.loc/L)).^(5/6) % For Rsw
      [diag(ones(Nscrn-1,1)) zeros(Nscrn-1,1)]+...
      [zeros(Nscrn-1,1) -diag(ones(Nscrn-1,1))]]; % Equal phase screens
b = [r0pw^(-5/3)
      r0sw^(-5/3)
      Rpw/1.33*(k/L)^(5/6)
      Rsw/1.33*(k/L)^(5/6)
      zeros(Nscrn-1,1)];
turb.r0i = (A\b).^(-3/5);                % Calculates r0i values
turb.lam = lambda;
turb.L = L;
turb.wind = wind;

```

Listing C.4. GSM_MCF_turb.m

```
function [Gam_pp, Gam_p] = GSM_MCF_turb(rho, w0, R0, lc, L, Cn2, lam, ...
    tol, flag)
% [Gam_pp, Gam_p] = GSM_MCF_turb(rho,w0,R0,lc,L,Cn2,lam,[tol],[flag])
% Returns the MCF for a GSM beam having propagated through turbulence, by
% numerically evaluating the parabolic equation. It assumes horizontal
% propagation with a constant Cn2 value. The MCF at the source is:
% Gamma(rho1, rho2) = exp(-(rho1^2 + rho2^2)/w0^2 - |rho1 - rho2|^2/lc^2
% - jk(rho1^2 - rho2^2)/(2R0))
% rho: Vector containing the locations where the MCF is evaluated
% w0: Beam radius at the source [m]
% R0: Radius of curvature at the source [m]
% R0 > 0: converging beam
% R0 < 0: diverging beam
% R0 = Inf: collimated beam
% lc: Coherence radius of beam at source [m]
% L: Propagation distance [m]
% Cn2: Index-of-refraction structure constant [m^-2/3]
% lam: Beam center wavelength [m]
% tol: Tolerance for the numerical integtations (defaults to 1e-6)
% flag: Whether or not to perform the numerical integration of
% Gamma(rho, 0, L) (defaults to true)
%
% Gam_pp: Evaluation of Gamma(rho, rho, L)
% Gam_p: Evaluation of Gamma(rho, 0, L)
% if flag == false && Cn2 == 0, Gam_p = zeros(1,length(rho))
%
% Created: 24 Nov 2010
% Modified: 1 Dec 2010
% By: Daniel J. Wheeler

if nargin < 9 || isempty(flag), flag = 1; end
if nargin < 8 || isempty(tol), tol = 1e-6; end

k = 2*pi/lam;
Theta0 = 1 - L/R0;
Lam0 = 2*L/(k*w0^2);
[~, ~, p0] = param2stats(Cn2, L, lam);

a = 1/2*(1/w0^2 + 2/lc^2 + (k*w0/2/R0)^2);
b = L^2/2/k^2*(1/w0^2 + 2/lc^2 + Theta0^2/w0^2/Lam0^2);
c = L/k*(1/w0^2 + 2/lc^2 - k^2*Theta0*w0^2/4/R0/L);
```



```

if p0 == Inf
    Gam_p = w0^2/8/b*exp(-(a - (c + 1j/2)^2/4/b)*rho.^2);
    Gam_pp = w0^2/8/b*exp(-rho.^2/4/b);
    return
end

turb = @(x, u, th, t) 8/3/p0^(5/3)*(x.^2 - 2*L*t/k.*x.*u.*cos(th) + ...
    (L*t.*u/k).^2).^5/6);

Int_p = @(x, u, th) u.*exp(-a*x.^2 - b*u.^2 + (c + 1j/2)*x.*u.*cos(th) ...
    - quadv(@(t) turb(x, u, th, t), 0, 1, tol));
Int_pp = @(x, u) u.*exp(-b*u.^2 - (L*u/p0/k).^5/3) .* besselj(0, x.*u);
Gam_p = zeros(1, length(rho));
Gam_pp = Gam_p;

for ind = 1:length(rho)
    if logical(flag)
        Gam_p(ind) = quadgk(@(u) quadv(@(theta) Int_p(rho(ind), u, ...
            theta), -pi, pi, tol), 0, Inf);
    end
    Gam_pp(ind) = quadgk(@(u) Int_pp(rho(ind), u), 0, Inf);
end

Gam_p = w0^2/8/pi * exp(-0*rho.^2) .* Gam_p;
Gam_pp = w0^2/4 * Gam_pp;

```

Listing C.5. GSMSource.m

```

function GSM = GSMSource(N, dl, w, sigc, lambda, bw, rate)
% GSM = GSMSource(N, dl, w, sigc, lammbda, bw, rate)
% Creates a Gaussian Schell-model source beacon. Uses the procedure by
% Gbur [Opt. Express, 14:7567-7578(2006)]. The field is normalized so
% that the average intensity at the center of the beam is 1.
%
% N:      Number of samples across square propagation grid (must be even)
% dl:     Sample spacing in the source plane [m]
% w:      Gaussian beam radius (1/e point of field) [m]
% sigc:   Spatial coherence radius of beam (1/sqrt(e) point) [m]
% lambda: Center wavelength of field
% bw:     Bandwidth [fraction of center frequency]

```

```

% rate: Pulse rate [pulses/cycle]
%
% GSM: Random GSM field
%
% Created: 14 Jul 2010
% By: Daniel J. Wheeler
% Modified: 7 Jan 2011

x = (-N/2 : N/2-1)*d1; % coordinate grid
[x y] = meshgrid(x);
r2 = x.^2 + y.^2;

c = 299792458; % speed of light in vac [m/sec]
nu = c/lambda; % mean optical frequency [Hz]
Dnu = nu*bw; % optical bandwidth [Hz]
Npulse = 2*nu*rate/Dnu; % expected number of pulses in interval

% sqrt of intensity profile
Theta = exp(-r2/w^2)/sqrt(rate/bw*sqrt(log(2)/pi));
% temporal pulse shape
Phi = @(t) exp(-(pi*Dnu*t).^2/(2*log(2))) .* exp(-li*2*pi*nu*t);

n = poissrnd(Npulse); % random number of pulses
t = (2*rand(1,n)-1) /Dnu; % random departure time of pulses
Kx = randn(1,n) / sigc; % random draws of spatial frequencies
Ky = randn(1,n) / sigc;

GSM = zeros(N); % random optical field
% sum over plane wave pulses
for idx = 1 : n
    GSM = GSM + Theta .* Phi(t(idx)) .* exp(-li*(Kx(idx)*x+Ky(idx)*y));
end
end

```

Listing C.6. GSMSource_temporal.m

```

function [GSM, Sout] = GSMSource_temporal(N, d1, w, sigc, lambda, ...
    bw, rate, Dt, S)
% [GSM,Sout] = GSMSource_temporal(N,d1,w,sigc,lammbda,bw,rate,[Dt],[S])
% Creates a Gaussian Schell-model source beacon that can temporally
% evolve. Uses the procedure by Gbur [Opt. Express, 14:7567-7578(2006)].
% The field is normalized so that the average intensity at the center of

```

```

% the beam is 1.
%
% N:      Number of samples across square propagation grid
% dl:     Sample spacing in the source plane [m]
% w:      Beam radius (1/e point of average field amplitude) [m]
% sigc:   Spatial coherence radius of beam (1/sqrt(e) point) [m]
% lambda: Center wavelength of field
% bw:     FWHM bandwidth [fraction of center frequency]
% rate:   Pulse rate [pulses/cycle]
% Dt:     Time step since previous iteration [s] (defaults to 0)
% S:      Structure containing the random values from the previous
%         iteration
%
% GSM:    Random GSM field
% Sout:   Structure containing the random value from this iteration
%
% Created: 20 Apr 2011
% By: Daniel J. Wheeler
% Modified: 21 Apr 2011

if nargin < 9,          S = []; end
if nargin < 8 || isempty(Dt), Dt = 0; end

if mod(N, 2) == 0
    x = (-N/2 : N/2-1)*dl;      % coordinate grid
else
    x = -(N-1)/2 : (N-1)/2)*dl;
end
[x y] = meshgrid(x);
r2 = x.^2 + y.^2;

c = 299792458;          % speed of light in vac [m/sec]
nu = c/lambda;         % mean optical frequency [Hz]
Dnu = nu*bw;          % FWHM optical bandwidth [Hz]
% spatial amplitude profile
Theta = exp(-r2/w^2)/sqrt(rate/bw*sqrt(log(2)/pi));
% temporal pulse
Phi = @(t) exp(-(pi*Dnu*t).^2/(2*log(2))) .* exp(-2j*pi*nu*t);

if isempty(S) || abs(Dt) >= 2/Dnu
    % fill entire interval with random pulses
    n = poissrnd(2*nu*rate/Dnu); % random number of pulses

```

```

t = (2*rand(1, n) - 1)/Dnu; % random departure time of pulses
Kx = randn(1, n)/sigc; % random draws of spatial frequencies
Ky = randn(1, n)/sigc;
elseif Dt > 0
t = S.t - Dt; % time shift the pulses
% delete pulses outside new interval
Kx = S.Kx(t >= -1/Dnu);
Ky = S.Ky(t >= -1/Dnu);
t(t < -1/Dnu) = [];
% generate new random pulses
n = poissrnd(Dt*nu*rate);
t = [t rand(1, n)*Dt + (1/Dnu - Dt)];
Kx = [Kx randn(1, n)/sigc];
Ky = [Ky randn(1, n)/sigc];
elseif Dt < 0
t = S.t - Dt; % time shift the pulses
% delete pulses outside new interval
Kx = S.Kx(t <= 1/Dnu);
Ky = S.Ky(t <= 1/Dnu);
t(t > 1/Dnu) = [];
% generate new random pulses
n = poissrnd(-Dt*nu*rate);
t = [t rand(1, n)*Dt - (1/Dnu + Dt)];
Kx = [Kx randn(1, n)/sigc];
Ky = [Ky randn(1, n)/sigc];
else
% use previous values
t = S.t;
Kx = S.Kx;
Ky = S.Ky;
end

GSM = zeros(N); % random optical field
% sum over random pulses
for idx = 1 : length(t)
GSM = GSM + Theta .* Phi(t(idx)) .* exp(-1j*(Kx(idx)*x + Ky(idx)*y));
end

Sout = struct('t', t, 'Kx', Kx, 'Ky', Ky);

```

Listing C.7. Integrate38.m

```

function int = Integrate38(f, dx, dy, dz)
% int = Integrate38(f, dx, [dy], [dz])
%   Performs up to 3-dimensional integration based on regularly
%   spaced samples using Simpson's 3/8 rule.  If the number
%   of samples across one dimension is not one more than a multiple of
%   three, the final one or two sample intervals is integrated using
%   either the trapizoid rule or Simpson's rule respectively.
%
%   f:      Samples of the function to be integrated
%   dx:     Spacing between samples along the first index
%   dy:     Spacing between samples along the second index (defaults to dx)
%   dz:     Spacing between samples along the third index (defaults to dx
%           in multi-dimensional arrays)
%
%   int:    Integration result
%
% Created:  14 Jun 2010
% By:      Daniel J. Wheeler
% Modified: 26 Apr 2011

if nargin < 4 && size(f, 3) > 1, dz = dx; end
if nargin < 3 || isempty(dy),   dy = dx; end

[m,n,s] = size(f);
if m == 1
    Sm = 1; % no integration
elseif m == 2
    Sm = dx/2*[1 1]; % Trapizoid rule
elseif m == 3
    Sm = dx/3*[1 4 1]; % Simpson's rule
elseif mod(m, 3) == 1
    Sm = 3*dx/8*[1 repmat([3 3 2], 1, (m-4)/3) 3 3 1]; % 3/8 rule
elseif mod(m, 3) == 2
    Sm = 3*dx/8*[1 repmat([3 3 2], 1, (m-5)/3) 3 3 7/3 4/3];% w/ Trapizoid
else
    Sm = 3*dx/8*[1 repmat([3 3 2], 1, (m-6)/3) 3 3 17/9 32/9 8/9];% w/ Simp
end

if n == 1
    Sn = 1; % no integration
elseif n == 2

```

```

        Sn = dy/2*[1;1];                                % Trapezoid rule
elseif n == 3
        Sn = dy/3*[1;4;1];                              % Simpson's rule
elseif mod(n, 3) == 1
        Sn = 3*dy/8*[1;repmat([3;3;2], (n-4)/3, 1);3;3;1]; % 3/8 rule
elseif mod(n, 3) == 2
        Sn = 3*dy/8*[1;repmat([3;3;2], (n-5)/3, 1);3;3;7/3;4/3];% w/ Trapezoid
else
        Sn = 3*dy/8*[1;repmat([3;3;2], (n-6)/3, 1);3;3;17/9;32/9;8/9];% w/ Simp
end

if s == 1
        Ss = 1;                                        % no integration
elseif s == 2
        Ss = dz/2*[1;1];                              % Trapezoid rule
elseif s == 3
        Ss = dz/3*[1;4;1];                              % Simpson's rule
elseif mod(s, 3) == 1
        Ss = 3*dz/8*[1;repmat([3;3;2], (s-4)/3, 1);3;3;1]; % 3/8 rule
elseif mod(s, 3) == 2
        Ss = 3*dz/8*[1;repmat([3;3;2], (s-5)/3, 1);3;3;7/3;4/3];% w/ Trapezoid
else
        Ss = 3*dz/8*[1;repmat([3;3;2], (s-6)/3, 1);3;3;17/9;32/9;8/9];% w/ Simp
end

int = zeros(1, s);
for ind = 1:s
        int(ind) = Sm*f(:, :, ind)*Sn;
end
int = int*Ss;

```

Listing C.8. `intvec.m`

```

function I = intvec(fun,y,a,b)
% I = intvec(fun,a,b)
% Performs the integration of a function over a vector input. Uses
% quadgk as a basis.
%
% fun:    Function handle with two inputs. The first is for the variable
%         of integration, and the second is for a variable parameter.
% y:     Input vector of the variable parameter

```

```

% a:      Starting point of integration
% b:      Ending point of integration
%
% I:      Integration results
%
% Created: 12 May 2011
% By: Daniel J. Wheeler

if length(a(:)) == 1, a = a*ones(size(y)); end
if length(b(:)) == 1, b = b*ones(size(y)); end

I = zeros(size(y));
for ind = 1:length(y(:))
    I(ind) = quadgk(@(x)fun(x,y(ind)),a(ind),b(ind));
end

```

Listing C.9. PhaseScrnGen.m

```

function phz = PhaseScrnGen(N ,dx, wind, time, rndstr, PSD, l0, L0, lg, ...
    sub)
% phz = PhaseScrnGen(N,dx,[wind],[time],[randstr],[PSD],[l0],[L0],[lg], ...
%     [sub])
% Generates a NxN random phase screen based on a normalized coherence
% length and a given sample spacing and power spectral density model.
% Assumes frozen turbulence flow. To produce a phase screen with a given
% r0, multiply the resulting screen by r0-5/6.
%
% N:      Propagation grid size (assumed to be even)
% dx:     Grid sample spacing [m]
% wind:   Wind velocity vector [m/s] (defaults to [0,0])
% time:   Propagation time (defaults to 0) [s]
% rndstr: Random number stream used to generate phase screens
%         (defaults to DefaultStream)
% PSD:   PSD model used to calculate each phase screen. Can be any
%         of the following:
%         'Kolmogorov': Kolmogorov power law (default)
%         'von Karman': Kolmogorov power law with inner and outer
%                       scale effects
%         'Atmospheric': Kolmogorov power law with inner, outer, and
%                       Hill bump effects
%         'Gaussian':   Gaussian power law

```

```

%           'Vacuum':          No turbulence (default for any other entry)
%  l0:      Inner scale size (defaults to 0) [m]
%  L0:      Outer scale size (defaults to Inf) [m]
%  lg:      Coherence radius for Gaussian spectrum [m] (1 sigma)
%           (defaults to 1)
%  sub:     Number of sub-harmonics to add to phase screen (defaults to 0)
%
%  phz:     Random phase screen
%
% Created:  19 Apr 2010
% Modified:  9 Aug 2010
% By:       Daniel J. Wheeler

if nargin<10 || isempty(sub),      sub = 0;          end
if nargin<9  || isempty(lg),      lg = 1;          end
if nargin<8  || isempty(L0),     L0 = Inf;        end
if nargin<7  || isempty(l0),     l0 = 0;          end
if nargin<6  || isempty(PSD),    PSD = 'Kolmogorov'; end
if nargin<5  || isempty(rndstr),  rndstr = RandStream.getDefaultStream; end
if nargin<4  || isempty(time),    time = 0;       end
if nargin<3  || isempty(wind),    wind = [0 0];    end

dkappa = 2*pi/(N*dx);
kx = (-N/2:N/2-1)*dkappa;
ky = kx';
kappa_x = kx(ones(N,1),:);
kappa_y = ky(:,ones(1,N));
kappa2 = kappa_x.^2 + kappa_y.^2;

switch lower(PSD)
    case 'kolmogorov'
        PSD_phi = 0.49 * kappa2.^(-11/6);
    case 'von karman'
        kappa_0 = 2*pi/L0;
        kappa_m = 5.92/l0;
        PSD_phi = 0.49 * exp(-kappa2/kappa_m^2) ...
            ./ (kappa2 + kappa_0^2).^(11/6);
    case 'atmospheric'
        kappa_0 = 2*pi/L0;
        kappa_l = 3.3/l0;
        PSD_phi = 0.49 * exp(-kappa2/kappa_l^2) ...
            .* (1+1.802*(sqrt(kappa2)/kappa_l)-0.254 ...

```



```

        *(sqrt(kappa2)/kappa_1).^(7/6)) ...
        ./ (kappa2 + kappa_0^2).^(11/6);
case 'gaussian'
    xi = sqrt(100); % argument of sqrt must be >> 1
    df = xi*lg/sqrt(2);
    dr = 2*sqrt(pi)*xi*df;
    PSD_phi = dr^2*exp(-kappa2*df^2)/(2*pi)^2;
otherwise
    phz = zeros(N);
    return
end
PSD_phi(N/2+1,N/2+1) = 0; % Zero mean phase screen

c = (randn(rndstr,N) + 1j*randn(rndstr,N)) .* sqrt(PSD_phi)*dkappa ...
    .* exp(-1j*time*(wind(1)*kappa_x + wind(2)*kappa_y));
phz = real(ift2(c, 1));

% Add in sub-harmonics
x = kappa_x*dx/dkappa;
y = kappa_y*dx/dkappa;
for p = 1:sub
    dk = 2*pi/(2^p*N*dx);
    kx = (-1:1)*dk;
    kx = kx(ones(3,1),:);
    ky = kx';
    k = sqrt(kx.^2 + ky.^2);

    switch lower(PSD)
        case 'kolmogorov'
            PSD_sh = 0.49 * k.^(-11/3);
        case 'von karman'
            PSD_sh = 0.49 * exp(-k.^2/kappa_m^2) ...
                ./ (k.^2 + kappa_0^2).^(11/6);
        case 'atmospheric'
            PSD_sh = 0.49 * exp(-k.^2/kappa_l^2) ...
                .* (1 + 1.802*(k/kappa_l) - 0.254*(k/kappa_l).^(7/6)) ...
                ./ (k.^2 + kappa_0^2).^(11/6);
        case 'gaussian'
            PSD_sh = dr^2*exp(-(k*df).^2)/(2*pi)^2;
    end
    PSD_sh(2,2) = 0;

```

```

cn = (randn(rndstr,3) + 1j*randn(rndstr,3)) .* sqrt(PSD_sh)*dk ...
    .* exp(-1j*time*(wind(1)*kx + wind(2)*ky));
for ind = 1:9
    phz = phz + real(cn(ind) * exp(1j*(kx(ind)*x + ky(ind)*y)));
end
end
phz = phz - mean(phz(:));

```

Listing C.10. PointSource.m

```

function point = PointSource(N, dl, dn, D, lambda, L, theta_x, theta_y)
% point = PointSource(N, dl, dn, D, lambda, L, [theta_x], [theta_y])
% Creates a point beacon based on the desired receiver plane parameters.
% Vacuum propagation results in a super-Gaussian irradiance pattern with
% parabolic plus linear phase.
%
% N:      Number of samples across square propagation grid (must be even)
% dl:     Sample spacing in the source plane [m]
% dn:     Sample spacing in the observation plane [m]
% D:      Diameter of illuminated region at receiver plane [m]
% lambda: Wavelength of field
% L:      Distance between source and observation planes [m]
% theta_x: Angular offset of point source in the x-direction [rad]
%          (defaults to 0 rad)
% theta_y: Angular offset of point source in the y-direction [rad]
%          (defaults to 0 rad)
%
% point:  Structure that holds the parameters that define the point
%          source beacon
%
% Created: 17 Apr 10
% Modified: 28 Apr 10
% By: Daniel J. Wheeler

if nargin<8 || isempty(theta_y), theta_y = 0; end
if nargin<7 || isempty(theta_x), theta_x = 0; end

x = (-N/2:N/2-1)*dn;
y = x';
xn = x(ones(N,1),:);

```

```

yn = y(:,ones(1,N));
r2 = xn.^2 + yn.^2;
field = exp(-(2/D)^100*r2.^50) ...
    .* exp(2j*pi/lambda*(r2/2/L - xn*tan(theta_x) - yn*tan(theta_y)));

point.field = AngSpecProp(field, lambda, dn, d1, -L);
point.lam = lambda;
point.d1 = d1;
point.dn = dn;
point.L = L;

```

Listing C.11. PropHorizTurb.m

```

function receive = PropHorizTurb(source, turb, rho, a1, a2, time, ...
    rndstr, PSD, l0, L0, sub)
% received = PropHorizTurb(source, turb, [rho],[a1],[a2],[time], ...
%     [rndstr],[PSD],[l0],[L0],[sub])
% Models horizontal propagation of a complex field through constant
% turbulence based of the contents of source and turb. Assumes frozen
% turbulence flow.
%
% source:      Structure defining the source field of the propagation.
%              Must contain the following fields:
%              field:  NxN complex field
%              d1:     Sample spacing in source plane [m]
%              dn:     Sample spacing in observation plane [m]
%              lam:    Wavelength of the field [m]
% turb:        Structure defining the constant turbulence model.
%              Must contain the following fields:
%              L:      Total propagation distance [m]
%              r0i:    Column vector containing r0 for each phase screen
%                    [m]
%              loc:    Row vector containing locations for each phase
%                    screen [m]
%              lam:    Wavelength of the field [m]
%              wind:   Wind velocity vector [m/s]
% rho:         Radius of transmission area [pix] (defaults to Inf)
% a1:          Extinction coefficient in absorbtion area (defaults to 25)
% a2:          Width of transition area [pix] (defaults to 1)
% time:        Propagation time (defaults to 0) [s]
% rndstr:      Random number stream used to generate phase screens

```

```

%           (defaults to DefaultStream)
% PSD:      PSD model used to calculate each phase screen.  Can be any
%           of the following:
%           'Kolmogorov':   Kolmogorov power law (default)
%           'von Karman':   Kolmogorov power law with inner and outer
%                           scale effects
%           'Atmospheric': Kolmogorov power law with inner, outer, and
%                           Hill bump effects
%           'Vacuum':       No turbulence (default for any other entry)
% l0:       Inner scale size (defaults to 0) [m]
% L0:       Outer scale size (defaults to Inf) [m]
%
% receive:   Complex field after atmospheric propagation
%
% Created:   19 Apr 2010
% Modified:  28 Apr 2010
% By:       Daniel J. Wheeler

if nargin<11 || isempty(sub),      sub = 0;                end
if nargin<10 || isempty(L0),      L0 = Inf;                end
if nargin<9  || isempty(l0),      l0 = 0;                end
if nargin<8  || isempty(PSD),     PSD = 'Kolmogorov';     end
if nargin<7  || isempty(rndstr),  rndstr = RandStream.getDefaultStream; end
if nargin<6  || isempty(time),    time = 0;              end
if nargin<5  || isempty(a2),      a2 = 1;                end
if nargin<4  || isempty(a1),      a1 = 25;               end
if nargin<3  || isempty(rho),     rho = Inf;              end

N = length(source.field);
if rho == Inf
    absorb = 0;
else
    absorb = AbsorptionBound(N, rho, a1 ,a2);
end

place = 0;          % Keeps track of location along propagation path
count = 1;
if turb.loc(1) == place          % In case phase screen exists at source
    phase = PhaseScrnGen(N, source.dl, turb.wind, time, ...
        rndstr, PSD, l0, L0, sub);
    field = source.field .* exp(absorb + 1j*phase*turb.r0i(1)^(-5/6));
    count = count+1;
end

```

```

else
    field = source.field;
end

d1 = source.d1;
for ind = count:length(turb.loc)    % Propagate to each phase screen
    d2 = (source.dn-source.d1)/turb.L*turb.loc(ind) + source.d1;
    field = AngSpecProp(field, source.lam, d1, d2, turb.loc(ind)-place);
    phase = PhaseScrnGen(N, d2, turb.wind, time, rndstr, PSD, l0, L0, sub);
    field = field .* exp(absorb + 1j*phase*turb.r0i(ind)^(-5/6));
    place = turb.loc(ind);
    d1 = d2;
end

if place < turb.L    % Final propagation
    receive = AngSpecProp(field, source.lam, d1, source.dn, turb.L-place);
else
    receive = field;
end
end

```

Listing C.12. SMF_coupling_hard.m

```

function eta = SMF_coupling_hard(D, wg, pg, lam, Rg, A)
% eta = SMF_coupling_hard(D, wg, pg, [Rg], [A])
% Gives mean coupling efficiency for a Gaussian Schell-model beam into a
% single-mode optical fiber assuming an on-axis circular aperture. All
% inputs must be either scalars or the same size for non-scalars.
%
% D:      Diameter of circular aperture [m]
% wg:     Average Gaussian beam radius (1/e point of field) [m]
% pg:     Spatial coherence radius of beam (1/e point) [m]
% lam:    Center wavelength of field [m]
% Rg:     Average beam radius of curvature (>0 diverging, <0 converging,
%         Inf collimated [default]) [m]
% A:      Coupling geometry (A = pi D Wm/(2 lam f)) (defaults to 1.121)
%
% eta:    Coupling efficiency
%
% Created: 24 Jan 2011
% By: Daniel J. Wheeler
% Modified: 28 Jan 2011

```

```

if nargin < 6 || isempty(A), A = 1.120906422778534; end
if nargin < 5 || isempty(Rg), Rg = Inf; end
B = (D/2./wg).^2 + (D/2./pg).^2 + A.^2 + 1j*pi*D.^2/4./lam./Rg;
eta = zeros(size(pg));
if matlabpool('size') == 0
    matlabpool open
    parfor ind = 1:length(pg(:))
        eta(ind) = summation(D, pg, B, ind);
    end
    matlabpool close
else
    for ind = 1:length(pg(:))
        eta(ind) = summation(D, pg, B, ind);
    end
end

if length(wg) == 1 && ~isinf(wg)
    eta = 2*(D/2/wg).^2 ./ (1 - exp(-2*(D/2/wg).^2)) .* eta;
elseif length(wg) > 1
    ind = ~isinf(wg);
    if length(D) == 1
        eta(ind) = 2*(D/2./wg(ind)).^2 ...
            ./ (1 - exp(-2*(D/2./wg(ind)).^2)) .* eta(ind);
    else
        eta(ind) = 2*(D(ind)/2./wg(ind)).^2 ...
            ./ (1 - exp(-2*(D(ind)/2./wg(ind)).^2)) .* eta(ind);
    end
end
eta = 2*A.^2 .* eta;

function s = summation(D, pg, B, ind)
s = 0;
p = 0;
while 1
    sp = abs(exp(p*log(D/2/pg(ind)) - gammaln(p+2)/2) ...
        * sqrt(hypergeom(1+p, 2+p, -B(ind))))^4;
    if isinf(sp) || isnan(sp) || sp < eps(s), break, end
    s = s + sp;
    p = p+1;
end

```

Listing C.13. SMF_normvar_full_speckle.m

```

function normvar = SMF_normvar_full_speckle(D, wg, pg)
% normvar = SMF_normvar_full_speckle(D, wg, pg)
%   Calculates normalized variance of a Gaussian Schell-model beam with
%   fully developed speckle coupling into a single-mode optical fiber
%   assuming an on-axis circular aperture.
%   All inputs must be either scalars or the same size for non-scalars.
%
%   D:           Diameter of circular aperture [m]
%   wg:          Average Gaussian beam radius (1/e point of field) [m]
%   pg:          Spatial coherence radius of beam (1/e point) [m]
%
%   normvar:     Normalized variance of coupling efficiency
%
% Created:   27 Jan 2011
% By:       Daniel J. Wheeler
% Modified: 28 Jan 2011

B = 2*(D/2./wg).^2 + 2*(D/2./pg).^2;
I2 = wg.^2.*(1 - exp(-2*(D/2./wg).^2));
if length(wg) == 1 && isinf(wg)
    I2 = D.^2/4;
elseif length(wg) > 1
    if length(D) == 1
        I2(isinf(wg)) = D^2/2;
    else
        I2(isinf(wg)) = D(isinf(wg)).^2/2;
    end
end

I3 = zeros(size(pg));
if matlabpool('size') == 0
    matlabpool open
    parfor ind = 1:length(pg(:))
        I3(ind) = summation(D, pg, B, ind);
    end
    matlabpool close
else
    for ind = 1:length(pg(:))
        I3(ind) = summation(D, pg, B, ind);
    end
end
end

```

```

I3 = D.^4/4 .* I3;
normvar = (I2.^2 - I3) ./ (I2.^2 + I3);

function s = summation(D, pg, B, ind)
s = 0;
p = 0;
while 1
    sp = (exp(p*log(D/sqrt(2)/pg(ind)) - gammaln(p+2)/2) ...
    * sqrt(hypergeom(1+p, 2+p, -B(ind))))^4;
    if isinf(sp) || isnan(sp) || sp < eps(s), break, end
    s = s + sp;
    p = p+1;
end

```

Listing C.14. SRIsim.m

```

function [out, err, b0] = SRIsim(fields, nSubAp, dx, td, D, d, lam, a, ...
    V, f, beta, etaq)
% [out,err,b0] = SRIsim(fields,nSubAp,dx,td,D,d,lam,a,V,f,beta,etaq)
% Simulates the performance of a self-referencing interferometer. Only
% includes the effects of shot noise.
%
% fields: 3-D array of fields that represent the spatial and temporal
%         sampling of the incident field during the detector integration
%         time. The first two demensions represent the spatial sampling,
%         while the third represents temporal sampling, assumed to be
%         equally sampled across detector integration time. (Spatial
%         demensions assumed to be square.)
% nSubAp: The number of subapertures across the detector (assumed even)
% dx:     Field spatial sampling size [m]
% td:     Detector integration time [s]
% D:      Receiver diameter (assumed circular) [m]
% d:      Subaperture width (assumed square and multiple of dx) [m]
% lam:    Center wavelength of field [m]
% a:      Single-mode fiber core radius [m]
% V:      Single-mode fiber normalized frequency
% f:      Fiber coupling lens focal length (assumed to be equivalent on
%         input and output of fiber)
% beta:   Fractional input power allocated to the signal path
% etaq:   Detector quantum efficiency
%

```



```

% out:      SRI phase measurements
% err:      Phase measurement error
% b0:      Coupling coefficient
%
% Created:   18 Apr 2011
% By:       Daniel J. Wheeler
% Modified:  29 Apr 2011

[~, N, Nt] = size(fields); % size of input field grid
Nd = round(nSubAp*d/dx)+1; % grid size of detector area
h = 6.62606896e-34;        % Planck's constant [J s]
c = 299792458;            % speed of light [m/s]
alpha = etaq/h/c*lam;     % converts integrated intensity to average counts
if mod(N,2) == 0
    [x, y] = meshgrid((-N/2 : N/2-1) * dx);
else
    [x, y] = meshgrid(-(N-1)/2 : (N-1)/2) * dx);
end
r = sqrt(x.^2 + y.^2);
mask = (r <= D/2);
options = optimset('Display', 'off', 'TolFun', eps);
sol = fsolve(@(x)uwEval(x, V), [1 1], options);
u = sol(1); w = sol(2);
k = 2*pi/lam;
M0 = k*a*w*V/sqrt(pi)/f * (u*besselj(0, k*a*r/f) - k*a*r/f*besselj(0, u) ...
    / besselj(1, u).*besselj(1, k*a*r/f)) ./ (u^2 - (k*a*r/f).^2) ...
    ./ (w^2 + (k*a*r./f).^2); % reference field amplitude shape
M0ref = zeros(Nd);
M0ref(:) = M0(abs(x) <= nSubAp*d/2 & abs(y) <= nSubAp*d/2);

% pre-allocate memory
Uin = zeros(Nd);
I1 = zeros([size(Uin) Nt]);
I2 = I1;
I3 = I1;
I4 = I1;
phi = I1;
b0 = zeros(1,Nt);
for ind = 1:Nt % determine intensity profile at detector
    U0 = fields(:, :, ind);
    b0(ind) = Integrate38(U0 .* M0 .* mask, dx);
    Uin(:) = U0(abs(x) <= nSubAp*d/2 & abs(y) <= nSubAp*d/2);
end

```

```

I1(:, :, ind) = abs(sqrt(beta)*Uin + sqrt(1-beta)*b0(ind)*M0ref ...
    *exp(-0j*pi/2)).^2/4;
I2(:, :, ind) = abs(sqrt(beta)*Uin + sqrt(1-beta)*b0(ind)*M0ref ...
    *exp(-1j*pi/2)).^2/4;
I3(:, :, ind) = abs(sqrt(beta)*Uin + sqrt(1-beta)*b0(ind)*M0ref ...
    *exp(-2j*pi/2)).^2/4;
I4(:, :, ind) = abs(sqrt(beta)*Uin + sqrt(1-beta)*b0(ind)*M0ref ...
    *exp(-3j*pi/2)).^2/4;
phi(:, :, ind) = angle(Uin*exp(-1j*angle(b0(ind))));
end
% perform spatial and temporal integration and add shot noise
if Nt == 1
    K1avg = alpha*SubApIntegrate(I1, nSubAp, dx, 1)*td;
    K2avg = alpha*SubApIntegrate(I2, nSubAp, dx, 1)*td;
    K3avg = alpha*SubApIntegrate(I3, nSubAp, dx, 1)*td;
    K4avg = alpha*SubApIntegrate(I4, nSubAp, dx, 1)*td;
else
    K1avg = alpha*SubApIntegrate(I1, nSubAp, dx, td/(Nt-1));
    K2avg = alpha*SubApIntegrate(I2, nSubAp, dx, td/(Nt-1));
    K3avg = alpha*SubApIntegrate(I3, nSubAp, dx, td/(Nt-1));
    K4avg = alpha*SubApIntegrate(I4, nSubAp, dx, td/(Nt-1));
end
K1 = poissrnd(K1avg);
K2 = poissrnd(K2avg);
K3 = poissrnd(K3avg);
K4 = poissrnd(K4avg);

out = atan2(K4 - K2, K1 - K3);

err = out - atan2(K4avg - K2avg, K1avg - K3avg);
err(err > pi) = err(err > pi) - 2*pi;
err(err < -pi) = err(err < -pi) + 2*pi;

function F = uwEval(x, V)
% F = uwEval(x)
% This function is used to solve for the u and w of single-mode fibers
% using fsolve
%
% x: Vector for initial guesses of u (x(1)) and w (x(2))
% V: Normalized frequency of the single-mode fiber
%
% Created: 18 Apr 2011

```

```

% By: Daniel J. Wheeler

F = [x(1)^2 + x(2)^2 - V^2
     x(1) * besselj(1, x(1)) * besserk(0, x(2)) ...
     - x(2) * besserk(1, x(2)) * besselj(0, x(1))];

function M = SubApIntegrate(I, nSubAp, dx, dt)
% M = SubApIntegrate(I,nSubAp,dx)
% Uses Simpson's 3/8 rule to spatially and temporally integrate over each
% subaperture. Assumes the field covers the detector region of interest,
% and the third index represents the temporal demension.
%
% I:      Intensity field to be integrated
% nSubAp: Number of subapertures across the detector
% dx:     Spatial sample spacing
% dt:     Temporal sample spacing
%
% Created: 18 Apr 2011
% By: Daniel J. Wheeler
% Modified: 26 Apr 2011

M = zeros(nSubAp);
n = (size(I, 1)-1)/nSubAp;
for ind = 1:nSubAp
    for jnd = 1:nSubAp
        M(ind, jnd) = Integrate38(I(n*(ind-1)+1 : n*ind+1, ...
                                   n*(jnd-1)+1 : n*jnd+1, :), dx, dx, dt);
    end
end
end

```

Listing C.15. param2stats.m

```

function [r0 R rho0] = param2stats(Cn2, L, lam)
% [r0 R rho0] = param2stats(Cn2, L, lam)
% Calculates the statistical field characteristics for light from a point
% source beacon propagating through constant atmospheric turbulence
%
% Cn2:     Index-of-refraction structure function coefficient [m^-2/3]
% L:      Propagation distance [m]
% lam:    Wavelength of the field [m]
%

```

```

% r0: Atmospheric coherence length
% R: Rytov number
% rho0: Coherence radius
%
% By: Daniel J. Wheeler

k = 2*pi/lam;
r0 = (5^(11/6)*pi*gamma(2/3)/(2^(43/6)*3^(4/3)*(gamma(11/6))^2 ...
      *(gamma(6/5))^(5/6))*Cn2*k^2.*L).^(-3/5);
R = 9*(3-sqrt(3))*sqrt(pi)*gamma(2/3)*gamma(7/6)*gamma(11/6) ...
    /(64*2^(1/6)*gamma(1/3))*Cn2*k^(7/6).*L.^(11/6);
rho0 = (5*pi*gamma(2/3)/(2^(14/3)*3^(1/2)*(gamma(11/6))^2) ...
        *Cn2*k^2.*L).^(-3/5);

```

Listing C.16. stats2param.m

```

function [Cn2 L] = stats2param(r0, R, lam)
% [Cn2 L] = stats2param(r0, R, lam)
% Calculates the atmospheric turbulence parameters necessary to produce
% the desired field statistical characteristics. Assumes a point source
% beacon and constant turbulence.
%
% r0: Atmospheric coherence length
% R: Rytov number
% lam: Wavelength of the field [m]
%
% Cn2: Index-of-refraction structure function coefficient [m^-2/3]
% L: Propagation distance [m]
%
% By: Daniel J. Wheeler

k = 2*pi/lam;
alpha = 5^(11/6)*pi*gamma(2/3) ...
        /(2^(43/6)*3^(4/3)*(gamma(11/6))^2*(gamma(6/5))^(5/6));
beta = 9*(3-sqrt(3))*sqrt(pi)*gamma(2/3)*gamma(7/6)*gamma(11/6) ...
        /(2^(37/6)*gamma(1/3));
Cn2 = 1./(alpha^(11/5)*(R/beta).^(6/5)*k^3.*r0.^(11/3));
L = (alpha/beta*R).^(6/5)*k.*r0.^2;

```

Bibliography

- [1] Andrews, L. C., W. B. Miller, and J. C. Ricklin. "Spatial coherence of a Gaussian-beam wave in weak and strong optical turbulence". *J. Opt. Soc. Am. A*, 11(5):1653–1660, 1994.
- [2] Andrews, Larry C. and Ronald L. Phillips. *Laser Beam Propagation through Random Media*. SPIE Press, Bellingham, WA, second edition, 2005.
- [3] Barchers, Jeffrey D., David L. Fried, and Donald J. Link. "Evaluation of the performance of a shearing interferometer in strong scintillation in the absence of additive measurement noise". *Appl. Opt.*, 41(18):3674–3684, 2002.
- [4] Barchers, Jeffrey D., David L. Fried, and Donald J. Link. "Evaluation of the performance of Hartmann sensors in strong scintillation". *Appl. Opt.*, 41(6):1012–1021, 2002.
- [5] Barchers, Jeffrey D., David L. Fried, Donald J. Link, Glenn A. Tyler, William Moretti, Terry J. Brennan, and Robert Q. Fugate. "The performance of wavefront sensors in strong scintillation". *Proc. SPIE*, 4839:217–227, 2003.
- [6] Barchers, Jeffrey D. and Troy A. Rhoadarmer. "Evaluation of phase-shifting approaches for a point-diffraction interferometer with the mutual coherence function". *Appl. Opt.*, 41(36):7499–7509, 2002.
- [7] Belen'kiĭ, M. S., A. I. Kon, and V. L. Mironov. "Turbulent distortions of the spatial coherence of a laser beam". *Sov. J. Quantum Electron.*, 7(3):287–290, 1977.
- [8] Belen'kiĭ, M. S. and V. L. Mironov. "Coherence of the field of a laser beam in a turbulent atmosphere". *Sov. J. Quantum Electron.*, 10(5):595–597, 1980.
- [9] Belen'kii, M. S. and V. L. Mironov. "Mean diffracted rays of an optical beam in a turbulence medium". *J. Opt. Soc. Am.*, 70(2):159–163, 1980.
- [10] Belen'kii, M. S. and A. P. Shelekhov. "Phase fluctuations when focusing light in a turbulence atmosphere". *Radiophys. Quantum El.*, 26(12):1096–1101, 1983.
- [11] Belen'kii, Mikhail S., Jeff Barchers, Eric Bruns, Deborah Fung, Richard Gallant, Clay Kirk, Hope Runyeon, Vincent Rye, and Josh Voass. "Laboratory Demonstration of Wavefront Based Stochastic Parallel Gradient Descent Adaptive Optics System". *Proc. SPIE*, 6708:paper 67080I, 2007.
- [12] Beran, Mark. "Propagation of a Finite Beam in a Random Medium". *J. Opt. Soc. Am.*, 60(4):518–521, 1970.

- [13] Beran, Mark J. “Coherence equations governing propagation through random media”. *Radio Sci.*, 10(1):15–21, 1975.
- [14] Buck, John A. *Fundamentals of Optical Fibers*. Wiley-Interscience, Hoboken, NJ, 2004.
- [15] Cai, Yangjian, Olga Korotkova, Halil T. Eyyuboğlu, and Yahya Baykal. “Active radar systems with stochastic electromagnetic beams in turbulence atmosphere”. *Opt. Express*, 16(20):15834–15846, 2008.
- [16] Casella, George and Roger L. Berger. *Statistical Inference*. Duxbury, Pacific Grove, CA, second edition, 2002.
- [17] Chen, Chunyi, Huamin Yang, Hui Wang, Shoufeng Tong, and Yan Lou. “Coupling plane wave received by an annular aperture into a single-mode fiber in the presence of atmospheric turbulence”. *Appl. Opt.*, 50(3):307–312, 2011.
- [18] Chun, Mark. “The Useful Field of View on an Adaptive Optics System”. *Publ. Astron. Soc. Pac.*, 110(745):317–329, 1998.
- [19] Corley, Melissa S. and Troy A. Rhoadarmer. “Evaluation of phase-shifting techniques for a self-referencing interferometer wavefront sensor”. *Proc. SPIE*, 5894:paper 58940R, 2005.
- [20] Corrsin, Stanley. “On the spectrum of isotropic temperature fluctuations in an isotropic turbulence”. *J. Appl. Phys.*, 22(4):469–473, 1951.
- [21] Dashen, Roger. “Path integrals for waves in random media”. *J. Math. Phys.*, 20(5):894–920, 1979.
- [22] deWolf, D. A. “Saturation of Irradiance Fluctuations Due to Turbulent Atmosphere”. *J. Opt. Soc. Am.*, 58(4):461–466, 1968.
- [23] Dikmelik, Yamaç and Frederic Davidson. “Fiber-coupling efficiency for free-space optical communication through atmospheric turbulence”. *Appl. Opt.*, 44(23):4946–4952, 2005.
- [24] Drexler, Kyle, Michael Roggemann, and David Voelz. “Use of a partially coherent transmitter beam to improve the statistics of received power in a free-space optical communication system: theory and experimental results”. *Opt. Eng.*, 50(2):025002 (7 pp), 2011.
- [25] Ellis, Troy R. *Shack-Hartmann and Interferometric Hybrid Wavefront Sensor*. Ph.D. thesis, Air Force Institute of Technology, 2011.
- [26] Eyyuboğlu, Halil T., Yahya Baykal, and Yangjian Cai. “Complex degree of coherence for partially coherent general beams in atmospheric turbulence”. *J. Opt. Soc. Am. A*, 24(9):2891–2901, 2007.

- [27] Fante, Ronald L. “Mutual coherence function and frequency spectrum of a laser beam propagating through atmospheric turbulence”. *J. Opt. Soc. Am.*, 64(5):592–598, 1974.
- [28] Frehlich, Rod G. and Michael J. Kavaya. “Coherent laser radar performance for general atmospheric refractive turbulence”. *Appl. Opt.*, 30(36):5325–5352, 1991.
- [29] Fried, D. L. “Optical Resolution Through a Randomly Inhomogeneous Medium for Very Long and Very Short Exposures”. *J. Opt. Soc. Am.*, 56(10):1372–1379, 1966.
- [30] Fried, David L. “Anisoplanatism in adaptive optics”. *J. Opt. Soc. Am.*, 72(1):52–61, 1982.
- [31] Fried, David L. “Branch point problem in adaptive optics”. *J. Opt. Soc. Am. A*, 15(10):2759–2768, 1998.
- [32] Fried, David L. “Scaling laws for propagation through turbulence”. *Atmos. Oceanic Opt.*, 11(11):982–990, 1998.
- [33] Fried, David L. “Adaptive optics wave function reconstruction when branch points are present”. *Opt. Commun.*, 200:43–72, 2001.
- [34] Fried, David L. and Jeffrey L. Vaughn. “Branch cuts in the phase function”. *Appl. Opt.*, 31(15):2865–2882, 1992.
- [35] Furutsu, K. “Statistical Theory of Wave Propagation in a Random Medium and the Irradiance Distribution Function”. *J. Opt. Soc. Am.*, 62(2):240–254, 1972.
- [36] Gbur, Greg. “Simulating fields of arbitrary spatial and temporal coherence”. *Opt. Express*, 14(17):7567–7578, 2006.
- [37] Gbur, Greg and Emil Wolf. “Spreading of partially coherent beams in random media”. *J. Opt. Soc. Am. A*, 19(8):1592–1598, 2002.
- [38] Goodman, Joseph W. *Statistical Optics*. Wiley-Interscience, New York, NY, 1985.
- [39] Goodman, Joseph W. *Introduction to Fourier Optics*. Roberts & Company, Englewood, CO, third edition, 2005.
- [40] Goodman, Joseph W. *Speckle Phenomena in Optics: Theory and Applications*. Roberts & Company, Englewood, CO, 2007.
- [41] Gori, F, M Santarsiero, G Piquero, R Borghi, A Mondello, and R Simon. “Partially polarized Gaussian Schell-model beams”. *J. Opt. A: Pure Appl. Opt.*, 3(1):1–9, 2001.

- [42] Gradshteyn, I. S. and I. M. Ryzhik. *Table of Integrals, Series, and Products*. Academic Press, San Diego, CA, sixth edition, 2000.
- [43] Ishimaru, Akira. *Wave Propagation and Scattering in Random Media*. IEEE Press, New York, NY, 1997.
- [44] Jackson, John David. *Classical Electrodynamics*. Wiley, Hoboken, NJ, third edition, 1999.
- [45] Jacob, Donald K., Martin B. Mark, and Bradley D. Duncan. “Heterodyne ladar system efficiency enhancement using single-mode optical fiber mixers”. *Opt. Eng.*, 34(11):3122–3129, 1995.
- [46] Janesick, James R. *Scientific Charge-Coupled Devices*. SPIE Press, Bellingham, WA, 2001.
- [47] Ji, Xiaoling and Xiaoqing Li. “Effective radius of curvature of partially coherent Hermite-Gaussian beams propagating through atmospheric turbulence”. *J. Opt.*, 12:035403 (5pp), 2010.
- [48] Kolmogorov, Andrei N. “The local structure of turbulence in an incompressible viscous fluid for very large Reynolds numbers”. *C. R. (Doki) Acad. Sci. U.S.S.R.*, 30:301–305, 1941.
- [49] Korotkova, Olga, Larry C. Andrews, and Ronald L. Phillips. “Model for a partially coherent Gaussian beam in atmospheric turbulence with application in Lasercom”. *Opt. Eng.*, 43(2):330–341, 2004.
- [50] Korotkova, Olga and Emil Wolf. “Changes in the state of polarization of a random electromagnetic beam on propagation”. *Opt. Commun.*, 246:35–43, 2005.
- [51] Lane, R. G., A. Glindemann, and J. C. Dainty. “Simulation of a Kolmogorov phase screen”. *Waves Random Media*, 2:209–224, 1992.
- [52] Lazzaroni, Massimo and Fabio E. Zocchi. “Optical coupling from plane wave to step-index single-mode fiber”. *Opt. Commun.*, 237:37–43, 2004.
- [53] Leader, J. Carl. “Atmospheric propagation of partially coherent radiation”. *J. Opt. Soc. Am.*, 68(2):175–185, 1978.
- [54] Lutmirski, R. F. and H. T. Yura. “Propagation of a Finite Optical Beam in an Inhomogeneous Medium”. *Appl. Opt.*, 10(7):1652–1658, 1971.
- [55] Ma, Jing, Fang Zhao, Liying Tan, Siyuan Yu, and Yuqiang Yang. “Degradation of single-mode fiber coupling efficiency due to localized wavefront aberrations in free-space laser communications”. *Opt. Eng.*, 49(4):045004 (6 pp), 2010.

- [56] Malacara, Daniel. *Optical Shop Testing*. Wiley, Hoboken, NJ, third edition, 2007.
- [57] Mandel, Leonard and Emil Wolf. *Optical Coherence and Quantum Optics*. Cambridge University Press, New York, NY, 1995.
- [58] Marcuse, D. “Loss analysis of single-mode fiber splices”. *Bell System Tech. J.*, 56(5):703–718, 1977.
- [59] Marcuse, D. “Gaussian approximation of the fundamental modes of graded-index fibers”. *J. Opt. Soc. Am.*, 68(1):103–109, 1978.
- [60] Notaras, James and Carl Paterson. “Point-diffraction interferometer for atmospheric adaptive optics in strong scintillation”. *Opt. Commun.*, 281:360–367, 2008.
- [61] Obukhov, A. M. “Structure of the temperature field in turbulent flow”. *Izv. Acad. Nauk. SSSR, Ser. Geogr. I Geofiz.*, 13(1):58–69, 1949.
- [62] Papoulis, Athanasios and S. Unnikrishna Pillai. *Probability, Random Variables, and Stochastic Processes*. McGraw-Hill, New York, NY, fourth edition, 2002.
- [63] Platt, Ben C. and Roland Shack. “History and Principles of Shack-Hartmann Wavefront Sensing”. *J. Refract. Surg.*, 17:S573–S577, 2001.
- [64] Ragazzoni, Roberto. “Pupil plane wavefront sensing with an oscillating prism”. *J. Mod. Opt.*, 43(2):289–293, 1996.
- [65] Rhoadarmer, Troy A. “Development of a self-referencing interferometer wavefront sensor”. *Proc. SPIE*, 5553:112–126, 2004.
- [66] Rhoadarmer, Troy A. and Jeffrey D. Barchers. “Noise analysis for complex field estimation using a self-referencing interferometer wave front sensor”. *Proc. SPIE*, 4825:215–227, 2002.
- [67] Rhoadarmer, Troy A. and Laura M. Klein. “Design of a spatially phase shifted self-referencing interferometer wave front sensor”. *Proc. SPIE*, 6306:63060K (12pp), 2006.
- [68] Ricklin, Jennifer C. and Frederic M. Davidson. “Atmospheric turbulence effects on a partially coherent Gaussian beam: implications for free-space laser communication”. *J. Opt. Soc. Am. A*, 19(9):1794–1802, 2002.
- [69] Riker, Jim F. “Scientific Advisory Board Beam Control Challenge—aka: Horizontal Propagation Compensation (HPC)”. AFRL/DES Technical Director Briefing on 15 May 2007.

- [70] Rimmele, Thomas R. “Recent advances in solar adaptive optics”. *Proc. SPIE*, 5490:34–46, 2004.
- [71] Roddier, François. “Curvature sensing and compensation: a new concept in adaptive optics”. *Appl. Opt.*, 27(7):1223–1225, 1988.
- [72] Roggemann, Michael C. “Fundamental considerations for wave front sensing with extended random beacons”. *Proc. SPIE*, 5552:189–199, 2004.
- [73] Roggemann, Michael C. and Byron M. Welsh. *Imaging Through Turbulence*. CRC Press, New York, NY, 1996.
- [74] Ruilier, C. “A study of degraded light coupling into single-mode fibers”. *Proc. SPIE*, 3350:319–329, 1998.
- [75] Ruilier, Cyril and Frédéric Cassaing. “Coupling of large telescopes and single-mode waveguides: application to stellar interferometry”. *J. Opt. Soc. Am. A*, 18(1):143–149, 2001.
- [76] Salem, M., T. Shirai, A. Dogariu, and E. Wolf. “Long-distance propagation of partially coherent beams through atmospheric turbulence”. *Opt. Commun.*, 216:261–265, 2003.
- [77] Sasiela, Richard J. *Electromagnetic Wave Propagation in Turbulence*. SPIE Press, Bellingham, WA, second edition, 2007.
- [78] Schell, A. C. *The Multiple Plate Antenna*. Doctoral dissertation, Massachusetts Institute of Technology, 1961.
- [79] Shaklan, Stuart and Francois Roddier. “Coupling starlight into single-mode fiber optics”. *Appl. Opt.*, 27(11):2334–2338, 1988.
- [80] Shirai, Tomohiro, Aristide Dogariu, and Emil Wolf. “Mode analysis of spreading of partially coherent beams propagating through atmospheric turbulence”. *J. Opt. Soc. Am. A*, 20(6):1094–1102, 2003.
- [81] Skellam, J. G. “The Frequency Distribution of the Difference Between Two Poisson Variates Belonging to Different Populations”. *J. R. Stat. Soc.*, 109(3):296, 1946.
- [82] Tatarskii, V. I. *The Effects Of The Turbulent Atmosphere On Wave Propagation*. U. S. Department Of Commerce, 1971.
- [83] Toyoshima, Morio. “Maximum fiber coupling efficiency and optimum beam size in the presence of random angular jitter for free-space laser systems and their applications”. *J. Opt. Soc. Am. A*, 23(9):2246–2250, 2006.

- [84] Tyson, Robert K. *Principles of Adaptive Optics*. Academic Press, Boston, MA, second edition, 1998.
- [85] Voiteskhovich, Valerii V., Dmitri Kouznetsov, and Dmitri Kh. Morozov. “Density of turbulence-induced phase dislocations”. *Appl. Opt.*, 37(21):4525–4535, 1998.
- [86] Vorontsov, Mikhail, Jim Riker, Gary Carhart, V. S. Rao Gudimetla, Leonid Beresnev, Thomas Weyrauch, and Lewis C. Roberts, Jr. “Deep turbulence effects compensation experiments with a cascaded adaptive optics system using a 3.63 m telescope”. *Appl. Opt.*, 48(1):A47–A57, 2009.
- [87] Wagner, R. E. and W. J. Tomlinson. “Coupling efficiency of optics in single-mode fiber components”. *Appl. Opt.*, 21(15):2671–2688, 1982.
- [88] Wang, S. C. H. and M. A. Plonus. “Optical beam propagation for a partially coherent source in the turbulent atmosphere”. *J. Opt. Soc. Am.*, 69(9):1297–1304, 1979.
- [89] Weyrauch, Thomas and Mikhail A. Vorontsov. “Atmospheric compensation with a speckle beacon in strong scintillation conditions: directed energy and laser communication applications”. *Appl. Opt.*, 44(30):6388–6401, 2005.
- [90] Weyrauch, Thomas, Mikhail A. Vorontsov, John W. Gowens II, and Thomas G. Bifano. “Fiber coupling with adaptive optics for free-space optical communication”. *Proc. SPIE*, 4489:177–184, 2002.
- [91] Wheeler, Daniel J. and Jason D. Schmidt. “Coupling of Gaussian Schell-model beams into single-mode optical fibers”. *J. Opt. Soc. Am. A*, 28(6):1224–1238, 2011.
- [92] Wheeler, Daniel J. and Jason D. Schmidt. “Spatial coherence function of partially coherent Gaussian beams in atmospheric turbulence”. *Appl. Opt.*, 50(21):3907–3917, 2011.
- [93] Wilbur P. Brown, Jr. “Second Moment of a Wave Propagating in a Random Medium”. *J. Opt. Soc. Am.*, 61(8):1051–1059, 1971.
- [94] Winzer, Peter J. and Walter R. Leeb. “Fiber coupling efficiency for random light and its applications to lidar”. *Opt. Lett.*, 23(13):986–988, 1998.
- [95] Wolf, Emil. *Introduction to the Theory of Coherence and Polarization of Light*. Cambridge University Press, 2007.
- [96] Wu, J. and A. D. Boardman. “Coherence length of a Gaussian-Schell beam and atmospheric turbulence”. *J. Mod. Opt.*, 38(7):1355–1363, 1991.

- [97] Wu, Jian. “Propagation of a Gaussian-Schell beam through turbulent media”. *J. Mod. Opt.*, 37(4):671–684, 1990.
- [98] Wyant, J. C. “Use of an ac heterodyne lateral shear interferometer with real-time wavefront correction systems”. *Appl. Opt.*, 14(11):2622–2626, 1975.
- [99] Xiao, Xifeng and David Voelz. “Wave optics simulation approach for partial spatially coherent beams”. *Opt. Express*, 14(16):6986–6992, 2006.
- [100] Yura, H. T. “Mutual Coherence Function of a Finite Cross Section Optical Beam Propagating in a Turbulent Medium”. *Appl. Opt.*, 11(6):1399–1406, 1972.
- [101] Zhu, Xiaoming and Joseph M. Kahn. “Free-Space Optical Communication Through Atmospheric Turbulence Channels”. *IEEE T. Commun.*, 50(8):1293–1300, 2002.

REPORT DOCUMENTATION PAGE

*Form Approved
OMB No. 0704-0188*

The public reporting burden for this collection of information is estimated to average 1 hour per response, including the time for reviewing instructions, searching existing data sources, gathering and maintaining the data needed, and completing and reviewing the collection of information. Send comments regarding this burden estimate or any other aspect of this collection of information, including suggestions for reducing the burden, to Department of Defense, Washington Headquarters Services, Directorate for Information Operations and Reports (0704-0188), 1215 Jefferson Davis Highway, Suite 1204, Arlington, VA 22202-4302. Respondents should be aware that notwithstanding any other provision of law, no person shall be subject to any penalty for failing to comply with a collection of information if it does not display a currently valid OMB control number.

PLEASE DO NOT RETURN YOUR FORM TO THE ABOVE ADDRESS.

1. REPORT DATE (DD-MM-YYYY) 15-09-2011		2. REPORT TYPE Doctoral Dissertation		3. DATES COVERED (From - To) Aug 2008 - Sep 2011	
4. TITLE AND SUBTITLE Modeling Self-Referencing Interferometers with Extended Beacons and Strong Turbulence				5a. CONTRACT NUMBER	
				5b. GRANT NUMBER F1ATA08350J002	
				5c. PROGRAM ELEMENT NUMBER	
6. AUTHOR(S) Wheeler, Daniel J., Maj, USAF				5d. PROJECT NUMBER ENGJON293D	
				5e. TASK NUMBER	
				5f. WORK UNIT NUMBER	
7. PERFORMING ORGANIZATION NAME(S) AND ADDRESS(ES) Air Force Institute of Technology Graduate School of Engineering and Management (AFIT/EN) 2950 Hobson Way WPAFB OH 45433-7765				8. PERFORMING ORGANIZATION REPORT NUMBER AFIT/DEO/ENG/11-12	
9. SPONSORING/MONITORING AGENCY NAME(S) AND ADDRESS(ES) Air Force Office of Scientific Research Kent Miller 3875 Randolph St., Suite 3112 Arlington, VA 22203 (703) 696-8573, kent.miller@afosr.af.mil				10. SPONSOR/MONITOR'S ACRONYM(S) AFOSR/NE	
				11. SPONSOR/MONITOR'S REPORT NUMBER(S)	
12. DISTRIBUTION/AVAILABILITY STATEMENT APPROVED FOR PUBLIC RELEASE; DISTRIBUTION UNLIMITED.					
13. SUPPLEMENTARY NOTES This material is declared a work of the U.S. Government and is not subject to copyright protection in the United States.					
14. ABSTRACT The overall purpose of this research was to better understand the performance of a self-referencing interferometer (SRI) when used with extended beacons in strong atmospheric turbulence. It was performed by assuming the extended beacon could be modeled as a Gaussian Schell-model beam, then analyzing the effect of propagating this beam through strong atmospheric turbulence. Since the operation of an SRI requires coupling this light into a single-mode optical fiber, analytic expressions of the mean and normalized variance of the coupling efficiency were derived. An improved noise model for the SRI was then developed that included all potential noise sources such as intensity fluctuations of the incident light, the single-mode fiber coupling efficiency, the spatial and temporal coherence properties of the light, and other additive noise sources. Whenever simplifying assumptions were used, the results were compared to numerically evaluated exact expressions or Monte Carlo simulations. Any resulting error was identified then typically compensated.					
15. SUBJECT TERMS Self-Referencing Interferometer, Extended Beacon, Strong Turbulence, Statistical Optics, Coherence Theory, Single-Mode Optical Fiber, Gaussian Schell-Model Beam					
16. SECURITY CLASSIFICATION OF:			17. LIMITATION OF ABSTRACT UU	18. NUMBER OF PAGES 212	19a. NAME OF RESPONSIBLE PERSON Jason D. Schmidt, Maj, USAF (ENG)
a. REPORT U	b. ABSTRACT U	c. THIS PAGE U			19b. TELEPHONE NUMBER (Include area code) (937) 255-3636, x7224; jason.schmidt@afit.edu

